

**DISTRIBUTED PROCESS ORIENTED MODELLING OF THE FUTURE  
IMPACT OF GLACIER MELT WATER ON RUNOFF IN THE LHASA  
RIVER BASIN IN TIBET**

DISSERTATION AN DER FAKULTÄT FÜR GEOWISSENSCHAFTEN  
DER LUDWIG-MAXIMILIANS-UNIVERSITÄT MÜNCHEN

VORGELEGT VON DIPL. GEOGR. MONIKA PRASCH

EINGEREICHT AM 3. AUGUST 2010

1. Gutachter: Prof. Dr. Wolfram Mauser
2. Gutachter: Prof. Dr. Karsten Schulz

Tag der Disputation: 17. November 2010



*Nyainqêntanglha Mountains, Tibet (24.09.2006)*

## ACKNOWLEDGEMENTS

The accelerating worldwide retreat of glaciers during recent years is one of the clearest signs of ongoing climate change. As a symbol for the impact of Global Climate Change (GCC), glacier shrinkage has attracted attention of the general public. While further increases in air temperatures due to rising greenhouse gas concentrations in the atmosphere are commonly accepted, the future rate of recession of glaciers and their influence on fresh water supplies remains controversial. Glaciers in High Asia in particular have recently been brought into focus by discussion of the IPCC statement on Himalayan glacier retreat.

The research projects *Brahmatwinn*, supported by the European Commission's Sixth Framework Program, and *GLOWA-Danube*, funded by the German Federal Ministry of Education and Research, BMBF, focus on comprehensive analysis of future water availability in mountainous watersheds, including snow and ice. Prof. Dr. Wolfram Mauser as head of the Chair of Geography and Remote Sensing at the Department of Geography of the Ludwig-Maximilians-Universität of Munich offered me the opportunity to participate in these projects. The multidisciplinary nature of these projects and the project members provided me with a diversified and enjoyable atmosphere for the preparation of this thesis, which I gratefully acknowledge.

As my doctoral advisor, Prof. Dr. Wolfram Mauser shared his enthusiasm for hydrological modelling, and it was a great pleasure for me to be involved in the further development of the PROMET model. I would like to cordially thank him for his support and the confidence he placed in me. His encouraging comments enabled me to develop my own ideas. He not only supported the progress of the thesis, but he also gave me the chance to give student courses at the university.

The provision of observation data within the framework of the *GLOWA-Danube* and *Brahmatwinn* projects was an important and considerable help in the realisation of the thesis. I want to greatly acknowledge in particular the provision of the Glacier Inventory Data for the Upper Danube basin by the Commission for Glaciology of the Bavarian Academy of Sciences and Humanities, the University of Innsbruck and the University of Zurich. The International Centre for Integrated Mountain Development ICIMOD, the Institute of Tibetan Plateau Research ITP, the German Weather Service DWD and the Austrian Weather Service ZAMG are also appreciated for providing weather and runoff data.

I would also like to express deep thanks to Prof. Dr. Karsten Schulz for his generous acceptance of the efforts associated with the second review of this thesis.

I am deeply grateful to Prof. Dr. Ulrich Strasser for sharing his knowledge of snow and ice modelling with me. He also provided me with an insight into various scientific procedures and introduced me to Dr. Markus "Wasti" Weber of the Commission for Glaciology of the Bavarian Academy of Sciences and Humanities.

I want to express my great thanks to Dr. Markus "Wasti" Weber for intensively discussing the basics of the details of glacier modelling with me and for our constructive teamwork



with the SURGES glacier model. With his obliging help, many questions concerning glaciers were answered. It was a pleasure for me to work with him on the same issues.

Many thanks go to Dr. Heike Bach, Vista GmbH, for offering me insight into the groundwater and routing parameterization of PROMET and her interest in runoff modelling in the Lhasa River basin.

I am grateful to my mentor Prof. Dr. Bettina Reichenbacher of the *LMU Mentoring GeoSciences* for her interest in my progress.

My great thanks go to all my PhD-fellows, namely the PROMET group Dr. Tobias Hank, Dr. Markus Muerth, Dr. Daniel Waldmann and Dr. Thomas Marke for our fruitful discussions. Dr. Thomas Marke in particular deserves thanks for supporting me in using the downscaling tool SCALMET.

For their cooperation in giving field trips and lectures I want to thank Dr. Daniel Waldmann, Dr. Matthias Bernhardt and Dr. Christoph Heinzeller. The translation of the Chinese Geological Map by Lu Dong is greatly appreciated.

My cordial thanks go to my office mates Ruth Weidinger, Franziska Koch, and Andrea Reiter, who also checked my manuscript. It is a pleasure for me to have become good friends beyond work not only with them, but also with Andrea Ebner, Inga May, Susan Niebergall and Dr. Caro Weiss.

All other colleagues who are not explicitly mentioned here are however included in my thanks, especially for the diverse discussions during lunch and coffee breaks. The friendly and constructive environment in the group makes working together really enjoyable. Many thanks go to all current and former members for the positive atmosphere and the help in various issues.

Finally, my cordial thanks go to my family, especially to my dear husband Martin for his unlimited interest and understanding.

## TABLE OF CONTENTS

<b>Acknowledgements.....</b>	<b>IV</b>
<b>Table of Contents .....</b>	<b>VI</b>
<b>List of Figures.....</b>	<b>VIII</b>
<b>List of Tables .....</b>	<b>XV</b>
<b>List of Acronyms .....</b>	<b>XVII</b>
<b>List of Symbols.....</b>	<b>XIX</b>
<b>List of Statistical Symbols.....</b>	<b>XXII</b>
<b>1 Introduction .....</b>	<b>1</b>
1.1 Climate Change and Glaciers in the Himalayas .....	2
1.2 Scientific Objectives and Outline of the Thesis.....	3
<b>2 The Lhasa River Basin .....</b>	<b>6</b>
2.1 Geology and Geomorphology.....	7
2.2 Climatology .....	10
2.3 Hydrology.....	13
2.4 Soils.....	15
2.5 Land Cover and Land Use.....	16
2.6 Glaciers of the Lhasa River Catchment.....	17
<b>3 Distributed, Process Oriented Hydrological and Glacier Modelling.....</b>	<b>20</b>
3.1 The PROMET Hydrological Model.....	21
3.1.1 Meteorological Data Provision .....	22
3.1.2 Land Surface Energy and Mass Balances.....	24
3.1.3 Soil Processes .....	25
3.1.4 Groundwater Flows.....	25
3.1.5 Runoff Formation .....	26
3.2 The SURGES Glacier Model .....	26
3.2.1 Characteristics of Glaciers.....	26
3.2.2 Requirements for Glacier Modelling and State of the Art .....	28
3.2.3 Subscale Approach.....	29
3.2.4 Meteorological Data Extrapolation.....	31
3.2.5 Mass and Surface Energy Balance of the Glacier .....	33
3.2.6 Snow Metamorphism .....	36

---

3.2.7	Glacier Geometry Adjustment.....	37
3.2.8	Method Discussion .....	38
3.3	Technical Aspects.....	39
<b>4</b>	<b>Model Input Data for the Lhasa River Basin .....</b>	<b>41</b>
4.1	Meteorological Drivers .....	42
4.2	Land Surface Data Parameterization.....	43
4.3	Derivation of Glacier Input Data for SURGES .....	45
4.3.1	Data Basis .....	46
4.3.2	Glacier Area.....	46
4.3.3	Glacier Elevation.....	47
4.3.4	Ice Thickness.....	48
<b>5</b>	<b>Model Validation .....</b>	<b>53</b>
5.1	Validation of the SURGES Glacier Model.....	53
5.2	Validation of Glacier Input Data Derivation.....	61
5.2.1	Glacier Area.....	61
5.2.2	Glacier Elevation.....	62
5.2.3	Ice Thickness.....	62
5.3	Validation of Model Results for the Lhasa Catchment.....	66
5.3.1	Meteorology.....	67
5.3.2	Glacier Mass Balance.....	76
5.3.3	River Runoff.....	80
<b>6</b>	<b>Model Results – The Impact of Future Climate Change .....</b>	<b>87</b>
6.1	The IPCC Future Climate Scenarios .....	87
6.2	Future Climatic Conditions in the Lhasa River Basin from 2001 to 2080 .....	89
6.3	Future Glacier Distribution and Ice Water Reservoir .....	100
6.4	Future Development of Snow- and Ice-Melt .....	106
6.5	The Future Water Balance.....	108
6.6	Analysis of the Influence of Ice-Melt on Runoff .....	113
<b>7</b>	<b>Conclusion and Outlook.....</b>	<b>125</b>
<b>8</b>	<b>Summary.....</b>	<b>129</b>
<b>9</b>	<b>References.....</b>	<b>132</b>
<b>10</b>	<b>Appendix.....</b>	<b>149</b>
<b>11</b>	<b>Curriculum Vitae .....</b>	<b>205</b>

## LIST OF FIGURES

Figure 2.1: Geographical position and topographic map of the Lhasa River (Kyi Chu) basin as sub basin of the Upper Brahmaputra catchment in Central Asia (based on ESRI (1999-2008), JARVIS ET AL. (2006) and REISE-KNOW-HOW VERLAG (2005)).....	6
Figure 2.2: Geological Map of the Lhasa River Catchment (modified to DAVIS ET AL. (2002) and CHEN (1990)).....	8
Figure 2.3: Relief of the Lhasa River Catchment based on the digital elevation model from the Shuttle Radar Topography Mission SRTM (JARVIS ET AL. 2006).....	9
Figure 2.4: Climatic sub-regions of the Lhasa River catchment with representative climate diagrams (based on CAS (1984) according to LEBER ET AL. (1995) and ICIMOD (2009)). .....	12
Figure 2.5: The Lhasa River basin with sub-basins and mean monthly runoff at the gauging stations Yangbajing, Pangdo, Tangga and Lhasa (based on ITP (2008), JARVIS ET AL. (2006), GARBRECHT AND MARTZ (1999)).....	13
Figure 2.6: Soil Units (FAO 90 classification system) in the Lhasa River catchment according to the Harmonized World Soil Database (version 1.1) (based on FAO ET AL. (2009)).....	15
Figure 2.7: German soil texture classes according to the Harmonized World Soil Database (version 1.1) and its percental distribution in the Lhasa River catchment (based on FAO ET AL. (2009)). .....	16
Figure 2.8: Land use and land cover distribution in the Lhasa River basin modified consistent with the NASA TERRA/MODIS land cover product (BOSTON UNIVERSITY 2004). .....	17
Figure 2.9: Distribution of glacier classes with illustrated examples in the Lhasa River basin (based on GOOGLE EARTH (2010), JARVIS ET AL. (2006), USGS (2009) and WDC (2009)).....	18
Figure 3.1: Correlation of the various spatial scales between the processes and the models applied to bridge the gap. ....	20
Figure 3.2: Schematic diagram of the components of PROMET and the interfaces between them. Boxes indicate components and arrows indicate interfaces through which data is exchanged (MAUSER AND BACH 2009, p.365). .....	22
Figure 3.3: Schematic diagram of SCALMET with required inputs and outputs (MARKE 2008, p. 41, modified).....	24
Figure 3.4: Meteorological and topographic characteristics determining the glacier mass balance (WEBER 2008, p. II, modified).....	27
Figure 3.5: Influencing factors for glacier modelling (OERLEMANS 2001, p. 2, modified). ..	29
Figure 3.6: Distribution of glaciers over several grid cells (left) and frequency distribution of glacier area per grid cell in the Lhasa River catchment (right) (based on WDC 2009).....	30

---

Figure 3.7: Illustration of the division of the glacier area into distinct levels (WEBER ET AL. 2009,p.10, modified).....	30
Figure 3.8: Scheme of implementation of the glacier model SURGES in PROMET, describing the spatial and temporal modelling cycle. ....	39
Figure 4.1: Distribution of parameterized land use and land cover classes in the Lhasa River basin, modified according to the NASA TERRA/MODIS land cover product (BOSTON UNIVERSITY 2004). ....	43
Figure 4.2: Intersected digital elevation model with glacier boundaries (left) and aggregated elevation levels of glaciers (right) (data source: ERSDAC 2009, WDC 2009).....	47
Figure 4.3: Area-elevation distribution of glaciers in the Lhasa River catchment.....	48
Figure 4.4: Relationship and coefficient of determination of the mean and maximum ice thickness of the glaciers in the Glockner, Venediger and Zillertaler mountain groups (map, left) according to the Upper Danube glacier inventory (based on WEBER ET AL. (2008A)).....	49
Figure 4.5: Decision tree for the derivation of the ice thickness distribution of the glaciers. ....	50
Figure 4.6: Example of the mean and distributed ice thicknesses of glaciers in the Lhasa River catchment, overlaid by the grid cell structure (based on ERSDAC (2009), WDC (2009)).....	51
Figure 4.7: Ice thickness - elevation distribution of the glaciers in the Lhasa River catchment.....	51
Figure 4.8: Flow chart of steps and data for the generation of the required input data to run the glacier model SURGES.....	52
Figure 5.1: Map of the test sites in the Upper Danube basin (based on: GLOWA-DANUBE (2001-2010), BAYERISCHE GLETSCHER (2009), WEBER ET AL. (2008A)). ....	53
Figure 5.2: Comparison of the evolution of the modelled snow water equivalent (blue) and the observed snow depth (red) at the Vernagt Ferner (MAROWSKY (2010), p. 64, modified).....	54
Figure 5.3: Comparison of modelled (red) and observed (blue and green) ice thickness changes 2006 (MAROWSKY (2010), p. 66, modified).....	55
Figure 5.4: Modelled and observed ice thickness of the Northern Schneeferner at the Zugspitze in Germany (based on BAYERISCHE GLETSCHER (2009)). ....	56
Figure 5.5: Different parts of the Vernagt Ferner with the grid cell structure covering the glacier (MAROWSKY (2010), p. 71, modified).....	56
Figure 5.6: Observed (line) and modelled (squares) specific mass balance in the four parts of the Vernagt glacier for the elevation levels in the mass balance season 1999 (MAROWSKY (2010), p.78, modified).....	57

Figure 5.7: Observed (line) and modelled (squares) specific mass balance in the four parts of the Vernagt glacier for the elevation levels in the mass balance season 2003 (MAROWSKY (2010), p.79, modified).....	57
Figure 5.8: Comparison of modelled (blue) and observed glacier extent (grey and black) for the Northern (left) and Southern (right) Schneeferner at the Zugspitze in Germany between 1979 and 20006 (MAROWSKY (2010), p.70, modified).....	58
Figure 5.9: Comparison of modelled daily runoff without considering ice-melt water (green), and with ice-melt water (turquoise), to observed values (red) at the gauge in Huben of the Ötztaler Ache from 1.1.2003 to 1.1.2005.....	59
Figure 5.10: Comparison of modelled daily runoff without subscale approach (blue), and with subscale approach (turquoise), to observed values (red) at the gauge in Huben of the Ötztaler Ache from 1.1.2003 to 1.1.2005.....	60
Figure 5.11: The glaciers of the validation area for ice thickness derivation in the Ötztal, Kaunertal and the Stubaital in Austria (based on ERSDAC (2009), WEBER ET AL. (2008A)). .....	63
Figure 5.12: Comparison of observed and deduced total ice volume of all glaciers with (left) and without (right) Hintereis and Gepatsch Ferner. ....	64
Figure 5.13: Comparison of observed and deduced ice volume of all glacier elevation levels with (left) and without (right) Hintereis and Gepatsch Ferner.....	65
Figure 5.14: Comparison of observed and deduced ice volume of the elevation levels of Rofenkar Ferner (left) and Kesselwand Ferner (right).....	66
Figure 5.15: Comparison of modelled (CLM ERA 40) and observed daily air temperatures for the Lhasa, Damshung and Meldro Gungkar stations.....	68
Figure 5.16: Development of modelled (CLM ERA 40) and observed monthly air temperatures for the Lhasa and Damshung stations. ....	68
Figure 5.17: Observed and modelled (CLM ERA 40) trend of the annual air temperature at the Lhasa and Damshung stations for 1980-2000. ....	68
Figure 5.18: Comparison of modelled (CLM ERA 40) and observed monthly precipitation for the Lhasa and Tangga (1971-2000), Pangdo (1976-2000) and Damshung and Meldro Gungkar stations (1980-2000).....	69
Figure 5.19: Development of modelled (CLM ERA 40) and observed monthly precipitation for the Lhasa (1971-2000) and Pangdo stations (1976-2000). ....	69
Figure 5.20: Daily time series of modelled (CLM ERA 40) and observed precipitation at the Lhasa station for the years 1997 and 1998. ....	70
Figure 5.21: Observed and modelled (CLM ERA 40) trend of the annual precipitation sum at the Lhasa and Pangdo stations.....	70
Figure 5.22: Development of observed and modelled CLM (ECHAM 5) monthly air temperature and precipitation at the Lhasa station for 1980-2000.....	72
Figure 5.23: Observed and modelled CLM ECHAM 5 trend of annual air temperature at the Lhasa and Damshung stations for 1980-2000. ....	72

Figure 5.24: Observed and modelled CLM ECHAM 5 trend of the annual precipitation sum at the Lhasa and Pangdo stations for 1970 / 1976-2000. ....	72
Figure 5.25: Hourly course of downscaled CLM (ERA 40) data in a randomly chosen January (left) and July (right) in Lhasa. ....	74
Figure 5.26: Daily course of downscaled CLM ERA 40 (left) and ECHAM 5 (right) data. .	75
Figure 5.27: Simulated total ice water reservoir and glacier area in the Lhasa River basin from 1970 to 2000 using CLM ERA 40 (left) and ECHAM 5 (right) data as meteorological drivers. ....	78
Figure 5.28: Comparison of derived accumulation on the Lanong Glacier (KANG ET AL. 2007A)(a) with simulations of snow water equivalent (b), air temperature and precipitation (c) and snow and ice water equivalent (d). ....	79
Figure 5.29: Monthly modelled and observed runoff at the Lhasa and Yangbajing gauges from 1971-2000 (ERA 40). ....	81
Figure 5.30: Comparison of observed and modelled annual runoff in Lhasa, Pangdo, Tangga and Yangbajing. ....	82
Figure 5.31: Annual modelled and observed runoff at the Lhasa gauges from 1971-2000 for ERA 40 (left) and ECHAM 5 (right) meteorological data. ....	83
Figure 5.32: Comparison of daily modelled and observed runoff at the Lhasa, Pangdo and Tangga gauges from 1996-2000 (CLM ERA 40).....	84
Figure 5.33: Development of daily observed and modelled runoff at the gauge in Lhasa from 1991 to 2000 (CLM ERA 40).....	84
Figure 5.34: Daily modelled and observed runoff at the Lhasa gauges for 1997 and 1998 (ERA 40).....	85
Figure 6.1: The IPCC SRES emission scenarios (left) and the development of global surface warming with uncertainty ranges (right) (IPCC 2007A, p.44 and IPCC 2007B, p. 14). ....	88
Figure 6.2: The development of annual air temperature, precipitation sum and global radiation in the Lhasa River catchment from 1971 to 2080 according to the downscaled CLM ECHAM 5 IPCC SRES scenarios. ....	90
Figure 6.3: Mean annual air temperature from 1971 to 2000 (top) and the changes in the periods of 2011 to 2040 (left) and of 2051 to 2080 (right) according to the A1B scenario (middle) and B1 scenario (bottom).....	92
Figure 6.4: Mean annual precipitation from 1971 to 2000 (top) and the changes in the periods of 2011 to 2040 (left) and of 2051 to 2080 (right) according to the A1B scenario (middle) and B1 scenario (bottom).....	93
Figure 6.5: The development of the annual percentage of snowfall in the Lhasa River catchment from 1971 to 2080 according to the CLM ECHAM 5 IPCC SRES scenarios. ....	95

Figure 6.6:	Mean annual percentage of snow precipitation from 1971 to 2000 (top) and the changes in the periods of 2011 to 2040 (left) and of 2051 to 2080 (right) according to the A1B scenario (middle) and B1 scenario (bottom). .....	96
Figure 6.7:	Reduction of percentage of snowfall at different elevation levels for the future periods 2011 to 2040 (blue (A1B) and yellow (B1)) and 2051 to 2080 (green (A1B) and red (B1)), compared to the past period. ....	97
Figure 6.8:	Mean annual days with snow cover (swe > 10 mm) from 1971 to 2000 (top) and the changes in the periods 2011 to 2040 (left) and 2051 to 2080 (right) according to the A1B scenario (middle) and B1 scenario (bottom). ....	98
Figure 6.9:	Changes in days with snow cover (swe > 10 mm) for the future periods 2011 to 2040 (blue (A1B) and yellow (B1)) and 2051 to 2080 (green (A1B) and red (B1)) compared to the past period.....	99
Figure 6.10:	The development of the glacier area in the Lhasa River catchment from 1971 to 2080 according to the IPCC SRES scenarios. ....	101
Figure 6.11:	The development of the water stored as ice equally distributed over the Lhasa River catchment from 1971 to 2080 according to the IPCC SRES scenarios. ....	101
Figure 6.12:	The development of annual snow precipitation in the Lhasa River catchment from 1971 to 2080 according to the IPCC SRES scenarios.....	102
Figure 6.13:	The development of the simulated ice water equivalent distribution from 1970 to 2080 over the decades according to the CLM ECHAM5 IPCC A1B scenario model run.....	104
Figure 6.14:	The development of the simulated ice water equivalent distribution from 1970 to 2080 over the decades according to the CLM ECHAM5 IPCC B1 scenario model run. ....	105
Figure 6.15:	Development of annual snowmelt in the Lhasa River catchment from 1971 to 2080 according to the CLM ECHAM 5 IPCC SRES scenarios. ....	106
Figure 6.16:	Development of annual ice-melt in the Lhasa River catchment from 1971 to 2080 according to the CLM ECHAM 5 IPCC SRES scenarios. ....	106
Figure 6.17:	Development of annual ice-melt and the number of days with complete snowcover (s.w.e. > 10 mm) in the Lhasa River catchment from 1971 to 2080, according to the IPCC SRES A1B (green) and B1 (blue) scenario.....	107
Table 6.9:	Changes in annual snow- and ice-melt in the Lhasa River catchment for the four scenarios.....	108
Figure 6.18:	Development of annual evapotranspiration in the Lhasa River catchment from 1971 to 2080 according to the CLM ECHAM 5 IPCC SRES scenarios. ....	108
Figure 6.19:	Mean annual evapotranspiration from 1971 to 2000 (top) and the changes in the periods of 2011 to 2040 (left) and 2051 to 2080 (right) according to the A1B scenario (middle) and B1 scenario (bottom).....	110



---

Figure 6.20: Development of the annual runoff in the Lhasa River catchment from 1971 to 2080 according to the CLM ECHAM 5 IPCC SRES scenarios. ....	111
Figure 6.21 Comparison of mean monthly runoff at the basin outlet between climate periods (left) and decades (right), according to the A1B scenario (top) and the B1 scenario (bottom). ....	111
Figure 6.22: Mean annual runoff from 1971 to 2000 (top) and the changes in the periods of 2011 to 2040 (left) and 2051 to 2080 (right), according to the A1B scenario (middle) and B1 scenario (bottom). ....	112
Figure 6.23: Mean annual ice-melt contribution to runoff from 1971 to 2000 (top), 2011 to 2040 (left) and 2051 to 2080 (right) according to the A1B scenario (middle) and B1 scenario (bottom). ....	114
Figure 6.24: Mean annual percentage of ice-melt on runoff from 1971 to 2000 (top) and in the periods of 2011 to 2040 (left) and 2051 to 2080 (right) according to the A1B scenario (middle) and B1 scenario (bottom). ....	115
Figure 6.25: Development of the annual percentage of glacier ice-melt in runoff at the Lhasa River catchment from 1971 to 2080 according to the CLM ECHAM 5 IPCC SRES scenarios. ....	116
Figure 6.26: Seasonal distribution of glacier ice-melt contribution and runoff for the three climate periods of 1971 to 2000, 2011 to 2040 and 2051 to 2080 according to the A1B scenario at the catchment outlet and Yangbajing. ....	117
Figure 6.27: Seasonal distribution of glacier ice-melt contribution and runoff for the three climate periods of 1971 to 2000, 2011 to 2040 and 2051 to 2080 according to the B1 scenario at the catchment outlet and Yangbajing. ....	117
Figure 6.28: Seasonal distribution of the percentage of glacier ice-melt contribution and runoff for the three climate periods of 1971 to 2000, 2011 to 2040 and 2051 to 2080, according to the A1B scenario at the catchment outlet and Yangbajing. ....	118
Figure 6.29: Seasonal distribution of the percentage of glacier ice-melt contribution and runoff for the three climate periods of 1971 to 2000, 2011 to 2040 and 2051 to 2080, according to the B1 scenario at the catchment outlet and Yangbajing. ....	118
Figure 6.30: Comparison of future runoff changes with and without consideration of ice-melt contribution at catchment outlet (left) and at Yangbajing (right) and for 2011 to 2040 (top) and from 2051 to 2080 (bottom) in comparison to the period 1971-2000 for the A1B IPCC SRES scenario run. ....	119
Figure 6.31: Comparison of changes in the mean daily courses of snow- and icemelt, precipitation and runoff for the three climate periods for the Lhasa River catchment under A1B IPCC SRES conditions. ....	120
Figure 6.32: Influence of glacier ice-melt water in periods with little monsoon precipitation at the basin outlet (left) and at Yangbajing (right). ....	121

Figure 6.33: Mean annual percentage of inputs and outputs to the water balance in the sub-catchments from 1971 to 2000 (top), and in the periods of 2011 to 2040 (middle) and 2051 to 2080 (bottom) according to the A1B scenario. .... 123

Figure 6.34: Mean annual percentage of inputs and outputs to the water balance in the sub-catchments from 1971 to 2000 (top), and in the periods of 2011 to 2040 (middle) and 2051 to 2080 (bottom) according to the B1 scenario. .... 124

## LIST OF TABLES

Table 2.1:	Characteristics of the climate classification zones of the CHINESE ACADEMY OF SCIENCES (1984) (modified consistent with LEBER ET AL. (1995)).	10
Table 2.2:	Basin areas and glacierized areas of the Lhasa River basin and sub-basins (based on ITP (2008), JARVIS ET AL. (2006), GARBRECHT AND MARTZ (1999)).	14
Table 2.3:	Advancing and retreating glaciers in High Asia from 1950 (YAO 2006, p. 277).	19
Table 4.1:	Required input data layers to run PROMET and SURGES and data sources for the Lhasa River catchment.	41
Table 4.2:	Required meteorological drivers (MAUSER AND BACH 2009).	42
Table 4.3:	Required parameters for description of the land surface (MAUSER AND BACH 2009).	44
Table 4.4:	Required parameters for soil texture parameterization (MAUSER AND BACH 2009).	45
Table 5.1:	Quality criteria for the simulated runoff of different model runs at the Huben gauge of the Ötztaler Ache from 1.1.2000 to 31.12.2005.	59
Table 5.2:	Comparison of total observed and deduced ice volume in the Ötztal, the Kaunertal and the Stubaital in Austria.	63
Table 5.3:	Characteristics of the Rofenkar and Kesselwand Ferner and comparison of observed and deduced ice volumes.	65
Table 5.4:	Comparison of downscaled CLM ERA 40 and observed mean values of air temperature and precipitation.	67
Table 5.5:	Comparison of simulated ECHAM 5 CLM and observed mean values of air temperature, precipitation and wind speed from 1980 – 2000, except precipitation for Lhasa and Tangga (1971-2000) and Pangdo (1976-2000).	71
Table 5.6:	Summary of glacier change recordings in Central Asia.	77
Table 5.7:	Simulated changes in glacial coverage and ice water reservoir in the Lhasa River basin from 1970 to 2000 for CLM ERA 40- and CLM ECHAM 5-driven model runs.	77
Table 5.8:	Runoff data availability at the four gauging stations in the Lhasa River catchment (based on: BRAHMATWINN 2006-2009, ITP 2008).	80
Table 5.9:	Quality criteria for modelled monthly runoff R and precipitation data P, driven by CLM ERA 40 meteorological data.	81
Table 5.10:	Mean annual runoff [m <sup>3</sup> /s] and precipitation [mm] for ERA40- and ECHAM 5-driven model runs at the four gauges for the climate period from 1971-2000.	83

---

Table 5.11: Quality criteria for modelled daily runoff, driven by CLM ERA 40 meteorological data. ....	84
Table 6.1: Projected global temperature changes and their likely range of the various scenarios from 2090-2099 relative to 1980-1999 (data source: IPCC 2007B). ....	88
Table 6.2: Significance levels $\alpha$ of the different Mann-Kendall trend values of Q (RAPP AND SCHÖNWIESE (1995), p. 62, modified). ....	89
Table 6.3: Changes in the mean annual air temperature in the Lhasa River basin for the four scenario runs. ....	91
Table 6.4: Changes in the mean annual precipitation sum in the Lhasa River basin for the four scenario runs. ....	94
Table 6.5: Simulated changes in snow precipitation in the Lhasa River catchment for the four IPCC SRES scenarios. ....	95
Table 6.6: Changes in the percentage of snowfall for different elevation levels in the basin. ....	97
Table 6.7: Changes in the number of days with snow cover of a swe > 10 mm. ....	99
Table 6.8: Changes in glacial coverage and stored ice water reservoir in the Lhasa River catchment for the four scenarios. ....	102
Table 6.10: Changes in annual evapotranspiration and water availability in the Lhasa River catchment for the four scenarios. ....	109

**LIST OF ACRONYMS**

a.s.l.	above sea level
ASTER	Advanced Spaceborne Thermal Emission and Reflection Radiometer
Brahmatwinn	Twinning European and South Asian River Basins to enhance capacity and implement adaptive management approaches
CLM	Climate mode
CON	IPCC scenario with constant year 2000 concentration values
COSMO	Consortium for Small Scale Modelling
DWD	Deutscher Wetterdienst
ECHAM	ECMWF Hamburg
ECMWF	European Centre for Medium Range Weather Forecasts
ELA	Equilibrium Line Altitude
ERA 40	ECMWF Re-analysis at a resolution of 40 km
ERSDAC	Earth Remote Sensing Data Analysis Center
FORTTRAN	Formula Translation
GCC	Global Climate Change
GCM	Global Climate model
GDEM	Global Digital Elevation Model
GIS	Geographic Information system
GLIMS	Global Land Ice Monitoring from Space
GLOWA	Globaler Wandel des Wasserkreislaufs (Global Change and the Hydrological Cycle)
IPCC	Intergovernmental Panel of Climate Change
IWRM	Integrated Water Resources Management
Ma	Million years
MODIS	Moderate Resolution Imaging Spectroradiometer
MPI-OM	Max-Planck-Institute Ocean Model
NASA	National Aeronautics and Space Administration
PROMET	Processes of Radiation, Mass and Energy Transfer
RADAR	Radio Detection and Ranging
RCM	Regional climate model
s.w.e.	snow water equivalent

SCALMET	Scaling Meteorological Variables
SRTM	Shuttle Radar Topography Mission
SURGES	Subscale Regional Glacier Extension Simulator
TOPAZ	Topographic Parameterization
UTM	Universal Transverse Mercator
w.e.	water equivalent
WDC	World Data Center For Glaciology and Geocryology
WGMS	World Glacier Monitoring Service
WGS 84	World Geodetic System 1984
ZAMG	Zentralanstalt für Meteorologie und Geodynamik

## LIST OF SYMBOLS

Symbol	Description	Unit
$\alpha$	albedo	
$\beta$	slope of the glacier surface	°
$\Gamma$	adiabatic lapse rate	K m <sup>-1</sup>
$\Delta t$	time step	s
$\varepsilon$	longwave emissivity of snow	
$\varepsilon_s$	shear strain rate	s <sup>-1</sup>
$\rho_a$	air density	kg m <sup>-3</sup>
$\rho_{ice}$	ice density	kg m <sup>-3</sup>
$\rho_{snow}$	snow density	kg m <sup>-3</sup>
$\sigma$	Stefan Boltzmann constant	W m <sup>-2</sup> K <sup>-4</sup>
$\tau_s$	shear stress	kPa
$A$	advective heat flux	W m <sup>-2</sup>
$ae$	error in glacierized area	m <sup>2</sup>
$B$	mean mass balance	mm w.e.
$b(z)$	specific glacier mass balance	mm w.e.
$C_G$	contribution of glacier melt water	mm
$c_i$	specific heat capacity of ice	J kg <sup>-1</sup> K <sup>-1</sup>
$C_{ice}$	contribution of glacier ice-melt water	mm
$c_P$	specific heat capacity of air at constant pressure $P$	J kg <sup>-1</sup> K <sup>-1</sup>
$c_{P,dry}$	specific heat capacity of dry air	J kg <sup>-1</sup> K <sup>-1</sup>
$c_w$	specific heat capacity of water	J kg <sup>-1</sup> K <sup>-1</sup>
$e$	vapour pressure	hPa
$E$	energy balance	W m <sup>-2</sup>
$e(z)$	correction factor for considering ice flow effects	mm
$E_{fr}$	energy for refreezing liquid water	mm
$E_w$	Saturation vapour pressure	hPa
$F$	shape factor for calculating the shear stress of valley glaciers	
$fr$	freezing fraction of liquid water storage	%

Symbol	Description	Unit
$G$	soil heat flux	$W m^{-2}$
$g_o$	gravitational acceleration on earth	$m s^{-2}$
$H$	sensible heat flux	$W m^{-2}$
$h_i$	ice thickness	m
$H_i$	specific melting heat of ice	$J kg^{-1}$
$H_{is}$	specific sublimation / resublimation heat of ice	$J kg^{-1}$
$h_s$	snow depth	m
$i$	number of glaciers	
$k$	albedo recession factor	$day^{-1}$
$l$	glacier level	
$LE$	latent heat flux	$W m^{-2}$
$liq$	maximum amount of stored liquid water in snow cover	mm
$M$	molar mass of air	$kg kmol^{-1}$
$m$	melt water	mm
$m_i$	melt water of ice	mm
$m_r$	glacier melt rate	$mm s^{-1}m^{-2}$
$m_s$	melt water of snow	mm
$n$	number of elevation levels	
$P$	air pressure	hPa
$P_l$	level air pressure	hPa
$PR$	precipitation	mm
$PR_R$	rainfall	mm
$PR_S$	snow fall	mm
$Q$	radiation balance	$W m^{-2}$
$Q_l$	longwave radiation balance	$W m^{-2}$
$Q_s$	shortwave radiation balance	$W m^{-2}$
$R$	universal gas constant for air	$J mol^{-1} K^{-1}$
$r$	latent heat of vaporization	$J kg^{-1}$
$R_{dif}$	diffuse solar radiation	$W m^{-2}$
$R_{dir}$	direct solar radiation	$W m^{-2}$



<b>Symbol</b>	<b>Description</b>	<b>Unit</b>
$R_{ij}$	longwave incoming solar radiation	$W\ m^{-2}$
$R_S$	solar radiation	$W\ m^{-2}$
$R_{wT}$	correlation coefficient for turbulent fluxes	
$S$	glacier area	$m^2$
$se$	amount of sublimation / resublimation	mm
$sh$	specific humidity	$kg\ kg^{-1}$
$sh_S$	specific humidity of surface	$kg\ kg^{-1}$
$S_{ice}$	snow-free glacier area	$m^2$
$S_l$	level glacier area	$m^2$
$s_l$	maximum liquid water storage capacity	%
$S_{l,icefree}$	level glacier area after ice melt	$m^2$
$swe$	snow water equivalent	mm
$T$	air temperature	K
$T_l$	level air temperature	K
$T_s$	surface temperature	K
$T_S$	surface temperature	K
$T_w$	wet bulb temperature	K
$u$	ice velocity	$m\ s^{-1}$
$V$	glacier volume	$m^3$
$v$	wind speed	$m\ s^{-1}$
$v_l$	level wind speed	$m\ s^{-1}$
$x,y,z$	direction in coordination system	
$z$	elevation a.s.l.	m
$z_b$	elevation of glacier bed a.s.l.	m
$z_{gc}$	elevation of grid cell a.s.l.	m
$z_s$	surface elevation a.s.l.	m

---

## LIST OF STATISTICAL SYMBOLS

---

Symbol	Description
$\alpha$	level of significance
$\sigma$	standard deviation
$a_j$	element of time series
$a_k$	element of time series
$j$	number of time series element
$k$	number of time series element
$n$	quantity of values
$p^{th}$	order of group
$Q$	test statistic of Mann-Kendall test
$q$	quantity of tied values
$T/N$	trend-to-noise ratio
$t_p$	quantity of data values
<i>trend</i>	absolute trend between beginning and end

---

# 1 Introduction

Global Climate Change (GCC) will impact future human livelihood as well as demographic, economic and land-use changes (IPCC 2007A, B). Future freshwater availability is a key factor for regional development, as not only drinking water but also food and energy production, health, and industrial development are all, to a certain extent, based on sufficient fresh water supply. In order to mitigate the water-related effects of GCC for societies, appropriate adaptation strategies and Integrated Water Resources Management (IWRM) options for potential changes must be developed. This in turn requires comprehensive knowledge of the future impacts of GCC on the water balance. Mountainous alpine headwaters play an especially significant role in the water balance of many large river basins. The temporal storage of water as snow and ice during wet periods in the high mountains, and its release during subsequent warm and often dry melting periods, makes the water release of snow and glaciers extremely important. Under these conditions, melt water is the last available water source. The term “water towers” hence reflects the importance of mountainous regions as freshwater resources (LININGER ET AL. 1998, VIVIROLI AND WEINGARTNER 2004, WEINGARTNER ET AL. 2007). However, glaciers are among the most sensitive systems in terms of climatic change. Besides air temperature and precipitation, radiation, humidity and several other meteorological conditions influence their mass balance and thus their appearance. The accelerating retreat of glaciers during recent years is one of the clearest signs of ongoing climate change (UNEP AND WGMS 2008), and has made them a symbol for the impact of GCC. Furthermore, after glaciers have melted, they will not be renewed in a continually warming climate. This is unlike snow storage, which is seasonally renewed, although the total amount is likely to decrease (BARNETT ET AL. 2005).

In order to assess the impacts of GCC in the headwater river basins of alpine mountain massifs and to establish IWRM systems, approaches and tools in twinning European and Asian basins, the *Brahmatwinn* project was funded as part of the European Commission's Sixth Framework Programme (FP6 2002-2006) (BRAHMATWINN 2006 – 2009). The large-scale river basins of the Upper Danube in Europe and the Upper Brahmaputra in Asia were chosen for the study, because they represent trans-boundary basins with mountain headwaters, which supply their densely populated forelands with freshwater. Water release of snow and ice from the mountains therefore is crucial for the water balance. Common challenges in the basins include droughts, flood protection during spring melt or heavy storms, competing water demands from agriculture, hydropower, rural, urban and industrial development, pollution and socio-economic and legal issues related to water allocation. In order to deduce appropriate IWRM options, *Brahmatwinn* consists of a multidisciplinary consortium with social and natural scientists and engineers from universities and small and medium enterprises from Europe and Asia. Additionally, stakeholders of both catchments from governmental and non-governmental organisations and enterprises were integrated, in order to identify appropriate adaptation strategies within a continuous dialogue. The present natural and socio-economic conditions in the basins were comprehensively assessed, and subsequent changes and vulnerabilities

were identified. Next, the impact of future climatic conditions on water resources was simulated for the period until 2080, and accordingly the IWRM system was developed and implemented. In order to determine the influence of future climate impact on the water balance, comprehensive socio-economic and hydrological simulations were carried out. In the latter, all processes such as snow- and ice-melt, precipitation, evapotranspiration, soil and groundwater release, and runoff formation in the river bed needed to be captured by the model. Since the headwaters of the Upper Brahmaputra are located in the Himalayas, which form the largest ice body outside the polar caps, snow and ice represent a unique freshwater reservoir in the basin (IPCC 2007c). Their meltwater release in the mountainous headwatersheds supports water availability in the large forelands of the Brahmaputra, and the future development of these reservoirs therefore is of particular importance in the modelling. To enable the capturing of all the processes, process knowledge about the Upper Danube River basin, which was developed within the project GLOWA-Danube (GLOWA-DANUBE 2001-2010), was applied to the Upper Brahmaputra. Adaptations of the GLOWA-Danube approach were required for various natural conditions such as, for example, the monsoonal climate and the related runoff regimes, while enhancements to reflect general conditions such as sparse data availability also had to be implemented into the model.

## **1.1 Climate Change and Glaciers in the Himalayas**

The further increase of air temperature due to rising greenhouse gas concentrations in the atmosphere is now commonly accepted, whereas the resulting future rate of glacier shrinkage and the date of their disappearance are quite hotly debated. The predicted melt from Himalayan glaciers in 2035, published by the United Nations Intergovernmental Panel on Climate Change in its 2007 report (IPCC 2007c, p. 493), and afterwards assessed as not substantial (IPCC 2010), recently brought the impact of GCC on glaciers in High Asia into public and scientific focus, as discussions at the last American Geophysical Union Fall meeting (KARGEL ET AL. 2009) or recently published papers demonstrate (e.g. ALFORD AND ARMSTRONG 2010, THAYYEN AND GERGAN 2010).

Studies of present glacier responses to GCC in the Himalayas show considerable variation due to widely varying mountain climatic conditions in the Himalayas. The variations range from glaciers in a steady state, or even sporadically advancing, to those retreating sharply. For instance, individual glaciers in the Karakoram expanded because of increasing precipitation (HEWITT 2005), whereas the Gangotri glacier retreated 23 m per year between 1985 and 2001 (HASNAIN 2001).

As well as the ambiguous future development of glaciers, both the influence of glacier meltwater release on fresh water supply and the impact of GCC on water availability are also controversial in the Himalayas. Due to growing water demands and an increasing temperature combined with precipitation changes, water shortage is likely to increase in South Asia, according to the IPCC (2007c). Increasing glacier melt water supply, which accounts for over 10 percent of runoff in drier regions, will alleviate the situation slightly. After the melt from glaciers, a further decrease in discharge is expected (IPCC 2007c). BARNETT ET AL. (2005) assume severe impacts especially in China, India and parts of Asia,

forming the Himalaya-Hindu Kush region, where glacier meltwater is assessed in general as forming 50 to 70 percent of the summer water flows in major rivers. As in the IPCC statement, an increased or steady meltwater release from glaciers, followed by a decrease after the melting, resulting in water shortages and droughts during dry seasons in some regions, is here presumed to be likely (BARNETT ET AL. 2005). These results are confirmed for Central Asia by further studies (CASASSA ET AL. 2009, REES AND COLLINS 2006, SINGH AND KUMAR 1997).

In contrast, THAYYEN AND GERGAN (2010) point to the varying climatic and hydrological conditions along the Hindu Kush – Himalayas, which result in differing influences of ice-melt water on runoff. In the eastern parts, where the Brahmaputra basin is located, they find monsoon precipitation having a major influence on runoff, and ice-melt a minor influence. In a small test basin with a glacierization of about 10 percent, the supply of ice-melt is assessed at between 7 and 13 percent. The future glacier melt water need not increase runoff in these regions (THAYYEN AND GERGAN 2010). Shifts in the timing and in the amount of the monsoon precipitation are quite significant for future water availability in the eastern Himalayas (BENISTON 2003).

The previous overview of studies of present glacier responses to GCC in the Himalayas and their influence on fresh water supply shows uncertainties in future development of glacier ice reservoirs and the amount of melt water release. To clarify the controversial role of glacier melt water among the other water balance variables, the detailed consideration of precipitation, snowmelt, evapotranspiration and ground- and soil-water storage in addition to glacier modelling is required under present and past climatic conditions. Thus, quantification of ice melt in correlation to the other components is enabled. To overcome deficits of general, non-distributed simulations and conclusions in previous analyses, the varying climatic and hydrological conditions in the Himalayas have to be considered in these studies.

## **1.2 Scientific Objectives and Outline of the Thesis**

The objective of this thesis is the development and utilization of a distributed modelling approach to determine the impact of GCC on glaciers, and their influence on future water availability in a Himalayan river basin under past and future climatic conditions. For this purpose, the spatial heterogeneity of complex basins with mountainous headwatersheds (for example, the Himalayas), and forelands with large river valleys, such as the Brahmaputra in Assam, needed to be captured synchronously by the model. This allows the simulation of all relevant processes under varying climatic conditions and varying hydrological regimes, with, for instance, the temporal storage of water as snow and glacier ice, and its later release.

The simulation of the amount of melt water released by a glacier is a further objective. As this depends on the snow-free area of the glacier (see section 3.2), a simulation of the duration of snow cover on all parts of a known glacier surface is required. Together with the energy balance of the ice surface, the amount of ice-melt water can be computed. The ice thickness distribution over the glacierized area, or in other words, the geometry of the

glacier ice reservoir, should be considered. This also includes likely geometry changes under future climatic conditions where necessary.

In order to determine the influence of glacier melt water on runoff, a separation of the portion of glacier meltwater from the total river runoff throughout the whole catchment is also required. A runoff routing component is therefore required in the hydrological model to simulate the flow of meltwater in the river channel.

The model should also be applicable under future climatic conditions. As a consequence, the use of universal parameters, the conservation of mass- and energy balances and a strict foundation on physical principles are objectives for the applied modelling approach (MAUSER AND BACH 2009, MOORE ET AL. 2009).

In addition, it should be possible to apply regional climate model (RCM) outputs as future meteorological drivers. Bridging the gap between different scales of data and processes therefore needs to be feasible. The spatial resolution of RCMs is in the range of 100 to 1000 km<sup>2</sup>, whereas the area of alpine glaciers often varies from a few ha to several km<sup>2</sup>. For the process description of the landsurface, which is limited by the area of the test basin as well as the availability of input data, a resolution of the order of 1 km<sup>2</sup> is adequate according to MAUSER AND BACH (2009).

An application in remote regions with sparse data availability, as it often is the case in the Himalayas because of missing observations, is the final goal of the modelling approach presented.

In order to achieve the objectives described above, expertise from the Upper Danube River basin, developed within the GLOWA-Danube project (GLOWA-DANUBE 2001-2010), is transferred to Asia and adapted to the prevailing conditions, such as different land use properties. The integrated model is applied under past and future climatic conditions in the Lhasa River basin in Tibet, a sub-basin of the Upper Brahmaputra. The natural conditions of the basin, determining the processes to be captured by the modelling approach, are described in Chapter 2. For this purpose geology and geomorphology, climatology and hydrology of the basin are introduced. The characteristics of the soils and the land cover and land use are also explained. Finally, the properties of the glaciers in the investigation area are specified.

In Chapter 3, the modelling approach is explained in detail. First, an overview of the PROMET hydrological model (MAUSER AND BACH 2009), including the SCALMET meteorological coupling tool (MARKE 2008) to use RCM outputs as meteorological drivers, is given (section 3.1). Next, the configuration of the SURGES glacier model (WEBER ET AL. 2008, PRASCH ET AL. 2009) is explained in detail (section 3.2). Since few data are available from the Lhasa River basin, the derivation of the input data required to run the model framework is introduced in Chapter 4. The emphasis thereby is on the description of the generation of the glacier characteristics to run SURGES. The model validation includes verification of the functionality of the glacier model and justification of the input data derivation. The utilization of the RCM data as meteorological drivers, which was done for the first time in this region, is checked in detail. After the application of the model approach in the investigation area is presented (Chapter 5), the results are introduced.

They contain a brief introduction of the applied climate scenarios and an analysis of the present and future climatic and hydrological conditions with an explanation of future glacier coverage. The influence of glacier melt on runoff is analysed in detail in Chapter 6. Finally, the model results are discussed and an outlook is given in the conclusion (Chapter 7). The thesis ends with a summary of the research (Chapter 8).

## 2 The Lhasa River Basin

The Lhasa River basin is located in the southern part of the Tibet Autonomous Region of the People's Republic of China in Central Asia along the northern ranges of the Himalayas. The watershed of the Lhasa River, locally known as Kyi Chu, defines the basin until its mouth at the Yarlung Tsangpo, in India called Brahmaputra, southeast of Tibet's capital Lhasa. With an area of 32,500 square kilometres it is ranked among large-scale catchments. The geographical coverage of the basin stretches from 29° to 31.3° Northern Latitude and from 90° to 93.4° Eastern Longitude. Figure 2.1 shows the topographic map of the Lhasa River catchment, as well as the location in Central Asia within the Upper Brahmaputra River basin including political boundaries.

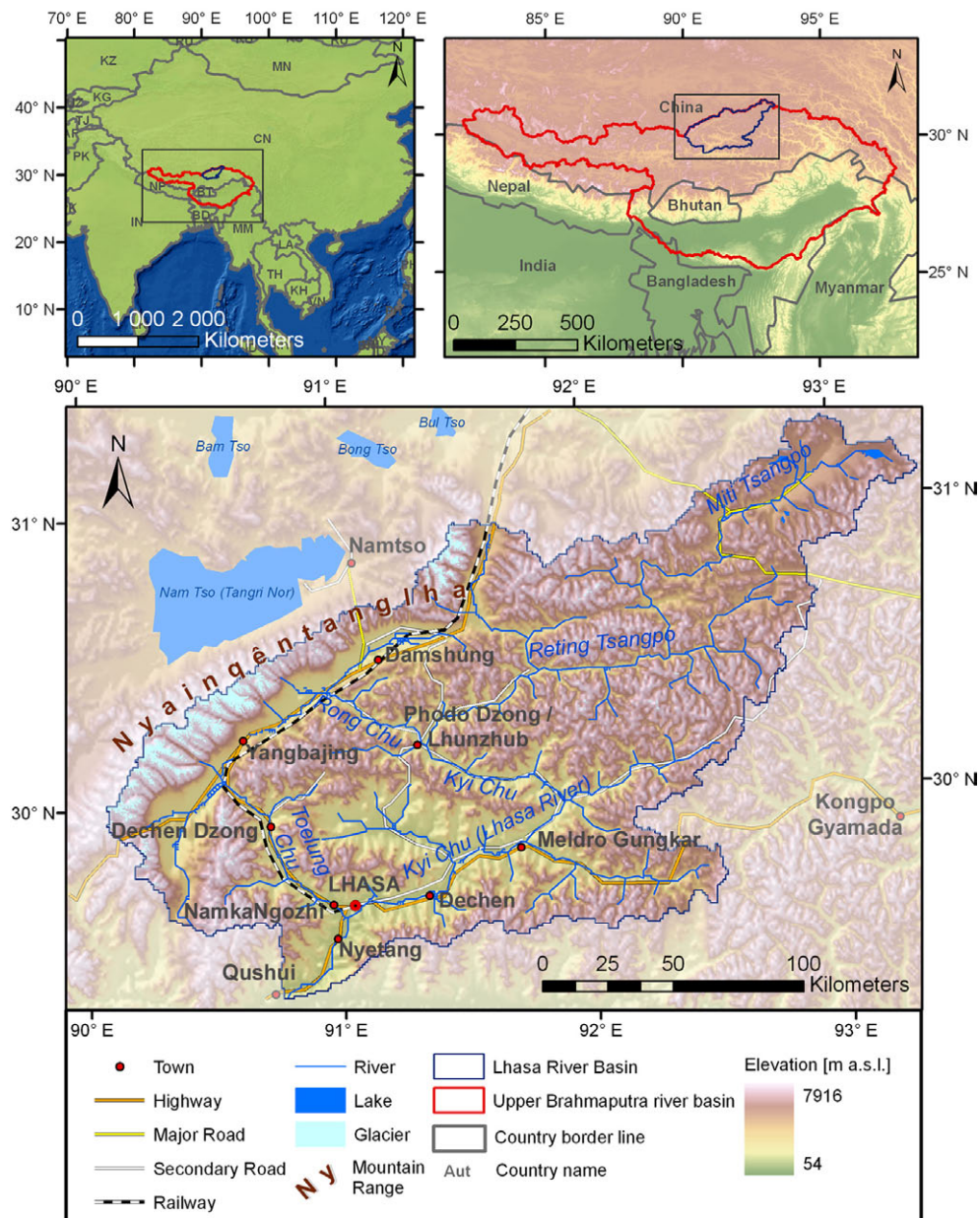


Figure 2.1: Geographical position and topographic map of the Lhasa River (Kyi Chu) basin as sub basin of the Upper Brahmaputra catchment in Central Asia (based on ESRI (1999-2008), JARVIS ET AL. (2006) and REISE-KNOW-HOW VERLAG (2005)).



The capital Lhasa and its surroundings within the Lhasa River catchment are the political, economical and cultural centre of Tibet (DAJUN 1995). According to the population census of China (DEPARTMENT OF POPULATION, SOCIAL, SCIENCE AND TECHNOLOGY STATISTICS OF THE NATIONAL BUREAU OF STATISTICS OF CHINA AND DEPARTMENT OF ECONOMIC DEVELOPMENT OF THE STATE ETHNIC AFFAIRS COMMISSION OF CHINA 2003) the prefecture of Lhasa, which largely coincides with the Lhasa River catchment, has approx. 474,500 residents (excluding the army), rising to 18 percent of the whole population in Tibet. 50 percent live in the capital city, where the population density of 4,207 residents per km<sup>2</sup> is comparable to that of Munich. Outside the city, it decreases to eight inhabitants per km<sup>2</sup>. Due to recent Chinese political activities, e.g. the completion of the Qinghai-Tibet railway between Golmud and Lhasa in 2006, the population is currently increasing. Furthermore, the natural conditions (see section 2.1 - 2.6) of the region around Lhasa permit crop farming in addition to the semi-nomadic herding that prevails in Tibet. Agriculture still dominates Tibetan economy, although as part of political activities industrial locations have been installed for the production of textile and handicrafts as well as for mining and electricity. Additionally, tourism has become more important during the last decade (DREYER 2003), and so energy and water demands are increasing. There are also plans to install hydropower plants for energy production (DAJUN 1995). As the Lhasa River catchment is partially glacierized, mainly along the northeastern watershed in the Nyainqêntangha Mountains, one of the main glacierized regions of Central Asia (YAO ET AL. 2006), meltwater release influences water availability in the catchment. Finally, as one of the test sites of the Brahmatwinn project (BRAHMATWINN 2006 - 2009), the region was visited during a field trip in September 2006, and so at least some sparse observation data are available. Taking into account the characteristics explained above, together with assessments of the impact of future climate change on the Tibetan Plateau in several studies (CHRISTENSEN ET AL. 2007, LI ET AL. 2008, LIU AND CHEN 2000, YAO ET AL. 2006, YOU ET AL. 2007, ZHU ET AL. 2001), the Lhasa River catchment can be regarded as an appropriate test site for the analysis of the influence of glaciers and their melt water release on water availability under future climatic conditions.

In the following chapter the physio-geographic conditions, including the glaciological setting, of the catchment are described in order to provide an overview of natural conditions in the basin.

## 2.1 Geology and Geomorphology

Geologically, the Lhasa River basin is located on the Lhasa terrane, which is separated from the Qiangtang terrane in the north by the Bangong-Nujiang suture and from the Indian terrane in the southern part by the Yarlung Tsangpo suture zone. This suture zone is identical to the rim of the Eurasian and Indian tectonic plate along the Himalaya Mountains. Between 50 and 55 million years ago, during the Eocene epoch of the Cenozoic Era in the Tertiary period, the Indian plate began to collide with the Eurasian plate. This continent-to-continent collision created a double thickness of crust and caused the uplift of the Tibetan Plateau as well as the formation of the highest mountain range in the world, the Himalayas. Since the Indian plate is still moving northeast against the

Eurasian plate, the formation and uplift continues today. Due to tectonic activity, earthquakes are frequent in the Lhasa river basin. The Yangbajing Graben, along the Nyainqêntanglha Mountains, is one of Tibet's especially active tectonic zones (PRESS AND SIEVER 1994, DAVIS ET AL. 2002, HE ET AL. 2007).

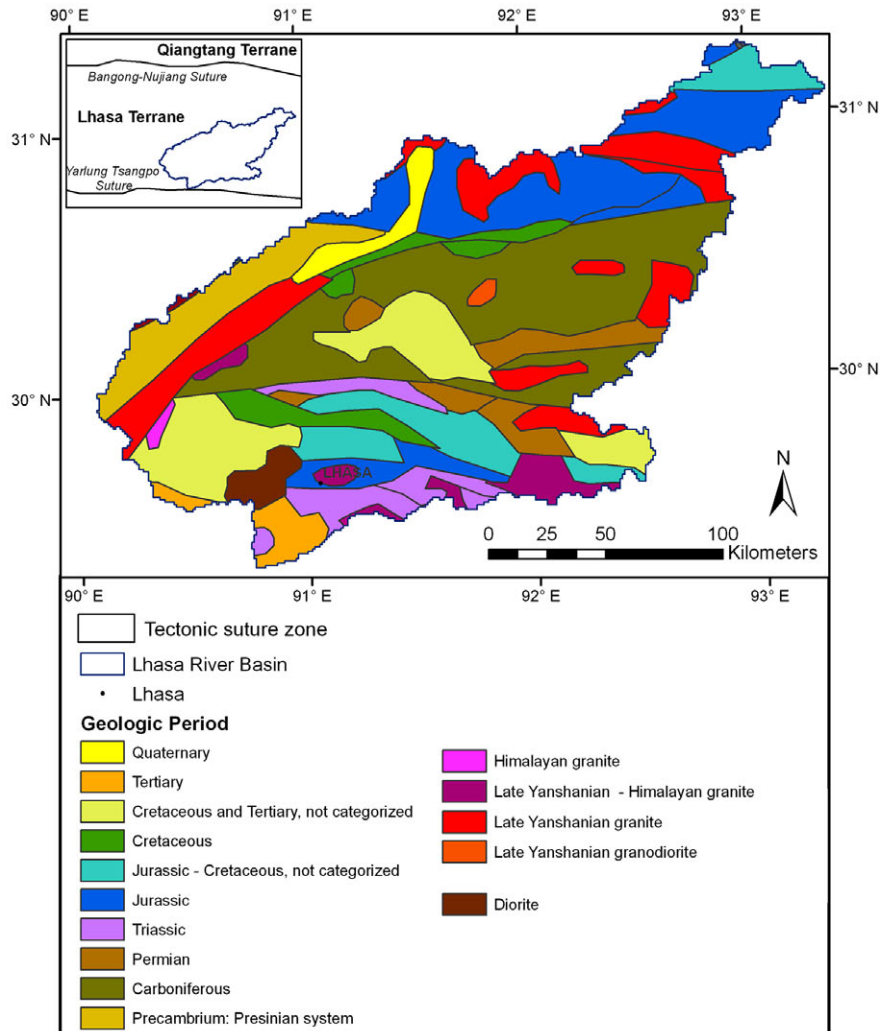


Figure 2.2: Geological Map of the Lhasa River Catchment (modified to DAVIS ET AL. (2002) and CHEN (1990)).

Figure 2.2 gives an overview of the main geological units of the Lhasa river basin according to the Geological Map of China (CHEN 1990). Stratigraphy of the basin starts with the Pre-Sinian Complex of the Precambrian era: the Nyainqêntanglha Mountains, consisting of a sedimentary sequence from the Carboniferous to the Cretaceous period, follow. In the northern parts, Jurassic and Cretaceous rocks are widely exposed, deposited as sandstones and shale during the subduction of the Thetyan ocean floor, whereas in the central regions Carboniferous and Permian rocks are found, which are mainly marble. In the central and southern parts of the catchment, uncategorized areas between Cretaceous and Tertiary and some Tertiary strata are exposed. Triassic, Jurassic and Cretaceous rocks appear in the southern areas around Lhasa. The northern part of the Yangbajing Graben is covered by Quaternary alluvium, and the river valleys are filled with glacial gravels. The relicts of the glaciation during the Pleistocene formed the landscape along the Nyainqêntanglha Mountains and around isolated mountain groups.

Due to magmatic intrusions, granite, granodiorite and diorite are spread over the catchment. In the northern and central parts, the intrusions are categorized to the Late Yanshanian epoch between 110 to 60 Ma: in southern parts they are classified as from the Late Yanshanian - Himalayan to the Himalayan epoch, which started approx. 60 Ma ago (HÖVERMANN AND LEHMKUHL 1994, PAN ET AL. 1993, CHEN 1990, YI AND XIURONG 1999).

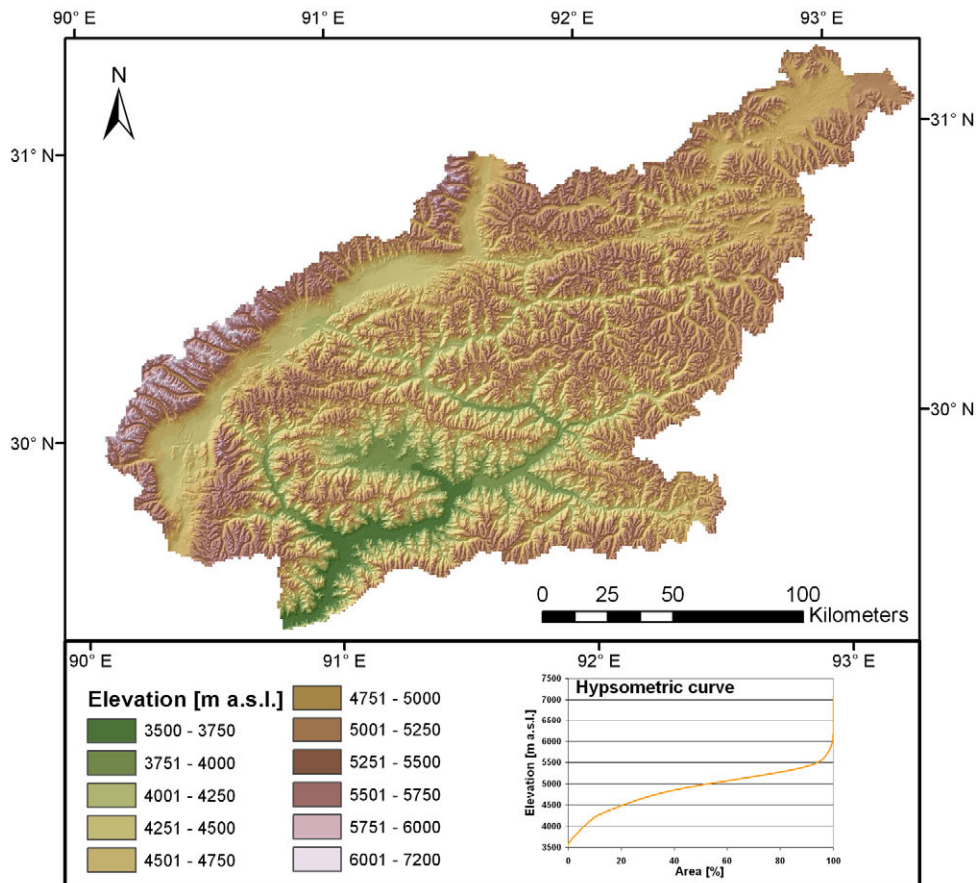


Figure 2.3: Relief of the Lhasa River Catchment based on the digital elevation model from the Shuttle Radar Topography Mission SRTM (JARVIS ET AL. 2006).

Due to the uplift of the Tibetan Plateau, the Lhasa River basin is characterized by an extraordinary mean elevation of 4,888 m a.s.l. The relief (Figure 2.3) stretches from 3,535 m a.s.l. at the conjunction of the Kyi Chu and the Yarlung Tsangpo, up to 7,162 m a.s.l. at the peak of the Nyainqêntanglha Feng in the Nyainqêntanglha Mountain range along the northwestern watershed. Only the river valley of the Kyi Chu around Lhasa, with a width of about five kilometres, and some tributary valleys in the south-western and central parts of the basin are below 4,000 m a.s.l., covering seven percent of the area. Fluvial processes as well as sand fields and dunes are characteristic of this geomorphologic zone (LEHMKUHL ET AL. 2002). As well as these valleys, the ten-kilometre-wide Yangbajing Graben, with elevations of between 4,000 m and 4,500 m a.s.l., and the source of the Miti Tsangpo in the northeast both form flat areas. Torrent valleys and gully erosion are distinctive in this zone (LEHMKUHL ET AL. 2002). In contrast, 75 percent of the catchment is characterized by mountainous relief of up to 5,500 m a.s.l., with relative altitude differences of 500 to 1,000 m and slopes of 20 to 40 degrees. They belong to the

steppe gully zone, where periglacial processes occur at above 5,100 m a.s.l. (LEHMKUHL ET AL. 2002). In the western basin on both sides of the Yangbajing Graben and the Nyainqêntanglha Mountains, steep slopes and the highest elevations are reached, with several peaks rising to above 6,000 m a.s.l. These mountains are cut by trough valleys, mainly sloping in a northwestern to southeastern direction. Most of the glaciers in the basin are located there. The dominant geomorphologic processes are glacial erosion and solifluction (LEHMKUHL ET AL. 2002). Apart from the trough valleys, the catchment in general slopes from northeast to southwest, cut by river valleys in this direction, although there are also a few with a northwest to southeast orientation.

## 2.2 Climatology

Its location on the Tibetan Plateau determines the climate of the Lhasa River catchment. Despite its latitudinal position in the subtropics, it is included in the *ice and snow climate zone E*, according to the climate classification by Köppen and GEIGER (1961), a zone characterized by an average temperature in the warmest month of below 10°C (DOMRÖS AND GONGBING 1988). A more differentiated pattern of climatic conditions is given in the classification by the CHINESE ACADEMY OF SCIENCES (1984), considering air temperature, air moisture and the growth of cultivated plants in the classification scheme. The classification is composed of climate zones (H III or H IV), climate types according to moisture (A, B or C) and the number of days with frost conditions (1, 2 or 3) (LEBER ET AL. 1995). Table 2.1 lists the characteristics of the classes in the investigation area. Their spatial distribution is illustrated in Figure 2.4.

*Table 2.1: Characteristics of the climate classification zones of the CHINESE ACADEMY OF SCIENCES (1984) (modified consistent with LEBER ET AL. (1995)).*

Class	Zone / Type	Mean air temp. of the warmest month [°C]	Number of days with mean air temp. $\geq$ 0°C	Annual accumulation of mean daily air temp. $\geq$ 0°C	Aridity-index (annual potential evapotranspiration to annual precipitation)	Accumulated precipitation from March to May [mm]	Mean lowest air temp. of the warmest month [°C]	Days from June to September with lowest air temp. $\leq$ 0°C
H III	Temperate zone	10 – 8	180 – 350	1,500 – 4,200				
H IV	Subfrigid zone	6 – 10	120 -- 180	1,000 – 1,500				
A	Moist type				$\geq 1.0$	$\geq 80$		
B	Semi-moist type				0.5 – 0.99	30 – 80		
C	Semi-arid type				0.25 – 0.49	10 – 30		
1	Mainly frost free						$\geq 5$	0
2	Slightly frost prone						$\geq 3$	$\geq 1$
3	Frost prone						$< 3$	$> 1$

The Lhasa River basin is thereby mainly classified in the *temperate climate zone (H III)*, with mean annual air temperatures of between 6 and 8°C in the southern part (1, 2) (e.g. Lhasa or Nimu) and between 0 and 5°C in the northern part (3) (e.g. Damshung). June is the warmest month, when mean monthly temperatures vary from 10°C in the north to 17°C in the south. The Nyainqêntanglha Mountains along the north-western borderline are ranked within the *subfrigid zone (H IV)* due to their higher elevation and subsequently lower temperatures. There, the mean annual temperatures range between -2 and -3°C. Permafrost soils, therefore, often develop. Temperatures from 6 to 10°C are reached during the warmest month. The snowline stretches from 5,800 to 6,000 m a.s.l. (KAISER ET AL. 2006). As a consequence, only the Nyainqêntanglha Mountains are permanently snow-covered.

The climate types relating to humidity are determined by the aridity index, which in turn is defined by the ratio of annual potential evapotranspiration to annual precipitation, as well as by the precipitation sum from March to May. These types reproduce the direction of the summer monsoon precipitation, which starts in April in the southeast of Tibet and advances to the northwest. The easternmost region of the basin is classified as *moist (A)*, with a precipitation sum of 600 to 800 mm (e.g. Jiali). The *semi-moist type (B)* follows, covering most of the basin (e.g. Meldro Gungkar). In this region, the summer monsoon starts in late May and delivers between 400 and 550 mm of precipitation until its end in early October. In July and August, more than 100 mm of average precipitation falls per month, accounting for at least 50 percent of annual precipitation. Along the Nyainqêntanglha Mountains, orographic precipitation falls when the monsoon strikes, especially in the southeast oriented valleys. The mountain range therefore marks the border between the *semi-moist (B)* and *semi-arid (C)* climate types along the northeastern edge of the basin. Coming to the southwestern regions, the monsoon starts later, in June, and precipitation decreases, reaching totals of between 300 and 450 mm. Additionally, lower elevation and higher temperatures, together with extremely high solar radiation resulting from the high elevation and the latitude, lead to arid spring and autumn months with high potential evaporation rates. The climate is therefore classified as *semi-arid (C)* (e.g. Lhasa). Moreover, a strong diurnal temperature course and high inter-annual variations in precipitation are characteristic of the whole catchment. For example, between 230 and 614 mm of annual precipitation were recorded at the Lhasa climate station between 1980 and 2004 (ICIMOD 2009). Since the monsoon is delayed in some years, the already short wet season of between 110 and 140 days is even further shortened, and can cause droughts in the worst cases. Reasons for these large differences can be found in circulation changes: on one hand, increasing winter surface pressure over the Tibetan Plateau and decreasing surface pressure in Siberia might strengthen the Tibetan High, which often leads to more precipitation and higher temperatures over the Tibetan Plateau. On the other hand, steeper pressure gradients from south to north due to increasing pressure over the North Indian Ocean, together with higher temperatures during the monsoon season, enhance the transport of moisture to the Tibetan Plateau. Hence, the region receives more precipitation (KANG ET AL. 2007).



The winter months are arid throughout the catchment due to dry air masses from the north and northeast. Only in the easternmost parts do warm fronts of the winter monsoon from the Bay of Bengal sporadically bring moist air masses. Snowfall is consequently rare, only in the *H III A* zone are snow and hailstorms frequent, from November until May. As solar radiation is extremely high because of the altitude (latitude), fallen snow melts away before noon in most parts of the catchment. From December to February, mean winter temperatures register slightly below 0°C in the southern, lower parts of the basin along the river valleys. They are classified as *mainly frost free* (1) or *slightly frost prone* (2), although the absolute minimum varies to around -10°C. In the northern part, this value represents the mean winter temperature, with an absolute minimum of about -24°C. Mean monthly temperatures of below 0°C are recorded from November until March. Accordingly, the region is classified as *frost prone* (3). The following figure gives an overview of the climate zones of the Lhasa River catchment and shows representative climate station data (LEBER ET AL. 1995, CHU ET AL. 2007, ICIMOD 2009).

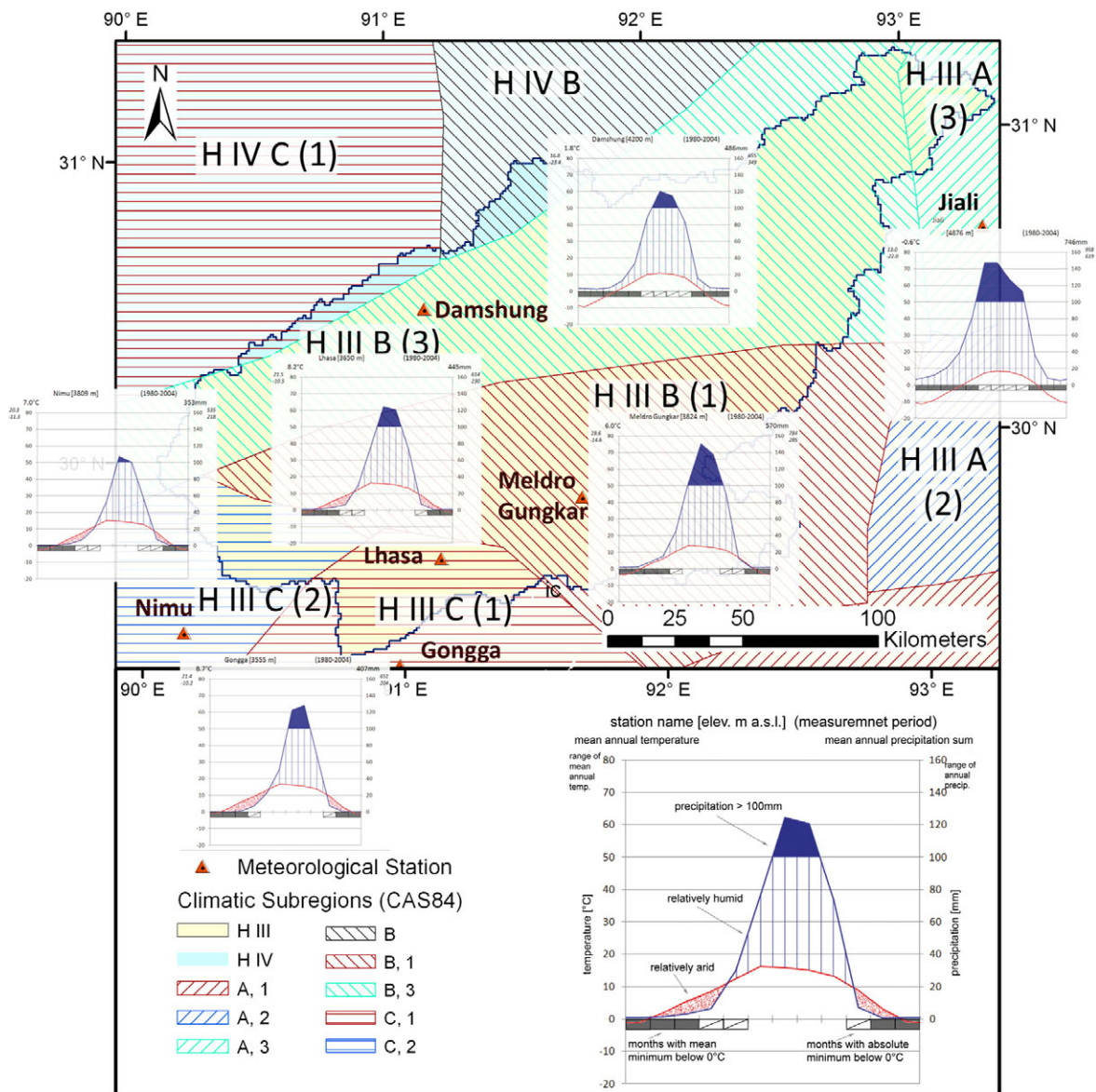


Figure 2.4: Climatic sub-regions of the Lhasa River catchment with representative climate diagrams (based on CAS (1984) according to LEBER ET AL. (1995) and ICIMOD (2009)).

## 2.3 Hydrology

The Lhasa River or Kyi Chu is the largest tributary, in the middle reach of the Yarlung Tsangpo, among five major tributaries in Tibet. Its catchment has an area of 32,800 km<sup>2</sup> at the junction with the Yarlung Tsangpo at Qushui, and delivers an average annual runoff of 335 mm or 279 m<sup>3</sup>/s, measured at the gauge in Lhasa, which is the last before the river's mouth. The Lhasa River is formed by the confluence of the Rong Chu and the Reting Tsangpo at the gauge of Pangdo. The sources of the Rong Chu are located in the Western Nyainqêntanglha Mountains, which form the watershed of the Lhasa River as well as of the Yarlung Tsangpo. Hence, they build the borderline between the exterior drainage system with the delta in the Bay of Bengal in the Indian Ocean and the endorheic basins of central and northern Tibet. The Reting Tsangpo originates in the northeastern part of the catchment, called Miti Tsangpo in the headwaters. After passing Lhasa, the Toelung Chu joins the Lhasa River, which also originates in the glacierized area of the Nyainqêntanglha Mountains. In the west and east of the basin, small catchments adjoin the Lhasa River basin.

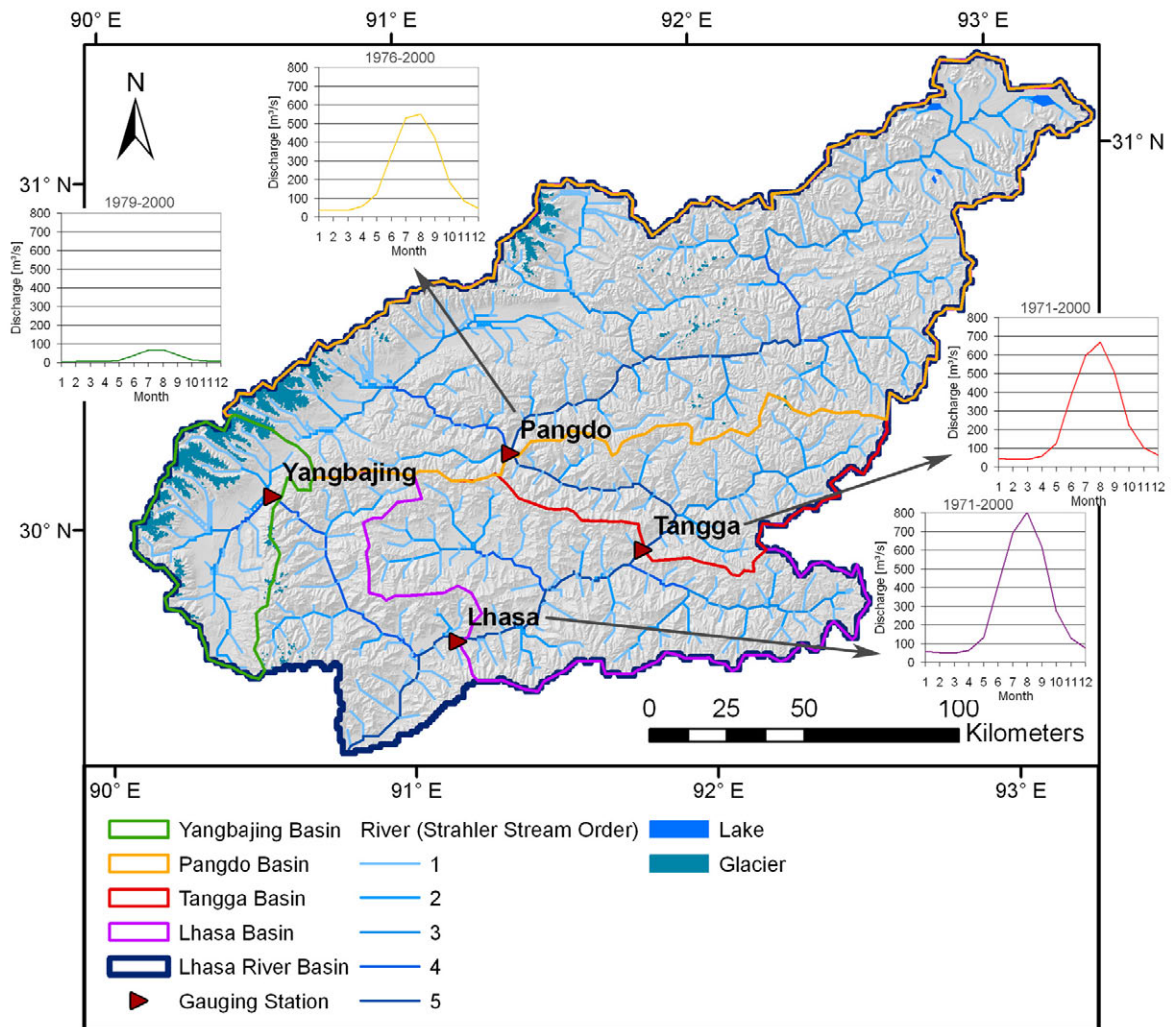


Figure 2.5: The Lhasa River basin with sub-basins and mean monthly runoff at the gauging stations Yangbajing, Pangdo, Tangga and Lhasa (based on ITP (2008), JARVIS ET AL. (2006), GARBRECHT AND MARTZ (1999)).

The Lhasa River is primarily fed by precipitation (46%), especially in its lower reaches. Meltwater from snow and glaciers (26%) and groundwater (28%) are its main sources in the upper reaches (DAJUN 1995, LIU ET AL. 2008, NING ET AL. 2001). The runoff regimes at the four gauging stations of the catchment for which data is available are similar. The temporal distribution of the mean annual runoff is shown, together with the watersheds of the sub-basins, which were derived from a Digital Terrain Model (JARVIS ET AL. 2006) using the TOPAZ software (GARBRECHT AND MARTZ 1999), in Figure 2.5; Table 2.2 gives an overview of the area, the glacial coverage and the mean annual discharge of the Lhasa River basin and its sub-basins. Due to the pronounced wet season during the summer monsoon and the dry season lasting the rest of the year, the runoff shows a clear seasonal cycle, with the flood peak reached in August. About 90 percent of the mean annual runoff is observed between May and November. As monsoon precipitation is the dominant factor in the runoff regime, it can be classified as a pluvio-nival regime where snow and ice-melt plays a secondary role in spring and autumn. In the winter season, runoff is low, because the rare precipitation falls as snow, which is mainly sublimated due to the dry air and extreme solar radiation in the lower regions. In higher areas it accumulates. Baseflow and small amounts of meltwater release contribute to the winter streamflow. Inter-annual variations in the runoff are high, for example, at the Lhasa gauge the discharge varied between 171 and 461 m<sup>3</sup>/s from 1956 to 2003 (ITP 2008), which approximates a variation of minus 50 to plus 100 percent.

*Table 2.2: Basin areas and glacierized areas of the Lhasa River basin and sub-basins (based on ITP (2008), JARVIS ET AL. (2006), GARBRECHT AND MARTZ (1999)).*

Basin gauge	Area [km <sup>2</sup> ]	Glacierized area [%]	Mean annual runoff [m <sup>3</sup> /s]
Mouth of Lhasa River	32,798	2.0	No data
Lhasa	26,339	1.3	279
Tangga	20,195	1.7	204
Pangdo	16,496	2.0	237
Yangbajing	2,719	11.5	23

Fertilizers and chemical pesticides are applied sparsely, and sewage drainage is rare, so water quality in the Lhasa River basin is good. According to DAJUN (1995) 88 m<sup>3</sup> of water are available per capita per day.

Although hydropower potential is estimated at 2,560,000 kW, which means 7.76 kW per capita, hydroelectric utilization is small at the moment. 83 medium- and small hydroelectric stations with a capacity of 26,124 kW were built as key stations of the Lhasa River Electric Net before 1983. Irrigation is subordinate, because only about 0.5 percent of the catchment is irrigated at present. For this purpose, 31 irrigation channels with a total transfer capacity of 115.5 m<sup>3</sup>/s and 14 reservoirs with a capacity of 26.37 m<sup>3</sup> have been implemented downstream of the Tangga gauge (DAJUN 1995).



## 2.4 Soils

The Harmonized World Soil Database (FAO ET AL. 2009), based on the Soil Map of China (SHI ET AL. 2004), provides detailed information about soil units and soil texture in the Lhasa River basin. Figure 2.6 shows the distribution of soil units in the investigation area, and Figure 2.7 gives an overview of the spatial distribution of the soil texture classes.

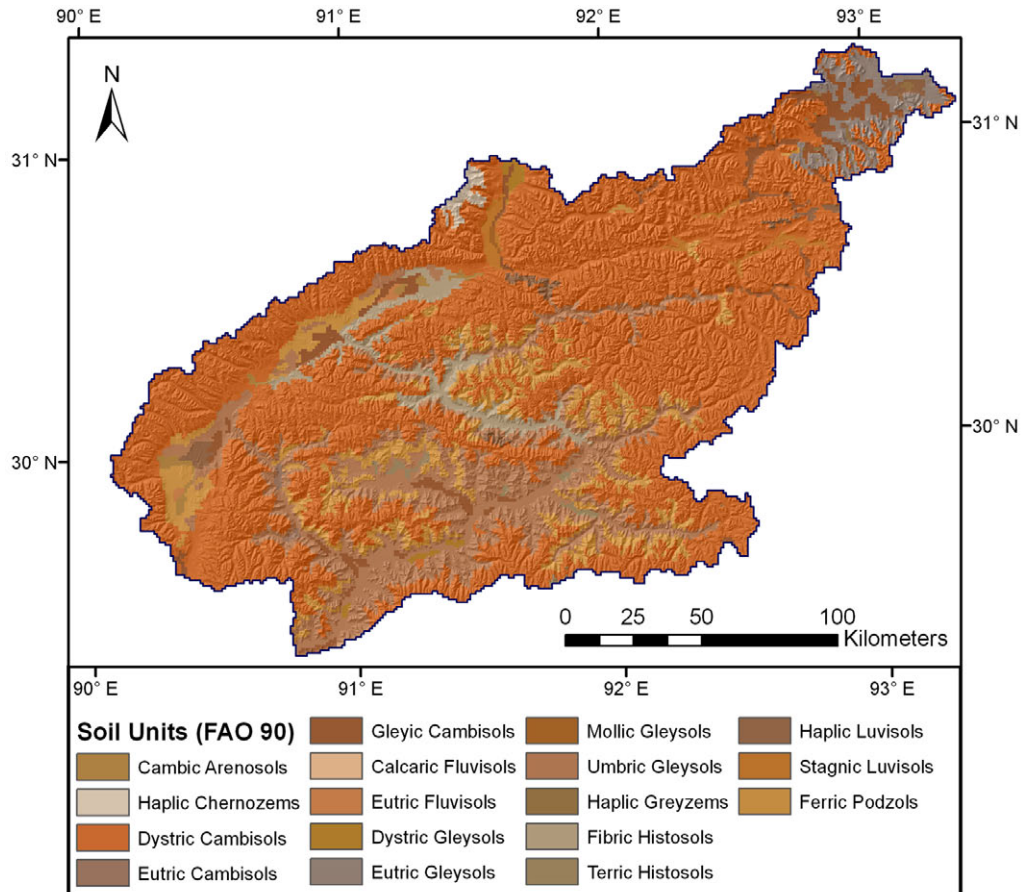


Figure 2.6: Soil Units (FAO 90 classification system) in the Lhasa River catchment according to the Harmonized World Soil Database (version 1.1) (based on FAO ET AL. (2009)).

Cambisols, which are weakly- to moderately developed soils, are predominant, especially in the higher areas. They are mainly composed of loamy sands. Permafrost occurs on the mountain tops along the Nyainqêntanglha Mountains. The diurnal freeze-thaw changes which determine the weathering processes and affect the soils are characteristic. Gleysols appear in the Lhasa River valley around Lhasa, the Toelung Chu valley and along the Reting Tsangpo, as well as in the northeastern area where the Miti Tsangpo has its sources. As well as loamy clays, sandy loam covers poor clay loam in some parts. In the central valley of the Rong Chu and the Kyi Chu around Pangdo, histosols composed of organic material can be found. Temporarily or permanently active flood plains and a high groundwater level are characteristic of these alluvial soils, which are composed of clay loam. Podzols with poor clay sands occur along parts of the Yangbajing Graben and on hill slopes in the central and southern river valleys. Additionally, isolated aeolian sand fields can be found in the catchment, due to sandstorms, resulting in loess in some areas, which permits little agricultural use. Sporadically, the soil units of Luvisols, Greyzems,

Chernozems and Arenosols occur in the catchment. Silty soils can be ignored, having a percentage below one (FAO ET AL. 2009, KAISER ET AL. 2006, SMITH ET AL. 1999).

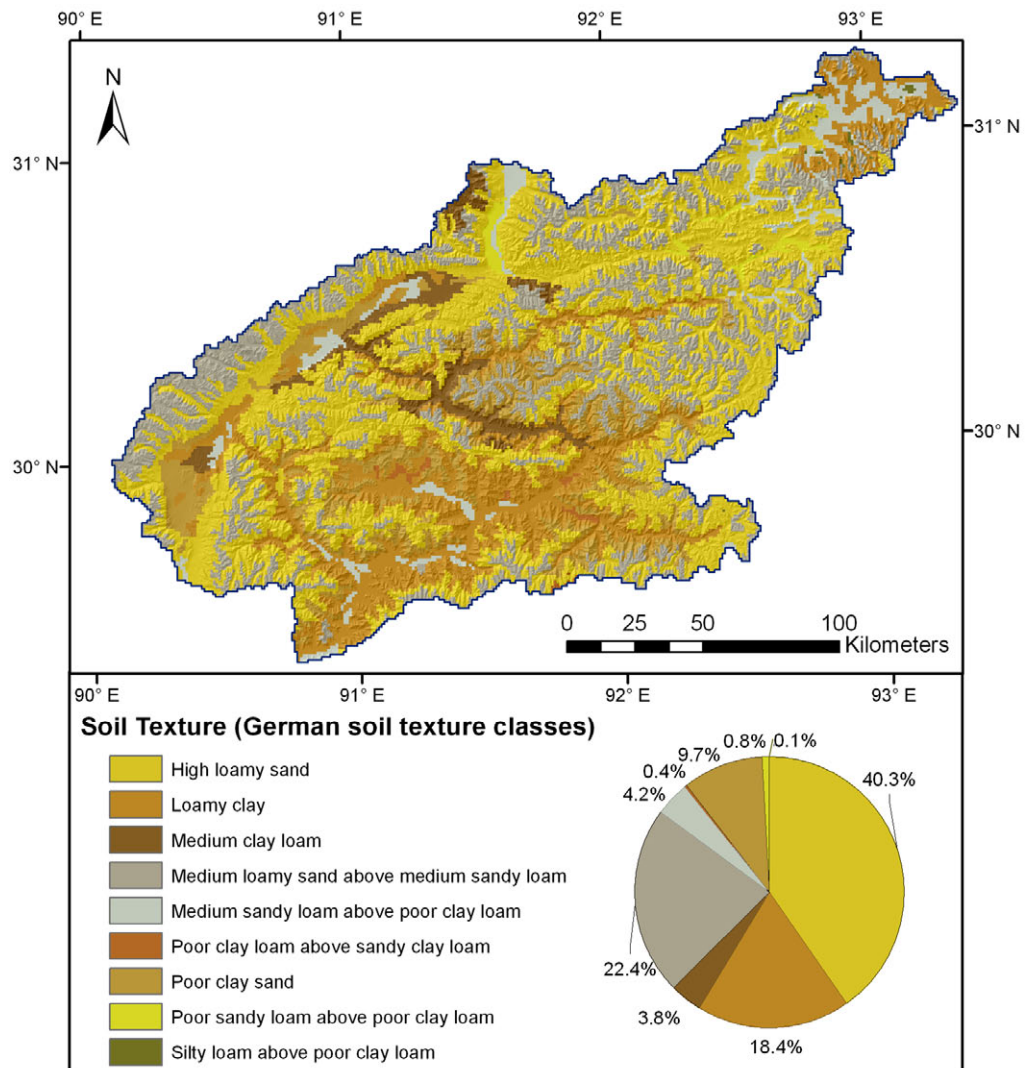


Figure 2.7: German soil texture classes according to the Harmonized World Soil Database (version 1.1) and its percental distribution in the Lhasa River catchment (based on FAO ET AL. (2009)).

## 2.5 Land Cover and Land Use

The Lhasa River catchment is classified into the dry midlatitudes ecozone, with grass steppe as its dominant land cover type, according to SCHULTZ (2005). Due to its geographical location and corresponding climatic, hydrological and pedological conditions, alpine grass- and shrublands prevail in the natural vegetation. Only a few juniper forests and riparian forests can be found along the wide river valleys, where even small wetlands exist. In the higher regions, bare rock and gravel are dominant in the paths of glaciers. Above 5,800 m a.s.l., snow follows, mainly along the Nyainqêntanglha Mountains (KAISER ET AL. 2006, MIEHE ET AL. 2000).

Physio-geographic conditions determine land use. Most of the area is used as pasture land, where semi-nomadic herding is practised. Hence, settlements are rare and small. Only the capital of the Tibet Autonomous Region, Lhasa, features as a residential area in the land use and land cover classification of the basin, which is derived from the NASA

TERRA / MODIS land cover product (BOSTON UNIVERSITY 2004) and is illustrated in Figure 2.8. Along the river valleys in the south, climatic conditions enable the cultivation of arable land. Barley is predominantly cultivated, due to its adaptability to the rough climatic conditions. Accompanied by milk, butter and a little yak meat, it is the staple food of the Tibetans. In recent decades, the cultivation of vegetables has been promoted to Chinese people settling in the Lhasa River basin. Greenhouses were built to extend the growing season, usually spanning from May to October, although annual variations are large due to the varying precipitation patterns of the monsoon (see section 2.2). Moreover, heavy grazing and wood-cutting for fuel also causes badlands and erosion in the Lhasa River basin (CHU ET AL. 2007, KAISER ET AL. 2006).

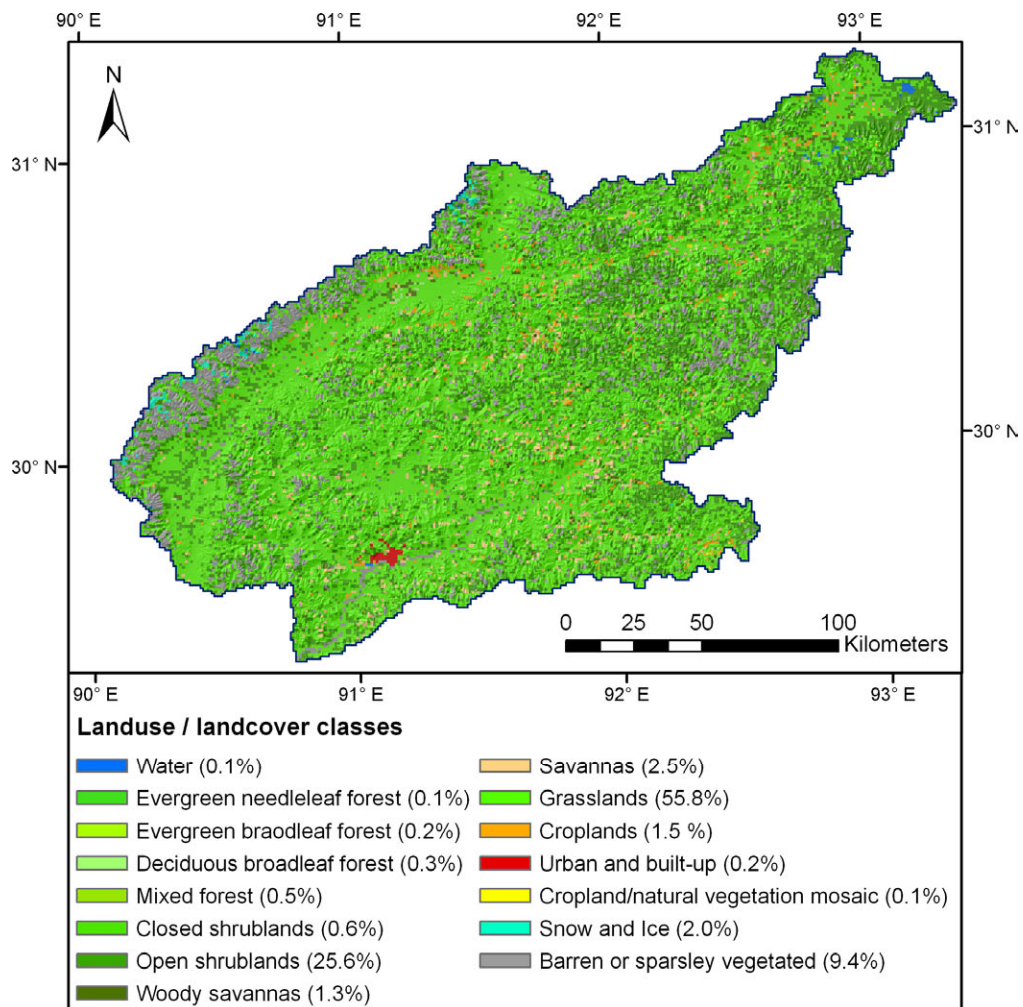


Figure 2.8: Land use and land cover distribution in the Lhasa River basin modified consistent with the NASA TERRA/MODIS land cover product (BOSTON UNIVERSITY 2004).

## 2.6 Glaciers of the Lhasa River Catchment

The Nyainqêntanglha Mountains are one of the main glacierized areas of Central Asia, alongside the Himalayas, the Kunlun Shan, the Karakorum and the Tian Shan ranges. 7,080 glaciers cover an area of 10,701 km<sup>2</sup>, and amount to a volume of 1,002 km<sup>3</sup> in total (YAO ET AL. 2006). Parts of the Western Nyainqêntanglha Mountains form the north-western watershed of the Lhasa River basin. Hence, most glaciers of the basin are located there, aided by the orientation of the valleys to southeast, where the monsoon



comes from, triggering orographic precipitation. West of Lhasa, on both sides of the Yangbajing Graben as well as at the peaks in the north-western basin, where the Nyainqêntanglha Mountains stretch over to their eastern range, glaciers can be found (see Figure 2.8). Altogether they cover 670 km<sup>2</sup>, equating to 2.1 percent of the total basin area. In the sub-basins, the percentage is higher due to the smaller sub-basin area. The Yangbajing sub-basin holds the highest glacial coverage, with 11.5 percent. Table 2.2 lists the glacial coverage of the sub-basins of the Lhasa River catchment.

Forty percent of the glaciers in the basin can be classified as *mountain glaciers* according to the Chinese Glacier Inventory (WDC 2009). This primary class includes glaciers adhering to mountainsides, and comprises cirque, niche and crater glacier types as well as hanging glaciers and groups of small ice units (RAU ET AL. 2005). The mountain glaciers are distinguished from *valley glaciers* by not yet having developed or by already having melted out of a valley. The Xibu Glacier, originating in the Nyainqêntanglha Feng with 7,162 m a.s.l., is the largest example of a valley glacier in the test site, with an area of 31 km<sup>2</sup>. As well as the glaciers along the mountain range, valley glaciers can also be found in the western area southeast of Mount Qungmoganzê (7,048 m a.s.l.), and the many trough valleys along the Nyainqêntanglha Mountains indicate the retreat of former valley glaciers into mountain glaciers. About 15 percent rank as *glacierets*, very small ice or snow masses without ice movement. They can be found all over the catchment, but in the north-eastern region they are predominant. Especially in this region, *rock glaciers* also occur, documenting permafrost regions. Figure 2.9 illustrates the afore-mentioned glacier types and their distribution in the Lhasa River catchment.

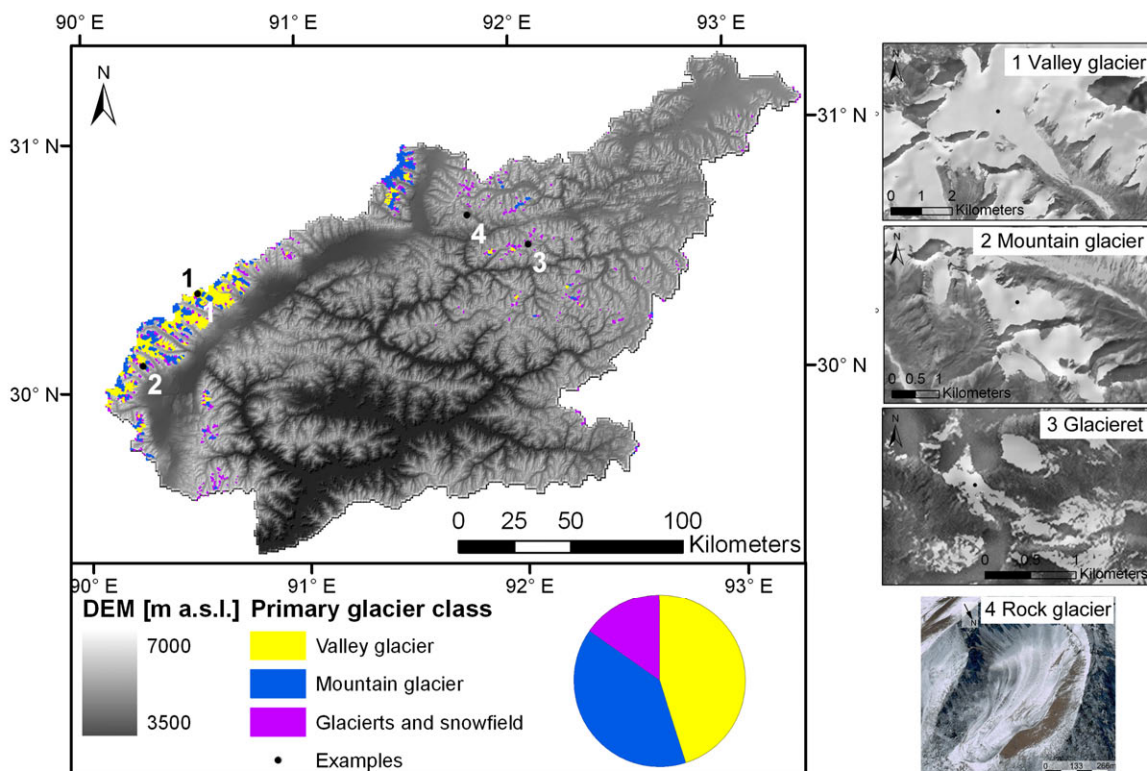


Figure 2.9: Distribution of glacier classes with illustrated examples in the Lhasa River basin (based on GOOGLE EARTH (2010), JARVIS ET AL. (2006), USGS (2009) and WDC (2009)).

All glaciers in the Lhasa River catchment rank among the *polythermal* (obsolete *sub-polar*) types (YAO 2006), which are characterized by a basal ice layer at the melting point, overlaid by a layer of cold ice. The surface layer above can seasonally warm to the melting point (PATERSON 1994). Due to climatic conditions (see section 2.2) accumulation and ablation are determined by the monsoon, and interact with each other. During the summer months the monsoon brings snow in the higher regions, although snow and ice-melt can occur depending on the air temperature. Measurements taken at the Lanong glacier close to the Nyainqêntanglha Feng show that snowmelt occurs during summer at an elevation of 5,800 m a.s.l. The beginning and ending of the monsoon precipitation determine the length of the dry period, with high solar radiation input before and afterwards promoting snow and ice-melt (KANG ET AL. 2007).

Since the Little Ice Age of about 1890, the glaciers in Central Asia have been retreating in general, although there were periods with positive mass balance and advancing glaciers during the late 1960s and 1970s. Since then, almost all glaciers have been retreating, especially during the 1990s when an intensification of melting was recorded as a result of the increasing temperatures on the Tibetan Plateau resulting from climate change. Table 2.3 gives an overview of the glaciers advancing and retreating in High Asia in different periods from 1950 onwards (YAO ET AL. 2006).

*Table 2.3: Advancing and retreating glaciers in High Asia from 1950 (YAO 2006, p. 277).*

<b>Time</b>	<b>Glaciers</b>	<b>Retreating glaciers [%]</b>	<b>Advancing glaciers [%]</b>	<b>Stationary glaciers [%]</b>
1950 – 1970	116	53.44	30.17	16.37
1970 – 1980	224	44.2	26.3	29.5
1980 – 1990	612	90	10	0
1990 to present	612	95	5	0

Overall, information about glaciers in Asia is sparse: particularly, detailed mass balance or ice volume data are hardly ever available. How the impact of future climate change on glacier mass balance and its influence on the water balance can be determined in spite of this situation is the subject of this thesis, and will be described in the following chapters.

### 3 Distributed, Process Oriented Hydrological and Glacier Modelling

To determine the impact of future climate change on glaciers and subsequently on the water balance of large-scale river basins, the modelling framework needs to capture all relevant processes in an accurate spatial and temporal resolution under past and future climatic conditions. This includes, regarding a glacier, processes for calculating meltwater release, and the quantification of further water balance components such as evapotranspiration, snowmelt, and soil and groundwater release for the calculation of the water balance. Hence, a glacier model and a hydrological model have to be coupled. Furthermore, the model approach must also be applicable under future climatic conditions. It should therefore be based on physical principles, use universal parameters and not require calibration. These measures ensure that the model results are valid under changing climatic conditions, because correlation derived under present conditions used in a calibration may not be valid anymore in the future. In addition, it should be possible to apply regional climate model (RCM) outputs as future meteorological drivers. Accordingly, energy and mass balances must be closed in coupling with climate models (MAUSER AND BACH 2009). Furthermore, bridging the gap between different scales of data and processes must be feasible. The spatial resolution of RCMs is in the range of 100 to 1,000 km<sup>2</sup>, whereas the area of mountain glaciers often varies between a few ha to several km<sup>2</sup>. For process description on the landsurface, which is limited by the area of the test basin as well as by the availability of input data, a resolution of the order of 1 km<sup>2</sup> is adequate, according to MAUSER AND BACH (2009). The processes acting on a glacier are usually below the scale of 1 km<sup>2</sup> in mountain glaciers. Figure 3.1 illustrates the various scales of the processes which should be adequately connected through the modelling approach.

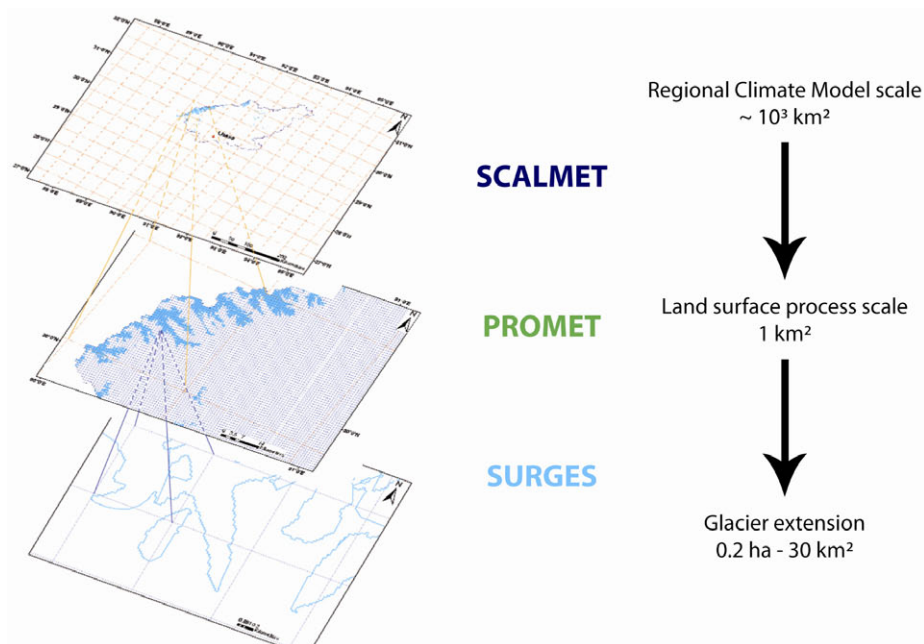


Figure 3.1: Correlation of the various spatial scales between the processes and the models applied to bridge the gap.

In this thesis, the glacier model SURGES (**S**ubscale **R**egional **G**lacier **E**xtension **S**imulator) (WEBER ET AL. 2008, PRASCH ET AL. 2009) was implemented in the PROMET (**P**rocesses of **R**adiation, **M**ass and **E**nergy **T**ransfer) (MAUSER AND BACH 2009) hydrological model to simulate the main glacial and the detailed hydrological processes, whereas the SCALMET (**S**caling **M**eteorological variables) (MARKE 2008) tool was used for coupling with RCMs. Figure 3.1 illustrates the applied models in the modelling framework bridging the various scales of the processes.

In the following sections, the PROMET model with the SCALMET coupling tool is introduced first (section 3.1). Secondly, the SURGES glacier model is described in detail (section 3.2). The reasons for choosing these models are explained through description of the demands on the models and the state of the art.

### 3.1 The PROMET Hydrological Model

In studies of the determination of glacier meltwater contribution to runoff under changing climatic conditions, simple conceptual hydrological models are commonly applied (HAGG ET AL. 2007, HORTON ET AL. 2006, HUSS ET AL. (2008), SINGH AND KUMAR 1997 or STAHL ET AL. 2008). Daily temperature and precipitation values are usually considered sufficient as meteorological input data for the conceptual models. Hence, sparse data requirements are a reason for the application of such hydrological models, especially in remote regions, although they do not close mass and energy balances. A direct coupling with climate models is, therefore, also impossible from the outset (MAUSER AND BACH 2009). Furthermore, the models are calibrated under present conditions. The derived correlations used in the calibration may change in the future, invalidating the empirical relationships. Consequently, the results for future climatic conditions are afflicted by considerable uncertainties. Therefore they should not be used for Climate Change impact assessment.

Moreover, these studies are largely carried out in small basins. A detailed simulation of the water flow considering vegetation growth, soil texture, groundwater flows and finally their interaction in routing the water in the river channel is therefore neglected. Conclusions are then drawn for larger regions according to these studies (SEVERSKIY 2009, BARNETT ET AL. 2005, CASASSA ET AL. 2009). For example, REES AND COLLINS (2006) assessed two hypothetical small river catchments in the Himalayas, and simulated the impact of climate change on the glaciers and their influence on runoff. According to the simulation results, they concluded the impact of GCC on glaciers and runoff in the Himalayas, considering regional differences, but without modelling the water flows downstream with the interactions of soil, vegetation, groundwater and other factors.

Accordingly, these models do not capture the demands for simulations in large-scale river basins under future climatic conditions. By contrast, the PROMET (an acronym of **P**rocesses of **R**adiation, **M**ass and **E**nergy **T**ransfer) model used in this study was developed in order to study the impact of climate change on the water balance in large-scale watersheds ( $A \sim 100\,000\text{ km}^2$ ). It is used within the GLOWA-Danube integrative research project (MAUSER AND LUDWIG 2002, LUDWIG ET AL. 2003, GLOWA-DANUBE 2009). The spatial heterogeneity of complex basins with mountain headwatersheds (for example the Alps) on the one hand, and mountain forelands with large river valleys such as the

Danube on the other hand is captured synchronously by the model. This allows the simulation of all relevant processes under varying climatic conditions and hydrological regimes. To achieve this, PROMET uses distinct components for meteorology, land surface energy and mass balances, vegetation, snow and ice, soil hydraulics and soil temperature and a groundwater and channel-flow component with hydraulic structures. The components fully interact and consider all processes related to water and energy fluxes. Within as well as throughout all its components and feedbacks, PROMET strictly conserves mass and energy. Figure 3.2 gives a schematic overview of the components mentioned and their interfaces for data exchange.

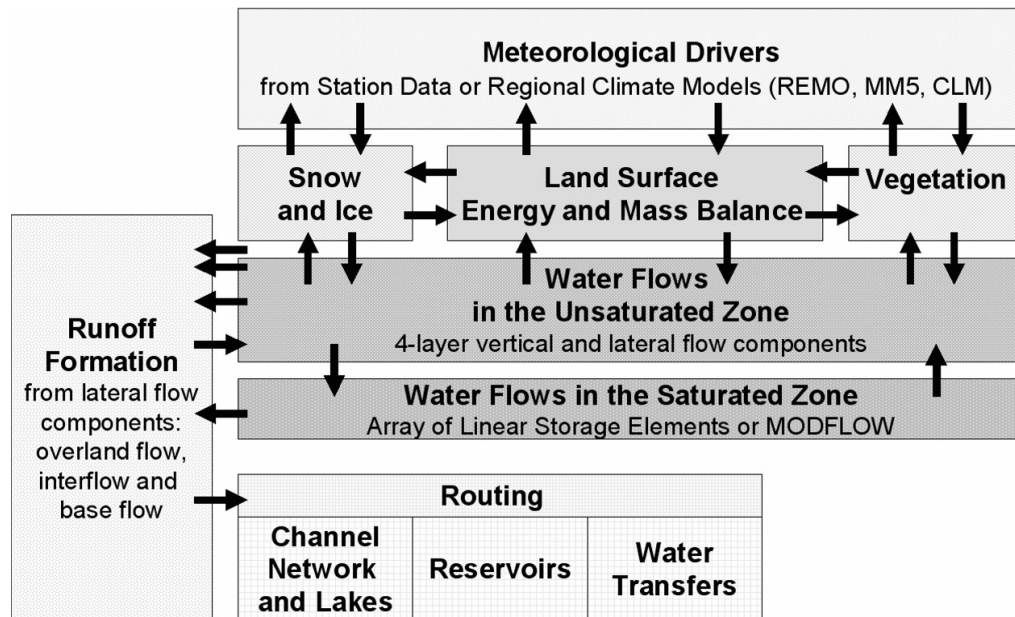


Figure 3.2: Schematic diagram of the components of PROMET and the interfaces between them. Boxes indicate components and arrows indicate interfaces through which data is exchanged (MAUSER AND BACH 2009, p.365).

PROMET is a fully spatially distributed raster model, which is used in the study with a resolution of 1 x 1 km. It runs in the study on an hourly time step. Together with mass and energy conservation, this characteristic forms the basis for coupling with regional climate models, which are also usually raster-based. Furthermore, PROMET is not calibrated to using measured discharge data to fully exploit the predictive capabilities of the physically based approach. It can therefore be used under past as well as future climatic conditions. PROMET has already been successfully applied to changing climatic conditions in the Upper Danube basin (MAUSER AND BACH 2009).

In the following paragraphs the components of PROMET are briefly described, except for the snow and ice component, where SURGES is implemented and which is explained in detail in section 3.2. For a further, more detailed description of the other components, please refer to MAUSER AND BACH (2009).

### 3.1.1 Meteorological Data Provision

In order to run PROMET, hourly data of air temperature, precipitation, air humidity, wind speed and incoming short and longwave radiation are required per grid cell. The



meteorology component provides PROMET with this data through (a) temporally and spatially interpolated station recordings or (b) downscaled regional climate models, by coupling with the SCALMET scaling tool (MARKE 2008). In the first case, for each time step an altitudinal gradient is deduced from the station recordings, which is then applied in the spatial interpolation using the elevation of each grid cell in the catchment to determine the “gradient” temperature. Secondly, the residuals between observed and gradient temperatures at the station locations are calculated. Depending on the inverse squared distance between station and grid cell, weighting factors are determined and interpolated residuals are added to the gradient temperature field. The measured values are consequently preserved. If a temporal interpolation is required, a cubic spline function is applied to all meteorological parameters except precipitation. The latter is classified under short events for a single recording and under long-term events for consecutive observations. Afterwards, the precipitation is distributed to the hours before the single event using a Gaussian distribution, or equally distributed in time for the continuous case (STRASSER AND MAUSER 2001, MAUSER AND BACH 2009).

In the second case, PROMET is coupled with the SCALMET scaling tool (Scaling Meteorological variables) (MARKE 2008). The tool connects models simulating the atmosphere with those operating on the land surface. To apply RCM data as meteorological drivers for modelling land surface processes at a spatial resolution of 1 x 1 km<sup>2</sup>, their coarse resolution, varying from 10 x 10 km<sup>2</sup> (e.g. REMO) to 50 x 50 km<sup>2</sup> (e.g. CLM) has to be refined. Two methods are common in overcoming the differences between the coarse resolution of global climate model (GCM) or RCM outputs and the high-resolution glacier or landsurface models (MOORE ET AL. 2009). In the first approach, measured meteorological data from the past are modified by adding or subtracting differences so that the temperature and precipitation changes of the climate model outputs are reproduced (HAGG ET AL. 2007, HUSS ET AL. 2008, SINGH AND BENGTTSSON 2004, SINGH AND KUMAR 1997). The second method applies statistical downscaling procedures to GCM or RCM outputs by using correlations between the model outputs and meteorological observations in the area of interest. Consequently, future climatic conditions are determined using the deduced correlation factors (e.g. RADIC AND HOCK 2006, HOFER ET AL. 2010, PAUL AND KOTLARSKI 2010). Dynamic downscaling of climate model outputs as a third method has not yet been seen in glacier studies (MOORE ET AL. 2009).

Since temperature and precipitation are insufficient meteorological drivers to run PROMET as deduced by the first method, and no observation data of other variables are available to deduce correlations for them as by the second method, the SCALMET tool contains methods for all required meteorological input data. In order to adequately remap RCM outputs, SCALMET uses different scaling techniques, ranging from direct interpolation methods, such as bilinear interpolation, to statistical approaches using empirical relations. Furthermore, quasi-physical methods, a combination of physically based approaches and statistical methods are also applied (MARKE AND MAUSER 2008). Topographical information (elevation, slope, aspect) is included in order to consider subgrid-scale heterogeneities and related natural climate gradients, which are particularly

important in mountainous terrain. For each time step, the elevation dependency of meteorological variables, strongly varying with terrain elevation, e.g. air temperature, is analyzed. A linear regression function is determined, which is then applied and these variables adjusted. Specific submodels are implemented to downscale wind speed, shortwave and longwave radiation (LISTON AND ELDER 2006, IZIOMON ET AL. 2003) to account for subscale heterogeneities within the remapping process. To maintain the mass and energy balance predetermined by the RCM outputs, special algorithms are integrated into SCALMET which systematically assure the conservation of mass and energy between the model scales. Since the temporal resolution of some regional climate models is less than one hour, a temporal interpolation routine is also implemented following the procedure applied for station recordings described above, in order to disaggregate the time step values to an hourly time basis. This routine runs prior to the downscaling processes.

The shortwave radiation fluxes can also be determined by using downscaled cloud cover values. Firstly, the potential incoming shortwave radiation is calculated, taking into account topographic and astronomic parameters (LISTON AND ELDER 2006). Afterwards, it is divided into direct and diffuse fractions, taking into account cloud coverage according to BURRIDGE AND GADD (1974). Since the downscaling techniques implemented in SCALMET are based on physical and statistical approaches, they are completely general and can be applied without any further parameterization in various regions. Figure 3.3 gives a schematic overview of SCALMET including input and output data (MARKE 2008).

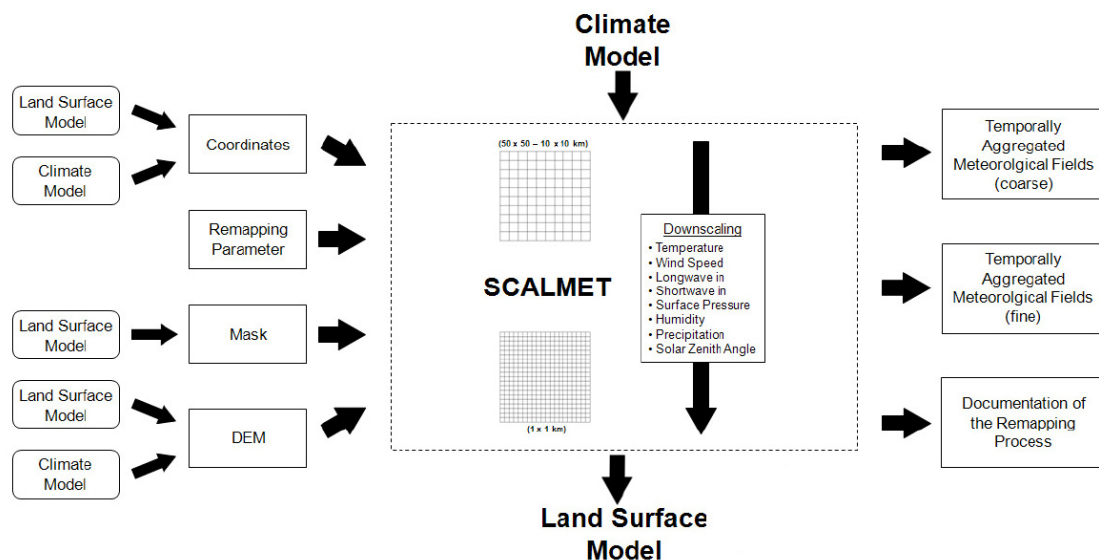


Figure 3.3: Schematic diagram of SCALMET with required inputs and outputs (MARKE 2008, p. 41, modified).

### 3.1.2 Land Surface Energy and Mass Balances

In order to close the energy and mass balances for vegetated and non-vegetated land surfaces, the land surface energy and mass balances component iteratively solves the energy balance equation by altering the surface temperature. Latent, sensible and ground heat flux, as well as reflected shortwave and emitted longwave radiation, are considered. Furthermore, transpired water vapour is transported into the free atmosphere consistent

with MONTEITH (1973) and CAMPBELL AND NORMAN (1998). In this step, the exchange of the results of the vegetation component is essential. This component models the water transports and carbon allocations in plants as a function of the specific canopy resistance, taking into account leaf area index, stomatal resistance, absorbed photosynthetically active radiation, temperature, humidity and soil moisture. Here, a distinction is made between two sub-components. The first sub-component, which was applied in this work, solves the Penman-Monteith equation (MONTEITH 1965) using factors for the water transport in plants described by JARVIS AND MORISON (1981) and BALDOCCHI ET AL. (1987). Leaf area index, plant height and albedo are taken either from literature, field measurements or remote sensing time series (MAUSER AND BACH 2009). In the second sub-component, the fully physiological, dynamic plant growth of active vegetation is modelled, based on FARQUHAR ET AL. (1980) and described in detail in HANK (2008). Accumulation and ablation of snow and ice are also calculated and the results are taken into account in closing the energy and mass balances. A detailed description of the ice and snow component with the SURGES glacier model implemented is given in section 3.2.

### **3.1.3 Soil Processes**

The 4-layer soil hydraulic and soil temperature component calculates the soil water content as a function of infiltration, exfiltration, percolation and capillary rise (EAGLESON 1978) as well as the vertical and lateral flows in and on the unsaturated soil. Due to the slope of the grid cells, lateral flows are calculated amongst them (MAUSER AND BACH 2009). The current temperature of soil is calculated, considering changes in soil moisture, soil freezing and soil surface energy balance and snow cover where required (MUERTH 2008).

### **3.1.4 Groundwater Flows**

The water flow in the saturated zone of a catchment and the exchange between the saturated zone and both the unsaturated soil layers and the channel network are captured by the groundwater sub-component. In addition to the option of coupling with the groundwater model MODFLOW (USGS 2010), a linear storage with an assumed time constant is allocated for each grid cell of the basin. Exchanges with the bottom soil layer through percolation and capillary rise are considered. Each storage element drains to the channel due to the time constant, which is defined by the distance to the main river channel, under the assumption that the largest distance equals one year of storage time. To grid cells lying close to the channel, an interval of one hour is allocated. By linearly interpolating between them, the time constant of all grid cells is assessed (MAUSER AND BACH 2009). Since the Lhasa River catchment is characterized by its mountainous relief, elevation and slope are also considered in the time constant. Hence, for grid cells above 5,000 m a.s.l. and slopes larger than 20 percent, the time interval is reduced to a fifth; for slopes larger than 30 percent it is reduced to one thirtieth. This equals a reduction from one week or one month in the second, to one day.

### 3.1.5 Runoff Formation

Accounting for the processes described, the runoff components of surface, fast and slow interflow and base flow are modelled per grid cell. On the assumption that every grid cell of the basin is part of the channel network, all cells are linked downstream following topography. The flow components are concentrated and routed through the channel network according to topography by the channel flow component. Surface flow is directly supplied to the channel, whereas interflow is delivered to major tributaries which are derived by using TOPAZ (GARBRUCH AND MARTZ 1999) and described in section 3.1.5. Flow velocities and changes in water storage in the channel are simulated using the Muskingum-Cunge-Todini approach (CUNGE 1969, TODINI 2007), which also maintains mass conservation. Runoff retention in reservoirs is also considered in PROMET. Furthermore, the man-made hydraulic structures component notes structures such as reservoirs and water transfers. Since the number and size of man-made structures in the Lhasa river basin is presently small (DAJUN 1995), they can be excluded from this study.

## 3.2 The SURGES Glacier Model

In this chapter the SURGES glacier model is described in detail. It is implemented in PROMET as part of the snow and ice component. The **Subscale Regional Glacier Extension Simulator SURGES** (WEBER ET AL. 2008, PRASCH ET AL. 2009) was developed by Dr. Markus Weber and the author within the framework of the GLOWA-Danube project, and implemented and used by the author in PROMET to simulate the impact of glacier melt water on the water balance. Hence, the emphasis in the modelling approach is on the hydrological processes of a glacier, which are described in the following section. The consequential requirements for the modelling approach are then introduced, together with the present state of the art. Subsequently, the details of the SURGES model are explained.

### 3.2.1 Characteristics of Glaciers

Prevailing meteorological and topographical conditions are the essential factors for the formation of glaciers. Solar radiation, air temperature, precipitation, wind speed and humidity as well as elevation, slope and exposure determine both the amount of snow accumulation and the subsequent ablation. When the snowpack outweighs the ablation over a long period, the snow on the ground compacts and ice is formed through the process of snow metamorphism. When the ice layer reaches approx. 20 to 30 m thickness (WINKLER 2009), it begins to move down the mountain slope as a result of the disequilibrium between accumulation and ablation area. Ice flow compensates this difference by moving the surplus of ice from the accumulation area to the ablation area. In general, two modes of movement can be distinguished: internal deformation of the ice causes shearing flow first, and basal sliding over the glacier bed is the second mode of ice flow. The shape of the terrain, the ice thickness, the temperature and the slope of the glacier bed determine the form and velocity of the ice flow (PATERSON 1994, OERLEMANS 2001).

These processes of accumulation and ablation divide the glacier into two areas, the accumulation zone with mass gain in the higher regions, and the ablation zone with mass loss below. They are separated by the equilibrium line altitude (ELA), where all processes are balanced. Figure 3.4 illustrates the meteorological and topographic characteristics determining the properties of a glacier.

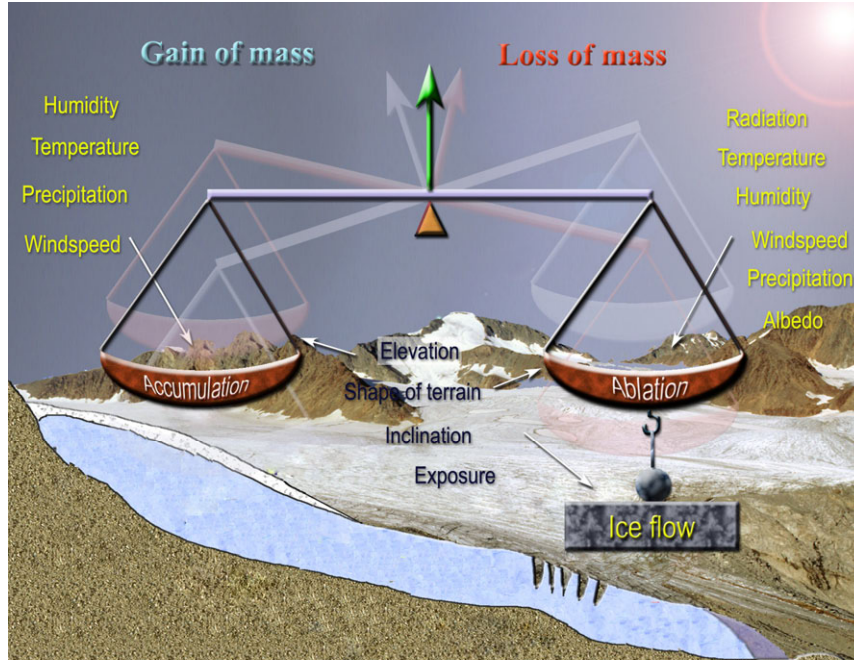


Figure 3.4: Meteorological and topographic characteristics determining the glacier mass balance (WEBER 2008, p. 11, modified).

Glaciers predominantly melt on their snow-free surface. Consequently, the amount of meltwater release by the glacier ice is roughly proportional to the snow-free area of the glacier. The water is directly delivered into the river channel and contributes to the runoff amount alongside precipitation, snowmelt, and soil and groundwater release. Depending on the total annual mass balance  $B$  [mm] of the glacier, more or less runoff is generated than in a non-glacierized basin. For negative mass balances ( $B < 0$ ), the ice storage is reduced and more water is available, whereas in the other case ( $B > 0$ ), precipitation is stored on the glacier and less water is available than in basins without glaciers.

The total mass balance  $B$  of a steady state glacier is zero, because the total amount of ablation is balanced by the entire accumulation (OERLEMANS 2001). Nevertheless, meltwater is released from the snow-free areas of a glacier during melting periods. A distinction can be made, then, between the ice-melt water release of the glacier  $C_{ice}$  [mm] and the total glacier contribution  $C_G$  [mm], which is proportional to the mass balance  $B$  [mm].  $C_G$  is defined as the overall change in ice volume  $V$  [ $m^3$ ] multiplied by ice density  $\rho_{ice}$  [ $kg\ m^{-3}$ ] (Eq. 3.1), whereas the total ice-melt  $C_{ice}$  is calculated by the integral over the snow-free area  $S_{ice}$  [ $m^2$ ] and the melt rate  $m_r$  [ $mm\ s^{-1}\ m^{-2}$ ] in the time step  $t$  [s] (Eq. 3.2).

$$C_G = -B = -\Delta V \cdot \rho_{ice} \quad (\text{Eq. 3.1})$$

$$C_{ice} = \int m_r \cdot S_{ice}(t) dt \quad (\text{Eq. 3.2})$$

The amount of  $C_{ice}$  is accordingly larger than  $C_G$  because ice-melt water is released from snow-free areas during one mass balance period, independently of the total mass balance  $B$ . In the case of complete snow cover over the glacier during one mass-balance year,  $C_{ice}$  is zero and no melt water is released, whereas  $C_G$  is negative.

These processes determine the meltwater contribution of a glacier to runoff. In order to simulate the impact of future climate change on glaciers and subsequently on the water balance, the following demands need to be considered by the modelling framework, in addition to the overall requirements described at the beginning of Chapter 3.

### **3.2.2 Requirements for Glacier Modelling and State of the Art**

The snow-free area of the glacier is required for the determination of the ice-melt water release. The duration of the snow cover on all parts of a glacier surface must therefore be calculated. In order to consider the small-scale processes on an alpine glacier, a subscale approach is chosen (see section 3.2.3). Accordingly, the amount of ice-melt water can be computed, together with the melt-rate, which depends on the energy balance of the ice surface. For these processes, the simulation of snow accumulation and of snow and ice ablation is required.

There are several models for simulating the glacier mass balance. In the course of studies which analysed the impact of climate change on glacier fed-rivers, conceptual temperature-index models were predominantly applied. They estimate the melt rate of snow and ice due to air temperature based on correlations which are assessed under present climatic conditions (BERGSTRÖM 1976, BRAITHWAITE AND ZHANG 1999, HOCK 2003, OERLEMANS ET AL. 1998, PELLICCIOTTI ET AL. 2005). Alternatively, energy balance models are used, which simulate snow- and ice-melt in solving the surface energy and mass balances (KLOK AND OERLEMANS 2002, STRASSER 2008, STRASSER AND MAUSER 2001, ZAPPA ET AL. 2003). Because of the underlying physics, they do not need calibration and are independent in space and time, which enables their transfer to other regions and application under future climatic conditions (STRASSER 2008). However, energy balance models require various meteorological variables such as solar radiation, air temperature, humidity, precipitation and wind speed, in contrast to the conceptual models, which often only need air temperature and precipitation. Since the required meteorological variables are provided by the meteorological component of PROMET (see section 3.1.1) and due to advantages such as transferability and application under future climatic conditions, an energy balance model is applied in this study (see section 3.2.5).

The quantity of ice storage limits meltwater release for glaciers that are no longer in a steady state. In these glaciers, the transport of ice from the accumulation to the ablation area is not balanced, and ice loss or gain occurs. Thus the ice thickness distribution over the glacierized area or, in other words, the geometry of the glacier ice reservoir, defines the duration of melting until the total melt. Hence, the dynamic adjustment of the glacierized areas is another precondition for determination of the melt water release under changing climatic conditions. For this purpose, mass balance models are coupled with ice flow models, for instance by LE MEUR ET AL. (2007) or ZOU AND OERLEMANS (1997). In order to simulate the ice flow and geometry changes of mountain glaciers, simple flowline

models (GREUILL 1992, OERLEMANS 1997) and complex 3-dimensional ice flow models (GUDMUNDSSON 1999, HUTTER 1982, JOUVET ET AL. 2008, 2009) were developed. The latter solve the Navier-Stokes equations in the simulations. Due to the complexity of the ice flow processes, all models need detailed information about the glacier bed geometry and ice thickness distribution. Since the required data are available only for a few glaciers, their application is limited to individual glaciers. This is one reason why glacier changes are crudely considered in long-term studies. Moreover, the computational needs of ice flow models are intensive. Consequently, they cannot be applied in simulating numerous glaciers in meso- or large-scale catchments. Contrary to these complex models, first studies try to parameterize the effect of ice flow as submergence and emergence. HUSS ET AL. (2010) recently proposed correlations between ice thickness changes and the mass balance, size and geometry of the glacier. Nevertheless, their application still requires further investigation. Accordingly, in this study a simple approach to the dynamical adjustment of the glacier geometry is chosen, as described in section 3.2.7.

Figure 3.5 summarizes the relationship between meteorological conditions and the consequences for glaciers, which should be considered in glacier and melt water release modelling.

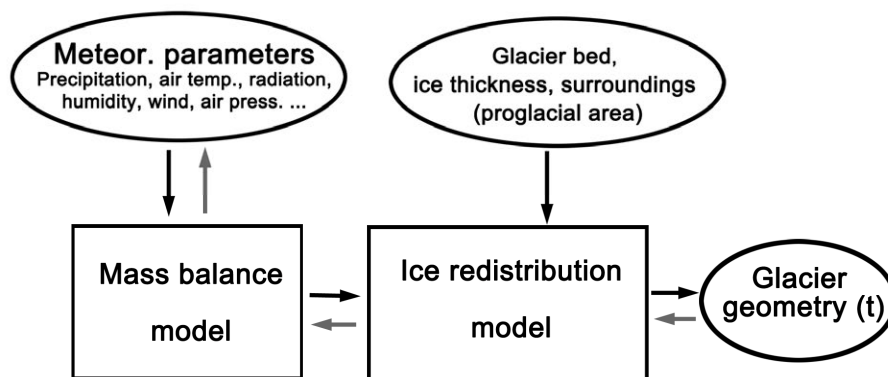


Figure 3.5: Influencing factors for glacier modelling (OERLEMANS 2001, p. 2, modified).

Next, the SURGES glacier model is introduced. First, the subscale approach and the extrapolation of meteorological data to all subscale elements are shown. The details of modelling the mass and surface energy balances of the glacier follow. Since snow accumulation and ablation are an essential part of the model, the details of the snow component of PROMET are given here as well. Finally, the simulation of snow metamorphism and ice redistribution is introduced.

### 3.2.3 Subscale Approach

A glacier is characterized by the mass balance and the geometry of the ice reservoir, which in turn depends on the prevailing meteorological and topographic conditions as described in the previous section. In the Lhasa River catchment, the dimensions and the geometric characteristics of the glaciers vary greatly as introduced in section 2.6. For instance, the areas per glacier vary from 0.2 ha to 31.1 km<sup>2</sup>. By contrast, the spatial resolution of PROMET is 1 x 1 km. Furthermore, the glacier area is often spread over several grid cells (see Figure 3.6, left), which are connected through ice flow. Only



30 percent of the grid cells are completely covered by a glacier, whereas for 27 percent of the grid cells less than 50 percent of the area is glacierized. Figure 3.6 (right) shows the frequency distribution of the glacier area per grid cell according to the Chinese Glacier Inventory (WDC 2009), which is introduced with the input data in section 4.3.

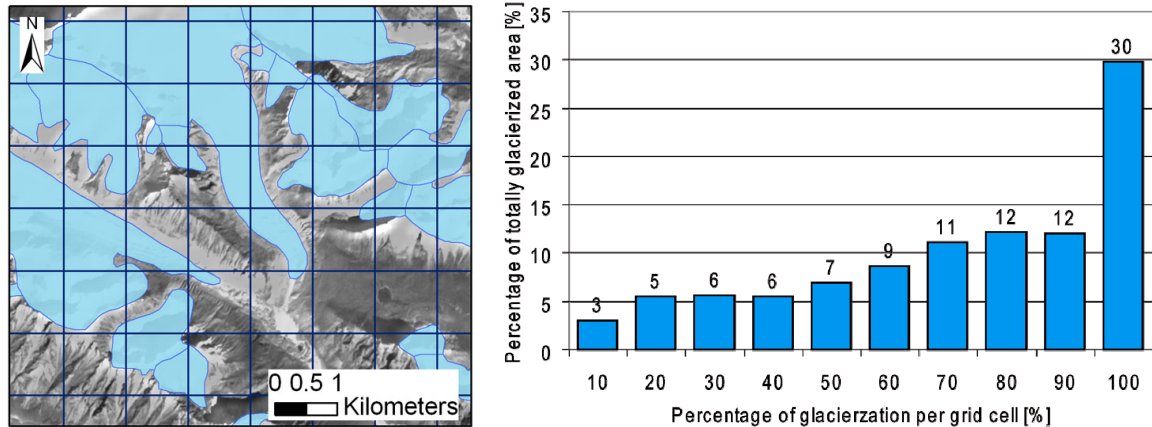


Figure 3.6: Distribution of glaciers over several grid cells (left) and frequency distribution of glacier area per grid cell in the Lhasa River catchment (right) (based on WDC 2009).

Within one grid cell, the glacier extends over an elevation range of up to 1,200 m. This stretch cannot be represented by the mean elevation of the 1 x 1 km grid cell. Consequently, to consider the complex glacier geometry and the related processes in the simulation of meltwater release (see section 3.2.1), the gap between the small-scale heterogeneous properties of a glacier and the spatial resolution of PROMET must be closed. For this reason, a subscale approach is applied in SURGES. In order to account for the complex glacier geometry, every glacier is divided into subscale units to approximate the area-elevation distribution. The glacier area is therefore intersected using digital elevation models. Neighbouring parts of the glacier with similar elevations are then merged, in defined distinct elevation intervals between the levels. Figure 3.7 illustrates the subdivision of the glacier area into elevation levels.

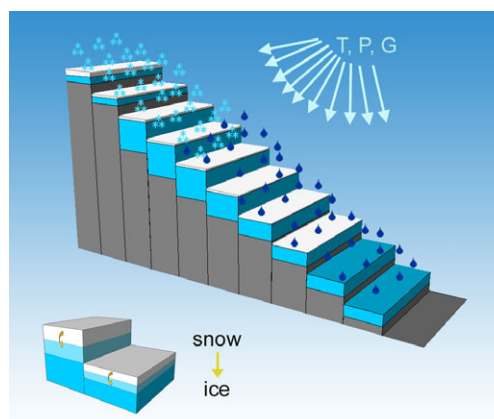


Figure 3.7: Illustration of the division of the glacier area into distinct levels (WEBER ET AL. 2009, p. 10, modified).

For each level, data about the specific ice thickness, the altitude of the glacier bed and the glacier area describe the glacier's properties. The subscale approach thus allows a better consideration of the characteristics of each individual glacier by approximation of the ice



thickness-area-elevation distribution for the meltwater release. For instance, a plane glacier tongue will have a larger snow-free ablation area than a steep one and will deliver more ice-melt water during the same time interval. The larger area of a plane elevation level than that of a steep one is captured by SURGES. Furthermore, the subscale approach allows the coexistence of accumulation and ablation zones and the handling of neighbouring non-glaciated areas on one grid cell. The modelling steps, which are carried out for all subscale elevation levels, are explained below.

### 3.2.4 Meteorological Data Extrapolation

The meteorology component of PROMET or SCALMET supplies every grid cell with hourly values of precipitation, air temperature, air humidity, incoming shortwave and longwave radiation, air pressure and wind speed (see section 3.1.1). In order to consider the elevation of the glacier levels, these data are extrapolated. First, the current surface elevation  $z_s [m]$  is determined by adding the present ice thickness  $h_i [m]$  and the current snow depth  $h_s [m]$  to the elevation of the glacier bed  $z_b [m]$ :

$$z_s = z_b + h_i + h_s \quad (\text{Eq. 3.3})$$

Next, the air temperature  $T [K]$  and air pressure  $P [hPa]$  are calculated for the various glacier levels. According to the present surface elevation  $z_s [m]$ , the level air temperature  $T_l [K]$  is determined by extrapolating the air temperature  $T [K]$  of the grid cell with the mean elevation  $z_{gc} [m]$ , assuming a linear, either dry or moist adiabatic lapse rate  $\Gamma [K m^{-1}]$ :

$$T_l = T + \Gamma (z_{gc} - z_s) \quad (\text{Eq. 3.4})$$

The dry adiabatic lapse rate is set to  $0.0098 K m^{-1}$  as the quotient of the gravitational acceleration  $g_o$  of  $9.81 m s^{-2}$ , and the specific heat capacity of dry air at a constant air pressure  $c_p$  of  $1,004.67 J kg^{-1} K^{-1}$ . The moist adiabatic lapse rate is determined by the process of condensation of water vapour, so that latent heat is released. Since this process depends on air temperature, the gradient is inversely proportional to air temperature and varies between  $0.003$  and  $0.009 K m^{-1}$ . In this study it is set to an average value of  $0.0065 K m^{-1}$  for an air pressure of  $1,000 hPa$  and an air temperature of  $273.15 K$  (KRAUS 2000).

In the case of level air temperatures  $T_l [K]$  above the melting point, the feedback of energy consumption by melting ice or snow on the glacier surface is taken into account. While the absorption of radiation and the turbulent fluxes over a snow- or ice-free area cause an increase in air temperature, the radiation input is consumed for melting over the glacier and cannot increase the air temperature. Therefore, the air temperature is reduced in the model under melting conditions according to WEBER (2008):

$$T_l = T_l \left(1 - \frac{(1-\alpha)R_s}{600}\right) \quad (\text{Eq. 3.5})$$

with  $\alpha$  representing the albedo (see also Eq. 3.17) and  $R_s [W/m^2]$  the solar radiation. The reduction is limited to a maximum of  $0.5 T_l$  in order to remain within a realistic range.

The level air pressure  $P_l$  [hPa] is calculated by the barometric formula with the gravitational acceleration on Earth  $g_o$  [ $9.81 \text{ m s}^{-2}$ ], the molar mass of the atmosphere  $M$  [ $0.028964 \text{ kg mol}^{-1}$ ] and the universal gas constant for air  $R$  [ $8.3143 \text{ Nm mol}^{-1} \text{ K}^{-1}$ ]:

$$P_l = P \left( 1 + \frac{\Gamma(z_s - z_{gc})}{T} \right)^{\frac{g_o M}{R}} \quad (\text{Eq. 3.6})$$

As the wind speed on a glacier is different from the wind above nonglacier areas, as provided by the climate model, it has to be adopted. The glacier wind  $v_l$ , a katabatic flow over glaciers is caused by the differences in heat between the snow-free, surrounding areas of a glacier and the comparatively cold glacier surface. The glacier wind is characterized by speeds of  $3$  to  $5 \text{ m s}^{-1}$  and increases with proximity to the glacier tongue (WEBER 2008). As it is very common over melting surfaces (OERLEMANS AND GRISOGONO 2002), it is considered in SURGES in a rather simple way for air temperatures above  $0^\circ\text{C}$ :

$$v_l = v + 0.0015 v (z - z_s) \quad (\text{Eq. 3.7})$$

The lower limit of the level glacier wind  $v_l$  [ $\text{m s}^{-1}$ ] is given by half of the wind speed of the grid cell  $v/2$ , whereas the upper limit  $v_{l,max}$  is determined by the air temperature according to KUHN (1978) as follows:

$$v_{l,max} = 0.61T \quad (\text{Eq. 3.8})$$

For differentiation of rain from snowfall by iteratively solving the psychrometer formula (Eq. 3.9), the wet-bulb temperature  $T_w$  [K] is calculated for all levels, considering the water vapour pressure  $e$  [hPa], the saturation vapour pressure of a wet surface  $E_w$  [hPa], the specific heat of air  $c_p$  [ $\text{J kg}^{-1} \text{ K}^{-1}$ ] at a constant air pressure  $P$  [hPa] and the latent heat of vaporization  $r$  [ $\text{J kg}^{-1}$ ]:

$$e = E_w - \frac{c_p P}{0.623r} (T - T_w) \quad (\text{Eq. 3.9})$$

The saturation vapour pressure of a wet surface  $E_w$  [hPa] is computed with the Magnus formula for positive air temperatures  $T$  [K] by:

$$E_w = 6.1078 \cdot e^{\frac{17.08085 \cdot (T - 273.15)}{234.175 + (T - 273.15)}} \quad (\text{Eq. 3.10})$$

For negative temperatures  $T$  [K] it is calculated by:

$$E_w = 6.1071 \cdot e^{\frac{22.4429 \cdot (T - 273.15)}{172.44 + (T - 273.15)}} \quad (\text{Eq. 3.11})$$

The latent heat of vaporization  $r$  [ $\text{J kg}^{-1}$ ] is calculated with the following equation:

$$r = 2500827 - 2360 \cdot (T - 273.15) \quad (\text{Eq. 3.12})$$

The specific heat of moist air  $c_p$  [ $\text{J kg}^{-1} \text{ K}^{-1}$ ] is determined with the specific heat capacity of dry air  $c_{p,dry}$  [ $1004.67 \text{ J kg}^{-1} \text{ K}^{-1}$ ], and the specific humidity  $sh$  [kg/kg] by:

$$c_p = c_{p,dy} (1 + 0.84 \cdot sh) \quad (\text{Eq. 3.13})$$

where the  $sh$  is given by:

$$sh = \frac{0.622 \cdot E_w}{P - 0.378 \cdot E_w} \quad (\text{Eq. 3.14})$$

All the other meteorological variables, e.g. precipitation or incoming radiation, are assumed to be constant throughout the grid cell and are taken from the meteorology component of PROMET or SCALMET without any adaptation. There is no indication in which way the amount of precipitation varies on one km<sup>2</sup>. Additionally, wind- and leeward effects are not considered in the modelling approach. In the next paragraph, modelling of the mass and energy balance on each glacier level, which is enabled by the extrapolation of the meteorological data, is described.

### 3.2.5 Mass and Surface Energy Balance of the Glacier

In order to determine the mass gain and loss of the glacier, the changes of the mass balance on its surface have to be calculated. The following calculation steps are similar for a snow and ice layer, only differentiated by varying material properties, e.g. the albedo  $\alpha$ . The algorithms are mainly based on WEBER (2008) and on the snow model ESCIMO, which was implemented in the snow component of PROMET (STRASSER AND MAUSER 2001), and enhanced and validated in various studies (MAUSER ET AL. 2007, PRASCH 2008A, B, STRASSER 2009).

First, the energy balance  $E [W m^{-2}]$  of the surface is calculated, taking into account the radiation balance  $Q [W m^{-2}]$ , the latent and sensible heat fluxes  $LE [W m^{-2}]$  and  $H [W m^{-2}]$ , and the energy supplied by solid or liquid precipitation  $A [W m^{-2}]$ :

$$E = Q + LE + H + A \quad (\text{Eq. 3.15})$$

The radiation balance consists of the sum of the shortwave  $Q_S [W m^{-2}]$  (Eq. 3.16) and longwave radiation balance  $Q_L [W m^{-2}]$  (Eq. 3.17). The amount of incoming direct  $R_{dir} [W m^{-2}]$  and diffuse solar radiation  $R_{dif} [W m^{-2}]$ , which is partly reflected due to the albedo  $\alpha$ , forms the shortwave radiation balance:

$$Q_S = (1 - \alpha) (R_{dir} + R_{dif}) \quad (\text{Eq. 3.16})$$

Since solar radiation contributes most to the surface energy under melting conditions, the albedo is of great importance. For conditions of snow and ice, it depends on many factors, e.g. grain size, density, impurity content, solar elevation etc. In this study, the albedo is set to 0.5 in the case of snow-free ice for the Lhasa River catchment, which is a relatively high value for glacier ice, similar to clean ice (PATERSON 1994). This value was chosen because of extremely dry and clean air on the Tibetan Plateau due to its elevation and latitude. In the case of snow covering the glacier, the albedo of freshly fallen snow (0.9) decreases due to changes in grain size, density and impurity content of the snow surface. The ageing curve of the albedo of freshly fallen snow is simulated following ROHRER (1992) (Eq. 3.17). The exponential reduction during the time interval  $\Delta t [s]$  since the last

considerable snow fall ( $0.5 \text{ mm}$  per hour) differs between air temperatures above and below freezing point, accounted for by changing recession coefficients  $k$ . For air temperatures above freezing point,  $k$  is set to  $0.05$  per day, whereas for air temperatures below, it is set to  $0.12$  per day. The decrease continues until a minimum value  $\alpha_{min}$  of  $0.55$  is reached, or until the next considerable snowfall happens. In this case it is reset to the maximum value of  $0.9$ .

$$\alpha = \alpha_{min}(t) + (\alpha(t-1) - \alpha_{min})e^{-k\frac{1}{24}} \quad (\text{Eq. 3.17})$$

For simulation of the longwave radiation balance  $Q_l [W m^{-2}]$  (Eq. 3.18), the incoming longwave radiation  $R_{li} [W m^{-2}]$ , provided by PROMET or SCALMET, is reduced, through the emission after the *Stefan-Boltzmann Law*, with the Stefan-Boltzmann constant  $\sigma$  of  $5.67 \cdot 10^{-8} W m^{-2} K^{-4}$ . In addition to the emissivity  $\varepsilon$ , which is  $1$  for snow and  $0.98$  for ice, it also depends on the current surface temperature  $T_s [K]$ , which is set to  $273.15 K$  for air temperatures above freezing point. If the air temperature is below this, the surface temperature is determined in an iterative procedure closing the energy balance (STRASSER 2008).

$$Q_l = R_{li} - \sigma \cdot \varepsilon \cdot T_s^4 \quad (\text{Eq. 3.18})$$

The turbulent fluxes are computed consistent with WEBER (2008). High mountain conditions above glaciers such as high wind speeds, dependency on elevation and changing surface roughness are particularly closely considered in the formulation. The sensible heat flux  $H [W m^{-2}]$  is proportional to the specific heat of air  $c_p [J kg^{-1} K^{-1}]$  (Eq. 3.13), and to the difference between the air temperature  $T [K]$  and the surface temperature  $T_s [K]$ :

$$H = 0.01182 \cdot \rho_a \cdot c_p \cdot R_{wT} \cdot v \cdot (T - T_s) \quad (\text{Eq. 3.19})$$

For the latent heat flux  $LE [W m^{-2}]$  the latent heat of vaporization  $r [J kg^{-1}]$  (Eq. 3.12) and the difference between the specific humidity of the air  $sh [kg kg^{-1}]$  (Eq. 3.14) and at the surface  $sh_s [kg kg^{-1}]$  are taken into account:

$$LE = 0.0092 \cdot \rho_a \cdot r \cdot R_{wT} \cdot v \cdot (sh - sh_s) \quad (\text{Eq. 3.20})$$

Thereby the air density  $\rho_a [kg m^{-3}]$  is calculated with the universal gas constant of air  $R_d$  of  $287 J kg^{-1} K^{-1}$  by:

$$\rho_a = \frac{P \cdot 100}{R_d \cdot T} \quad (\text{Eq. 3.21})$$

In both equations,  $R_{wT}$  stands for a correlation coefficient which describes the turbulent exchange according to WEBER (2008). The factor permits an approximate physically-based description of the fluxes in considering the stability of the atmospheric layering due to the air temperature  $T [K]$ , the surface air temperature  $T_s [K]$  and the wind speed  $v [m s^{-1}]$ . For stable layering,  $R_{wT}$  is proportional to the gradient of the air temperature  $T$  and the surface temperature  $T_s$ , while the efficiency of the turbulent exchange decreases with

increasing wind speeds  $v$  (Eq. 3.22a). The correlation is limited to a value of 0.2 for large temperature gradients in combination with high wind speeds, because this case rarely occurs in nature (Eq. 3.22b). For a negative temperature gradient, labile layering is assumed. In this case  $R_{wT}$  is set to 0.4 (Eq. 3.22c) (WEBER 2008).

$$R_{wT} = 0.438 - 0.119 \frac{T - T_S}{v} \quad \text{for } T > T_S \text{ and } (T - T_S) < 3.68v \quad (\text{Eq. 3.22a})$$

$$R_{wT} = 0.2 \quad \text{for } T > T_S \text{ and } (T - T_S) > 3.68v \quad (\text{Eq. 3.22b})$$

$$R_{wT} = 0.4 \quad \text{for } T \leq T_S \quad (\text{Eq. 3.22c})$$

In the case of precipitation an advective flux  $A$  [ $W m^2$ ] is used to account for the energy balance  $E$  [ $W m^2$ ] depending on its phase. As the threshold wet-bulb temperature  $T_w$  is set at 2°C, a distinction is made between rain (Eq. 3.23a) and snowfall (Eq. 3.23b). In the first case the flux is proportional to the specific heat of water  $c_w$  of  $4,180 J kg^{-1} K^{-1}$ , whereas in the second case it is relative to the specific heat of ice  $c_i$  of  $2,100 J kg^{-1} K^{-1}$ . Additionally, the amount of precipitation  $PR$  [ $mm$ ] and the difference between air or wet temperature  $T$  [ $K$ ] or  $T_w$  [ $K$ ] and surface temperature  $T_S$  [ $K$ ] are considered.

$$A = PR_R \cdot c_w (T - 273.15) \quad (\text{Eq. 3.23a})$$

$$A = PR_S \cdot c_i (T_w - T_S) \quad (\text{Eq. 3.23b})$$

After these calculations, the energy balance  $E$  [ $W m^{-1}$ ] (Eq. 3.15) is computed. If it is positive, the amount of meltwater  $m$  [ $mm$ ] during the time interval  $\Delta t$  [ $s$ ] of snow or ice is calculated as follows, where  $H_i$  is the specific melting heat of ice of  $337,500 J kg^{-1}$ :

$$m = \frac{E \cdot \Delta t}{H_i} \quad (\text{Eq. 3.24})$$

Due to the quick release of glacier meltwater and the generally large amount of surface runoff in the mountains (LAMBRECHT AND MAYER 2009), in SURGES, the melt water  $m$  of glaciers is immediately supplied to the surface runoff of PROMET. By contrast, the meltwater  $m$  release of snow is handled similarly to rain, and drains into the soil layers or supplies surface runoff, taking into account varying land cover characteristics.

In order to determine the mass balance per elevation level, the sublimation or resublimation process is also considered, which is especially important in cold, dry regions with high radiation input, as it is the case in the Lhasa River catchment. The mass change conducted by this process  $se$  [ $mm$ ] per time step  $\Delta t$  [ $s$ ] is calculated considering the latent heat flux  $LE$  [ $W m^{-1}$ ] and the specific sublimation heat of snow and ice  $H_{is}$  of  $2,835,500 J kg^{-1}$ :

$$se = \frac{LE \cdot \Delta t}{H_{is}} \quad (\text{Eq. 3.25})$$

Alongside sublimation or resublimation, the amount of snowfall  $PR_S$  determines the mass gain on a glacier surface. As described above, it is distinguished from rain by a threshold wet-bulb temperature. In the case of rainfall, the temporal storage capacity of snow for

liquid water  $liq$  [mm] is considered in a simple approach. It is assumed that up to a certain, empirical amount,  $s_l$  [%] of the total snow water equivalent  $swe$  [mm] (Eq. 3.26), the snow cover can store liquid water (DENOTH 2003, FERNANDEZ 1998):

$$liq = \frac{s_l}{100} \cdot swe \quad (Eq. 3.26)$$

Rain or modelled melt water is stored until the maximum storage capacity is reached. Next, the surplus water is added to melt water, whereas rain on ice is passed accordingly to ice-melt water and so to the runoff, without any intermediate storage.

In the case of existing liquid water storage and air temperatures below freezing point, it is assumed that fraction  $fr$  [%] of the liquid water storage refreezes. The energy  $E_{fr}$  [ $W m^{-1}$ ] (Eq. 3.27) expended in the refreezing process during the timer interval  $\Delta t$  [s] is considered in the energy balance.

$$E_{fr} = \frac{fr}{100} \cdot H_{is} \cdot t \quad (Eq. 3.27)$$

Finally, the specific mass balance  $b(z)$  [mm] is determined per elevation level:

$$b(z) = PR_s + PR_R + se - m - liq \quad (Eq. 3.28)$$

If the calculated melt  $m$  [mm] exceeds the required melt for an existing snow layer, the energy surplus is determined and accordingly expended in for melting the ice layer. In the case of a complete melting of the ice layer, the glacier level area is subsequently treated as ice-free rock surface.

### 3.2.6 Snow Metamorphism

The formation of glacier ice starts with snow metamorphism. The  $50 - 70 \text{ kg/m}^3$  density of freshly fallen snow increases due to meteorological conditions, e.g. melting and refreezing processes, wind or a fresh snow cover, which compact the snow. If snow outlasts an ablation period, it is termed firn, with densities of  $400 - 830 \text{ kg/m}^3$ . Finally, the compaction proceeds and glacier ice is formed, with densities of  $830 - 917 \text{ kg/m}^3$ . The duration of this metamorphism differs from region to region due to meteorological conditions, and varies from years, in alpine regions, to centuries, in Polar Regions (PATERSON 1994, WINKLER 2009).

Snow compaction, and consequently, snow layers with different snow densities, are not considered in the modelling approach. To approximate the mean thickness of the snow and ice layers according to the water equivalent, an average snow density  $\rho_{snow}$  of  $290 \text{ kg/m}^3$ , which is referred to as “settled snow” (PATERSON 1994, p. 9), and an ice density  $\rho_{ice}$  of  $910 \text{ kg/m}^3$  is therefore assumed. In order to simulate the metamorphism from snow to ice in SURGES, the snow layer, which outlasts a defined number of ablation periods, is partly added to the ice water equivalent in a rather simple estimation. Even though firn is not distinguished specifically, changes with respect to the energy balance are taken into account by the simulation of changes in the albedo down to a value of 0.55 (see Eq. 3.17).

In the test site of the Lhasa River catchment, not only accumulation but also ablation takes place during the monsoon. Furthermore, alternating melting and refreezing was observed up to 5,800 m a.s.l. (KANG ET AL. 2008). These processes accelerate snow metamorphism. Thus, after a period of one year, similar to the estimation by KANG ET AL. (2008), half of the snow layer is transformed to ice in this study.

### 3.2.7 Glacier Geometry Adjustment

Finally, changes in the glacier geometry have to be considered in the simulation. Since the glacier area and the ice reservoir determine the melt water release as described in section 3.2.1, capturing the glacier geometry is essential for the results, especially in long-term studies under changing climatic conditions where the glaciers are no longer in a steady state. In combination with specific mass balance, the ice reservoir of the elevation level determines the quantity and duration of ice-melt water release. In order to consider changes of the glacier area during the modelling period, the total area of the glacier  $S [m^2]$  as sum of all elevation level areas  $S_l [m^2]$  is reduced according to the melt from ice on a specific elevation level. In this case, the area of the ice-free glacier level  $S_{l,icefree} [m^2]$  is subtracted from the total glacier area:

$$S = \sum_{l=1}^n S_l - \sum_{l=1}^n S_{l,icefree} \quad (\text{Eq. 3.29})$$

This enables the quite simple adaptation of the surface within the subscale approach of SURGES.

The ice reservoir of the glacier level is not only influenced by the mass balance and snow metamorphism, but also by the effect of ice flow (see section 3.2.1). The complexity of the relevant processes requires detailed information about the glacier's geometry and cannot be simulated in a simple approach on the catchment scale (see section 3.2.2). In fact, the effect of the ice flow in transporting ice from the accumulation to the ablation area is quite relevant to the ice reservoir. The amount of ice which is delivered from the accumulation area and gained in the ablation area should be considered. A correction factor  $e(z) [mm]$ , added to the mass balance  $b(z) [mm]$  at the elevation level enables this consideration:

$$h_i = b(z) + e(z) \quad (\text{Eq. 3.30})$$

In the accumulation area  $e(z) [m]$  is negative, assuming mass loss, whereas in the ablation area it is positive, simulating mass gain. At equilibrium line altitude (ELA), where the mass balance equals zero,  $e(z)$  is also assumed to equal zero.

However, the determination of the value of  $e(z)$  requires detailed data analysis for different glaciers to cover various topographic and meteorological factors. For the Vernagt Ferner in Austria, where the ELA is located at 3,300 m a.s.l., MAROWSKY (2010) proposed the following parameterization for this glacier  $e(z) [m]$  at the level elevation  $z_{sl} [m]$ :

$$e(z) = 0.017 \cdot (z_{sl} - 3,300) \quad (\text{Eq. 3.31})$$

Since this parameterization is only valid for the Vernagt Ferner, general investigations which allow the derivation of a universal parameterization of the factor are required. Due to data availability and the location of the Lhasa River basin, this was not possible in the present thesis. Accordingly, the geometry changes of the glacier are considered without regarding the ice flow.

All applied parameters of SURGES are listed in Appendix 1. The formula symbols are summarized in the list of symbols (p. XIX).

### **3.2.8 Method Discussion**

The glacier simulator SURGES within the model PROMET, as described in the previous paragraphs, focuses on the effect of the processes in determining the melt water release under changing climatic conditions. This hydrological focus results in the neglect of some small-scale processes on the glacier so far. Wind-induced snow transport and the small-scale shading caused by the surrounding mountains which principally facilitate the formation of glaciers in some cases, has so far been neglected. The longwave radiation flux of neighbouring snow-free rock areas, which accelerates the melting of the glacier along its boundary, has not been considered. The phenomena of surging or debris-covered glaciers, which are secondary in the Lhasa River basin have also so far been excluded, as has the effect of transporting ice from the accumulation to the ablation area due to the ice flow. This means that the glaciers melt away earlier in the lower ranges in the simulations than in reality, whereas in the higher areas the loss of ice thickness is underestimated. This in turn leads to a smaller ablation area in the lower ranges. Thus the melt water release is slightly underestimated and the glacier's existence may be longer in simulations than in reality. Furthermore, glacier advance cannot be simulated. However, under climate warming conditions, ice flow decreases because of shrinking area, as is the case in the Lhasa River basin. Finally, the ice flow ceases for small glaciers, as is the case with the Northern Schneeferner in Germany, for example. Moreover, SURGES includes simplifications in the description of snow metamorphism, neglecting the influence of meteorological conditions during the period before and the related compaction processes. Accordingly, the metamorphism is simulated similar for every year in contrary to reality.

The approach nevertheless enables the distributed simulation of the main processes for determination of the melt water release of all glaciers in a catchment. The properties of each single glacier are considered in as much detail as possible by the approximation of the ice thickness-area-elevation distribution. This includes capturing the small-scale glacier properties below the process scale of PROMET of 1 x 1 km for the simulation of energy and mass balances. Furthermore, the coexistence of rain- and snowfall, of the accumulation and ablation zones of a glacier and the neighbouring non-glacierized areas on one raster element can be handled. Geometry changes in the glacier are considered in reducing the glacier area after the ice-melt at given elevation levels, although the implementation of ice flow effects could improve the determination. Moreover, SURGES can be applied under past as well as future climatic conditions, since it is physically based and uses globally valid parameterizations. Through the implementation of SURGES in PROMET, the



influence of the melt water release of glaciers for the water balance can be determined in a spatially distributed way over the complete large-scale catchment. Finally, in adjusting the scale differences with the SCALMET tool, RCMs can be applied as meteorological input data. They make the application of the modelling approach independent of meteorological station data. This is especially important in remote mountain regions.

Before the input data for running the modelling framework are described in detail (Chapter 4), the technical aspects of the modelling approach are briefly explained.

### 3.3 Technical Aspects

Figure 3.8 gives a schematic overview of the spatial and temporal computational cycle of PROMET, including the implementation of SURGES.

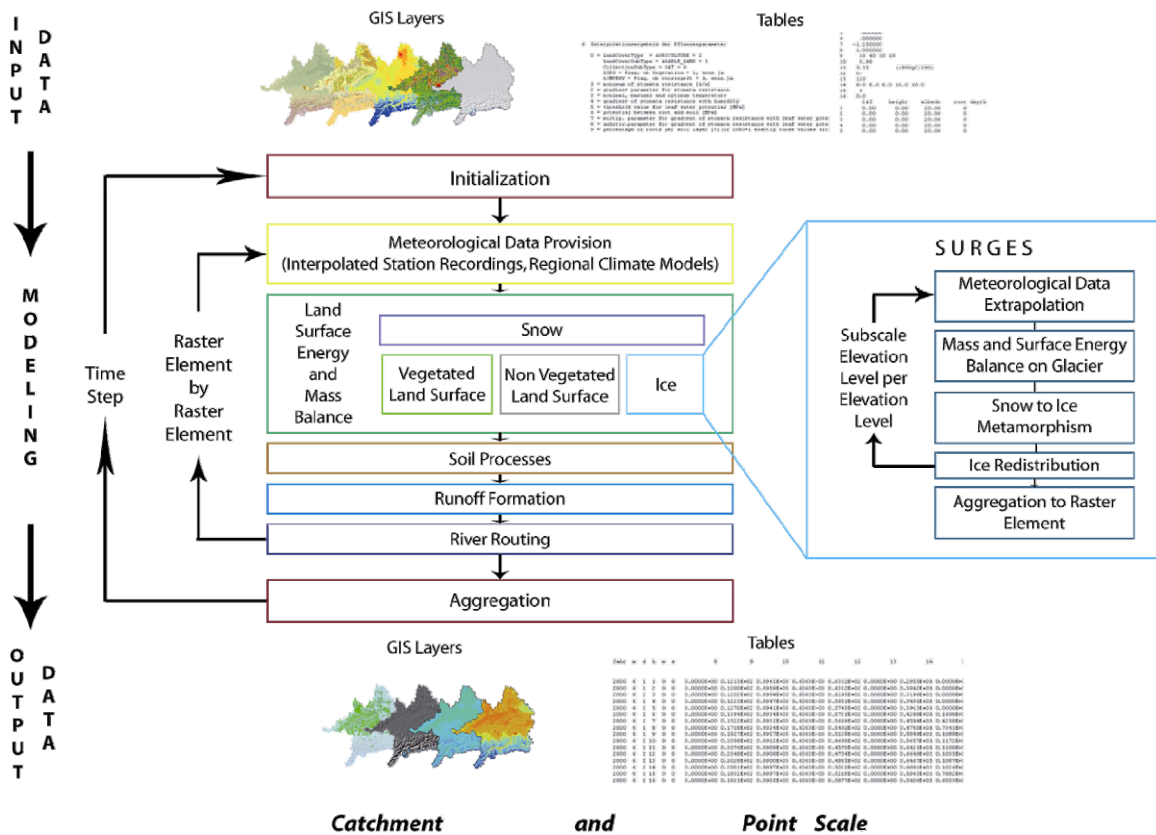


Figure 3.8: Scheme of implementation of the glacier model SURGES in PROMET, describing the spatial and temporal modelling cycle.

First, all data describing the present conditions of the grid cell, including the glacier elevation levels where required, are initialized according to the simulation results of the previous time step or the input data. Next, the following steps are carried out within a loop for each raster element. Firstly, the meteorological data are provided by the meteorology component. Secondly, the energy and mass balances for all land surfaces are calculated, considering vegetated and non-vegetated land surfaces as well as snow and ice cover if necessary, whereby the energy and mass balances are closed. If a grid cell is (partly) glacierized, SURGES is called. The meteorological data for all subscale elevation levels are extrapolated and the energy and mass balances are calculated. Then, snow to ice metamorphism is considered. Finally, the data are aggregated for the glacier area and

passed on to the other model components. There, they are consolidated with the values for the non-glacierized area per grid cell. Mass and energy balances are accordingly conserved. Next, the soil and groundwater processes and the runoff formation are modelled. After this procedure has been carried out for all grid cells, the water flow in the river channel is calculated. Finally, the output data are generated for this time step, aggregated where required, and the cycle is started again. In addition to hourly outputs, daily and monthly values can be produced for each grid cell. They are available either at selected points in the catchment area or spatially distributed across the catchment scale.

All the model components are written in FORTRAN and can be run in the Microsoft Windows environment on a standard personal computer. For the Lhasa River catchment, modelling one year takes about 4.5 hours. The annual model output of the whole Lhasa River watershed in daily resolution requires approx. 105 Mbytes per model output variable.

## 4 Model Input Data for the Lhasa River Basin

In order to run the SURGES and PROMET models, input data describing the natural characteristics of the catchment are required. Gridded GIS (geographic information system) layers describe the distribution of the required parameters in the basin, and plant and soil parameters are provided in data tables for each land cover and soil texture class, because they are assumed to be homogenous throughout the whole catchment. Table 4.1, Table 4.3 and Table 4.4 give an overview of the required input data layers and the plant and soil parameters.

In general, all data layers are processed as raster data with a spatial resolution of one square kilometre in the coordinate system UTM, zone 45 N, WGS 84. Since sparse data is available for the Lhasa River catchment, publicly accessible data is used as far as possible, which are listed in Table 4.1. The compilation of the data in remote regions and the transferability of the model approach are also introduced here, focussing on the compilation of the glacier properties needed to run SURGES, because it is the first application of the model approach outside the Alps. First, the applied meteorological data are explained (section 4.1), followed by the introduction of the land surface data parameterization (section 4.2). Afterwards, a detailed description of the compilation of the glacier properties, which is essential to run SURGES, follows (section 4.3).

*Table 4.1: Required input data layers to run PROMET and SURGES and data sources for the Lhasa River catchment.*

<b>Input data set</b>	<b>Data source</b>
Watershed	Digital terrain analysis of SRTM with TOPAZ (GARBRECHT AND MARTZ 1999)
Elevation [m a.s.l.]	SRTM (JARVIS ET AL. 2006)
Surface slope [%]	Digital terrain analysis of SRTM with TOPAZ
Surface aspect	Digital terrain analysis of SRTM with TOPAZ
Land use / land cover classes	NASA TERRA/MODIS land cover product (BOSTON UNIVERSITY 2004)
Soil texture classes	Harmonized World Soil Database (FAO ET AL. 2009)
Accumulated upstream area [km <sup>2</sup> ]	Digital terrain analysis of SRTM with TOPAZ
Channel slope [%]	Digital terrain analysis of SRTM with TOPAZ
Flow direction	Digital terrain analysis of SRTM with TOPAZ
Channel width [m]	Deduced, based on field data
Manning's roughness parameter	Deduced, based on field data
Groundwater storage time [h]	Deduced, based on the digital terrain analysis of SRTM with TOPAZ
Meteorological values (see Table 4.2)	COSMO-CLM outputs (CLM 2010), downscaled with SCALMET
Subscale glacier area [m <sup>2</sup> ]	Chinese glacier inventory (WDC 2009)
Subscale glacier elevation [m a.s.l.]	Aster GDEM (ERSDAC 2009)
Subscale ice thickness [m]	Deduced, based on WDC (2009) and ERSDAC (2009)

## 4.1 Meteorological Drivers

Since no meteorological station recordings with the required parameters (see Table 4.2) are available in a temporal resolution appropriate to run PROMET on an hourly time step, output data from the RCM COSMO-CLM are used. COSMO stands for **CO**nsortium for **S**mall scale **MO**delling. It is a nonhydrostatic operational weather prediction model, which is applied operationally and further developed by several national weather services. CLM is the abbreviation for the **cl**imate **mo**de of the model (CLM 2010). For the Lhasa River catchment the spatial resolution of the data is  $0.44^\circ$  ( $\sim 50 \times 50$  km), whereas the temporal resolution is three hours. Two methods are used for driving the CLM: Simulations, driven by ERA 40 reanalysis data (UPPALA ET AL. 2005) from the European Centre for Medium Range Weather Forecasts (ECMWF) are applied for the past to reduce GCM simulation biases, since they are based on meteorological observations. Moreover, the CLM is driven by the coupled ocean-atmosphere GCM ECHAM 5 / MPI-OM (ROECKNER ET AL. 2003, JUNGCLAUS ET AL. 2006), because it realistically simulates the 20<sup>th</sup> century South Asian monsoon compared to other GCMs (KRIPALANI ET AL. 2007). For future climatic conditions, solely the application of ECHAM 5 is possible because of missing observations for the future, which build the basis of the ERA 40 data. The CLM provides data fields of air temperature, precipitation, incoming shortwave and longwave radiation, wind speed, sea level pressure and cloud cover percentage for the period from 1960 to 2080. For the future period from 2000 to 2080, the data fields are available for the IPCC SRES scenarios A1B, B1, A2 and the Constant-Year-2000-concentrations run (see section 6.1). Within the framework of the Brahmatwinn project (BRAHMATWINN 2006-2010), bias correction methods were applied to the CLM air temperature as well as to precipitation during the monsoon months in the whole Upper Brahmaputra basin, described in DOBLER AND AHRENS (2008). The revised data were used for this study. As described in section 3.1.1, the SCALMET tool scales the CLM output down to a resolution of  $1 \times 1$  km and disaggregates the data temporally to a resolution of one hour. Thus, the data can be applied to run PROMET and SURGES. The quality of the CLM data in the Lhasa River basin is discussed in section 5.3.1.

Table 4.2: Required meteorological drivers (MAUSER AND BACH 2009).

Parameter	Unit
Air temperature	°C
Precipitation	mm
Air humidity	%
Wind speed	m/s
Incoming shortwave and longwave radiation	W/m <sup>2</sup>
or cloud coverage	%

## 4.2 Land Surface Data Parameterization

Data fields of topography (elevation, surface slope and aspect), land use and land cover, soil texture, groundwater storage time and various river characteristics are required as input data for the description of the landsurce PROMET (see Table 4.1 and section 3.1).

For topographic properties, the generally available digital elevation model of the Shuttle Radar Topography Mission SRTM (JARVIS ET AL. 2006) was applied in the Lhasa River basin. The model was up-scaled step-by-step from a resolution of 90 x 90 m up to 1 x 1 km per grid cell using the bilinear interpolation method. Slope and aspect were deduced from the digital elevation model using the terrain analysis tool TOPAZ (GARBRUCH AND MARTZ 1999), which was also applied in the hydrological catchment analysis. Alongside the watershed of the catchment and the sub-catchments (see Figure 2.5), the main channel network with the channel slope and the flow direction are the main outcomes of TOPAZ. They, in turn, are required to run the river routing component of PROMET (section 3.1.5). Channel width is also needed. It was derived under the assumption that it correlates with the accumulated upstream area, also provided by TOPAZ, consistent with MAUSER AND BACH (2009). To determine the flow velocity, Manning's roughness parameter is needed. For the Lhasa River basin it was deduced by fieldwork during a field campaign in Tibet in September 2006 according to the methods of BARNES (1967). For the simulation of groundwater flows, the distance to the main river channel is required, which is also provided by TOPAZ. Depending on the distance, the storage time constant is set as described in section 3.1.4.

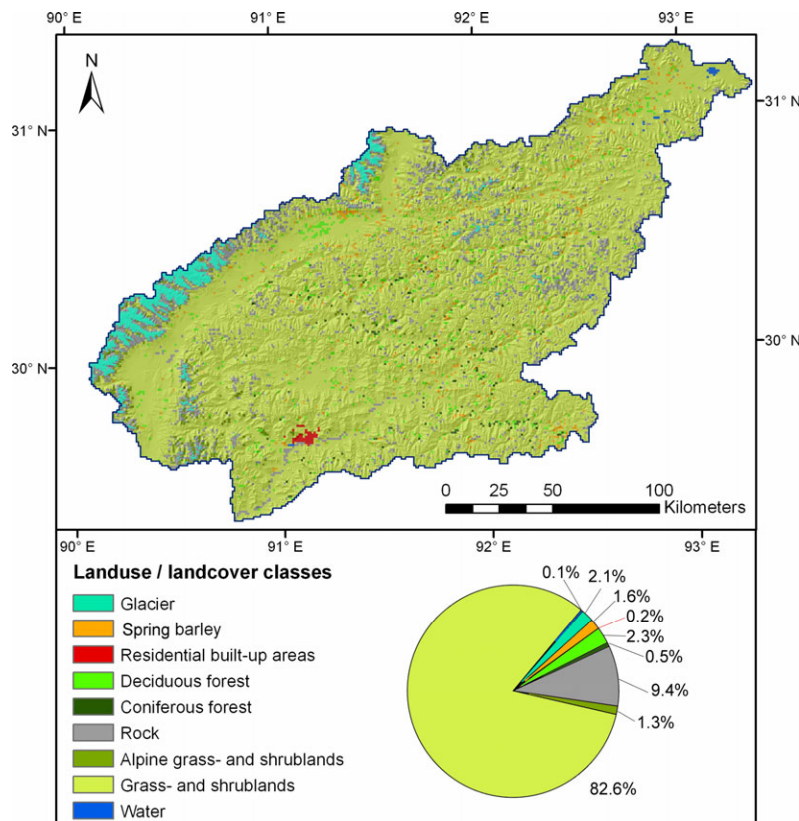


Figure 4.1: Distribution of parameterized land use and land cover classes in the Lhasa River basin, modified according to the NASA TERRA/MODIS land cover product (BOSTON UNIVERSITY 2004).

The NASA TERRA/MODIS land cover product (BOSTON UNIVERSITY 2004) provides information about land cover and land use in the Lhasa River catchment (Figure 2.9). The classification was modified by intersecting it with the Chinese Glacier Inventory (WDC 2009) to obtain a consistent data set. All grid cells which are partly glacierized were predisposed to rock. Since several classes cover less than one percent of the basin, similar categories were merged for the parameterization. Needleleaf forests and mixed forests were aggregated to the coniferous forest class and amount to 0.5 percent of the basin area, whereas broadleaf forests, woody savannas and closed shrubland were grouped into deciduous forests, which together cover 2.4 percent of the area. Moreover, all cropland classes, which only cover 1.6 percent of the catchment, were summarized as spring barley, which is widely cultivated in Tibet (see section 2.5). While open shrublands, savannas and grassland are used for grazing throughout the whole catchment, these classes are coexistent at a spatial resolution of 1 x 1 km. Furthermore, they have similar characteristics according to field data. They are therefore grouped under grass- and shrublands in this study. Figure 4.1 shows the distribution of the aggregated classes in the Lhasa River catchment.

In order to simulate water transport in plants as well as the energy and mass balances of the land use classes in considering their different properties (see section 3.1.2), the parameters listed in Table 4.3 are required. Within the basin, the classes are uniformly parameterized under the assumption that the properties of the different classes are similar throughout the whole catchment.

*Table 4.3: Required parameters for description of the land surface (MAUSER AND BACH 2009).*

<b>Parameter</b>	<b>Unit</b>
Minimal stomatal conductance	m/s
Slope of stomatal conductance with irradiance	-
Cardinal temperatures	K
Slope of inhibition of stomatal resistance with air humidity	-
Slope and threshold of stomatal inhibition with soil suction	MPa
Root depth	m
Daily leaf area index	m <sup>2</sup> /m <sup>2</sup>
Daily plant height	m
Daily albedo	%

The parameterization for the non-vegetated classes of rock, residential areas, glaciers and water, as well as for the small percentage of forests, was adopted from the classifications applied in Europe in a variety of studies. Further details can be found in MAUSER AND BACH (2009), HANK (2008) and MAUSER AND SCHÄDLICH (1998). According to literature and data from the field survey 2006, the parameterization of spring barley was adapted to the conditions of Tibet. There, it is grown in April and harvested from August to September (TASHI 2005). The maximum plant height in the model was set to 0.8 m. The course of the daily albedo and the daily leaf area index were adapted, taking measured plant densities into account. The grass- and shrubland which accounts for 83 percent of

the basin area, was divided into areas above 5,500 m a.s.l. and slopes larger than 40 percent, where less grazing is assumed than in the ranges with smaller slopes or those located below 5,500 m a.s.l. On the basis of the parameterization of natural grassland in Europe, the growing height was reduced. The course of the leaf area index and the albedo were modified accordingly. In doing this, the grazing and the lower plant density were considered. The plants are assumed to grow slightly taller in the higher and steeper regions because of missing grazing, although their growth is limited by the altitude and the soil formation under natural conditions. Pictures of the investigation area in Appendix 2 give an impression of the land use.

In order to model the water processes in the soil, the soil component of PROMET (see section 3.1.3) needs soil texture classes, which were taken from the Harmonized World Soil Database (FAO ET AL. 2009, see section 2.4 and Figure 2.6). The required parameters for the classes, listed in Table 4.4, were adapted from the parameterization according to MAUSER AND BACH (2009) and MUERTH (2008). Since the mountainous relief characterizes the Lhasa River catchment and the soil depth as observed in the field, the soil depth was modified due to elevation and slope. For grid cells above 5,000 m a.s.l. and slopes steeper than 20 percent, a total depth of 0.9 m was assumed, whereas for slopes steeper than 30 percent it was reduced to 0.5 m. In all other cases, it was set to 1.5 m. In differentiating the depth, the slower soil formation processes in higher regions due to climate, topography and broken bedrocks is also considered.

*Table 4.4: Required parameters for soil texture parameterization (MAUSER AND BACH 2009).*

<b>Parameter</b>	<b>Unit</b>
Thickness per soil layer	m
Pore size distribution index per layer	
Saturated conductivity per layer	m/s
Effective pore volume fraction per layer	%
Bubbling pressure head	MPa
Depth of groundwater table	m

With these input data, the hydrological model PROMET can be run. In order to simulate the glaciers with SURGES, subscale glacier characteristics are required. Their derivation is explained in detail in the following chapter. Firstly, the data basis is synthesized. Secondly, the processing of the data is explained.

### **4.3 Derivation of Glacier Input Data for SURGES**

In order to run SURGES, the area-elevation distribution of all glaciers and the ice thickness for all elevation levels is required as input data for all glacierized grid cells in the test basin (Table 4.1). These data are only available for a small percentage of glaciers worldwide, e.g. for the Bavarian glaciers of the Zugspitze (BAYERISCHE GLETSCHER 2009), the Vernagtferner in Austria (MAROWSKY 2010) and the Rhone Glacier in Switzerland (FARINOTTI ET AL. 2009), as the detailed collection of these data necessitates intensive campaigns. In most cases, glaciers are located in impassable alpine regions, and the data

recording itself is very complex. Whereas large amounts of data exist for the glacier areas, due to topographic maps, aerial photos and a variety of satellite images with different temporal and spatial resolutions, ice thickness recording requires detailed measurements, because it varies a lot within one glacier. During recent decades, several methods have been applied, ranging from surface drilling to surface- or airborne-radio echo sounding and ground-penetrating radar or impulse radar (REES 2006). However, most of these techniques do not provide distributed data, and so the point measurements must be inter- and extrapolated. Furthermore, these procedures are expensive and time-consuming.

The surface elevation of glaciers can be determined by using photogrammetric methods at the glacier surface, from airplanes or satellites. Digital terrain models are produced with laser scanning or synthetic aperture radar data. The spatial resolution depends on the system, for example data from the SRTM (JARVIS ET AL. 2006) have a resolution of 90 m.

Various groups, such as the Global Land Ice Monitoring from Space (GLIMS) (RAUP ET AL. 2007), the World Glacier Monitoring Service (WGMS 2009) and the National Snow and Ice Data Center/ World Data Center for Glaciology (NATIONAL SNOW AND ICE DATA CENTER 2009), work on the collection and completion of all available data and provide interested groups with these data. They also monitor the glaciers to gain information about changes.

#### **4.3.1 Data Basis**

In general, the availability of glacier data is poor in the Lhasa River catchment, because of the reasons described above. Moreover, the political situation in Tibet in the past has restricted access both to this region and to Chinese data. In the course of changes, the World Data Center For Glaciology and Geocryology in Lanzhou in China has recently offered the Chinese Glacier Inventory for free download ([http://wcdqg.westgis.ac.cn/DATABASE/Glacier/glacier\\_inventory.asp](http://wcdqg.westgis.ac.cn/DATABASE/Glacier/glacier_inventory.asp)). It comprises polygons of the glacier areas and additional information about the coordinates, area, length, elevation, classification category and mean ice thickness of glaciers in China, compiled by the Cold and Arid Regions Environmental and Engineering Research Institute of the Chinese Academy of Sciences (WDC 2009).

Generally available elevation data about the earth's surface are offered by digital elevation models such as: the SRTM data (JARVIS ET AL. 2006), at a resolution of 90 m and an accuracy of  $\pm 10$  m; and the ASTER Global Digital elevation model GDEM, at a resolution of 30 m and an accuracy of  $\pm 7-14$  m, provided by the Ministry of Economy, Trade, and Industry of Japan and the United States National Aeronautics and Space Administration (ERSDAC 2009).

In the following paragraphs, the derivation of the area-elevation distribution and ice thickness for the Lhasa River basin is explained in detail. The subsequent flow chart of Figure 4.8 summarizes the steps of data generation.

#### **4.3.2 Glacier Area**

The Chinese Glacier Inventory completely covers the Lhasa River catchment. It provides data for the glacier areas from the year 1970 as polygons. The polygons were derived by digitizing aerial photographs and maps. The area of the glaciers thus varies between 0.2



ha of small glacierets and 31.1 km<sup>2</sup> of large glaciers, such as the Xibu glacier at Mount Nyainqêntanglha. Additional information includes the mean length, ranging from 100 m to 10 km, the width of the glaciers and a primary classification category (see Figure 2.9). For a few glaciers the names are also given (WDC 2009). This information is identical to the glacier boundary layer of the GLIMS data set (Li 2003). According to the data set, an area of 670 km<sup>2</sup> is glacierized in the Lhasa River basin, which corresponds to two percent of the catchment area. Figure 2.9 shows the glaciation, and Table 2.2 lists the percentage of the glacier areas for each sub catchment.

### 4.3.3 Glacier Elevation

In order to obtain the subscale elevation of the glaciers, the ASTER GDEM (ERSDAC 2009), which was recorded in the year 2000, is used because of its high spatial resolution. First, the digital elevation model and the deduced slope are intersected with the glacier boundaries of the Chinese Glacier Inventory. Secondly, the elevation data are aggregated to levels at intervals of 100 m, ranging from 4,800 to 7,100 m a.s.l. in the Lhasa River catchment. Since the elevation model was recorded in the year 2000 and is combined with the glacier boundaries of 1970, on average about 6 to 10 m w.e. (FRAUENFELDER AND KÄÄB 2009) melted away. Consequently, the elevation data are slightly too low. However, this average value is approximately within the range of accuracy of the elevation model of  $\pm 7-14$  m (ERSDAC 2009). Furthermore, the air temperature of the climate model CLM is downscaled to the grid cells with SCALMET (see section 3.1.1) and then extrapolated for each level due to its elevation, with a gradient of 0.65 K per 100 m in dry and 0.98 K per 100 m in moist air (see section 3.2.4), causing further deviations. Taking into account the uncertainty in all of the data, the chosen interval of 100 m seems appropriate and remains within the limits of accuracy. The slope is averaged by weighting it by area within the aggregation steps. In this process, each glacier is considered separately, and so the elevation levels are not aggregated among different glaciers. This enables modelling the ice flow for every single glacier in future simulations with an enhanced SURGES model. Next, the area per elevation level is calculated.

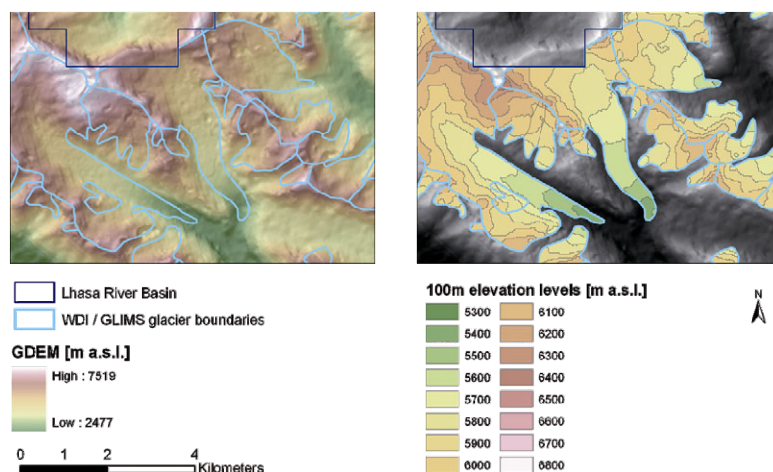


Figure 4.2: Intersected digital elevation model with glacier boundaries (left) and aggregated elevation levels of glaciers (right) (data source: ERSDAC 2009, WDC 2009).

Figure 4.2 shows the steps of the derivation of the elevation levels for the example of the Boda and Qingga glacier region of the Nyainqêntanglha Mountains. On the left, the glacier boundaries and the DGM are shown, and the derived elevation levels of the glaciers are illustrated on the right. The area-elevation distribution of all glaciers in the catchment is given in Figure 4.3. Most glacier areas can be found at between 5,600 and 6,000 m a.s.l. (78%). The areas above this level amount to 14 percent, with 8 percent of the glacier area located below it.

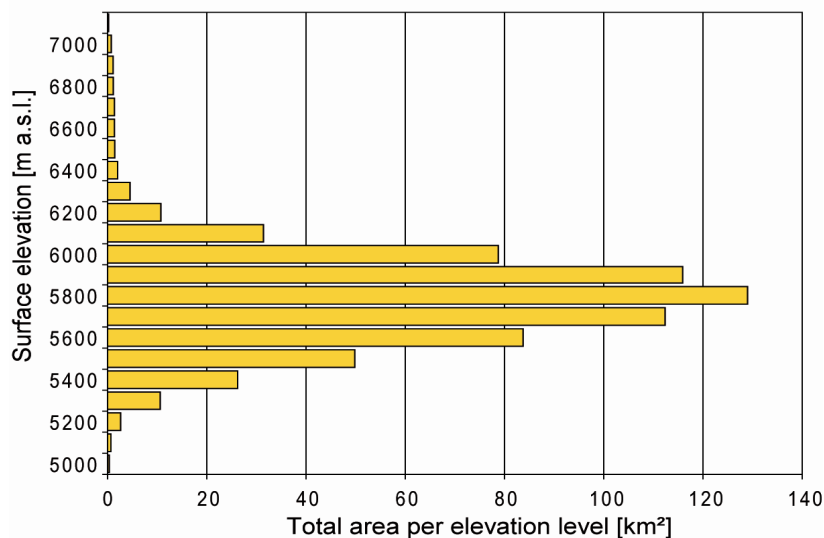


Figure 4.3: Area-elevation distribution of glaciers in the Lhasa River catchment.

#### 4.3.4 Ice Thickness

The Chinese Glacier Inventory (WDC 2009) contains the mean values of ice thickness per glacier. To consider the different ice thickness distribution of a glacier in more detail than assuming a homogenous ice block, the mean ice thickness must be modified for all elevation levels of the glacier. Several studies have been conducted to deduce the ice thickness distribution of surface characteristics. Among them are inverse methods based on modelling (THORSTEINSSON ET AL. 2003). However, they concentrate on Arctic or Antarctic ice sheets. FARIONOTTI ET AL. (2009) recently introduced an approach to estimating the ice thickness distribution based on the principles of ice-flow mechanics and mass-turnover. Since this method requires the flowlines and the ice-flow catchments as well as the glacier boundaries for each glacier, it cannot be applied to large areas such as the Lhasa River basin. An alternative method, offered by HAEBERLI AND HOELZLE (1995), is based on the assumption of a correlation between surface slope, glacier length and ice thickness. In a comparable approach, the mean ice thickness of the Chinese Glacier Inventory is modified for all elevation levels of the glacier according to its slope and position on the glacier. While the glacier thins out to its edges and the glacier front, the slope of the bedrock is one of the dominant factors in the ice thickness distribution of a glacier. The steeper the slope of the glacier, the thinner is its ice (PATERSON 1994). Therefore, the glacier elevation levels are grouped for the ice thickness modification according to slope, which is deduced from the digital elevation model on the assumption that the surface slope is approximately similar to the bedrock surface, because no further

information is available. A distinction is made between very steep levels with a slope larger than  $45^\circ$ , steep levels with a slope of between  $25^\circ$  and  $45^\circ$ , levels with a slope of between  $15^\circ$  and  $25^\circ$  and finally levels with a slight slope of below  $15^\circ$ . For these categories, the mean ice thickness values of the inventory are modified by the factor described below. To assess the modifying factor, parts of the glacier inventory data, applied in the *GLOWA-Danube* project (WEBER ET AL. 2008A), were analysed. This inventory comprises all available data, including considerable detailed ice thickness recordings and the area-elevation distribution of the glaciers in the Upper Danube catchment. Glacierets, mountain and valley glaciers are principally found in this region. The glacier area varies from about 19 ha to 15 km<sup>2</sup> (Gepatsch Ferner, Austria), and mean ice thickness extends to 111 m (Hintereis Ferner, Austria). Since the geometry and area of the glaciers in the Lhasa River catchment resemble that of the glaciers in the Upper Danube basin, conclusions of analogy for the ice thickness distribution seem to be appropriate. To this purpose, the relationship between the maximum and the average ice thickness was analyzed for the Glockner, Venediger and Zillertaler mountain groups (Figure 4.4). According to the data and by assuming a linear correlation, the maximum ice thickness of the levels is 1.7 times the mean ice thickness of the glacier. Eighty-two percent of the relationship can be explained by this factor, as shown in Figure 4.4.

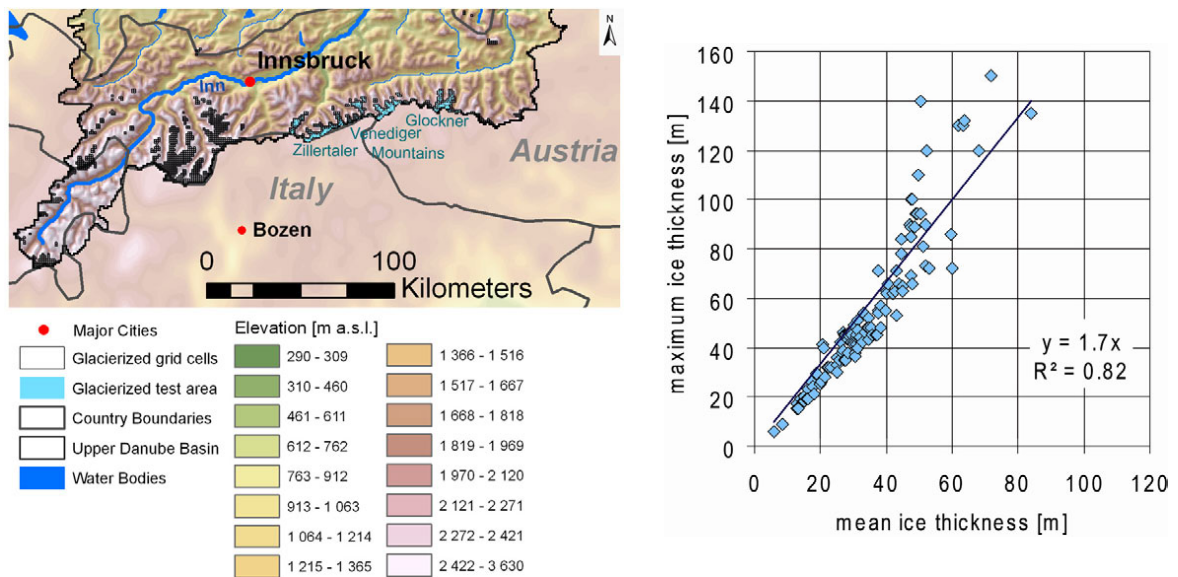


Figure 4.4: Relationship and coefficient of determination of the mean and maximum ice thickness of the glaciers in the Glockner, Venediger and Zillertaler mountain groups (map, left) according to the Upper Danube glacier inventory (based on WEBER ET AL. (2008A)).

To remain within a reasonable range, these values are limited by ice thicknesses calculated with the following equation:

$$h_i = \frac{\tau_s}{F \rho_{ice} g_o \sin \beta} \quad (\text{Eq. 4.1})$$

This formula allows the estimation of ice thickness  $h_i$  [m] with ice density  $\rho_{ice}$  [kg m<sup>-3</sup>], gravitational acceleration  $g_o$  [m s<sup>-2</sup>] and glacier slope  $\beta$  [°], assuming perfect plasticity of the ice. The shear stress  $\tau_s$  [kPa] varies between 50 and 150 kPa, so 100 kPa is often

taken as an average value. To consider the shape of glaciers in alpine terrain, a valley-factor  $F$  between 0.45 and 0.85 should also be inserted (PATERSON 1994). In the Lhasa River catchment a value of 0.7 is used as mean valley factor, because glacier width and shape are required for detailed determination values of ice thickness at the centre-line, and the data are not available for the Lhasa River basin. For steep levels and for the upper and lower levels of the glacier where it is usually thinner,  $h_i$  is calculated with shear stresses of 50 kPa whereas at elevation levels in the middle of the glacier with smaller slopes, a shear stress of 100 kPa is applied to calculate the limits for the ice thickness estimation. After this step, steep glacier levels have a thinner ice layer and flatter levels have a higher one.

As mentioned earlier, the elevation level position at the glacier is also considered. As the glacier thins out towards its edges and the glacier front, the ice thickness of the highest and lowest elevation level is set to the calculated value with a shear stress of 50 kPa, and limited to a maximum value of 20 m. According to the glacier inventory data applied in the GLOWA-Danube project (GLOWA-DANUBE 2001-2010), several measurements of alpine glaciers showed that this value is not usually exceeded (WEBER ET AL. 2008A). Furthermore, the special case of glaciers with only one elevation level is also considered in using the mean ice thickness of the inventory without any modifications. Finally, all initial ice thickness values are limited to a minimum value of 10 meters, to buffer the settling time of the model during the first model year. The decision tree in Figure 4.5 shows the derivation of the ice thickness distribution, including the distinct values applied.

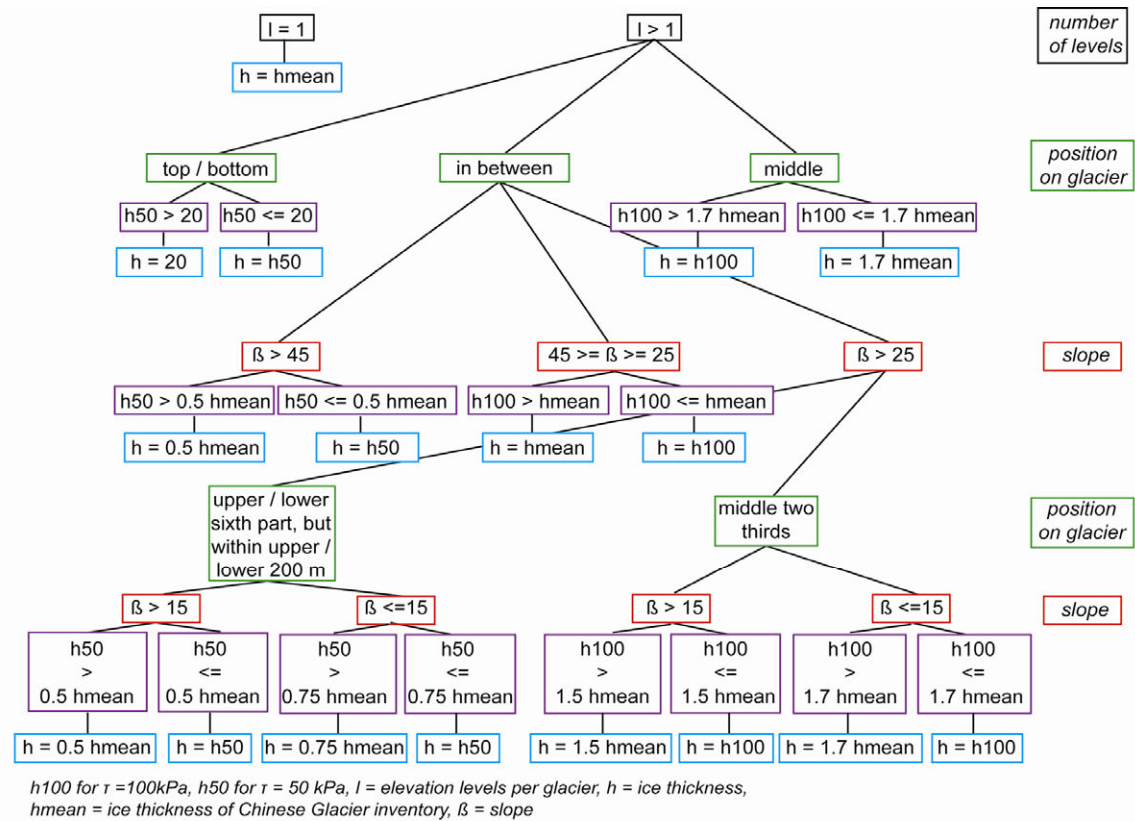


Figure 4.5: Decision tree for the derivation of the ice thickness distribution of the glaciers.

An example is illustrated in Figure 4.6, which shows the mean ice thickness of the Chinese Glacier Inventory on the left as well as the ice thickness distribution of the elevation levels after the described modifications. On the right, the grid cell structure, which overlays the glaciers, is shown.

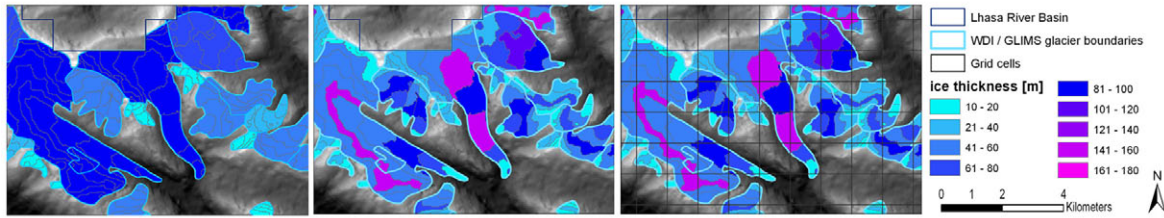


Figure 4.6: Example of the mean and distributed ice thicknesses of glaciers in the Lhasa River catchment, overlaid by the grid cell structure (based on ERSDAC (2009), WDC (2009)).

According to the deduced ice thickness, 34 km<sup>3</sup> of water is stored as ice, which amounts to 1,037 mm water per km<sup>2</sup>, distributed equally over the whole Lhasa River catchment. The maximum ice thickness can be found between 5,300 and 6,000 m a.s.l., whereas on the lower and higher levels the ice is thinner. Reasons are the glacier edges, where the ice is thinner than in the middle, which are often located above and below an elevation range of 5,300 and 6,000 m a.s.l. (Figure 4.7). Moreover, in higher areas steeper slopes can be found.

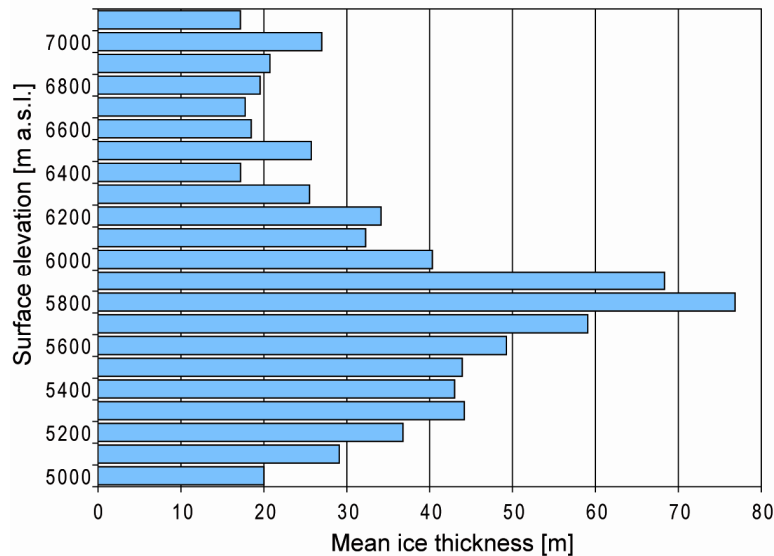


Figure 4.7: Ice thickness - elevation distribution of the glaciers in the Lhasa River catchment.

Before the glacier data input is completed, the ice thickness is subtracted from the surface elevation to obtain the mean elevation of the glacier bed for every level. Finally, the glacier levels, together with the glacier area, the elevation and the ice thickness are intersected with the grid cell structure. The required input data to run SURGES are thereby generated for all glacierized grid cells. The flow chart of Figure 4.8 clarifies the steps of the procedure, including the applied data.



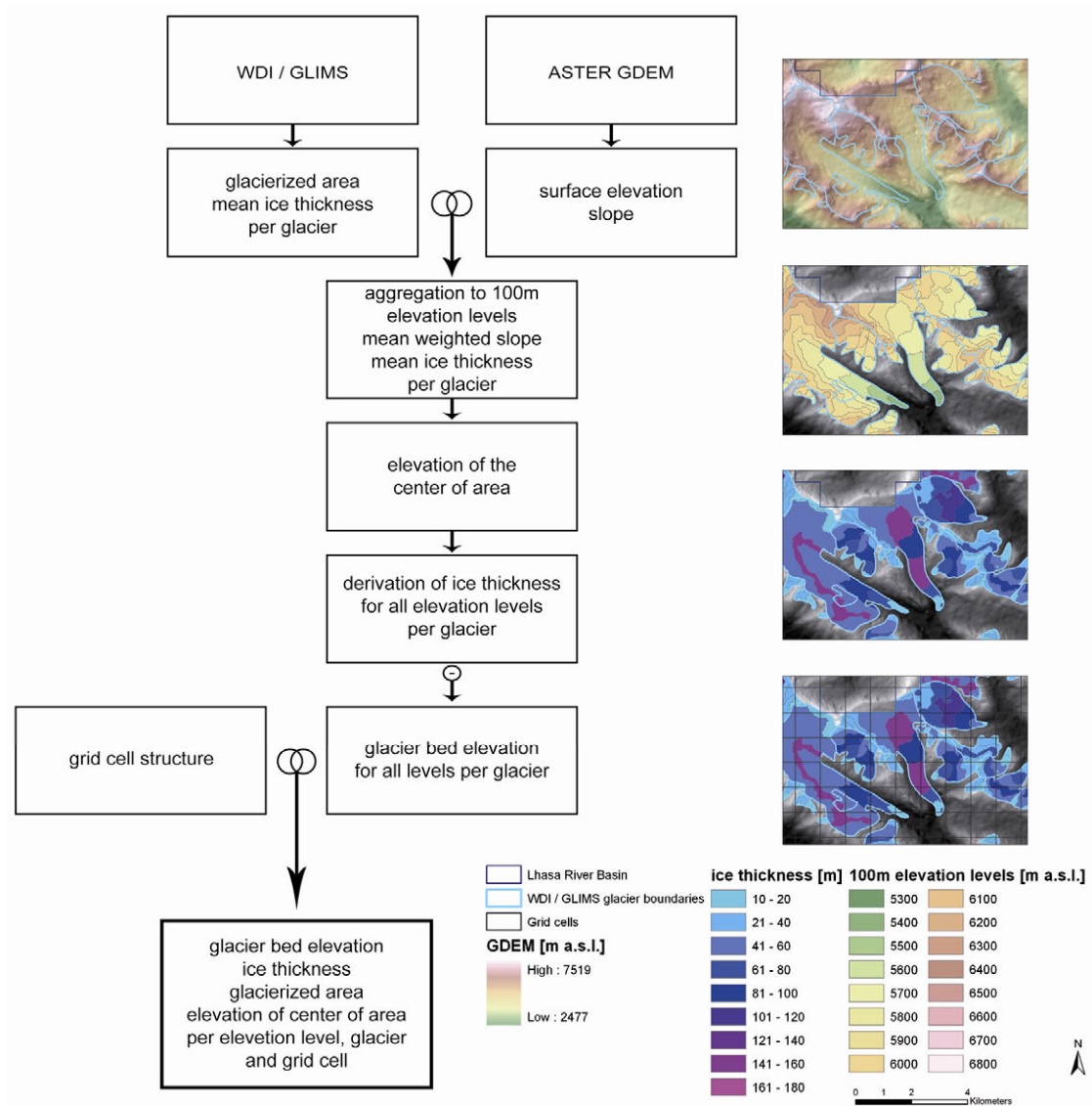


Figure 4.8: Flow chart of steps and data for the generation of the required input data to run the glacier model SURGES.

## 5 Model Validation

Modelling the impact of climate change on glaciers and on the water balance in the Lhasa River catchment requires validation of the modelling approach introduced. In order to check that the relevant processes are captured, the model results are compared to observations of the past. The following validation steps are carried out: First, the processes on the glacier, such as accumulation and ablation of snow and ice, are checked. Next, the reproduction of glacier geometry changes over a long time period is evaluated. As the study focuses on meltwater release from glaciers, the simulated runoff of a highly glacierized basin is compared to measured runoff, whereby the necessity of the subscale approach is also tested. In the next step in validation, the accuracy of the derivation of glacier input data is checked. Finally, the performance of the modelling framework in the Lhasa River basin is evaluated. This includes the accuracy of the downscaled CLM meteorological data, the glacier changes and the water balance during the period of 1971 to 2000.

### 5.1 Validation of the SURGES Glacier Model

Detailed observation data are required for validation of the glacier processes, which are generally rare. Additionally, the model results must not be altered by errors in the input data. Consequently, boundary conditions such as topography and meteorology must be as reliable as possible. For this reason, SURGES is applied to places which fulfil these requirements for validation of the glacier processes. Since neither detailed meteorological station recordings nor glacier observations are available in the Lhasa River basin, the Schneeferner at the Zugspitze in Germany, the Vernagt Ferner in Austria and the gauge of Huben of the Öztaler Ache in Austria were chosen for validation of the model (see Figure 5.1).

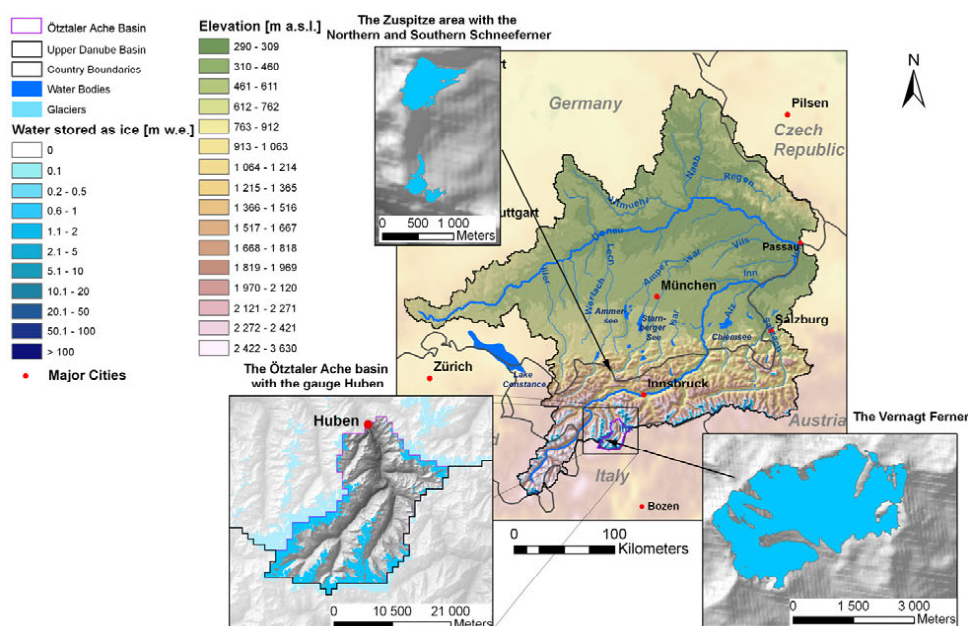


Figure 5.1: Map of the test sites in the Upper Danube basin (based on: GLOWA-DANUBE (2001-2010), BAYERISCHE GLETSCHER (2009), WEBER ET AL. (2008A)).

Within the framework of GLOWA-DANUBE (2001-2010), detailed data describing the geometry and the ice reservoir are provided for the three chosen test sites, sometimes even for several time steps (WEBER ET AL. 2008A). Furthermore, meteorological drivers of a comparatively high spatial and temporal resolution are available in the form of numerous station recordings by the German and Austrian weather service DWD and ZAMG. Figure 5.1 provides an overview of the location of the test sites within the Upper Danube basin.

The mass balance of a glacier is determined by the accumulation of snow and the ablation of snow and ice afterwards. Several studies have validated snow accumulation and ablation of the PROMET snow component on the point scale by comparing modelled s.w.e. values to observation data at weather stations. The spatial distribution of the modelled snow cover on the catchment scale was compared to observed snow coverage, deduced from NOAA AVHRR images. These studies showed that the model can reproduce snow dynamics at the point and spatial scale (BACH ET AL. 2008, PRASCH ET AL. 2008B, STRASSER AND MAUSER 2001). In order to determine the model performance on a glacier, a detailed validation study at the Vernagt Ferner in Austria was carried out by MAROWSKY (2010). In this study, the evolution of snow depth observations at the Vernagt Ferner, at an elevation of 3,000 m a.s.l. (BRAUN ET AL. 2004), are compared with the modelled s.w.e. at this elevation level for the first half of the year 2005. Although no evidence of snow quantity can be given, because no snow density observations are available for converting the s.w.e. values into snow depth, the duration of the snow cover is similar. Synchronous accumulation and ablation periods can be seen on the chart in Figure 5.2. Consequently, the dynamics are reproduced by the model on a glacier. The date of complete snow cover melt is especially important for simulation of the glacier ice-melt, because it determines the duration of the melting period.

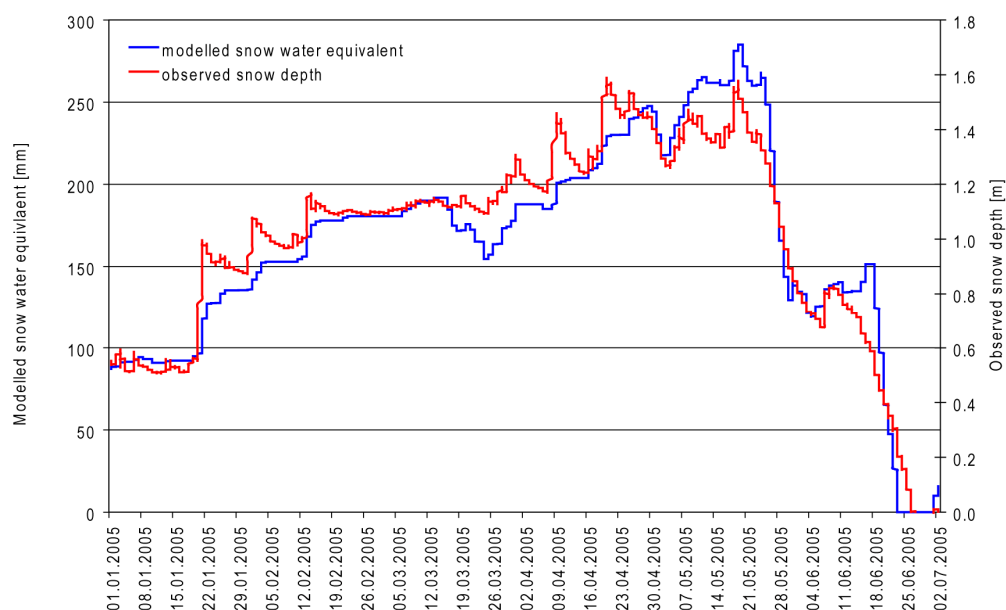


Figure 5.2: Comparison of the evolution of the modelled snow water equivalent (blue) and the observed snow depth (red) at the Vernagt Ferner (MAROWSKY (2010), p. 64, modified).



The ice ablation period was validated by MAROWSKY (2010), in comparing observed ice thickness changes with modelled changes. Figure 5.3 shows the comparison for the year 2006. For the measurements of relative ice thickness changes, an ablatometer was installed on the glacier surface (Figure 5.3, method 1, blue). With a second instrument, the relative changes of the ice thickness were deduced from observed hydrostatic pressure changes (Figure 5.3, method 2, green). Although the absolute values of the observation differ, the strong ablation period during July and the proximate snow cover in August are in accordance and reproduced by SURGES, meaning that the ice ablation period is also captured.

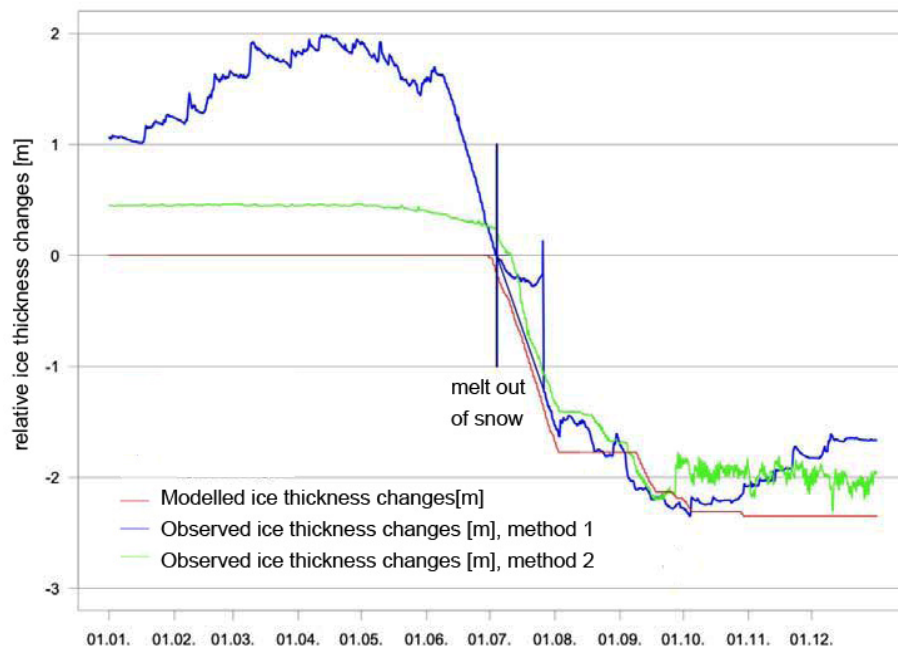


Figure 5.3: Comparison of modelled (red) and observed (blue and green) ice thickness changes 2006 (MAROWSKY (2010), p. 66, modified).

By comparing modelled and observed ice thickness observations on the glacier scale of the Northern Schneeferner at the Zugspitze in Germany from 1970 to 2006, the accurate simulation of glacier development is validated over a long period. Figure 5.4 shows the observed ice thickness of the years 1970, 1979, 1990, 2000 and 2006 (red) with the simulated ice thickness (light blue) and the evolution of the snow water equivalent (blue). The observations are correctly reproduced by the model. Furthermore, the period with high snowfall rates during the winters at the beginning of the 1980s and the subsequent gain in ice mass is captured by SURGES. The extraordinarily long ablation period of summer 2003 is also accurately simulated. Although this validation step only offers the comparison at five time steps during this period, it shows the performance of the model over a long time period. Only if snow and ice accumulation and ablation are simulated correctly over the complete period, the observed ice thickness values are reproduced by the model.

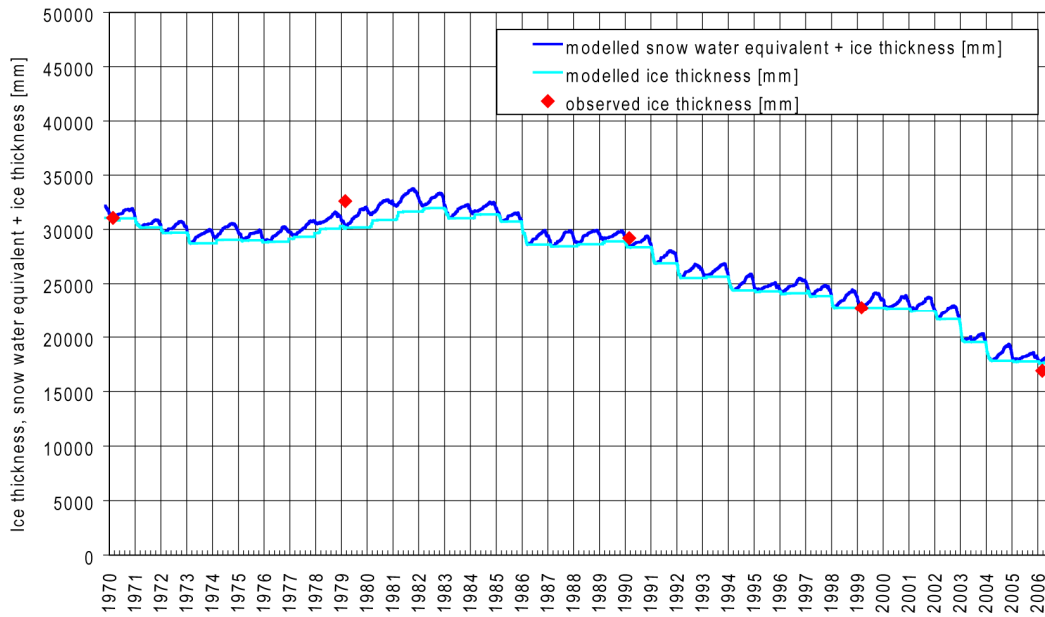


Figure 5.4: Modelled and observed ice thickness of the Northern Schneeferner at the Zugspitze in Germany (based on BAYERISCHE GLETSCHER (2009)).

By comparing the modelled and measured mass balances of the Vernagt Ferner, MAROWSKY (2010) validated the specific mass balance of each glacier elevation level. To achieve this, the Vernagt Ferner was divided into different parts, taking into account the grid cell structure as illustrated in Figure 5.5.

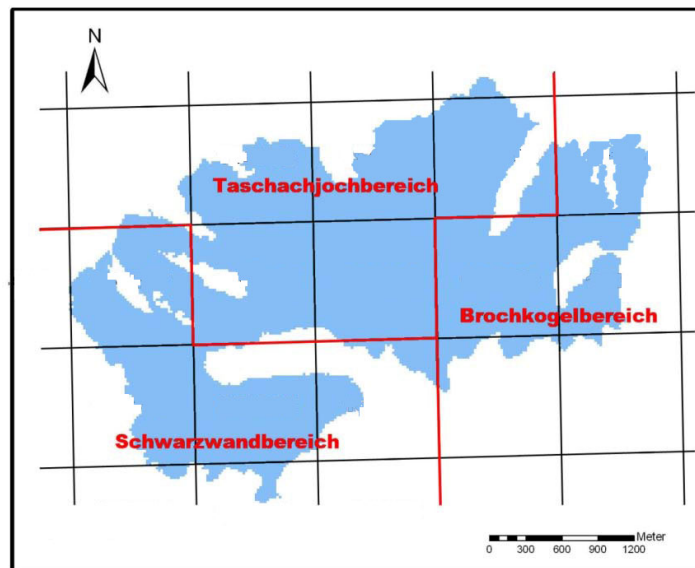


Figure 5.5: Different parts of the Vernagt Ferner with the grid cell structure covering the glacier (MAROWSKY (2010), p. 71, modified).

The comparison of two years with opposite weather conditions is presented here. While 1999 is characterized by above-average snowfall during the winter (Figure 5.6), the extraordinarily warm, dry summer of 2003 subsequently caused a long ablation period (Figure 5.7). The measured values are symbolized by lines, and the modelled mass balances are represented for each grid cell of the Vernagt Ferner. The area-elevation distribution of the mass balance season is also displayed in grey in the background.

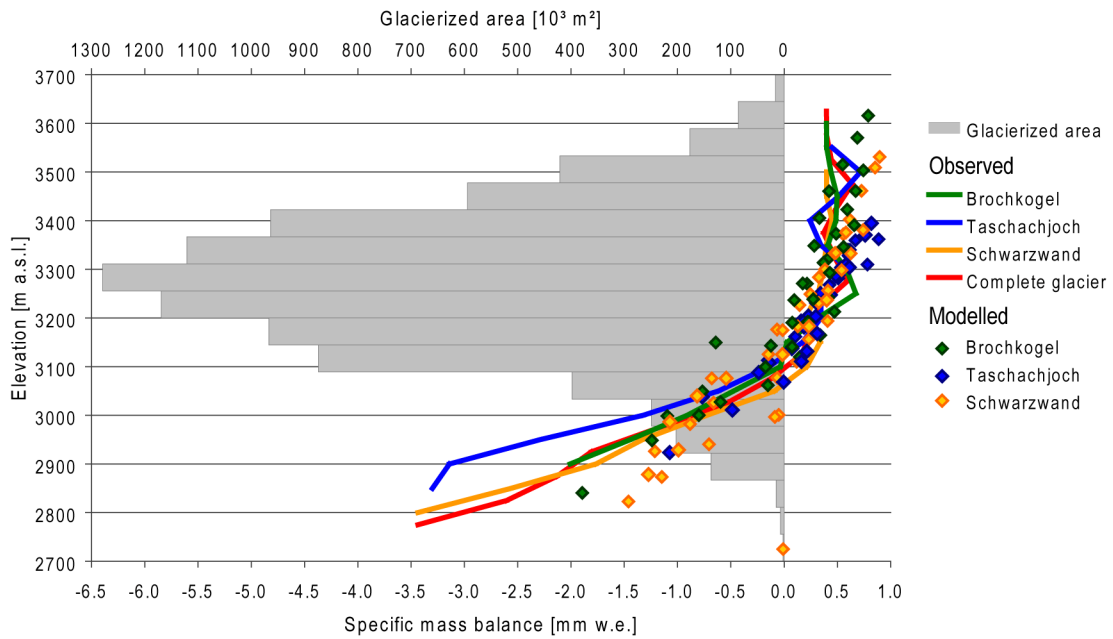


Figure 5.6: Observed (line) and modelled (squares) specific mass balance in the four parts of the Vernagt glacier for the elevation levels in the mass balance season 1999 (MAROWSKY (2010), p.78, modified).

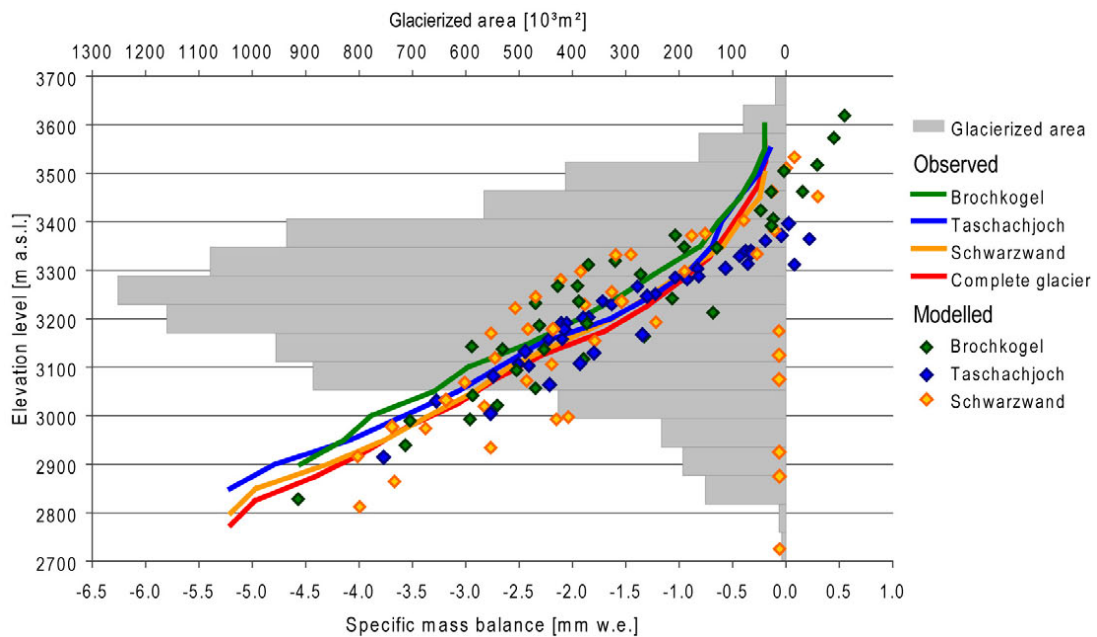


Figure 5.7: Observed (line) and modelled (squares) specific mass balance in the four parts of the Vernagt glacier for the elevation levels in the mass balance season 2003 (MAROWSKY (2010), p.79, modified).

In both cases, the modelled specific mass balance values are almost consistent with the measurements in all parts of the glacier. Various situations with large accumulation areas (specific mass balance > 0) in 1999 and extreme ablation areas (specific mass balance < 0) in 2003 are well reproduced by SURGES, except for the slight overestimation of the accumulation area in 2003. Positive mass balances were simulated at the highest elevation levels on contrary to observations, where negative mass balances were

observed for the complete Vernagt Ferner, although the accumulation observations in 2003 were afflicted with uncertainties at these elevation levels.

Values with a specific mass balance of 0 (x-axis) are elevations levels, where the ice has melted in the simulations. This is possible because the observations represent the average value of the complete grid cell. This comparison shows that the mass balance is captured by SURGES under different weather conditions for large glaciers separated into several grid cells. The extrapolation of the meteorological input data (see section 3.1.1) over the glacier elevation levels at the subscale therefore realistically simulates the situation in the total glacier area.

In order to validate glacier geometry changes, the modelled and observed glacier areas were compared for the Northern and Southern Schneeferner as presented in Figure 5.8. The original areas of 1979 are illustrated in black, whereas the grey areas show the extent mapped in 2006. The blue areas symbolize the modelled areas of the year 2006. The comparison shows deviations at the edges of the glaciers, in particular at the glacier tongues, where the model result is falsified by anthropogenic modifications in the skiing area (MAROWSKY 2010). Additionally, ice redistribution is not considered in this simulation. The ice flow is low because of the small extent of the Zugspitze glaciers, and so this effect can be neglected. Since the longwave radiation flux of neighbouring snow-free rocks is not simulated in SURGES, the accelerated melting during the breakup of glaciers in different parts with increasing surrounding rock areas is not reproduced. In this case, the melting is simulated too slowly, and a uniform ice thickness distribution on the elevation levels enforces this effect on the edges. In contrast, the melt from thick areas is simulated too quickly, so a conclusion of at least a partial compensation by the two effects can be drawn. Nevertheless, the congruence over a modelling period of 26 years dominates, especially in the parts of the glaciers where most ice is stored.

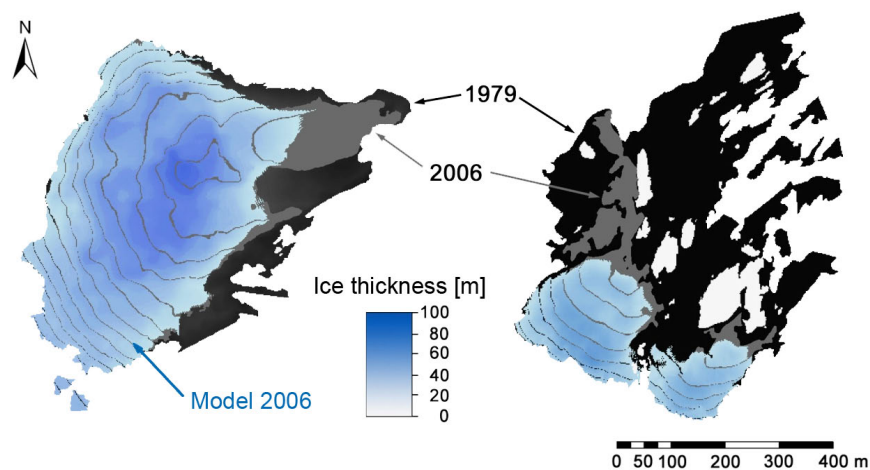


Figure 5.8: Comparison of modelled (blue) and observed glacier extent (grey and black) for the Northern (left) and Southern (right) Schneeferner at the Zugspitze in Germany between 1979 and 2006 (MAROWSKY (2010), p.70, modified).

Since this study focuses on the impact of glacier melt on the runoff, the next step is to validate the reproduction of the runoff by the model framework in an alpine glacierized catchment. The necessity of the subscale approach to simulate the glaciers on the

1 x 1 km size is also tested. As described above, the Huben gauge of the Ötztaler Ache, with a glacial coverage of 8 percent, was chosen (see Figure 5.1).

In order to determine the influence of ice-melt on runoff, the results of three different model runs were analysed. In the first model run, the runoff was simulated without considering glaciers and subsequently the ice-melt contribution. In the second model run, the glacier ice reservoir was equally distributed on the 1 x 1 km grid cell, and in the third simulation, the glaciers were considered in the subscale approach as introduced in section 3.2.3. The results for the period from 1.1.2000 to 31.12.2005 were compared to discharge observations by Huben. This period was selected because the glacier inventory for this basin reproduced the status of the year 2000. Table 5.1 lists the coefficient of determination  $R^2$  and the Nash-Sutcliffe efficiency coefficient (NASH AND SUTCLIFFE 1970), in the following referred to as NSC, as quality criteria for the various model runs, whereas Figures 5.9 and 5.10 show the runoff course of the different simulations for two years from 1.1.2003 to 1.1.2005.

Table 5.1: Quality criteria for the simulated runoff of different model runs at the Huben gauge of the Ötztaler Ache from 1.1.2000 to 31.12.2005.

Model runs	without ice, subscale approach	with ice, no subscale approach	with ice, subscale approach
Coefficient of determination	0.66	0.57	0.82
Nash-Sutcliffe efficiency coefficient	0.57	0.29	0.82

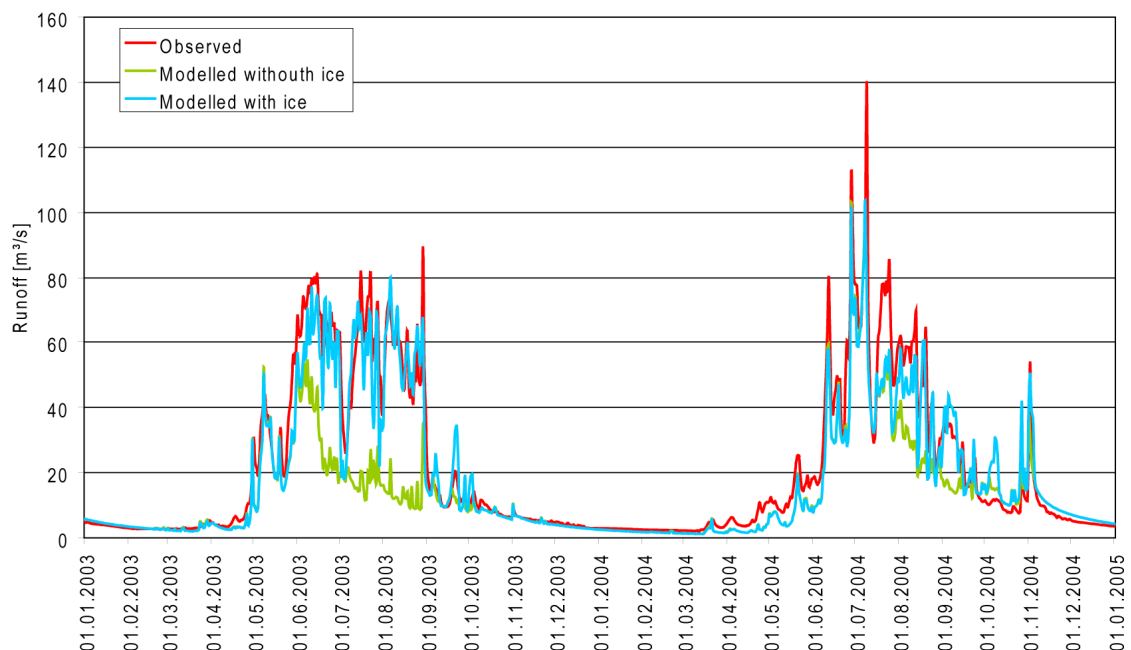


Figure 5.9: Comparison of modelled daily runoff without considering ice-melt water (green), and with ice-melt water (turquoise), to observed values (red) at the gauge in Huben of the Ötztaler Ache from 1.1.2003 to 1.1.2005.

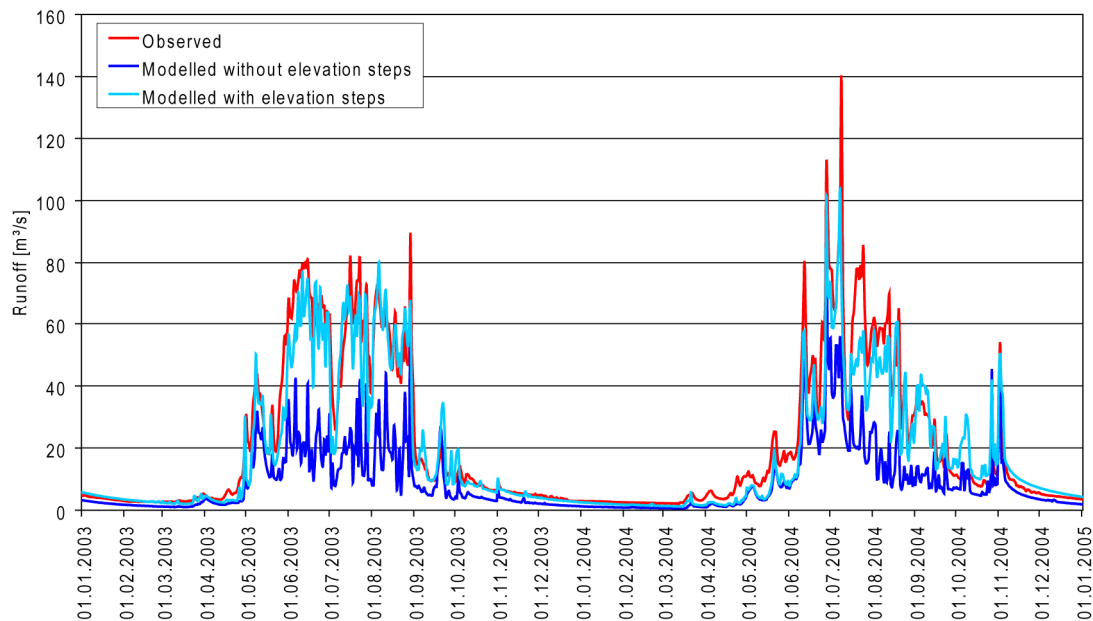


Figure 5.10: Comparison of modelled daily runoff without subscale approach (blue), and with subscale approach (turquoise), to observed values (red) at the gauge in Huben of the Ötztaler Ache from 1.1.2003 to 1.1.2005.

The clear improvement in the coefficient of determination and the NSC from 0.57 or 0.29 respectively to 0.82 in the model run, considering ice on the subscale, shows the positive influence of this approach on the runoff. The comparison of the quality criteria for the first two model runs even shows that the influence of the ice-melt on runoff is less than the influence of the subscale approach, because the criteria are higher for the subscale simulations without considering ice than for the results with ice, equally distributed over the complete grid cell. A comparison of development of the runoff of the different model runs with the observed discharge in Huben confirms and clarifies the result.

Simulating the glacier meltwater release with SURGES reproduces the runoff, whereas a considerable amount of water is missed during the summer months in the simulation without ice-melt. The glacier meltwater clearly contributes to the runoff, especially in the case of the extraordinary summer of 2003. In June, when the lower glacierized elevation levels become snow-free, a noticeable ice-melt water contribution to runoff starts. The percentage rises with the increase of snow-free glacier areas and culminates in August. With the first snowfalls in the highest mountain areas in September, the snow-free areas are reduced and the percentage of ice-melt decreases. During winter when the glaciers are completely covered with snow, meltwater release from the glaciers almost stops. This development of meltwater release is similar across years, but the amount, the beginning and end of ice-melt contribution depends on the prevailing weather conditions. In 2004, glacier melt did not start until July and contributed less water to the runoff in Huben than in 2003 (see Figure 5.9). The amount nonetheless remains essential for the simulation of the daily discharge.

A comparison of the second model run with the equally distributed ice on the grid cell clarifies the necessity of the subscale approach. The dynamics of the glacier melt water release cannot be reproduced in considering the ice storage as uniformly distributed on

the grid cell of one square kilometre, and so the dynamics and the amount of the runoff peaks are not reproduced. The reason for the deviations is the simultaneous melt of the snow cover of the entire grid cell. No melt water is contributed from the ice at the beginning of the melting period, whereas water is released from the whole grid cell after the snow melt. Furthermore, the snow cover of some glacierized grid cells in the highest mountains might outlast the whole summer season. As a consequence, no melt water is released from these areas, whereas the ice cover of the lower grid cells with thin ice layers melts away quite quickly. Additionally, glacierized areas are larger when distributed to the whole grid cell, and determine the amount of melt water release (see section 3.2.1). Accordingly, the water release at Huben is less than in the simulation with consideration of the glacier's area-elevation distribution. Since the meltwater release from the glacier is determined by the snow-free glacier area, the dynamics for the runoff cannot be captured without considering the area-elevation distribution of the glacier. The coexistence of snow-covered and snow-free parts on one grid cell is also the reason for the improved reproduction of runoff dynamics in the subscale approach without ice in the example introduced (Figure 5.10).

This step in the validation process also shows the performance of the hydrological model PROMET in the reproduction of the runoff in Huben. The components of PROMET are not validated in detail, because several studies have proven the quality of the model, including MAUSER AND BACH (2009), STRASSER AND MAUSER (2001) and LUDWIG AND MAUSER (2000). Its performance in the Lhasa River basin is shown in section 5.3.3.

Relevant processes on glaciers are reproduced by SURGES as shown in the previous steps, although there are processes which are not adequately reproduced, such as wind-induced snow transport, latent heat fluxes of the surroundings and ice redistribution (see section 3.2.8). Nevertheless, snow and ice accumulation and ablation, geometry changes and meltwater release to runoff are captured by SURGES. Furthermore, it has been demonstrated that not only consideration of ice, but also the subscale approach used in SURGES, is required to model the runoff course adequately in alpine regions with mountain glaciers with small-scale heterogenic properties.

## **5.2 Validation of Glacier Input Data Derivation**

In this section, the derivation of the input data to run SURGES, as shown in Chapter 4, is validated. The accuracy of the glaciated area and the elevation of the glacier levels are discussed first, and the derivation of the ice thickness distribution is then tested. The procedure introduced is similarly carried out in the Austrian Alps and compared to detailed glacier inventory data (WEBER ET AL. 2008A) because, as noted earlier, no observation data are available in the Lhasa River basin.

### **5.2.1 Glacier Area**

The glacier boundaries are taken from the Chinese Glacier Inventory, which is based on topographic maps and aerial photos of the year 1970 in the region of the Lhasa River basin (WDC 2009). According to MI ET AL. (2002) and SALERNO ET AL. (2008), the editors of the inventory which covers the test basin, the uncertainty of glacier area determinations



by topographic maps or aerial photos is in the 5 percent range. This value is confirmed by other studies, e.g. by WANG ET AL. (2009). Hence, the total error  $ae$  of the glacier area in the Lhasa River basin is  $0.2 \text{ km}^2$ , calculated by:

$$ae = \sqrt{(S_1 \cdot 0.05)^2 + \dots + (S_i \cdot 0.05)^2} \quad (\text{Eq. 5.1})$$

with the glacier area  $S \text{ [m}^2\text{]}$  and the number of glaciers  $i$ . In respect of a total glacier area of  $670 \text{ km}^2$ , this seems justifiable.

### 5.2.2 Glacier Elevation

The elevation levels of the glacier areas are deduced from the Aster GDEM (ERSDAC 2009) with a spatial resolution of 30 m and an accuracy of  $\pm 7 - 14 \text{ m}$ , as described in section 4.3.2. In the processing steps which generate the subscale levels, the elevation values are aggregated to levels with an interval of 100 m, meaning that the maximum deviation within the elevation level is 50 m, which is comparable to a temperature difference of below 0.5 K and therefore has a minor influence, especially considering the uncertainties of meteorological data. The GDEM was recorded in the year 2000, whereas the glacier boundaries of the CGI are from 1970. According to FRAUENFELDER AND KÄÄB (2009), the glacier volume of the Nyainqêntanglha Mountains has decreased by 6 to 10 m w.e. during this period. The surface elevation is therefore slightly too low, but the deviation is within the range of accuracy of the GDEM and of the aggregated level elevation, and so the data can be combined. The resulting changes in the slope, deduced from the GDEM and applied in calculating the ice thickness, might in turn also have changed. Nevertheless, after averaging of the values for the different elevation levels, this is considered to be negligible.

### 5.2.3 Ice Thickness

In order to complete the required input data to run SURGES, the ice thickness per elevation level is deduced. Since no ice thickness data except the mean ice thickness of the CGI are available for the Lhasa River basin, the method used to deduce ice thickness with generally available data (see section 4.3.4) is similarly carried out in the Ötztal, in parts of the Kaunertal and in the Stubaital in the Austrian Alps (Figure 5.11). The results are later compared to the Austrian glacier inventory, which provides detailed observation data for this region (FISCHER 2009, FISCHER ET AL. 2007, LAMBRECHT AND KUHN 2007, SPAN ET AL. 2005), and was applied in the GLOWA-Danube project (WEBER ET AL. 2008A,B). As the area and geometry of the glaciers are similar to those of the glaciers in the Lhasa River basin (see sections 2.6 and 4.3.4) this validation approach seems appropriate. However, the factor for maximum ice thickness was deduced from the Austrian glacier inventory, but no data from the validation area were used in the derivation step (see section 4.3.4) and no other data are available for validation.



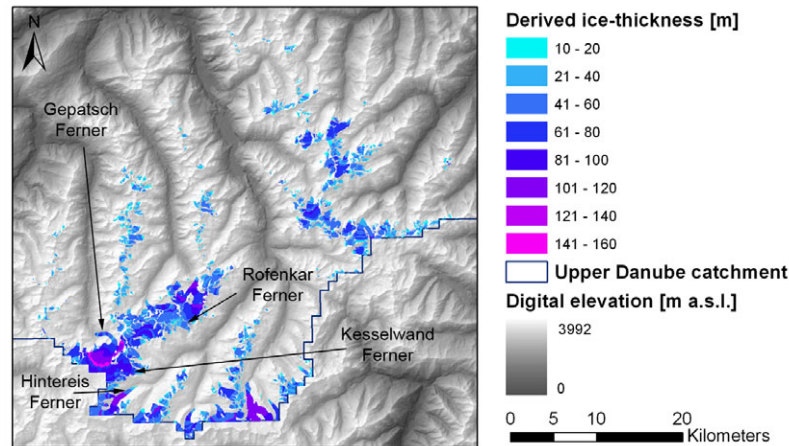


Figure 5.11: The glaciers of the validation area for ice thickness derivation in the Ötztal, Kaunertal and the Stubaital in Austria (based on ERSDAC (2009), WEBER ET AL. (2008A)).

In the method used to derive the ice thickness distribution of the glaciers, the Aster GDEM (ERSDAC 2009) and the glacier boundaries of the Austrian glacier inventory are applied as input data. In order to proceed on the assumption of a given mean ice thickness per glacier as is the case in the CGI, a mean ice thickness  $h_i$  [m] was calculated with Eq. 5.2 and consideration of the glacier area  $S$  [m<sup>2</sup>]. This formula is based on the BAHR ET AL. (1997) volume-area correlation and modified for the Austrian Alps by WEBER ET AL. (2008A).

$$h_i = 0.0285 \cdot S^{0.36} \quad (\text{Eq. 5.2})$$

With these data, ice thickness per elevation level was derived according to the decision tree seen in Figure 4.5.

In order to check the quality of the deduced ice thickness, the derived ice volumes were compared with the inventory data. Deviations are caused by ice thickness, because the glacier area is identical in both data sets, and comparison of the volumes allows consideration of the quantity of glacier ice. The water reservoir is therefore essential in this study. First, the total volume of all glaciers is compared to the Austrian glacier inventory. The volume deduced is 0.22 km<sup>3</sup> smaller, which equals a deviation of two percent. This corresponds to a mean ice thickness of 54 m overall and a deviation of 1 m (see Table 5.2). In comparison to uncertainties of ice thickness values for the Austrian Alps of between 3 m and 300 m (FISCHER 2009), the deviation is small.

Table 5.2: Comparison of total observed and deduced ice volume in the Ötztal, the Kaunertal and the Stubaital in Austria.

	Total ice volume [km <sup>3</sup> ]	Mean ice thickness [m]
Observed ice reservoir	9.651	55
Deduced ice reservoir	9.431	54
Difference	0.220	1
Deviation [%]	2	2

In the next step, the observed ice volume and the deduced ice volume are compared. The linear regression, forced through the origin, shows that the deduced ice volumes have been slightly underestimated. Nevertheless, 95 percent of the variance of the volumes can be explained by the coefficient of determination (Figure 5.12, left). To further clarify the quality of the derivation approach, the deduced ice volume of every elevation level was compared to the observed volumes. Here, the coefficient of determination is 0.74 and the slope of the linear regression is 0.76. The deviations are accordingly larger than for the average glacier values (Figure 5.13, left). The distribution of the values in the chart shows somewhat overestimated deduced values for smaller ice volumes, whereas the larger ones are slightly underestimated.

The observed ice volumes larger than  $60 \cdot 10^6 \text{ m}^3$  in Figure 5.11 can be attributed to the Gepatsch and Hintereis Ferner, which have very narrow valleys. The valley geometry is only considered in the applied approach by one general valley factor of 0.7 (see section 4.3.4), which depends on the ratio of glacier width to ice thickness on the centre line (PATERSON 1994). Since these values are not available for every glacier, a mean valley factor was taken. In the applied method, the slope and position of the elevation level are quite dominant. Hence, in cases where the glacier geometry is crucial, the derivation of the ice thickness is not fully captured by the methodology. In order to clarify the influence of the Hintereis and Gepatsch Ferner, the analysis was repeated without the values of the two glaciers. Figure 5.12 (right) and Figure 5.13 (right) show the results of this analysis. Although the coefficients of determination remained similar, the slope of the regression changed: the bias of the derived glacier volumes is smaller without the two glaciers. A further reason for deviations is the cut-off of glacier parts located along the southern watershed of the Upper Danube, due to the spatial resolution of  $1 \times 1 \text{ km}$ . The area-volume relationship therefore delivers different mean ice thickness values.

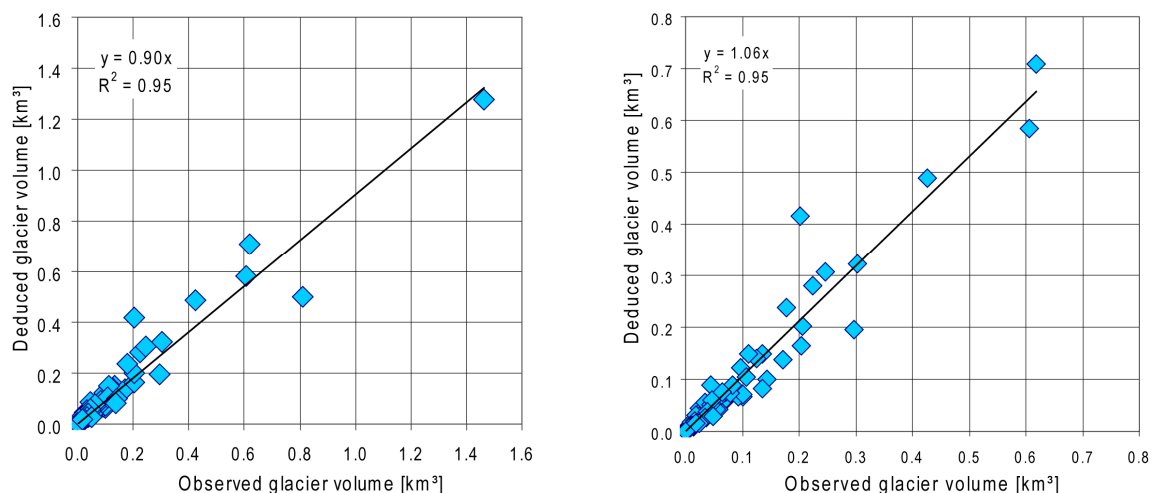


Figure 5.12: Comparison of observed and deduced total ice volume of all glaciers with (left) and without (right) Hintereis and Gepatsch Ferner.

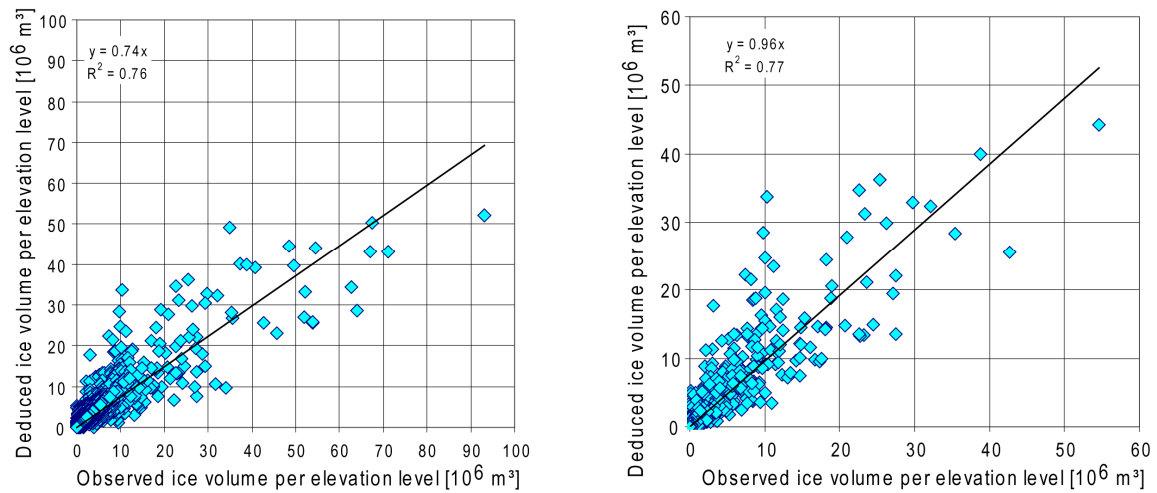


Figure 5.13: Comparison of observed and deduced ice volume of all glacier elevation levels with (left) and without (right) Hintereis and Gepatsch Ferner.

Finally, the volumes of the elevation levels of two glaciers are compared. An average mountain glacier with an area of 1 km<sup>2</sup> was chosen, the Rofenkar Ferner, and a large valley glacier with an area of 4.7 km<sup>2</sup>, the Kesselwand Ferner, was also selected. Both glaciers are marked in Figure 5.11: their characteristics and a comparison of their volumes are listed in Table 5.3.

Table 5.3: Characteristics of the Rofenkar and Kesselwand Ferner and comparison of observed and deduced ice volumes.

Glacier	Area [km <sup>2</sup> ]	Observed ice volume [km <sup>3</sup> ]	Deduced ice volume [km <sup>3</sup> ]	Volume difference [%]	Observed mean ice thickness [m]	Deduced mean ice thickness [m]	Ice thickness difference [m]
Rofenkar Ferner	1.0	0.046	0.045	-6	46	49	-3
Kesselwand Ferner	4.7	0.330	0.320	-3	70	68	-2

The overall deviation of the ice volume varies between 3 and 6 percent for the two selected glaciers, which corresponds to a difference of 2 m or respectively 3 m of mean ice thickness. The comparison of the ice volumes of the elevation levels shows an overestimation of the smaller Rofenkar Ferner, whereas for the Kesselwand Ferner a slight underestimation is seen (Figure 5.14). This confirms the results of the comparison of all glacier elevation volumes as discussed above. The coefficients of determination of 0.97 and 0.89 demonstrate that the approach enables the derivation of a realistic ice distribution solely using generally available data. Moreover, the approximately 5 to 10 percent uncertainty in ice thickness observations arising from the measurement system and the properties of ice and bedrock should also be taken into account. For the Austrian Alps with ice thickness values of between 3 m and 300 m, the uncertainty equals 0.15 m to 30 m (FISCHER 2009). Accordingly, the method of derivation of ice thickness distribution for the elevation levels, which requires, by comparison to other methods, relatively little time and effort, seems to be reliable. The deviations are also within the accuracy range of the digital elevation model, which amounts to between  $\pm 7$  and 14 m (see section 5.2.2).

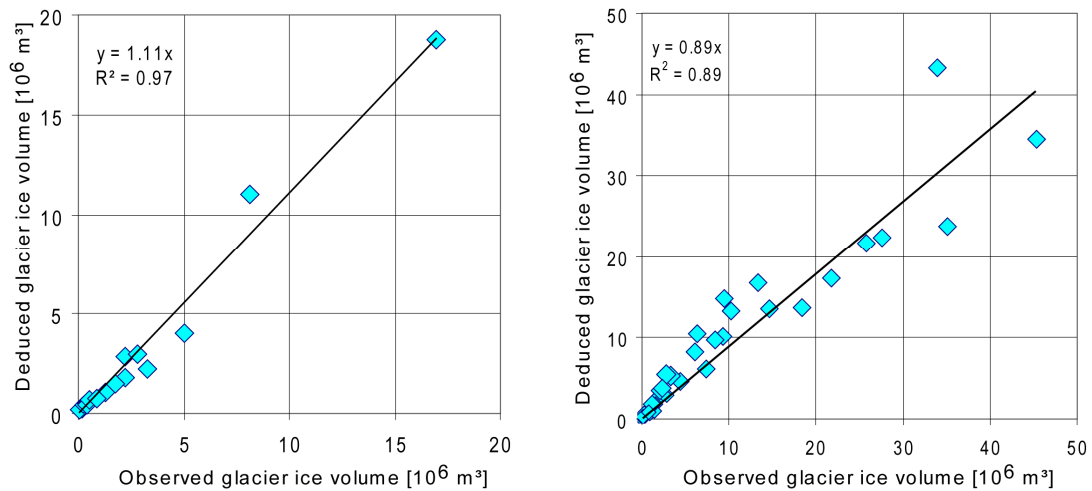


Figure 5.14: Comparison of observed and deduced ice volume of the elevation levels of Rofenkar Ferner (left) and Kesselwand Ferner (right).

In comparison to other methods for the estimation of the ice thickness distribution of alpine glaciers, the applied approach may be less accurate, but requires a minimum of input data and is accordingly applicable in remote and larger areas. For example, the method used by FARINOTTI ET AL. (2009) requires a set of ice flowlines and the corresponding catchments, in addition to a digital elevation model and glacier outlines. The distribution of mass balance and parameters describing the ice-flow dynamics are also needed. For remote and larger regions such as the Lhasa River catchment, these data are not available. Consequently, the approach is limited to small mountain ranges or individual glaciers (FARINOTTI ET AL. 2009).

Altogether, the validation of the deduced glacier inventory data, containing glacier areas, elevation levels and ice thickness distribution, showed that the method results in realistic input data for use of SURGES. Although the ice thickness distribution cannot be tested in the Lhasa River catchment, the transfer seems justifiable as the area and the geometry of the glaciers is similar to those of the Eastern Alps. The modest requirements of time and effort, in combination with the minimum of required input data, allow application in remote regions without further data. The focus on the hydrological impact, however, requires a reliable area-elevation distribution, as this determines meltwater release alongside meteorological conditions as described in section 3.2.1.

### 5.3 Validation of Model Results for the Lhasa Catchment

The model approach reproduces the processes on a glacier for meltwater release and runoff, as shown in section 5.1. As the derived input data for the model are reasonable, they are applied to the Lhasa River catchment. In order to check the performance of PROMET including SURGES in the investigation area, they are applied for the period from 1971 to 2000. The quality of the CLM data is described first, and then the modelled glacier mass balance in the Lhasa River basin is validated. The simulated runoff is finally compared to observations.

### 5.3.1 Meteorology

Meteorological station recordings are insufficient to run the model, and so data from the RCM COSMO-CLM (CLM 2010, see section 4.1) are used as meteorological drivers. The SCALMET tool scales the data down to the required spatial resolution of 1 x 1 km, and the CLM data are disaggregated to a temporal resolution of one hour, as described in section 3.1.1. As SCALMET was validated in detail in MARKE (2008), only the quality of the downscaled CLM output data in the Lhasa River basin is checked in this study. The CLM ERA 40 outputs are therefore compared to the few meteorological station recordings at Lhasa, Damshung and Meldro Gungkar (see Figure 2.4). Daily air temperature and precipitation measurements were provided by ICIMOD (2009) for 1980 to 2000. As part of the Brahmawinn project (BRAHMATWINN 2006-2009), ITP (2008) provided monthly precipitation values for the gauging stations of Lhasa and Tangga from 1971 to 2000, and for Pangdo from 1976 to 2000 (see Figure 2.4).

The comparison of the downscaled CLM ERA 40 with the observed mean values of air temperature and precipitation is summarized in Table 5.4. The air temperatures are slightly underestimated by the CLM data, whereas the precipitation sum is overestimated, except for Meldro Gungkar. The deviations vary from 3 percent in Meldro Gungkar to 37 percent in Lhasa. To clarify the deviations, daily and monthly values are analysed below.

*Table 5.4: Comparison of downscaled CLM ERA 40 and observed mean values of air temperature and precipitation.*

Station and time period	Air temperature [°C]			Precipitation sum [mm]		
	Observation	Down-scaled CLM ERA 40	$\Delta$	Observation	Down-scaled CLM ERA 40	$\Delta$
Lhasa (1980-2000)	8.1	7.2	-0.9	426	584	158
Meldro Gungkar (1980-2000)	6.0	5.3	-0.7	548	532	-16
Damshung (1980-2000)	1.8	1.7	-0.1	464	543	80
Pangdo (1976-2000)		no data		538	647	91
Tangga (1971-2000)		no data		517	561	44

The comparison of the downscaled and observed daily air temperatures is shown in Figure 5.15, together with the linear regression and the coefficients of determination. 78 to 86 percent of the variance in the measurements can be explained by the CLM ERA 40 data at the stations, although the CLM data slightly underestimate the air temperatures. The spread between observations and modelled values for lower temperatures can be explained by analysing the development of monthly air temperatures as illustrated for the stations of Lhasa and Damshung in Figure 5.16.

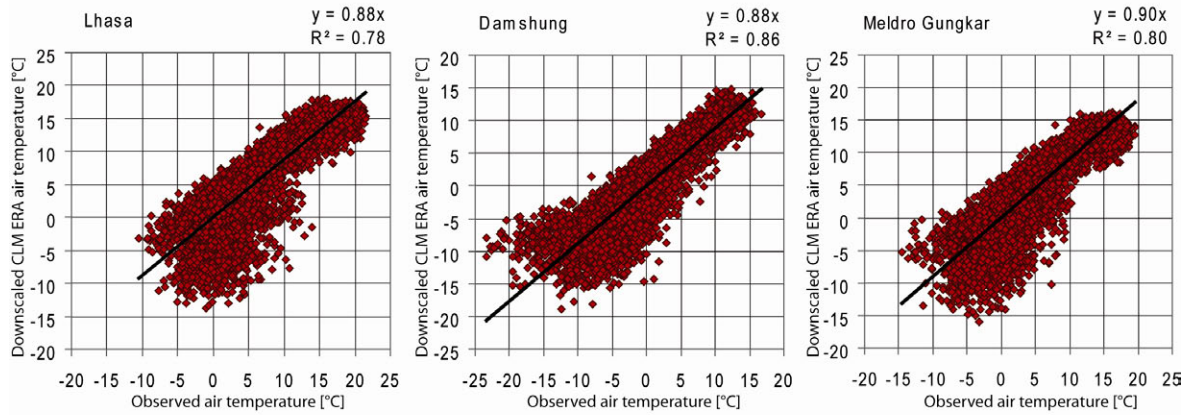


Figure 5.15: Comparison of modelled (CLM ERA 40) and observed daily air temperatures for the Lhasa, Damshung and Meldro Gungkar stations.

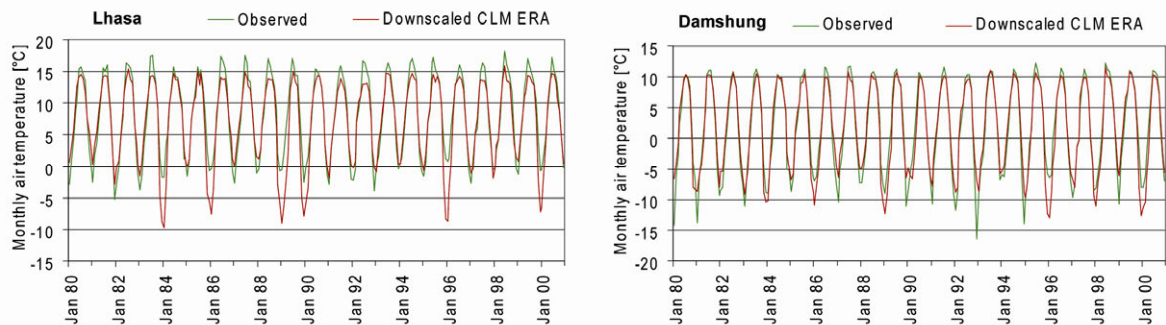


Figure 5.16: Development of modelled (CLM ERA 40) and observed monthly air temperatures for the Lhasa and Damshung stations.

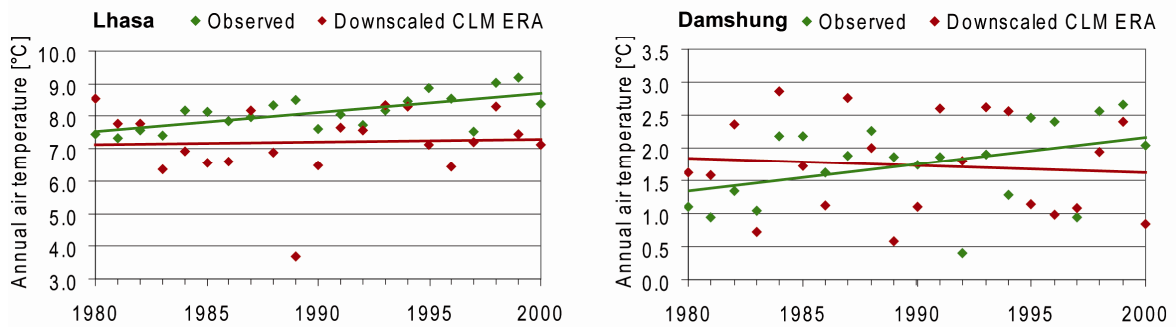


Figure 5.17: Observed and modelled (CLM ERA 40) trend of the annual air temperature at the Lhasa and Damshung stations for 1980-2000.

The minimum air temperatures are clearly underestimated for some years, e.g. 1996, whereas for other years they are overestimated, e.g. 1993, causing greater variance in the comparison of low temperatures. While the air temperatures between the minimum and maximum are reproduced by the downscaled CLM data, the maximum values are slightly underestimated: no overestimation can be seen. The described deviations also explain the difference between the observed and simulated trend of the annual air temperatures from 1980 to 2000, as shown in Figure 5.17. The years 1989 and 1996 are especially noticeable for Lhasa and Damshung, with sizeable underestimations of the minimum temperature. The observed trend is thus not reproduced by the downscaled CLM ERA 40 data. The analysis of Meldro Gungkar delivers similar results (see Appendix 3).



The comparison of observed and simulated monthly precipitation shows a coefficient of determination of between 0.64 and 0.76 (Figure 5.18). The monthly time series clarify deviations (Figure 5.19 and Appendix 4). Although they are approximately reproduced by the model, there are some years in which the deviations between observed and modelled precipitation are large. For the years 1986, 1992 and 1994, the precipitation sum is overestimated for all stations, whereas underestimations can be seen for 1996. During the last decade, from 1991 to 2000, the deviations become smaller with high accuracy in 1998, for instance. Despite deviations in the precipitation amount, the monthly course is reproduced by the downscaled CLM ERA 40 values.

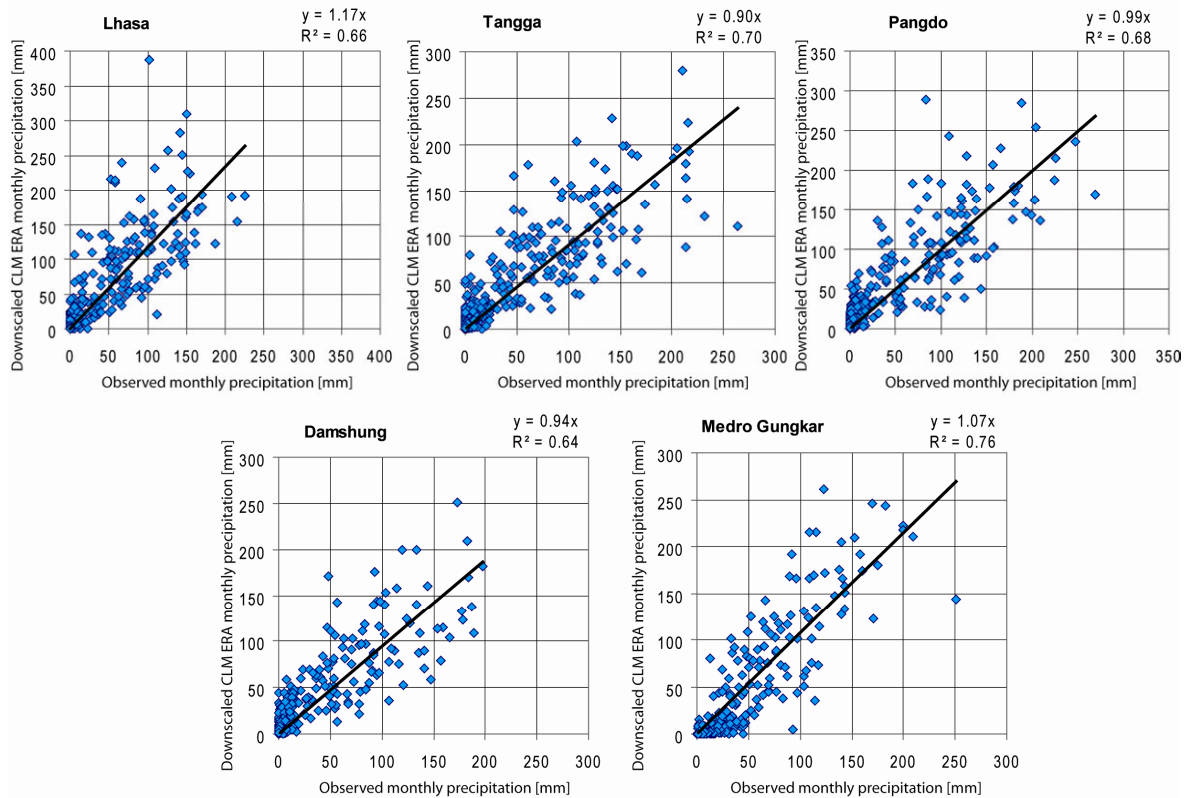


Figure 5.18: Comparison of modelled (CLM ERA 40) and observed monthly precipitation for the Lhasa and Tangga (1971-2000), Pangdo (1976-2000) and Damshung and Meldro Gungkar stations (1980-2000).

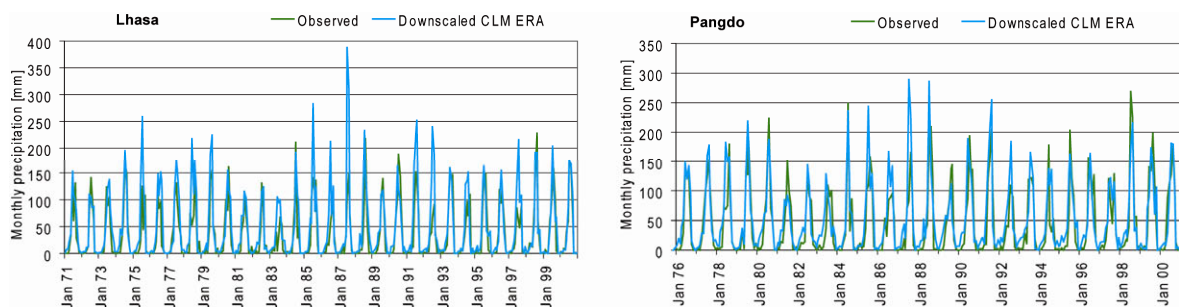


Figure 5.19: Development of modelled (CLM ERA 40) and observed monthly precipitation for the Lhasa (1971-2000) and Pangdo stations (1976-2000).

By contrast to the monthly values, daily precipitation values are not captured by the model output. This is the case for years reproducing the total amount, as well as for years with

large deviations, as shown for the years of 1998 (-2%) and 1997 (+103%) at the Lhasa station in Figure 5.20. The deviations vary between  $\pm 20$  mm per day, but without special pattern. The values, aggregated to monthly sums, are reproduced when the total amount is similar to observations.

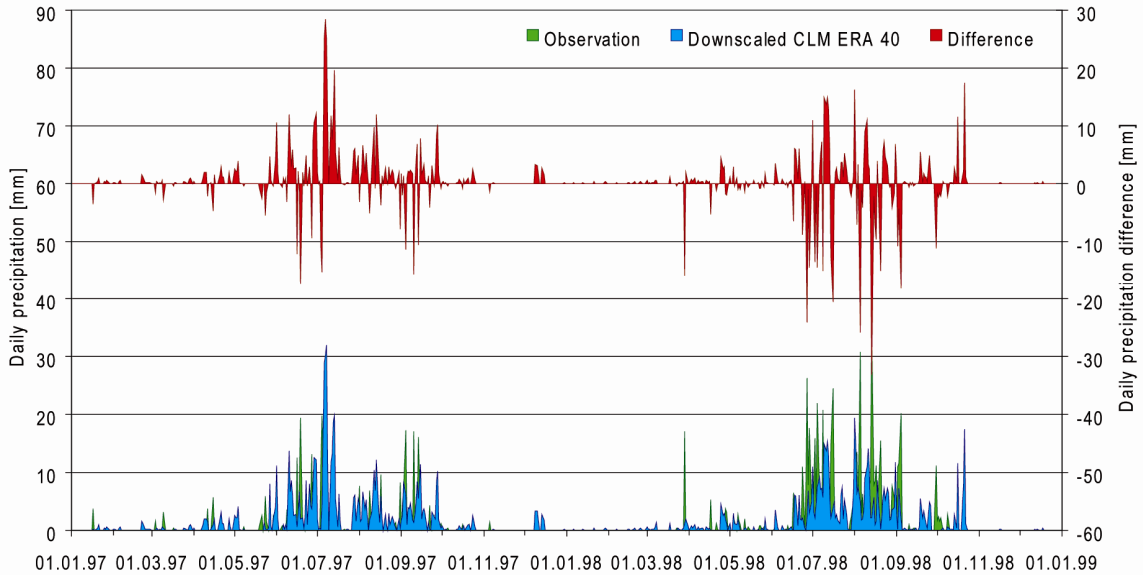


Figure 5.20: Daily time series of modelled (CLM ERA 40) and observed precipitation at the Lhasa station for the years 1997 and 1998.

The deviations described influence the modelling of the precipitation trends during the past period from 1971-2000. Accordingly, the trend is not clearly reproduced by the model. For Lhasa the positive trend is similar, but for Pangdo there is no trend simulated contrary to the observations (Figure 5.21 and Appendix 5). Nevertheless, the deviations are smaller than those for air temperature trends.

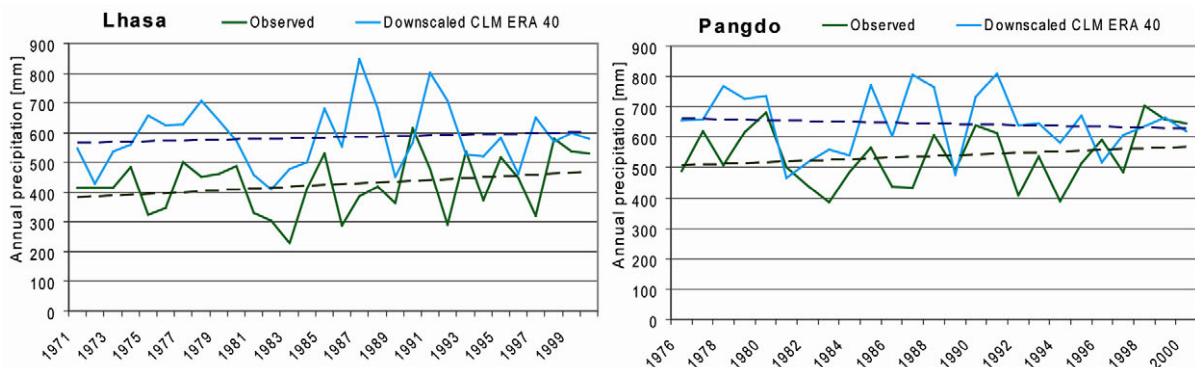


Figure 5.21: Observed and modelled (CLM ERA 40) trend of the annual precipitation sum at the Lhasa and Pangdo stations.

For the simulation of future climatic conditions, the CLM is driven by the ECHAM 5 / MPI-OM global model (see section 4.1). In order to validate the downscaled ECHAM 5-driven CLM data, the model results are compared to the stations' recordings for the climate period of 1971 to 2000. Unlike the ERA driven model output, which is based on observation data, the ECHAM 5-driven data, as a climate model, cannot reproduce the chronology of the meteorological conditions. The model output should, however,



reproduce the meteorological conditions and the climate signal. Consequently, the average values, the seasonal course with minimum and maximum values and the trend of the data should be comparable to observed data. The mean simulated and observed values of air temperature and precipitation for the stations are listed in Table 5.5. The recorded air temperature is reproduced for the stations by the model, except that in Damshung where the temperature is overestimated by 0.6 K. The mean precipitation sum of Damshung and Pangdo is overestimated by the CLM ECHAM 5 data, but the deviations are within 10 percent, whereas in Lhasa the overestimation reaches 22 percent. The precipitation sum is slightly underestimated for Meldro Gungkar and Tangga. In comparison to the CLM ERA 40-driven temperature and precipitation values, the deviations seen are smaller. Consequently, the mean meteorological conditions are reproduced by the CLM ECHAM 5 model run. Taking into account technical difficulties in precipitation observation and the resulting deviations up to 10 percent (BAUMGARTNER AND LIEBSCHER 1996), the average results seem to be reasonable.

*Table 5.5: Comparison of simulated ECHAM 5 CLM and observed mean values of air temperature, precipitation and wind speed from 1980 – 2000, except precipitation for Lhasa and Tangga (1971-2000) and Pangdo (1976-2000).*

Station and time period	Air temperature [°C]			Precipitation sum [mm]		
	Observation	Down-scaled CLM ECHAM5	$\Delta$	Observation	Down-scaled CLM ECHAM5	$\Delta$
Lhasa (1980-2000)	8.1	7.9	-0.2	426	524	97
Meldro Gungkar (1980-2000)	6.0	6.0	0.0	548	481	-67
Damshung (1980-2000)	1.8	2.4	0.6	464	511	48
Pangdo (1976-2000)		no data		538	587	41
Tangga (1971-2000)		no data		517	513	-4

Examples of both observed and modelled monthly air temperature and precipitation are illustrated for the station Lhasa in Figure 5.22. The seasonal cycles are captured by the model output, with the monsoon precipitation during the summer months and the dry winters, although there are overestimations of precipitation during the pre-monsoon time in April and May, taking into account that the annual values cannot be reproduced by a climate model. The comparison of the monthly simulated and observed values also shows simulation of a reasonable range of minimum and maximum values. Two January temperatures, however (1987, 1988), are simulated at a clearly lower level than all observations.

Finally, the trend of annual air temperature and precipitation is determined, to validate the reproduction of the climate signal by the downscaled CLM ECHAM 5 model outputs.

Figure 5.23 shows the trends of observed and simulated annual air temperatures for the Lhasa and Damshung stations, and the chart for Meldro Gungkar can be seen in Appendix 6. Although there are deviations, the increasing temperature trend is simulated for all stations, in contrast to the CLM ERA 40-driven model outputs. This can also be seen for the precipitation, where no significant trend is obvious. The linear trend lines however tend to develop in opposite directions (Figure 5.24 and Appendix 7).

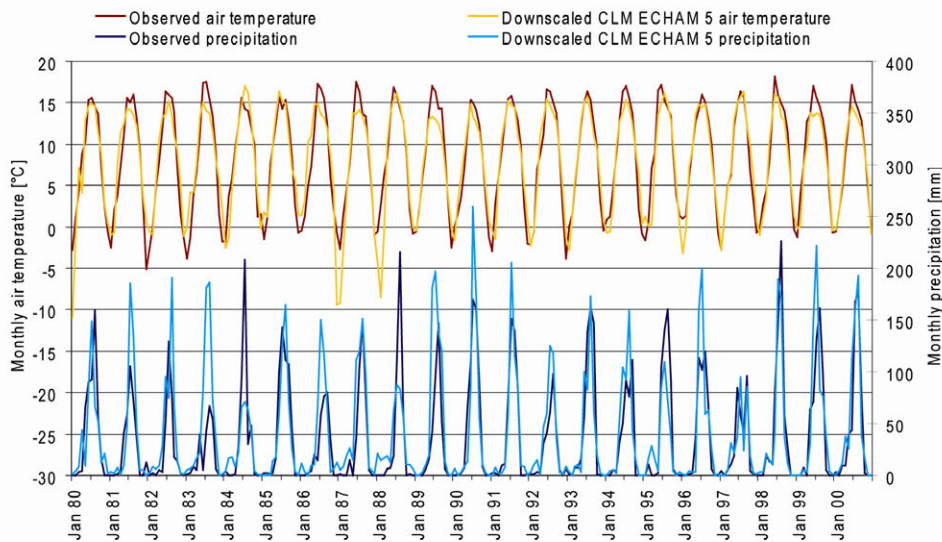


Figure 5.22: Development of observed and modelled CLM (ECHAM 5) monthly air temperature and precipitation at the Lhasa station for 1980-2000.

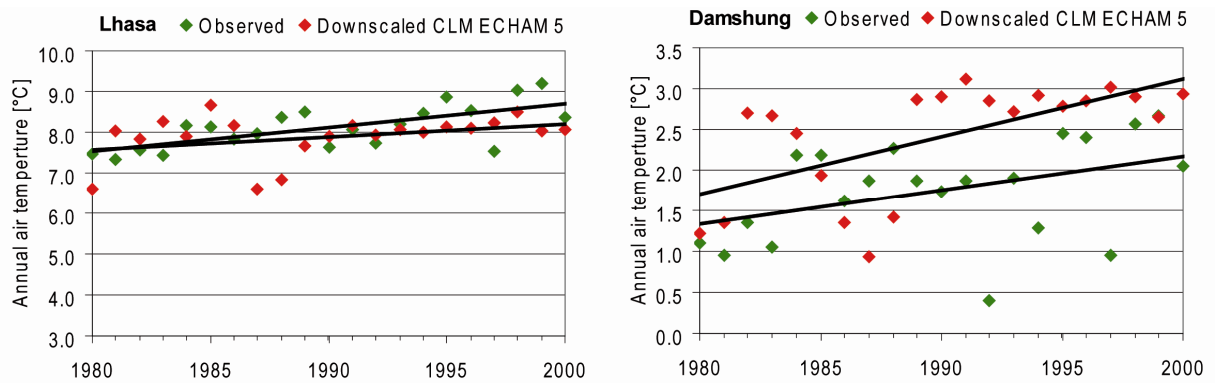


Figure 5.23: Observed and modelled CLM ECHAM 5 trend of annual air temperature at the Lhasa and Damshung stations for 1980-2000.

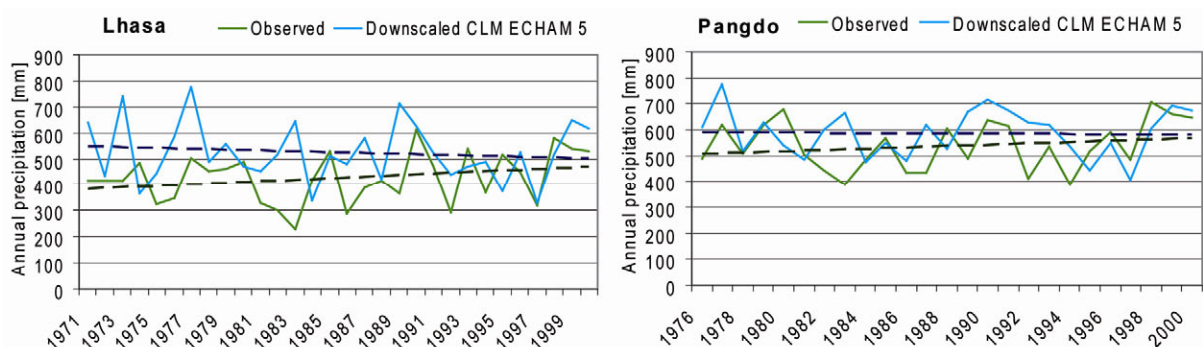


Figure 5.24: Observed and modelled CLM ECHAM 5 trend of the annual precipitation sum at the Lhasa and Pangdo stations for 1970 / 1976-2000.

Overall, the quality of the outputs of the ECHAM 5-driven CLM model runs is better than those of ERA 40-driven simulations, regarding the mean and extreme values and trends in the period of 1971/1980 to 2000. As a result, the climatic conditions are reproduced by the ECHAM 5 CLM data in the Lhasa River basin. This result is consistent with DOBLER AND AHRENS (2010).

The comparison, however, validates only air temperature and precipitation. Since no further meteorological observations are available, the daily and hourly course of the other meteorological variables which determine the energy balance of a glacier, e.g. solar radiation (see section 3.2.5), are analysed consistently by comparing them to statistics from the WMO station in Lhasa (see Appendix 8, U.S. DEPARTMENT OF ENERGY 2010, CRAWLEY ET AL. 1999). Figure 5.25 shows the modelled hourly course of several meteorological variables in Lhasa on randomly chosen January and July days. During January, a clear diurnal variation in the air temperature can be seen, whereas the variation in July is small. Since the winter is characterized by dry conditions without appreciable precipitation or cloudiness, the direct solar radiation input determines the temperature course reproduced by the model outputs. The global radiation input shows similarity to the astronomically possible value, which is in accordance with the observed data and is caused by the clear sky conditions, dry, clean air and high elevation of the Tibetan Plateau. By contrast, the modelled relative humidity fluctuates at around 60 percent in January. Compared to a daily January average of 28 percent of the WMO statistics, it is too high. In July, the monsoon precipitation dominates the weather in Lhasa. Consequently, cloudy and rainy weather causes a solar radiation input similar to January's, because the direct radiation input is minimized. This is in consistency with the statistical values of the WMO station recordings. Relative humidity varies, on average, between 40 and 80 percent in July, and so the modelled values reproduce the July conditions (Figure 5.25). The daily course over a year for a CLM ERA 40 and ECHAM 5 model run in Lhasa is shown in Figure 5.26. The graphs reproduce the characteristics of a dry winter with high solar radiation input, whereas in summer the cloud coverage during the monsoon reduces global radiation. The absolute values are within a realistic range for all variables. The relative humidity is in the range of the mean observed values of about 20 percent in winter. Consequently, the hourly values during the randomly chosen January (Figure 5.25) can be seen as an outlier.

Although there are deviations between the observed and the CLM model output data, as analysed in the previous validation steps, the situation with monsoon precipitation in summer and dry winters is reproduced. Overall, the daily and monthly values are in accordance with the observations, regarding average and extreme values, although the ECHAM 5-driven results are better than the ERA 40 model outputs. The chronology of precipitation is not captured by the CLM ERA 40 run, but the average hourly course is given realistically. Taking into account uncertainties in meteorological measurements, and the fact that the data are climate model outputs with coarse resolution which is then further downscaled by SCALMET, their application seems to provide realistic meteorological conditions for simulating the processes in an hourly resolution as required by the models. Furthermore, the climatic signal is reproduced by the ECHAM 5 model run.

Therefore, the CLM ECHAM 5 can be applied for simulation of future conditions, and the results can be compared to past simulations in order to assess climatic changes. To sum up, the application of the downscaled CLM data as meteorological drivers seems to be appropriate in the Lhasa River basin.

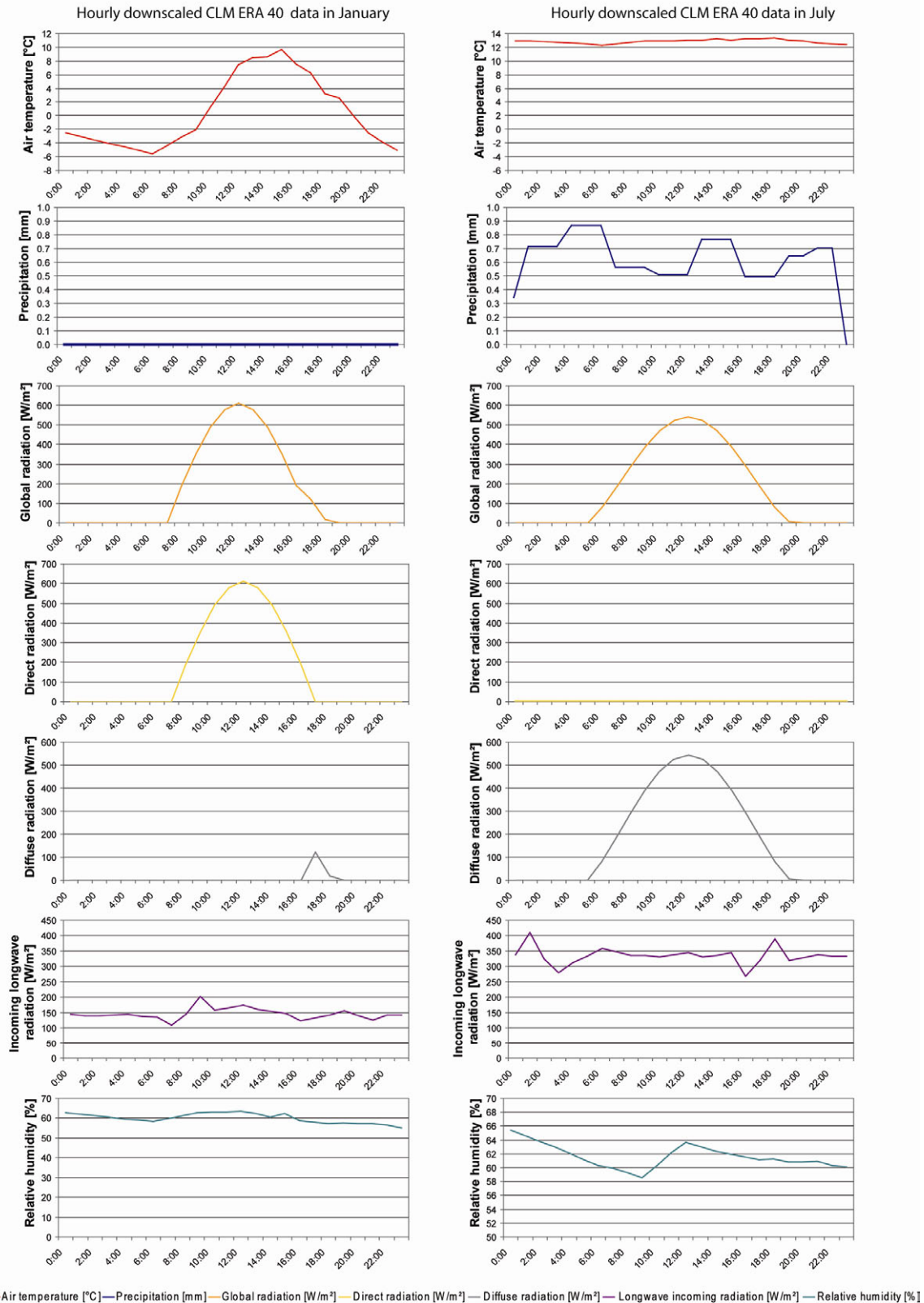


Figure 5.25: Hourly course of downscaled CLM (ERA 40) data in a randomly chosen January (left) and July (right) in Lhasa.

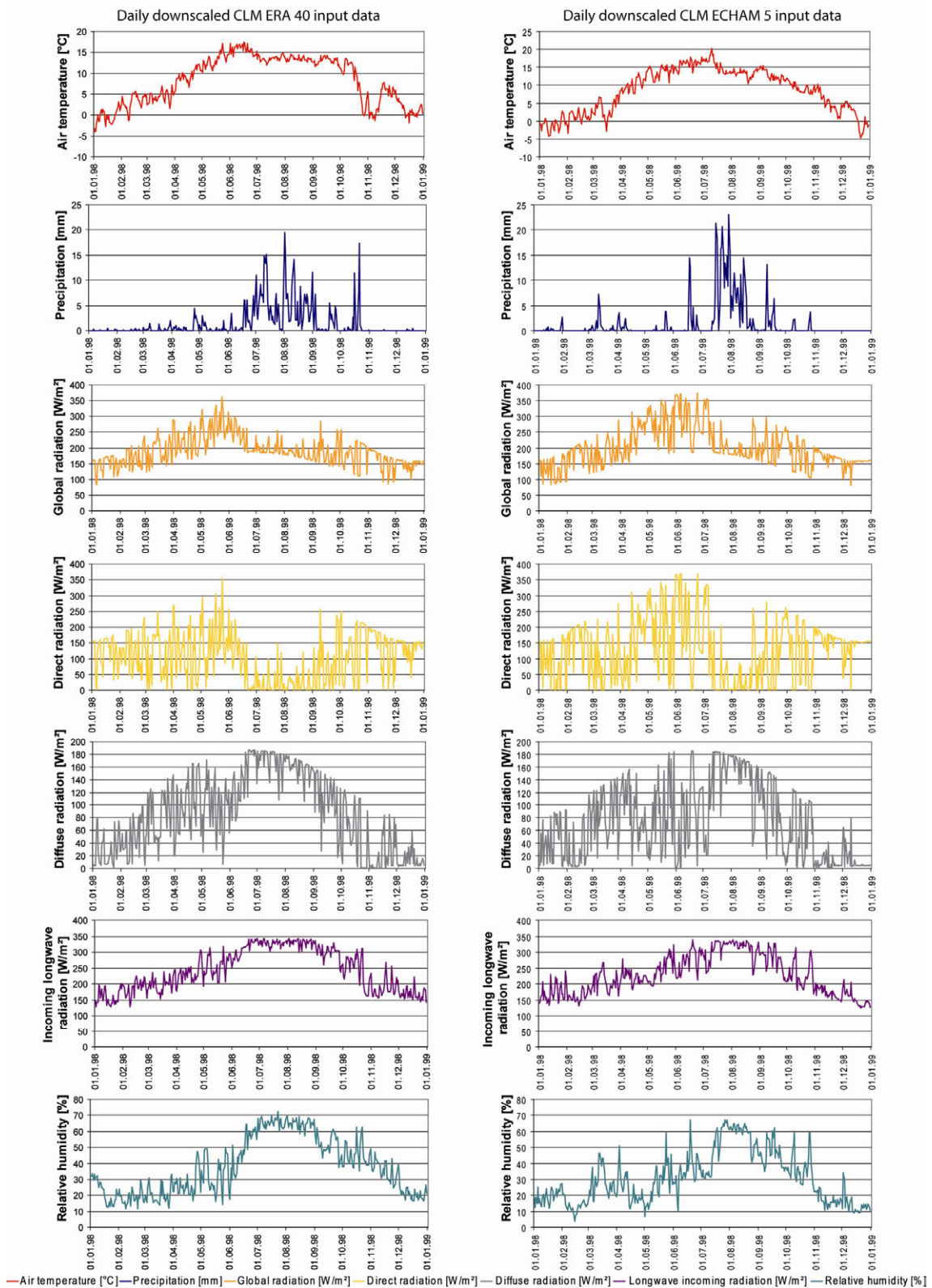


Figure 5.26: Daily course of downscaled CLM ERA 40 (left) and ECHAM 5 (right) data.

The meteorological stations used for the validation are all located in the valleys and do not provide information about the model's performance in the mountains where the glaciers are located. Since no meteorological station recordings are available, the fact that glacier mass balance depends not only on air temperature and precipitation, but also on radiation balance and latent and sensible heat fluxes, conclusions may be drawn about the quality



of the meteorological data in the mountain regions. Moreover, a comparison of simulated and observed runoffs gives evidence of the quality of the precipitation in the catchment. On the assumption that the models capture snow and glacier mass balances and simulate water-related processes using reliable meteorological data as shown above (see section 5.1), the following validation steps for glacier mass balance and runoff also offer feedback on the quality of the meteorological input data.

### 5.3.2 Glacier Mass Balance

Information about glacier changes in Central Asia during recent decades is sparse compared to the information available about Central Europe (UNEP AND WGMS 2008). The available sources describe the general trend of glacier changes on the Tibetan Plateau. Some give statements about different mountain ranges, and only a few glaciers are investigated in detail; for instance, several studies of the glacier Urumqihe S. No. 1 in the Tianshan Mountains exist (UNEP AND WGMS 2008, YAO ET AL. 2004). Unfortunately, these glaciers are located outside the test basin. Thus, conclusions regarding glacier changes in the test site have to be drawn not taking this information into account. Remote sensing data can additionally be applied for determination of the changes in the glacier area.

According to UNEP AND WGMS (2008), glacier retreat was dominant in Central Asia during the 20<sup>th</sup> century, although in the 1960s and 1970s glaciers gained mass and advances were observed. Since the 1980s, the retreat proceeded, and it accelerated in the 1990s. While some glaciers advanced until the 1990s, e.g. in the Kunlun Mountains or in the Tanggula Mountains, a general retreat is recorded thereafter, with only a few exceptions. The mass balance loss is calculated as having been 0.2 to 0.3 m w.e. per year since the 1960s (YAO ET AL. 2004). The mountain range of the Nyainqêntanglha Shan, one of the main glacier areas on the Tibetan Plateau, whose western part includes the main glacier areas along the north-western watershed of the Lhasa River catchment, is often listed separately in glacier studies. YAO ET AL. (2004) quote annual glacier retreat as about 30 to 40 m. The ongoing glacier retreat is documented by the negative mass balances of 0.8 m in 2006 of the Gurenhekou Glacier and 1.6 m of the Zhadang Glacier in the Nyainqêntanglha Mountains near Lhasa (YAO ET AL. 2007). A glacier length retreat of 10 m per year for the Lanong and Zhadang Glacier and of 39 m per year for the Xibu Glacier was observed between 1970 and 2007 according to KANG ET AL. (2007B). A glacier area retreat of 15.4 percent in the region around Lake Nam Co, in the Northern region of the basin, was found for the years 1970 to 2000 (YAO ET AL. 2007). As part of the Brahmatwinn project, a detailed glacier change study for the Lhasa River basin was conducted by KÄÄB ET AL. (2008) and FRAUENFELDER AND KÄÄB (2009). By comparing multi-temporal optical remote sensing data from the Landsat and ASTER sensors with the Chinese Glacier Inventory, they found a total change of +2 to -63 percent in various glacier areas with a decreasing glacier size from 1970 onwards. Using various area-volume relations they estimate a mass balance change of -0.2 to -0.3 m w.e. per year (FRAUENFELDER AND KÄÄB 2009). The data are summarized in the following table, whereas the simulated changes of glacial coverage and the ice water reservoir in the Lhasa River

basin for both meteorological drivers of CLM ERA 40 and CLM ECHAM 5 are listed in Table 5.7.

Table 5.6: Summary of glacier change recordings in Central Asia.

Data source	Region	Period	Mass balance changes [m w.e. / a]	Area changes [%]
UNEP AND WGMS (2008)	Himalayas	1977-1999	-0.4	
	Himalayas	1999-2004	-0.8	
	China	1960-2000		-6
	Tien Shan	20 <sup>th</sup> century		-25 – -35
	Pamirs	20 <sup>th</sup> century		-30 – -35
	Northern Afghanistan	1960-2000		< -50
YAO ET AL. (2004)	Chinese part of High Asia	1960-2000	-0.2 – - 0.3	-5.8 – -10.5
LI ET AL. (2009)	Himalayas	1960-2000		-2.2 – -9.0
FRAUENFELDER AND KÄÄB (2009)	Lhasa River Basin		-0.2 – 0.3	-21
	$A_{\text{glacier}} < 0.1 \text{ km}^2$			-63.1
	$0.1 < A_{\text{glacier}} < 0.5 \text{ km}^2$			-41.1
	$0.5 < A_{\text{glacier}} < 1.0 \text{ km}^2$			-30.5
	$1.0 < A_{\text{glacier}} < 5.0 \text{ km}^2$	1970-2000		-18.5
	$5.0 < A_{\text{glacier}} < 10.0 \text{ km}^2$			-11.2
	$10.0 < A_{\text{glacier}} < 20.0 \text{ km}^2$			-5.8
	$A_{\text{glacier}} > 20 \text{ km}^2$			+1.9
YAO ET AL. (2007)	Area around Nam Co	1970-2000		-15.4

Table 5.7: Simulated changes in glacial coverage and ice water reservoir in the Lhasa River basin from 1970 to 2000 for CLM ERA 40- and CLM ECHAM 5-driven model runs.

Global Climate Model	Glacier area [km <sup>2</sup> ]			Total glacier ice water equivalent [m]			Ice water reservoir [mm/km <sup>2</sup> ]		
	1970	2000	$\Delta$ [%]	1970	2000	$\Delta$ per a	1970	2000	$\Delta$ [%]
ERA 40	666	475	-29	34001	22027	-0.6	1040	674	-35
ECHAM 5	666	532	-20	34001	27280	-0.3	1040	834	-20

For the past 30 years, a decrease of 20 (CLM ECHAM 5) and 29 percent (CLM ERA 40) of the glacier area is simulated. This is within the range of the retreat of the studies introduced here (see Table 5.6). For the ice-water reservoir, an average mass loss of 0.3 m (ECHAM 5) and 0.6 m w.e. per year (ERA 40) is modelled. In comparison with the

results for this area (see Table 5.6), the ECHAM 5 mass loss is consistent, whereas in the ERA 40 run the decrease is overestimated. The daily developments of the glacier area and the ice water reservoir are shown in Figure 5.27 for the ERA 40 and the ECHAM 5 driven model runs. At the beginning of the 1970s, glacier area slightly increased in both model runs, although a small decrease in ice volume is simulated. Due to the modelling of snow-to-ice metamorphosis after one year, the glacier area increases at the beginning of the 1970s, because the snow cover outlasts the metamorphosis period. This development is consistent with the observations of glacier increase around the 1960s and 1970s (YAO ET AL. 2004). The overall ice water reservoir nonetheless shrinks slightly, due to ice-melt in other parts of the catchment where the snow cover melts away. Afterwards, a retreat is modelled for both the ice volume and the glacier area, which is stronger in the ERA 40-driven model run than in the ECHAM 5-driven one. The observed acceleration of the retreat during the 1990s (YAO ET AL. 2004) is not reproduced by the simulation. Reasons for the differences from observations can be seen in the deviations between observed and modelled meteorological conditions. As described above, the observed temperatures and precipitation sums are not captured by the CLM ERA 40 and ECHAM 5 model outputs for all years, and so the exact time series is not reproduced by the model. The glacier retreat for the climate period on average is nonetheless reproduced, particularly by the model run driven by ECHAM 5.

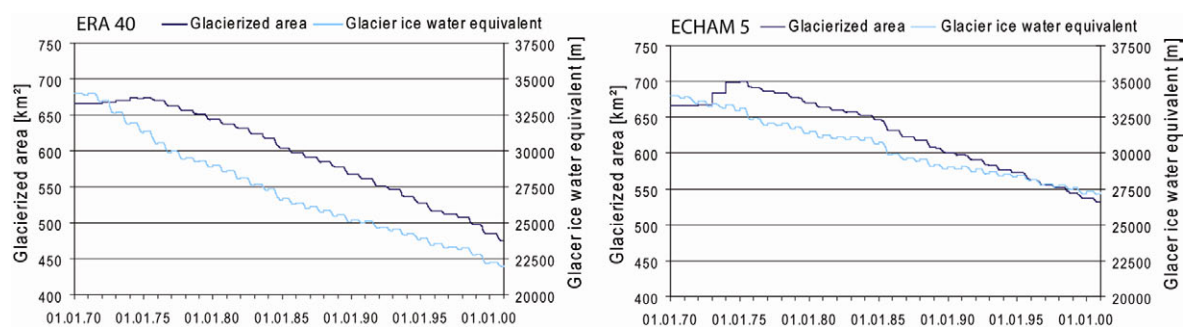


Figure 5.27: Simulated total ice water reservoir and glacier area in the Lhasa River basin from 1970 to 2000 using CLM ERA 40 (left) and ECHAM 5 (right) data as meteorological drivers.

The comparison of the accumulation series from the Nyainqêntanglha Mountain Peak at 5,850 m a.s.l., deduced from an ice core in the Lanong Glacier and published by KANG ET AL. (2007A), and the modelled series confirms differences between observed and simulated annual mass balance values. On the assumption that the metamorphosis from snow to ice occurs within one year due to the summer precipitation and the simultaneous melting phase, KANG ET AL. (2007A) reconstructed a period with substandard annual accumulation during the 1970s and an increase from the late 1980s on, as can be seen in Figure 5.28a. In the simulated development of the snow water equivalent without considering the ice reservoir, this increase is not reproduced (Figure 5.28b). The simulated time series of the ice and snow water equivalent (Figure 5.28d) at this elevation level are in accordance with the substandard accumulation of the 1970s and the subsequent increasing mass balance, although the accumulation slightly declines again, in contrast to the ice core data. The increase in the ice reservoir during the late 1970s and the beginning of the 1980s, with the minimum values in between, is captured by the



simulation. Since KANG ET AL. (2007A) conclude that the accumulation is strongly correlated to the precipitation pattern of the region, although the deduced increase in the 1990s is larger than that observed at meteorological stations in the Lhasa River basin, the annual CLM ERA 40 precipitation and temperature from 1971 to 2000 is shown in Figure 5.28c. No increase has been determined since the mid 1980s. Consequently, the precipitation trend is in accordance with that of snow accumulation. However, the precipitation trend in the observed data (see Figure 5.24) shows a slight increase.

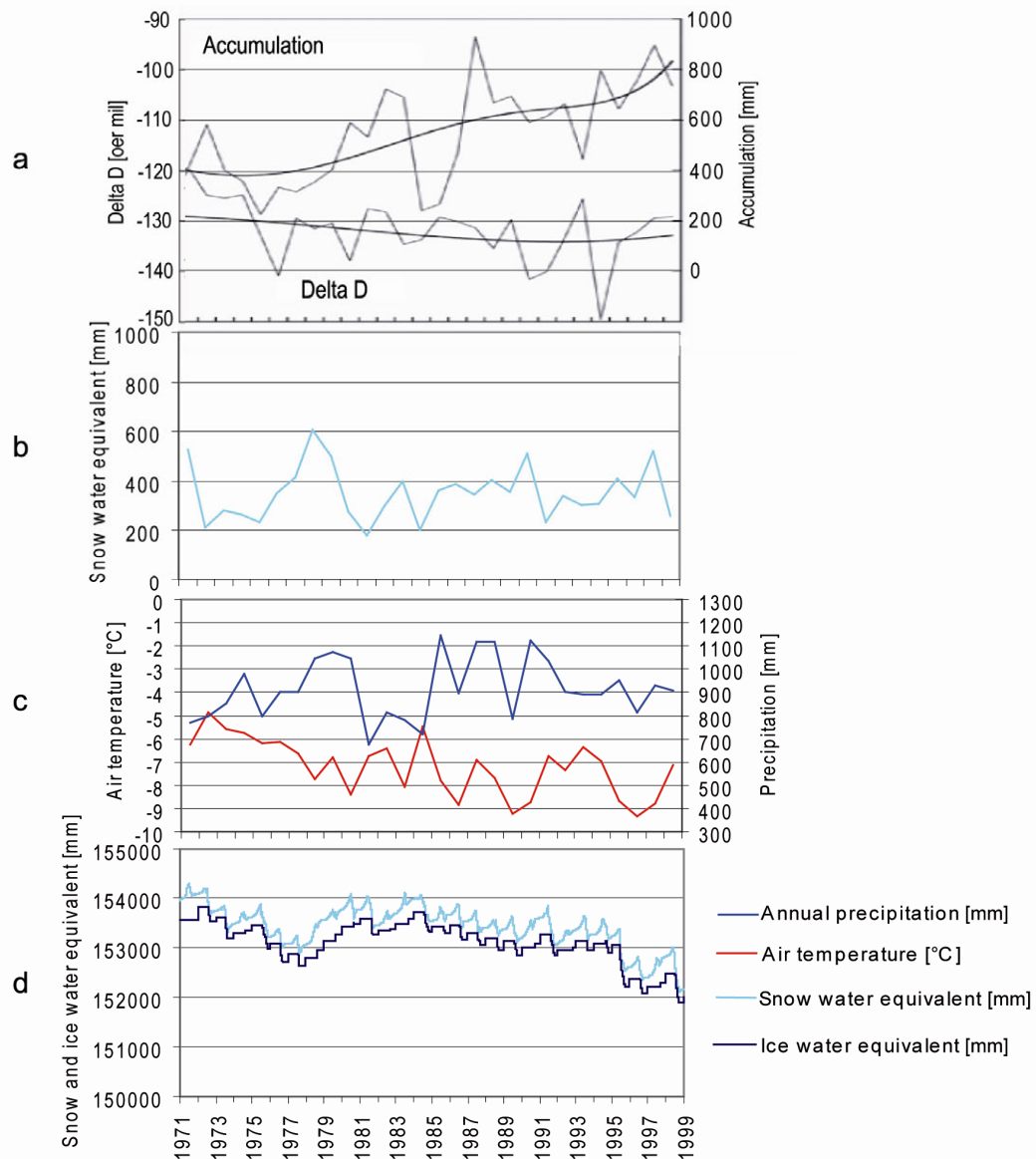


Figure 5.28: Comparison of derived accumulation on the Lanong Glacier (KANG ET AL. 2007A)(a) with simulations of snow water equivalent (b), air temperature and precipitation (c) and snow and ice water equivalent (d).

The reasons for the deviations between the simulation and the ice-core values are manifold. In addition the uncertainties in the ice core data, the assumption of the snow to ice metamorphosis over one year according to KANG ET AL. (2007A) seems to be very general. No annual variance in weather conditions are considered thereby. Furthermore, processes such as wind drift and small-scale shading of the surrounding mountains are not considered in the models, although these processes can add snow to the

accumulation. Since the annual accumulation is close to the precipitation sum, and therefore larger than the modelled one, this might be the case here. Consequently, the snow-melt which, according to KANG ET AL. (2007A), occurs during summer, causes snow cover melt during some years in the model. This is not assumed for the ice-core. Nevertheless, the simulated mass balance values are consistent with the precipitation values. Accordingly, the relevant processes for mass balance simulation are reproduced, and the deviations can be traced back to differences between observed and CLM ERA 40 meteorological conditions.

As previously shown, the climate signal of the past 30 years is reproduced for loss of glacier area as well as for the ice reservoir, at least in the CLM ECHAM 5 driven model runs. The general observations, lacking detailed measured mass balance series in the Lhasa River basin, only enable a general comparison of the trends on the Tibetan Plateau: no confirmation of a similar evolution of the glaciers in the test site can be given. Nevertheless, taking into account the coarse resolution of the meteorological CLM data and their uncertainties, the performance of the model setup in this remote region seems to reproduce the glacier dynamics.

### 5.3.3 River Runoff

In order to validate the simulated runoff in the Lhasa River basin, two models runs, driven by downscaled CLM ERA 40 and CLM ECHAM 5 meteorological data, were carried out from 1.1.1970 to 31.12.2000, on a temporal resolution of one hour. Due to PROMET's spin up, the first model year is not considered in the validation. The model results are compared to runoff observations, which are provided at four gauging stations in the Lhasa River catchment (see section 2.3) for various time periods, as listed in Table 5.8, by ITP (2008) in BRAHMATWINN (2006-2009).

*Table 5.8: Runoff data availability at the four gauging stations in the Lhasa River catchment (based on: BRAHMATWINN 2006-2009, ITP 2008).*

Gauging station	Time period	
	Monthly runoff data	Daily runoff data
Lhasa	Jan 1971 – Dec 2000	1.1.1991 – 30.12.2000, gap: Feb. 1991
Tangga	Jan 1971 – Dec 2000	1.1.1991 – 31.12.2000
Pangdo	Jan 1976 – Dec 2000	1.1.1991 – 30.12.2000, gap: 1996
Yangbajing	Jan 1979 – Dec 2000	–

First, the modelled monthly runoff is compared to the observed data at the four gauging stations. The coefficient of determination  $R^2$  and the NSC are calculated for ERA 40-driven model runs for the period of 1971 to 2000, as well as for the three decades of the same period (Table 5.9). Whereas between 78 and 85 percent of the variance in the runoff data can be explained by the model for all periods, the NSC varies between 0.14 and 0.61 for the gauges in Lhasa, Pangdo and Tangga. However, the coefficient increases in the last of the three decades, in accordance with the accuracy of the modelled precipitation sum. The quality criteria for the modelled precipitation are listed correspondingly in Table 5.9. Here, the recordings of the Lhasa, Pangdo and Tangga

stations are assumed to represent the precipitation of the sub-basins, because no more station data are available for these areas. As the precipitation data have been more consistent with station recordings since 1996, the period from 1996 to 2000 is also considered. In this period, both maximum  $R^2$  and NSCs, with values from 0.85 to 0.89, are reached.

Table 5.9: Quality criteria for modelled monthly runoff  $R$  and precipitation data  $P$ , driven by CLM ERA 40 meteorological data.

Period	Criterion	Lhasa		Pangdo		Tangga		Yangbajing	
		R	P	R	P	R	P	R	P
1971 – 1980	$R^2$	0.84	0.72	-	-	0.85	0.75	-	-
	NSC	0.22	0.46	-	-	0.47	0.71	-	-
1981 – 1990	$R^2$	0.79	0.61	0.79	0.64	0.79	0.69	0.85	-
	NSC	0.14	0.17	0.22	0.51	0.33	0.69	-2.15	-
1991 – 2000	$R^2$	0.79	0.71	0.78	0.75	0.80	0.76	0.85	-
	NSC	0.49	0.50	0.56	0.73	0.61	0.76	-2.59	-
1996 – 2000	$R^2$	0.88	0.78	0.87	0.79	0.89	0.78	0.88	-
	NSC	0.85	0.70	0.86	0.79	0.88	0.77	-1.87	-
1971 – 2000	$R^2$	0.80	0.68	0.78	0.72	0.81	0.73	0.85	-
	NSC	0.31	0.39	0.39	0.66	0.48	0.72	-4.70	-

The results for the gauge of the smallest sub-catchment, Yangbajing, differ from those of the other stations. Its  $R^2$  is within the range of the three other gauges, varying between 0.85 and 0.88, but the NSC remains below zero. The development of the monthly observed and modelled runoff for the Lhasa and Yangbajing gauges in Figure 5.29 shows the reason for the negative NSC. The runoff course is in fact reproduced for both gauges, but the amount of runoff is clearly overestimated by the Yangbajing model. However the absolute deviations are not larger than for the Lhasa gauge, but the amount of runoff is many times smaller. Accordingly, this results in a low NSC at Yangbajing. There is a strong correlation, also shown for the other gauges (Appendix 9), between the quality of precipitation and runoff. Although no precipitation recordings are available for that part of the test basin, the conclusion can be drawn that the reason for this deviation is overestimation of precipitation by the CLM.

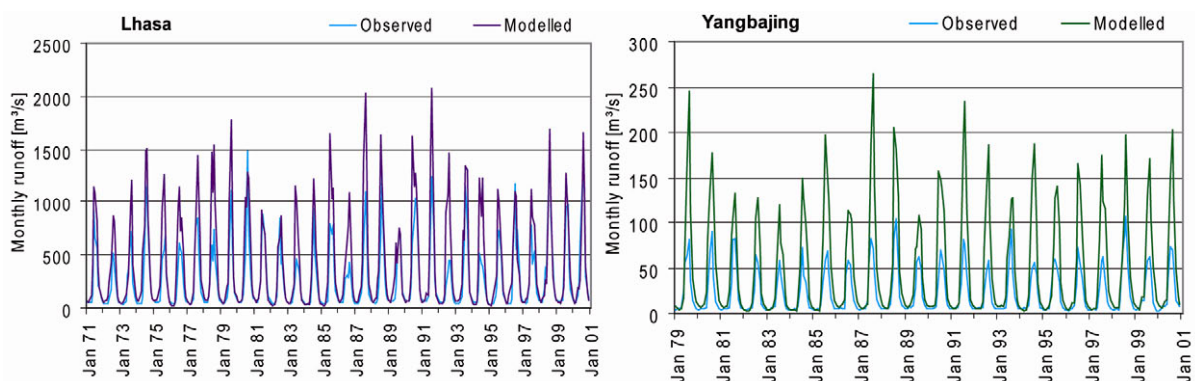


Figure 5.29: Monthly modelled and observed runoff at the Lhasa and Yangbajing gauges from 1971-2000 (ERA 40).

The comparison of average runoff and annual precipitation during the climate period from 1971 to 2000 with the observed data (Table 5.10) confirms the influence of precipitation. In all cases, both runoff and precipitation are overestimated for the past 30 years, whereas the averages for 1996 to 2000 show only slight deviations which can be traced back to precipitation. In this comparison, the ECHAM 5 model runs are also taken into account, as the climate model is intended to capture the values of the climate period rather than single years. The deviations are smaller for the runoff and for the precipitation sum than in the ERA 40 model runs, which is in accordance with the smaller deviations in the glacier changes (see section 5.3.2). At the Yangbajing gauge, the largest overestimation, of 124 (ERA 40) or 84 percent (ECHAM 5), is simulated. The uncertainties in precipitation are also the reason for the deviations in the simulated interannual variability in runoff, as Figure 5.30 shows for all four gauges.

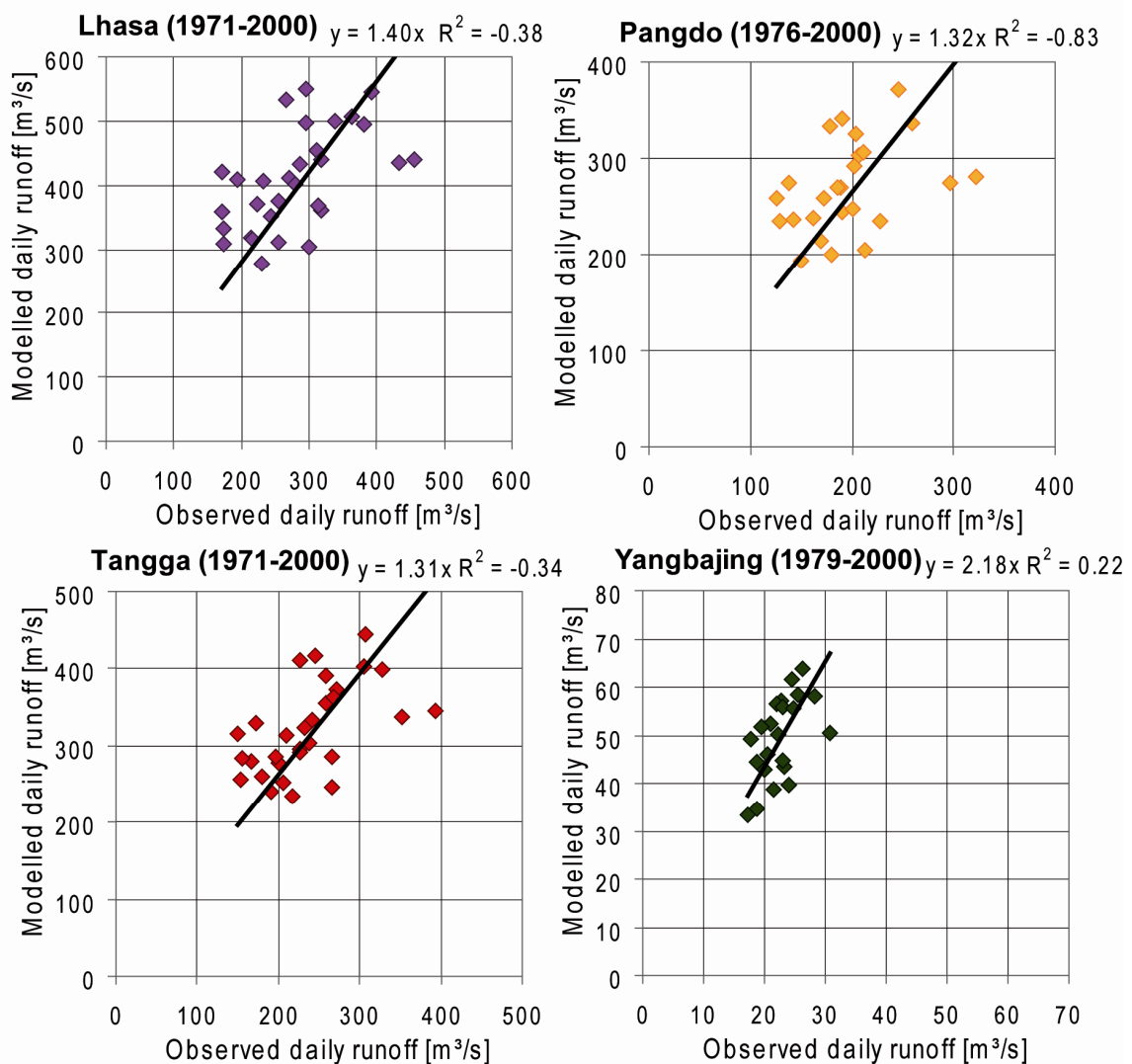


Figure 5.30: Comparison of observed and modelled annual runoff in Lhasa, Pangdo, Tangga and Yangbajing.

Table 5.10: Mean annual runoff [ $m^3/s$ ] and precipitation [ $mm$ ] for ERA40- and ECHAM 5-driven model runs at the four gauges for the climate period from 1971-2000.

Period	Mean	Lhasa		Pangdo		Tangga		Yangbajing	
		R	P	R	P	R	P	R	P
1971 – 2000	Observed	279	426	196	538	237	517	23	-
	ERA 40	408	584	270	647	321	561	50	-
	$\Delta$ ERA 40 [%]	+46	+37	+37	+20	+36	+8	+124	-
	ECHAM 5	351	524	233	587	278	513	41	-
	$\Delta$ ECHAM 5 [%]	+26	+23	+19	+9	+17	-1	+84	-
1996 – 2000	Observed	360	484	248	617	295	598	23	-
	ERA 40	400	572	255	609	311	547	51	-
	$\Delta$ ERA 40 [%]	+11	+18	+3	-1	+5	-9	+117	-
	ECHAM 5	351	527	234	586	282	500	42	-
	$\Delta$ ECHAM 5 [%]	-2	+9	-5	-5	-5	-17	+83	-

Nevertheless, the runoff trend during the climate period should be reproduced by the model. This, as with the precipitation trends (see Figure 5.16), is not the case. Whereas the increase in runoff for the ERA 40 run is slightly underestimated, no trend is simulated for the ECHAM 5 run, as shown in Figure 5.31 and Appendix 10. Again, the enhanced agreement in the amount of runoff can be discerned for the years 1996 to 2000.

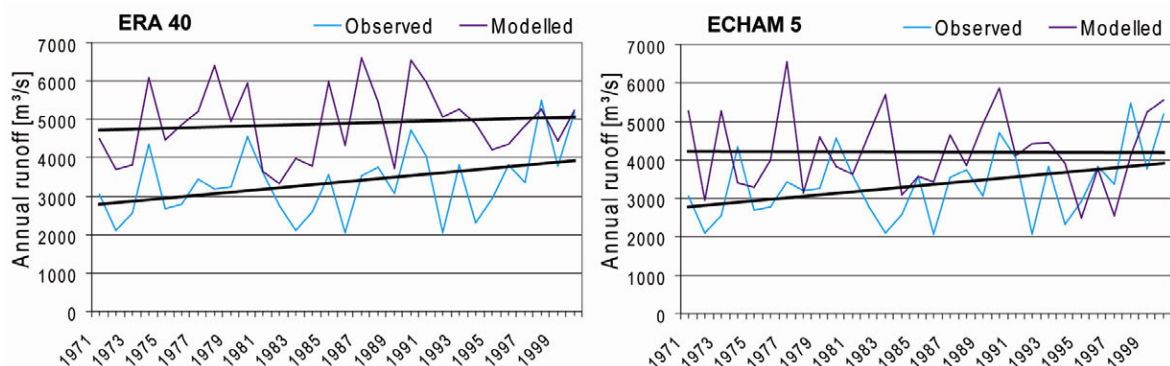


Figure 5.31: Annual modelled and observed runoff at the Lhasa gauges from 1971-2000 for ERA 40 (left) and ECHAM 5 (right) meteorological data.

Next, daily runoff measurements are compared with the modelled discharges at the Lhasa, Pangdo and Tangga gauges, considering the CLM ERA 40 data. Since the CLM precipitation best fits the observations from 1996 to 2000 as described above, validation of the daily values is focused on this period. Figure 5.32 shows the comparison for daily runoff values at the three gauges mentioned.

About 72 percent of the variance of the streamflow data set can be explained by the model results for all three gauges, according to the coefficient of determination, which was calculated for a linear regression forced through the origin. Small biases of 7 and 8 percent show slight underestimation of the runoff for the five years in Tangga and Pangdo, whereas no bias is calculated for Lhasa.

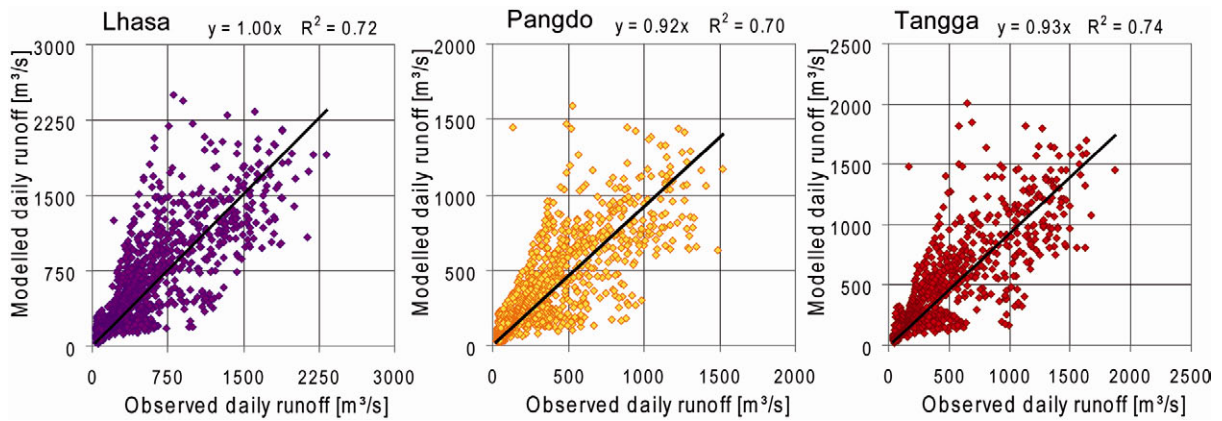


Figure 5.32: Comparison of daily modelled and observed runoff at the Lhasa, Pangdo and Tangga gauges from 1996-2000 (CLM ERA 40).

The NSCs, listed in Table 5.11, vary between 0.67 and 0.73 at the three gauges for the period from 1996 to 2000. The results seem contradictory to the analysis results presented earlier where daily precipitation values are not reproduced by the CLM model output data, however, the modelled precipitation fits well to the observed one in the chosen period. The high correlation can therefore be explained. In considering the whole decade from 1991 to 2000, an overestimation is assessed at all gauging stations, as shown in Table 5.11, in Figure 5.33 and in Appendix 11 and Appendix 12.

Table 5.11: Quality criteria for modelled daily runoff, driven by CLM ERA 40 meteorological data.

Period	Criterion	Lhasa	Pangdo	Tangga
1996 – 2000	R <sup>2</sup>	0.73	0.72	0.75
	NSC	0.67	0.70	0.73
1991 – 2000	R <sup>2</sup>	0.67	0.65	0.67
	NSC	0.34	0.41	0.44

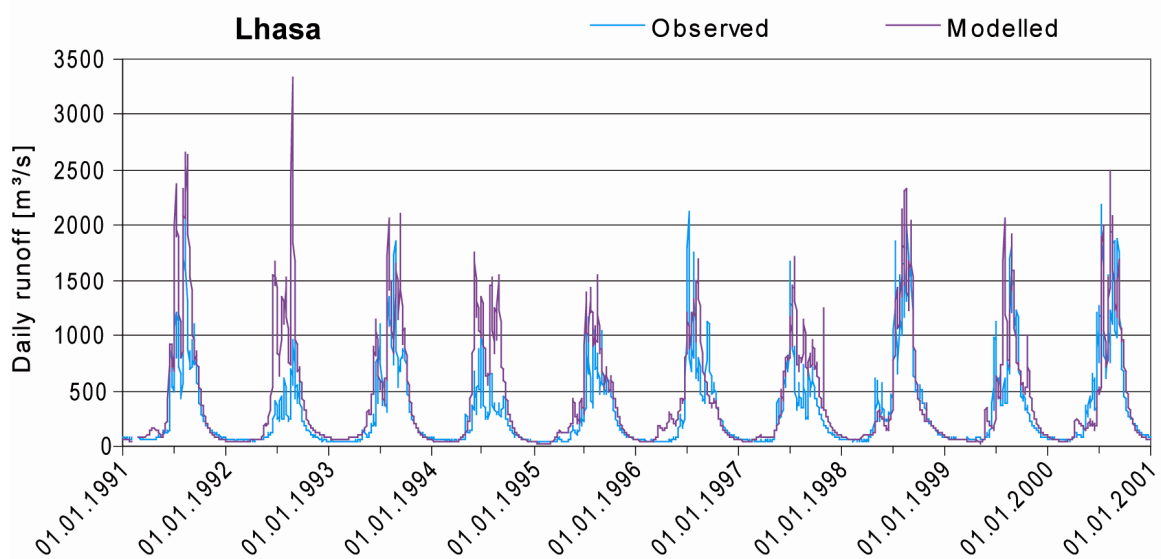


Figure 5.33: Development of daily observed and modelled runoff at the gauge in Lhasa from 1991 to 2000 (CLM ERA 40).



In order to further clarify the runoff development, the modelled and observed river discharge is illustrated in Figure 5.34 for the year 1997, where the precipitation is largely overestimated, and for the year 1998 which has, as analysed above, high correlation (see Figures 5.19, 5.20 and 5.21). While the observed course is reproduced by the runoff, it is overestimated by 43 percent for 1997, whereas a slight underestimation of 4 percent is simulated for 1998. Furthermore, the development of the runoff in combination with precipitation shows a general conformity in the runoff with the peaks during the monsoon, the decline afterwards and finally the low flow during winter. Nevertheless, there are disparities of some days between the simulations and the observations, which can be traced back to the deviations in the precipitation pattern. As this is only the precipitation at the Lhasa station, differences from the areal rain- and snowfall are possible. The precipitation deviations are in any case consistent with the runoff deviations. The peaks during the summer of 1997 can be particularly clearly seen. The missing precipitation of May 1998 causes an underestimation in the simulated discharge. The outstanding peak at the end of October 1997 can be traced back to the occurrence of unobserved precipitation. The level of the runoff peak suggests stronger deviations in other parts of the catchment. Additional precipitation during wintertime does not cause direct output in the streamflow, because it is stored as snow. The correlation between runoff and precipitation is also reproduced for the other years.

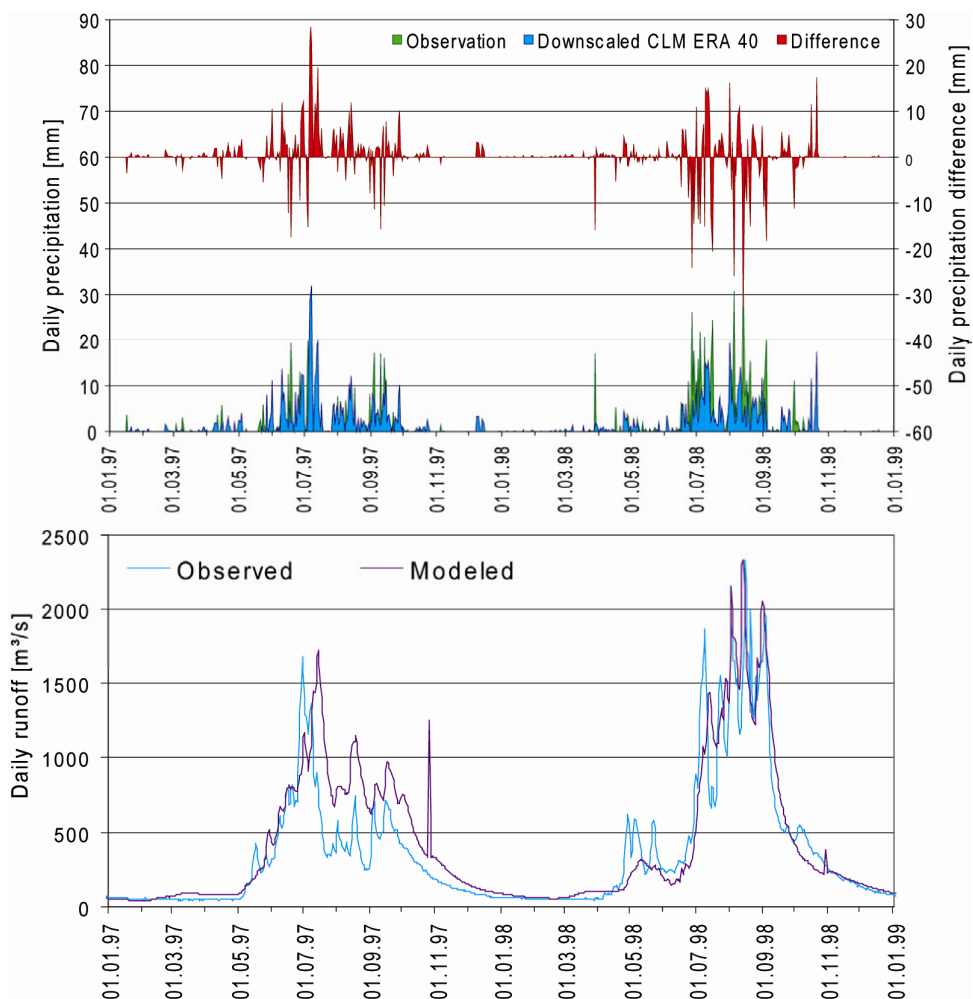


Figure 5.34: Daily modelled and observed runoff at the Lhasa gauges for 1997 and 1998 (ERA 40).

To sum up, the validation of the runoff proves agreement between the modelled and observed values where the precipitation data are similar to observed data. No exact daily runoff can therefore be simulated using climate model output data as meteorological drivers. Differences may also be caused by lack of consideration of lakes, water reservoir management and water withdrawal, e.g. for irrigation. The amount is, however, small according to DAJUN (1995). Finally, Manning's roughness value is assumed to be constant for all water levels. Flood plains are also not included.

The validation nevertheless showed that the approach can reproduce glacier and hydrological dynamics in an appropriate temporal as well as spatial resolution. Taking into account uncertainties in input and validation data due to missing observations, the challenge of coupling between different scales and the subscale consideration of glaciers up to the coarse climate model output of the CLM, the quality of the results is adequate.



## 6 Model Results – The Impact of Future Climate Change

The model framework captures the relevant processes to simulate the influence of glacier meltwater release on runoff for past and present climatic conditions, as presented in the previous chapter. As the models are physically based, use universal parameters and are not calibrated using measured discharges, they are applicable to future climatic conditions with appropriate performance. In order to determine the impact of future climate change on the glaciers and their meltwater release, a number of future climate scenarios are analysed. In the following chapter, the effect on runoff is identified. The future climate scenarios are introduced in the following section; afterwards, the results of the scenario simulations are presented.

### 6.1 The IPCC Future Climate Scenarios

Global concentrations of greenhouse gases have been increasing due to human activities since 1750, and clearly already exceed pre-industrial values today. As a result, the global surface temperature has been, and is still, rising, and the positive trend will continue in the future. The magnitude of the increase depends on human activities and natural factors, such as future greenhouse gases emissions, solar activity, land surface properties and others. The INTERGOVERNMENTAL PANEL ON CLIMATE CHANGE (IPCC) (2007A, B) distinguishes between four different emission scenario families resulting from alternative developments in demography, economy and technology until the year 2100 in the IPCC Special Report on Emission Scenarios (SRES) (NAKIĆENOVIĆ AND SWART 2000). A large proportion of the uncertainties in future emissions is covered. The scenario families are characterized as follows:

Scenario family A1 combines the rapid introduction of new, more efficient, technologies with fast economic growth. Until the mid-century, the population will increase and then decline. The technology changes in the energy system are divided into three groups; fossil intensive (A1FI), non-fossil energy sources (A1T), and a balance across all sources (A1B). A heterogeneous world with a continuously growing population and a regionally oriented economic development is assumed by scenario A2. The technological changes are slower than in the other scenarios. Scenario B1 supposes a convergent world with a population peak in the mid-century (similar to A1), combined with rapid changes in economy and the introduction of clean, resource-efficient technologies. While B1 focuses on global solutions, the B2 scenarios assume local solutions to economic, social and environmental sustainability. Continuous global population growth and an intermediate economic development with less rapid and more diverse technologies than in B1 and A1 go together with an orientation towards environmental protection and social equity (NAKIĆENOVIĆ AND SWART 2000).

As a result of the different storylines, a range of increasing future greenhouse gas concentrations is assumed. Subsequently, surface temperature increase varies between scenarios. The development of the greenhouse gases from 2000 to 2100, including carbon dioxide, methane, nitrous oxide and other important gases, is illustrated for the various scenarios on the left in Figure 6.1, together with the 80<sup>th</sup> percentile and the full

range of scenarios published since the SRES report. The development assumes no additional climate policies. On the right, the development of the global surface warming with the standard deviation range of the individual models is shown. The likely ranges for the scenarios are symbolized as bars on the side, and the orange line shows the simulated temperature increase assuming that all radiative forcing agents were constant at year 2000 values (IPCC 2007A, B). Table 6.1 summarizes the projected global averages of the temperature changes between 2090 and 2099, in comparison to those of 1980 to 1999.

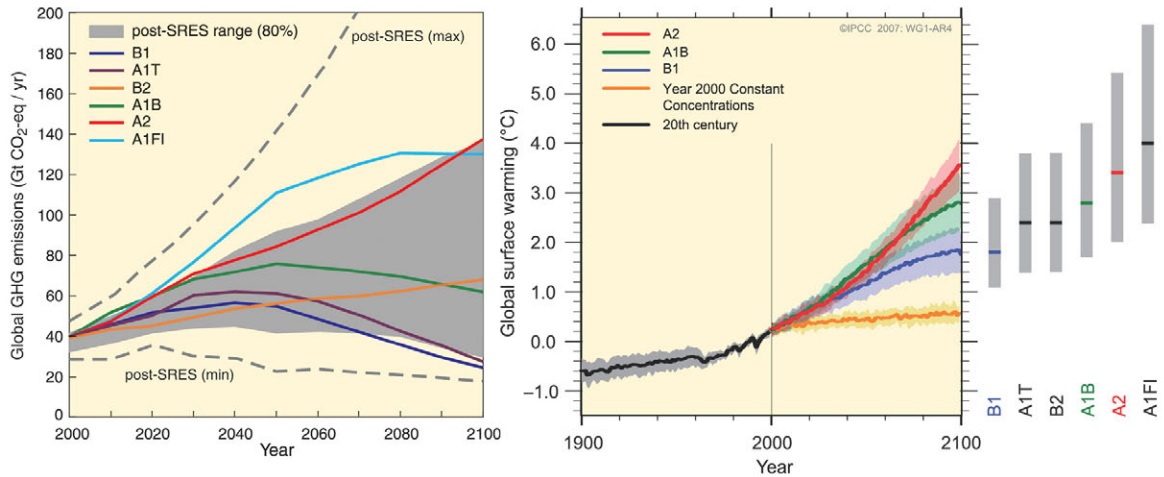


Figure 6.1: The IPCC SRES emission scenarios (left) and the development of global surface warming with uncertainty ranges (right) (IPCC 2007A, p.44 and IPCC 2007B, p. 14).

Table 6.1: Projected global temperature changes and their likely range of the various scenarios from 2090-2099 relative to 1980-1999 (data source: IPCC 2007B).

Scenario	Best estimate temperature change [°C]	Likely range of temperature change [°C]
Constant Year 2000 concentrations	0.6	0.3 - 0.9
A1B	2.8	1.7 – 4.4
A1FI	4.0	2.4 – 6.4
A1T	2.4	1.4 – 3.8
A2	3.4	2.0 – 5.4
B1	1.8	1.1 – 2.9
B2	2.4	1.4 – 3.8

In order to obtain a range of likely climate change scenarios, the IPCC SRES scenarios A1B, A2 and B1 were chosen for the future simulations. The Constant Year 2000 concentration scenario offers the option of analysing a possible future development without including further increasing greenhouse gas emissions, and so was also applied and is referred to as CON. The analysis of spatial changes focuses on the A1B scenario, because its development is assumed to be very likely, due to mid-line economic growth and subsequent greenhouse gas emissions. The results of the B1 scenario are also discussed in detail, to offer an overview of possible future changes for a more moderate

temperature increase in contrast to the A1B scenario. The spatial distribution of the results for the A2 and CON run are illustrated in the appendix.

Downscaled CLM ECHAM 5 model outputs were used as meteorological drivers. Consequently, to assess changes in comparison to the past, the CLM ECHAM 5-driven simulation results were used.

## 6.2 Future Climatic Conditions in the Lhasa River Basin from 2001 to 2080

In this section, the future climatic conditions in the Lhasa River basin according to the different IPCC scenario from 2001 to 2080 are described. The mean annual air temperature, the precipitation sum and the global radiation are analysed first, and then seasonal changes are investigated. In order to derive absolute changes, the mean values of the past climate period from 1971 to 2000 are compared to those for the future periods of 2011 to 2040 and 2051 to 2080. The trend-to-noise ratio  $T/N$  gives evidence about the trend, considering the absolute *trend* between the beginning and the end of the time periods and the standard deviations  $\sigma$  (Eq. 6.1).

$$T / N = \frac{trend}{\sigma} \quad (Eq. 6.1)$$

Because normal distribution of meteorological data is not given in most cases, a trend analysis based on MANN (1945) and KENDALL (1970) was also applied. This test enables the assessment of the significance of a trend without presuming normal data distribution in valuating a relative increase or decrease of the series. The test statistic  $Q$  is calculated as shown in Eq. 6.2 for more than 10 values, taking into account the quantity of values  $n$ , the series elements  $a_j$  and  $a_k$  ( $j > k$ ), the quantity of data values  $t_p$  in the  $p^{th}$  group and the quantity of tied values  $q$ :

$$Q = \frac{\sum_{k=1}^{n-1} \sum_{j=k+1}^n sgn(a_j - a_k)}{\frac{1}{18} \left[ n(n-1)(2n+5) - \sum_{p=1}^q t_p(t_p-1)(2t_p+5) \right]} \quad (Eq. 6.2)$$

The level of significance  $\alpha$  is allocated to the various values of  $Q$ , as listed in Table 6.2 (RAPP AND SCHÖNWIESE 1995). For the Mann-Kendall trend test, the excel template MAKESENS by SALMI ET AL. (2002) was applied in this study.

Table 6.2: Significance levels  $\alpha$  of the different Mann-Kendall trend values of  $Q$  (RAPP AND SCHÖNWIESE (1995), p. 62, modified).

<b>Q</b>	<b><math>\alpha</math></b>
> 1.645	< 0.1
> 1.960	< 0.05
> 2.576	< 0.01
> 3.290	< 0.001

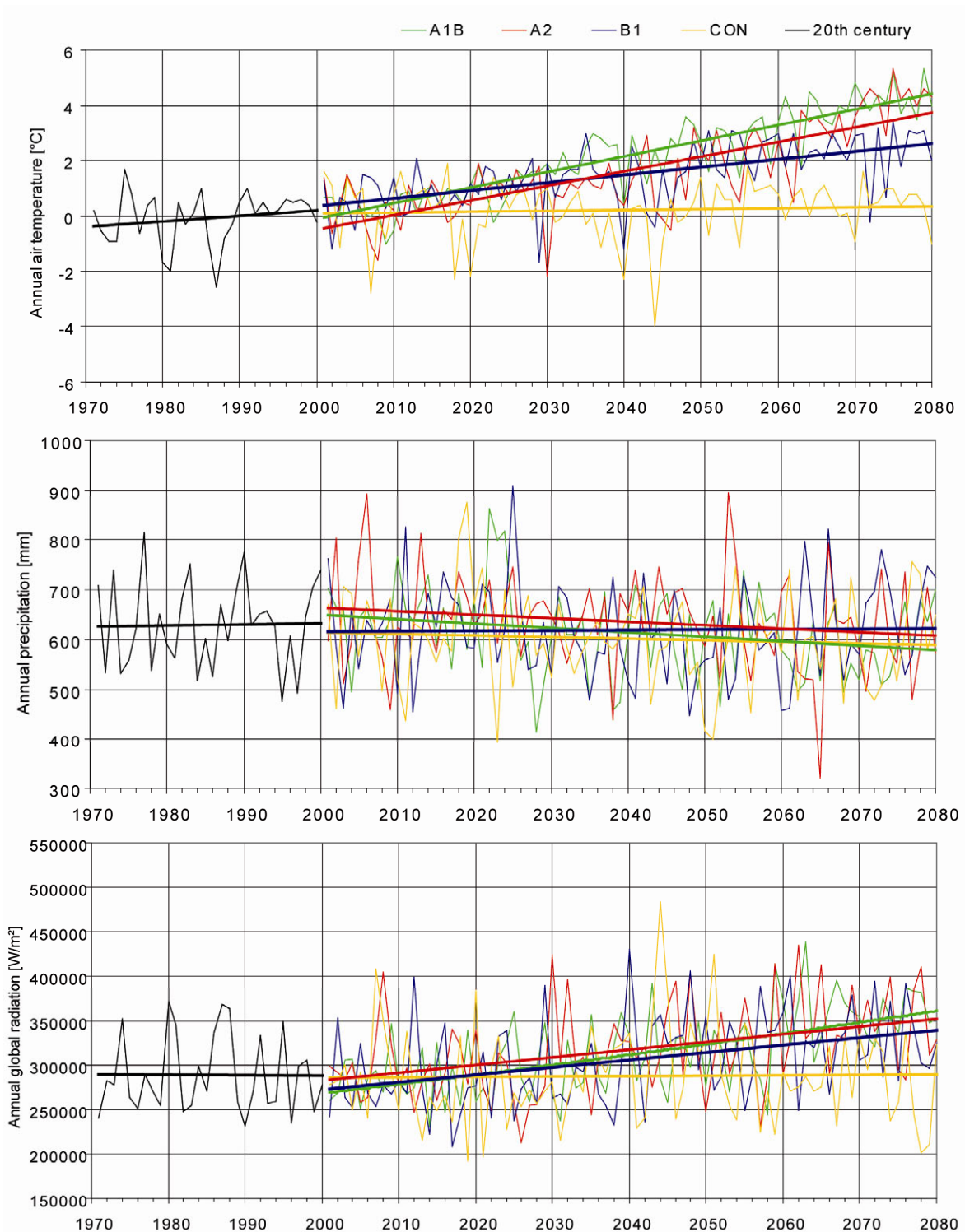


Figure 6.2: The development of annual air temperature, precipitation sum and global radiation in the Lhasa River catchment from 1971 to 2080 according to the downscaled CLM ECHAM 5 IPCC SRES scenarios.

Figure 6.2 shows the annual linear trends of mean air temperature, precipitation, and global radiation in the Lhasa River basin from 1971 to 2080 according to the downscaled CLM ECHAM 5 model output. An average air temperature of  $-0.1^{\circ}\text{C}$  was simulated for the test site for the earlier period, with an absolute increase of  $0.7\text{ K}$  at a level of significance of  $0.05$ . The positive trend continues in the scenarios A1B (green), A2 (red) and B1 (blue), similar to the global trends as shown in Figure 6.1. The graph ends in the year 2080, and

so the increase in the A1B scenario is strongest, with 4.6 K, in contrast to the global trend to 2100. The air temperature of the A2 scenario does not exceed the A1B values until the 2070s, whereas the rise of the B1 air temperature slows down after 2060, with an absolute increase of 2.4 K. In the period before 2060, the increase in air temperature in the three scenarios is relatively similar. According to the Mann-Kendall trend test, the positive trend of the temperature development is significant on the 0.001 level for all three scenarios (see Appendix 13). By contrast, the CON scenario (yellow) has an exceptional position with no increases in greenhouse gas emissions, as described above. Consequently, no significant trend can be analyzed. However, an absolute increase of 0.4 K is assessed for the future period. The global radiation input develops parallel to the air temperature at a confidence interval of 0.95 in the future. For the past, the development of the radiation differs from that of air temperature, and no trend can be assessed. The four scenarios modelled opposite trends for the annual precipitation sum. While the absolute trend is almost constant for the past and the B1 scenario run, a decrease is simulated for A1B, A2 and CON. However, the annual trend is only significant for the A1B scenario at a level of 0.05. For the other scenario runs, the standard deviation exceeds the simulated changes, and the range of fluctuation grows in the future time series. Precipitation shows large interannual variations especially in the A2 scenario run (Figure 6.2). The table in Appendix 14 summarizes the statistical analysis of annual mean air temperature, precipitation and global radiation.

*Table 6.3: Changes in the mean annual air temperature in the Lhasa River basin for the four scenario runs.*

Meteorological variable	1971 – 2000	Scenario	2011 – 2040		2051 – 2080	
				Δ		Δ
Mean annual air temperature [°C]	-0.1	A1B	1.4	+1.4	3.6	+3.6
		A2	0.8	+0.9	3.1	+3.2
		B1	1.0	+1.1	2.4	+2.4
		CON	0.1	+0.2	0.5	+0.6

The mean annual air temperature in the Lhasa River basin was -0.1°C from 1971 to 2000 (Table 6.3). It varies between -9°C on the highest mountain peaks of the Nyainqêntanglha Mountain range and 10°C in the Lhasa valley close to the catchment outlet (see Figure 6.3, top). According to the A1B scenario, the temperature increases by 1.4 K until the future period of 2011 to 2040, whereas the increase in B1 is 1.1 K on average. As shown in Figure 6.3 (left) the changes are not equally distributed over the basin in both scenarios. In the valleys and in the south-eastern areas, the increase varies between 1 K (B1) and 1.5 K (A1B), whereas in the mountain ranges and in the north-west the temperature rises between 1.5 K (B1) and 2 K (A1B). This bisection of the basin with larger changes in the north-west and smaller ones in the south-east continues in the period from 2051 to 2080 (Figure 6.3, right). The differences between the two chosen scenarios are also larger than those of the previous period. While a temperature increase between 3 K and 4 K is simulated by the A1B scenario, the B1 scenario causes a

temperature rise of 1.5 K to 3 K from the 1971 to 2000 period. The average changes for the three climate periods of air temperature are summarized for all scenarios in Table 6.3.

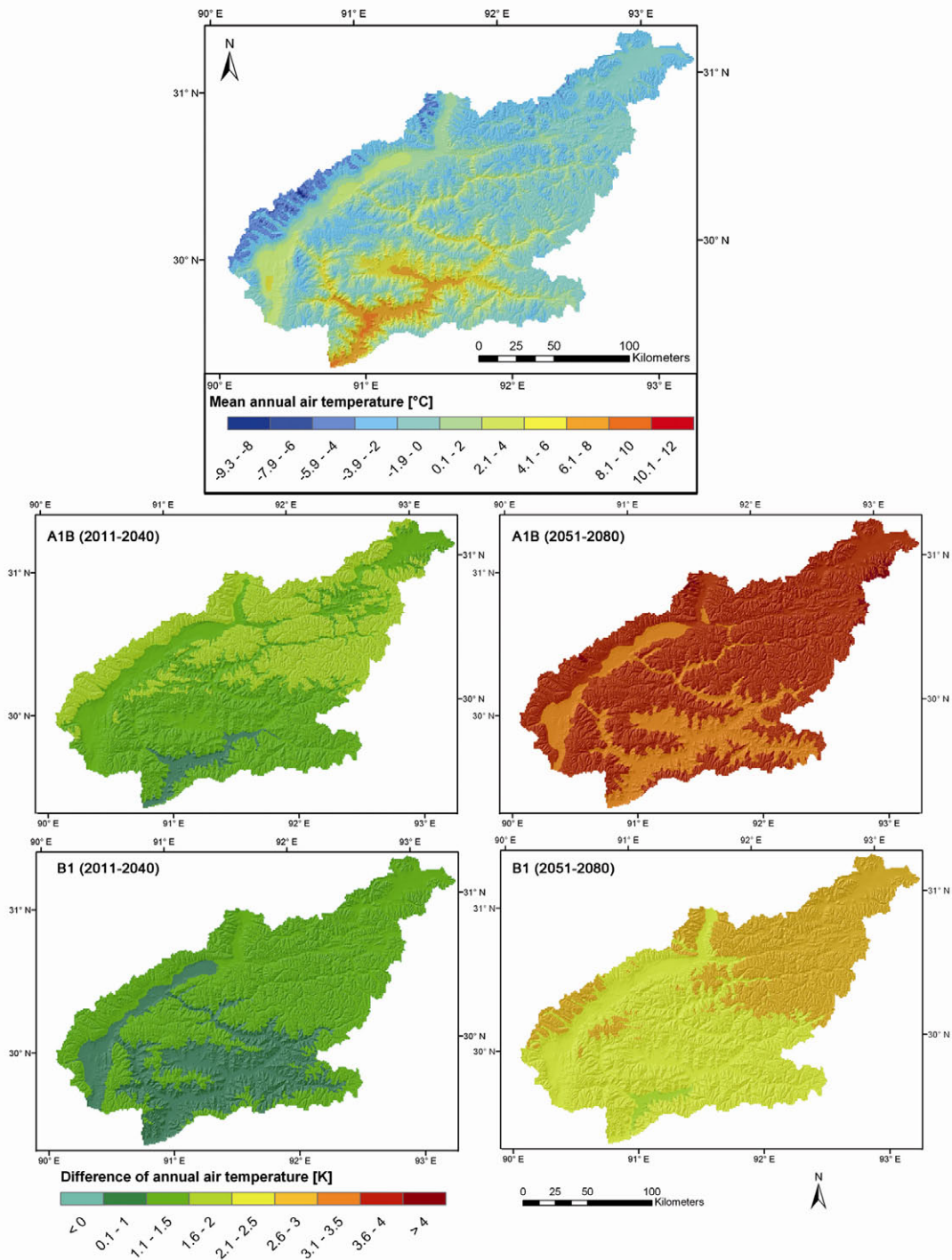


Figure 6.3: Mean annual air temperature from 1971 to 2000 (top) and the changes in the periods of 2011 to 2040 (left) and of 2051 to 2080 (right) according to the A1B scenario (middle) and B1 scenario (bottom).

Although the precipitation changes are small on average and only significant for the A1B scenario, there are clear differences in the spatial pattern of the future periods in some regions (Figure 6.4). From 2011 to 2040, an increase of up to 75 mm is modelled for the south-eastern parts in both scenarios, whereas in the central northern parts, a decrease of up to 25 mm (B1) and 50 mm (A1B) is simulated. In the north-western regions, almost no



changes can be seen. Due to the monsoon direction, precipitation decreases from the south-east to the northern parts of the basin (see section 2.2 and Figure 6.4, top). Moreover, a gradient with elevation during the monsoon following PUTKONEN (2004) is evident in the simulation (Figure 6.4, top). According to the scenario simulations, wetter basin areas will gain more precipitation and drier regions will receive less precipitation in the future.

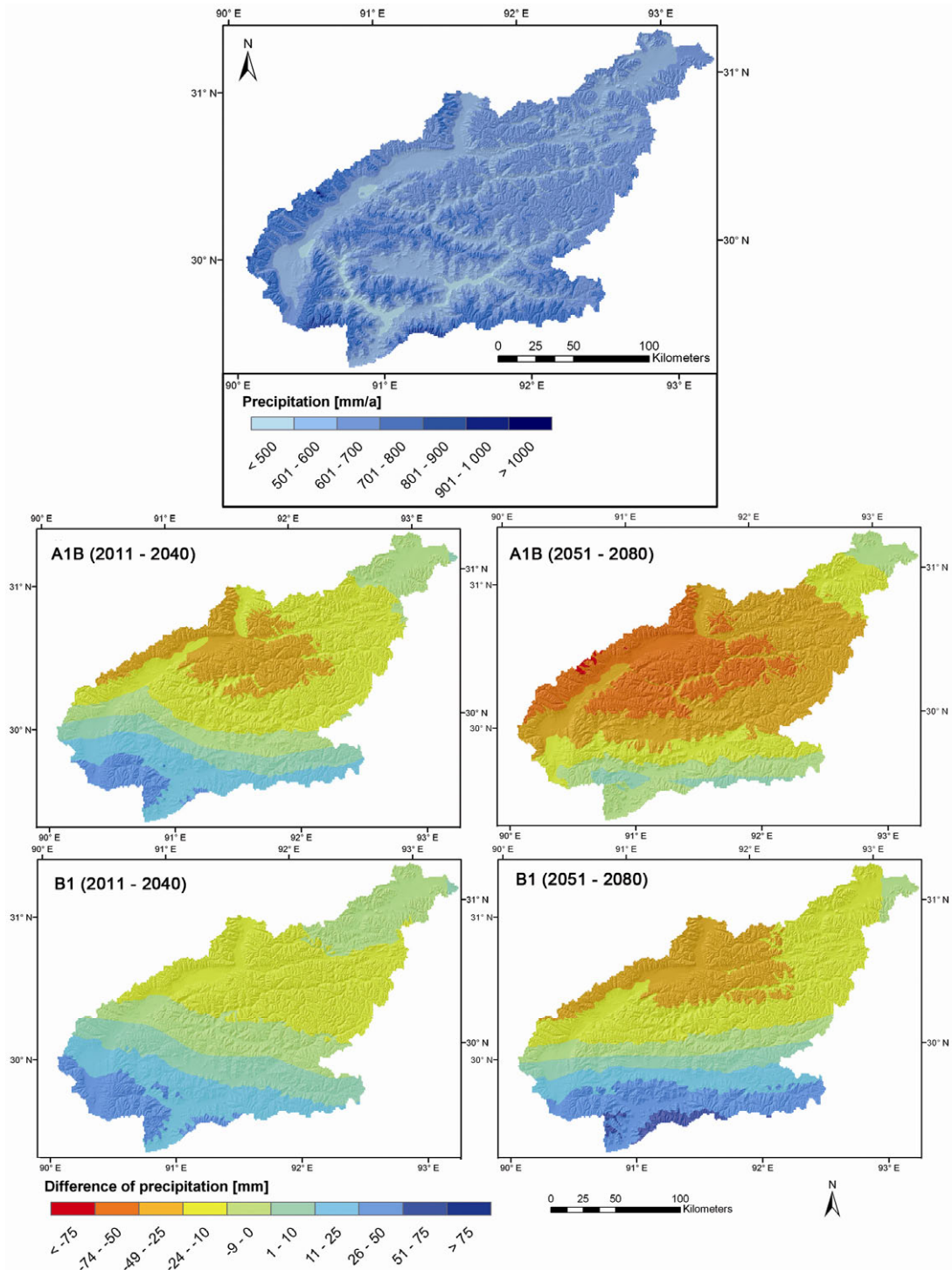


Figure 6.4: Mean annual precipitation from 1971 to 2000 (top) and the changes in the periods of 2011 to 2040 (left) and of 2051 to 2080 (right) according to the A1B scenario (middle) and B1 scenario (bottom).

This trend continues from 2051 to 2080, although the border between precipitation loss and gain shifts from a northeast – south-western to a clear west – east direction. Precipitation increase is simulated in the A1B scenario only for small regions, whereas the decrease reaches 75 mm. In the B1 scenario, the areal fractions of the two parts remain constant, with changes in the range of -75 to + 50 mm (Figure 6.4, bottom). Table 6.4 lists the annual precipitation sums and changes for the three decades.

*Table 6.4: Changes in the mean annual precipitation sum in the Lhasa River basin for the four scenario runs.*

Meteorological variable	1971 – 2000	Scenario	2011 – 2040		2051 – 2080	
				Δ [%]		Δ [%]
Mean annual precipitation sum [mm]	630	A1B	621	-1	596	-5
		A2	646	+3	615	-2
		B1	629	0	626	-1
		CON	612	-3	594	-6

As the seasonal course of the precipitation, caused by the monsoon and interaction between the meteorological variables, is essential for snow and ice-melt, the average trends for the Lhasa River basin for winter (October – March) and summer (April – September) are discussed. The statistical values are compiled in Appendix 15. The significant annual temperature increase (0.05 level) cannot be seen in winter or summer in the past: the absolute trend is below standard deviation. This is also the case for the CON scenario. By contrast, the rise for the scenarios A1B, A2 and B1 is significant on a level of confidence of 99.9 percent in both seasons. While the trend for the first two scenarios and the past is greater in winter than in summer, it inverts for the B1 scenario. The temperature increase in all scenarios ranges from 0.5 K (CON) to 5.0 K (A1B) in winter, and from 0.4 K (CON) to 4.2 K (A1B) in summer. No significant trend is determined for precipitation development, except for the A1B scenario. This is also the case for winter and summer in all scenarios and for the past. Nevertheless, there are significant changes in some months. In January, February, April, May and July, precipitation clearly decreases according to the A1B scenario. By contrast, an increase is simulated in the B1 scenario for February, which is balanced by a decrease in January. The changes in all other months are small (for details see Appendix 15).

Not only the amount of precipitation is relevant for the water balance, and particularly for the glaciers, but also its type (rain or snow). For this reason, the quantity of snowfall is also analysed here. The negative trend of the percentage of snowfall on the annual precipitation sum during the period from 1971 to 2000 continues in the future scenarios. While the percentage was in the 28 percent range in the past, it will decrease to between 12 and 25 percent (depending on scenario) until 2080. The trend is strongest for the A1B scenario and slight for the CON run (Figure 6.5). It represents a reduction of between 1 and 6 percent in the first future climate period, 2011 to 2040. From 2051 to 2080, the decrease varies from between the past period by 3 and 14 percent (see Table 6.5).



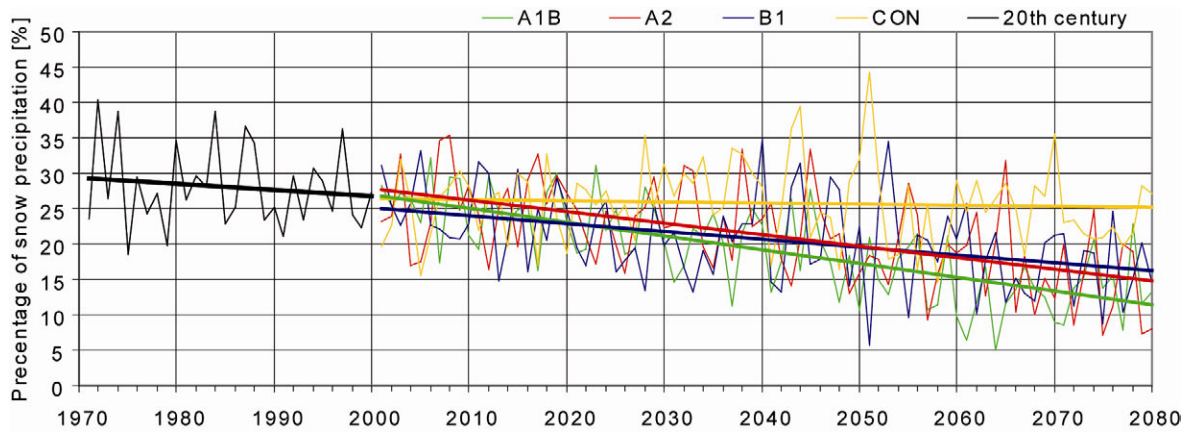


Figure 6.5: The development of the annual percentage of snowfall in the Lhasa River catchment from 1971 to 2080 according to the CLM ECHAM 5 IPCC SRES scenarios.

Table 6.5: Simulated changes in snow precipitation in the Lhasa River catchment for the four IPCC SRES scenarios.

Meteorological variable	1971 – 2000	Scenario	2011 – 2040		2051 – 2080	
				Δ		Δ
Percentage of snow precipitation [%]	28	A1B	22	-6	14	-14
		A2	24	-4	17	-11
		B1	22	-6	18	-10
		CON	27	-1	25	-3

The spatial comparison of the percentage of snowfall between the period from 1971 to 2000 and the two future periods is shown in Figure 6.6. The highest proportion of snowfall is reached along the Nyainqêntanglha Mountains and in the northeastern parts of the basin, with 40 to 100 percent, because percentage of snowfall correlates to elevation. Nevertheless, only a small area with the highest mountain peaks gains more than 60 percent of snowfall. From 2011 to 2040, the reduction rises to 10 percent for almost the entire area in both the A1B and the B1 scenario simulations. The decrease reaches 20 percent in the northeastern Nyainqêntanglha Mountains. The spatial pattern of the trend continues in the 2051 to 2080 period. In accordance with the air temperature changes, it is stronger in the A1B run than in the B1-driven simulation (Figure 6.6).

Analysis of the reduction in snowfall over various elevation levels in the catchment (see Figure 6.7 and Table 6.6) shows uneven distribution. In areas above 5,500 m a.s.l. the decrease reaches a maximum of about 10 percent for the first future period in both scenarios. Below this elevation, it varies at about 5 percent. The decrease becomes larger in the second period, with values of between 20 percent (B1) and 33 percent (A1B) in the higher areas. A reduction of 2 to 13 percent is modelled for altitudes below 5,500 m a.s.l. The percentage of snowfall making up total precipitation consequently declines. The present percentage of snowfall will thus be shifted to regions located 500 m higher. This trend continues, and leads to a shift of 1,000 m to 1,500 m a.s.l. in the worst case, the A1B scenario (see Table 6.6). Consequently, the regions with glaciers are particularly

affected. The inequality between elevation levels is partly caused by the pattern of the temperature increase, which is larger in higher regions, as described above (see Figure 6.3). The precipitation decrease is also larger along the Nyainqêntanglha Mountains (see Figure 6.4).

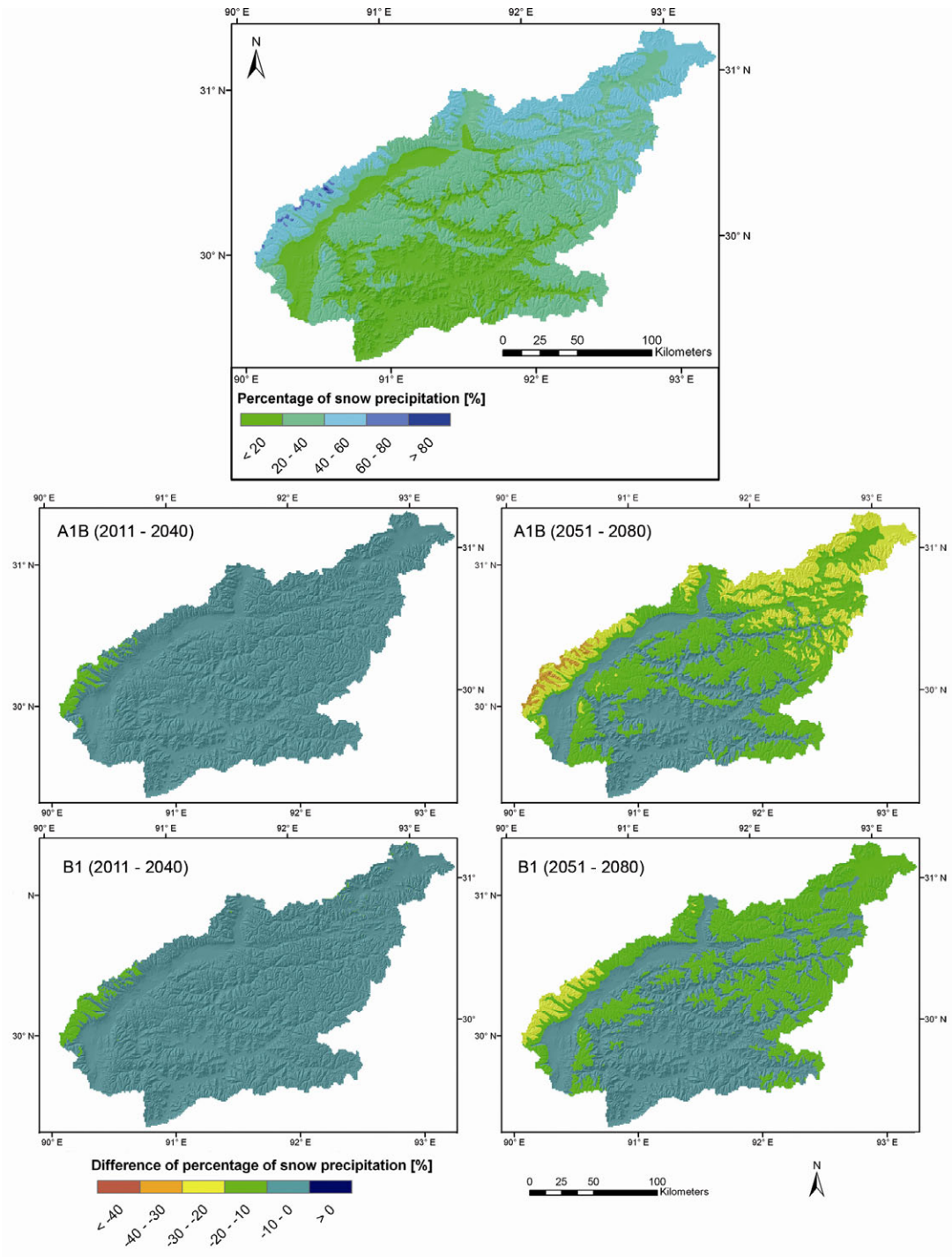


Figure 6.6: Mean annual percentage of snow precipitation from 1971 to 2000 (top) and the changes in the periods of 2011 to 2040 (left) and of 2051 to 2080 (right) according to the A1B scenario (middle) and B1 scenario (bottom).

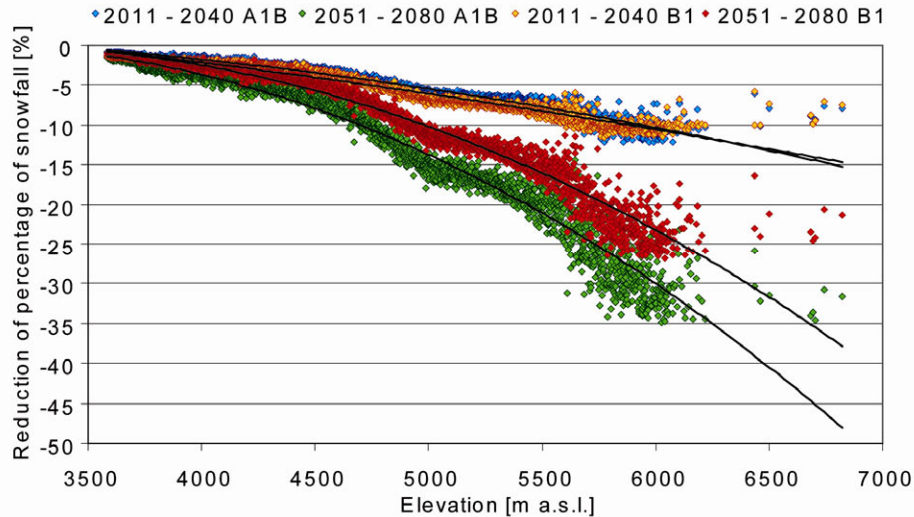


Figure 6.7: Reduction of percentage of snowfall at different elevation levels for the future periods 2011 to 2040 (blue (A1B) and yellow (B1)) and 2051 to 2080 (green (A1B) and red (B1)), compared to the past period.

Table 6.6: Changes in the percentage of snowfall for different elevation levels in the basin.

Elevation [m a.s.l.]	Percentage of basin area [%]	1971 – 2000	A1B		B1	
			2011 – 2040 $\Delta$	2051 – 2080 $\Delta$	2011 – 2040 $\Delta$	2051 – 2080 $\Delta$
3500 – 3999	5.75	5	-1	-3	-2	-2
4000 – 4499	14.47	11	-2	-5	-3	-4
4500 – 4999	32.03	23	-4	-11	-5	-8
5000 – 5499	42.48	35	-7	-17	-7	-13
5500 - 5999	5.00	48	-9	-26	-10	-20
6000 – 6499	0.25	58	-10	-31	-10	-24
> 6500	0.02	73	-9	-33	-8	-23

As the duration of complete snow coverage determines the melting period of the ice, it was also analysed. Figure 6.8 shows the number of days with snow coverage larger than 10 mm s.w.e. in the Lhasa River catchment. In the lowest valleys, snow cover exists only for a few days. The duration increases with rising elevation. In areas above 5,000 m a.s.l. snow cover lasts about three months. Only above 6,500 m a.s.l. does it last almost the whole year, according to the simulation. Compared to Europe, this duration is very short. Reasons for the differences include the dissimilarity of the precipitation pattern, with rare snow fall during winter and high precipitation in summer time. Although snow also falls during the monsoon, rain is observed up to elevations of at least 5,800 m a.s.l. (KANG ET AL. 2007, KAISER ET AL. 2006).

According to the B1 scenario run, small regions of the southern river valleys will be characterized by an increasing number of days with snow cover in the future, as a result of the increasing precipitation in the southern parts of the catchment. Furthermore, on the mountain peak of the Nyainqêntanglha, above 7,000 m a.s.l., a small increase is also

simulated. By contrast, the duration of snow cover in all other regions is reduced. For the A1B scenario, it is reduced throughout the Lhasa River basin except at the Nyainqêntanglha Mountain Peak (see Figure 6.8).

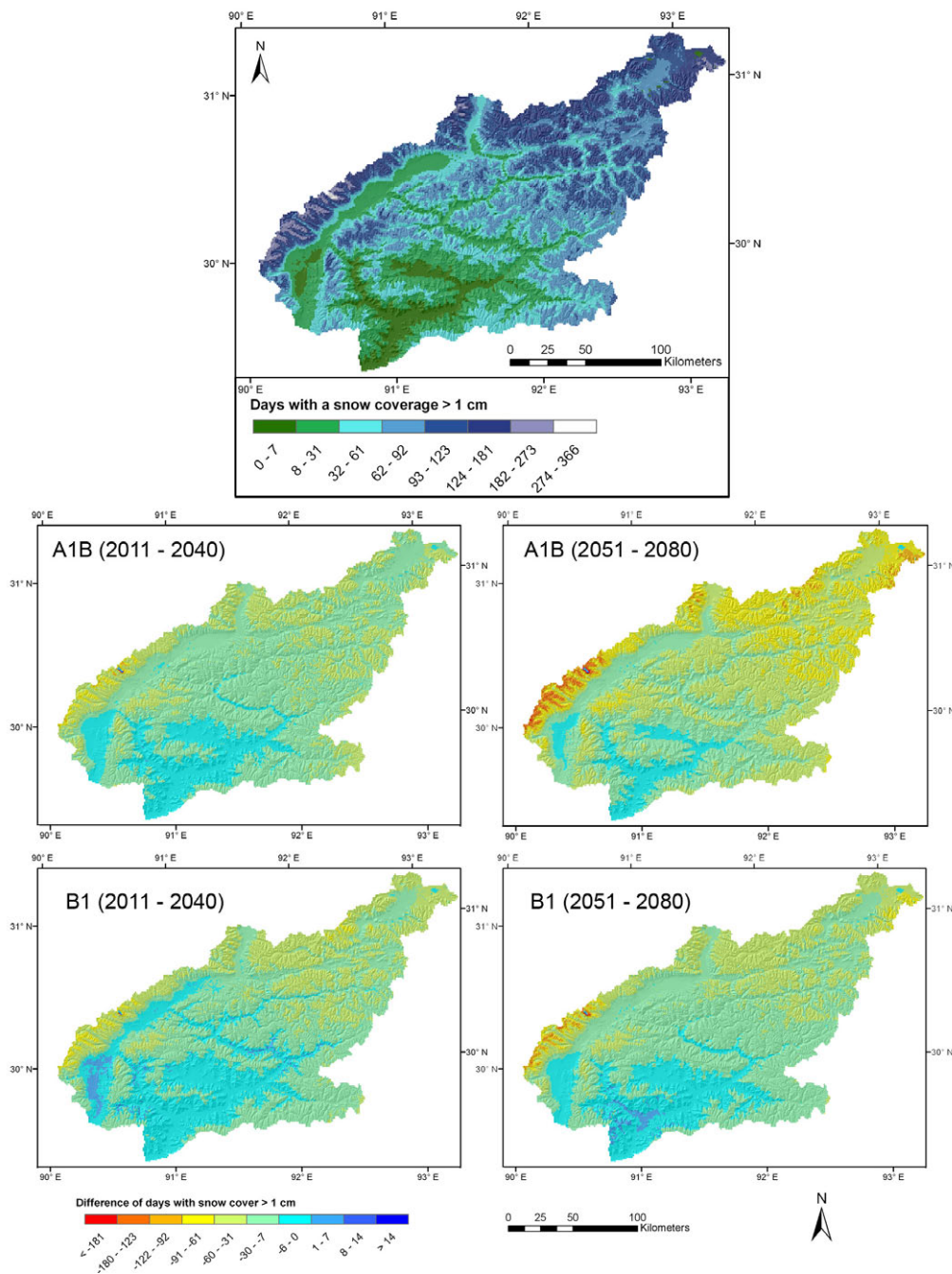


Figure 6.8: Mean annual days with snow cover (swe > 10 mm) from 1971 to 2000 (top) and the changes in the periods 2011 to 2040 (left) and 2051 to 2080 (right) according to the A1B scenario (middle) and B1 scenario (bottom).

The reduction is not equally distributed across all elevation levels. As shown in Figure 6.9 and Table 6.7, the changes to the past are similar in the A1B and B1 scenario runs for the first period, from 2011 to 2040, whereas in the second period, from 2051 to 2080, the decrease in the A1B scenario is very high. Consequently, the snow cover below 4,000 m a.s.l. will last only for a few hours. The duration of the snow cover increases slightly to two and a half months in areas above 6,000 to 6,500 m parallel to elevation rise, which



represents a reduction of four months compared to the past period. In the other periods and in the B1 scenario run, changes of about 30 percent are simulated, reaching 50 percent in the lowest and the highest regions. A shift in the number of snow days of about 500 m a.s.l. is modelled. At elevation levels above 5,500 m a.s.l. with glaciers, this causes a shortening of snow cover duration of between two and three months. Moreover, the different future precipitation patterns of the two scenario runs are reproduced by the snow cover duration, in addition to the larger temperature increase in the higher regions. A clear precipitation decrease in the higher regions, especially in the Nyainqêntanglha Mountains, is simulated in both the A1B and the B1 runs, whereas increasing precipitation is modelled for the lower south-western and southern parts (see Figure 6.4), particularly in the B1 scenario. The decrease is accordingly smaller in regions between 3,700 and 4,500 m a.s.l. in the B1 run than in the A1B run. A slight increase of the snow cover period is even simulated in the B1 scenario for the period from 2051 to 2080 for some regions in the lower elevation range.

Table 6.7: Changes in the number of days with snow cover of a swe > 10 mm.

Elevation [m a.s.l.]	1971 – 2000	A1B		B1					
		2011 – 2040 Δ	2051 – 2080 Δ	2011 – 2040 Δ	2051 – 2080 Δ				
3500 – 3999	5	2	-3	0	-5	3	-3	3	-2
4000 – 4499	16	8	-8	4	-12	12	-4	9	-7
4500 – 4999	48	30	-18	18	-31	34	-14	30	-18
5000 – 5499	89	59	-29	34	-54	59	-30	59	-30
5500 - 5999	147	100	-48	54	-93	100	-47	87	-60
6000 – 6499	199	136	-63	73	-125	139	-60	113	-86
> 6500	330	267	-62	219	-110	256	-73	184	-146
Basin	64	41	-23	24	-40	43	-21	41	-23

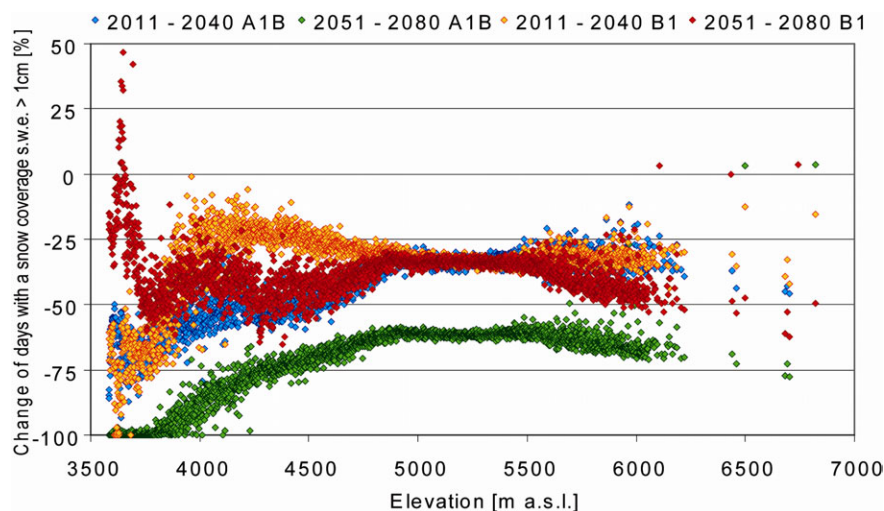


Figure 6.9: Changes in days with snow cover (swe > 10 mm) for the future periods 2011 to 2040 (blue (A1B) and yellow (B1)) and 2051 to 2080 (green (A1B) and red (B1)) compared to the past period.

According to the applied ECHAM 5 CLM IPCC SRES scenarios, the future meteorological conditions in the Lhasa River basin will change considerably. The air temperature will increase throughout the basin, while the average precipitation changes are small. The spatial pattern of the shifts nonetheless divides the basin into regions with an increase, in the south, and those with a decrease, in the central and north-western parts. As a consequence, the amount of snowfall and the number of days with complete snow coverage will be reduced. Higher regions, where the glaciers are located, are particularly affected. The impact of the changing climatic conditions on glacier distribution and on the ice water reservoir is presented in the following chapter.

### **6.3 Future Glacier Distribution and Ice Water Reservoir**

The retreat of glacial coverage during the period from 1971 to 2000, as described in section 5.3.2, will continue in the future. The magnitude of the decrease both in glacier area and in water stored as glacier ice is similar to the past period up to 2020 (see Figures 6.10 and 6.11) in all scenario simulations, reflecting future meteorological conditions. Both air temperature and precipitation develop similarly until 2020. Afterwards, the future trends differ between scenarios. While the decrease is strongest in the A1B scenario, corresponding to the largest temperature increase, the A1 scenario run simulates the lowest shrinkage among the increasing emission scenarios until 2070. In the subsequent decade, the A2 temperature increase exceeds the A1B increase, and results in an acceleration of glacial retreat. Hence, the A2 trend rises above the glacial decrease of the B1 scenario simulation.

In determining glacier mass balance, both air temperature development and the amount of snow precipitation must be considered when explaining the glacier trends. As a consequence, years with above average snow precipitation (see Figure 6.12) can be identified in the development of the ice water equivalent. Hence, the retreat in the B1 scenario in the 2020s is largest, but slows down by 2070, in accordance with its larger amount of simulated snowfall by comparison with the other scenario runs. Although snowfall decreases further, glacier melt slows down during the last decade of the A1B and B1 results. As the glaciers retreat into the highest mountain areas until the 2070s in this simulation, enough snowfall is nevertheless simulated to enable the glacier retreat to be stabilized. Together with the slowdown of the temperature trend, the reduced retreat can be explained. The mass loss during the previous decades can however not be balanced, and so glacier shrinkage is largest in the A1B scenario in total in 2080.

The CON-driven model run, without significant changes in meteorological conditions after 2020, takes an exceptional position. The ice water equivalent fluctuates around the 2020 period: an equilibrium state is reached by the glaciers in which mass gain and mass loss are almost balanced over the years. Average annual mass balances of -0.04 m and -0.05 m in the future periods of 2011 to 2040 and 2051 to 2080 respectively confirm the result (see Table 6.8). Glacier area nonetheless decreases in the simulation. Disregarding the simulation of ice movement, and consequently the transport of mass gain from the accumulation region to ablation region, causes a more pronounced melting of the ice in the lower areas. For this reason, the glacier area trend is totally different from the

development of the ice water reservoir. However, ice redistribution should be considered in simulations under changing climatic conditions: the results for the scenarios with increasing temperature can be assumed to be reliable. With enlargement of surface area and reduction of ice thickness, ice flow would accelerate the retreat of the glaciers. Without consideration of ice transport, a lower limit to the retreat is simulated. The ice movement of retreating glaciers also slows down as the area shrinks, finally coming to a halt. For this reason, the ice movement can be neglected in the final phase of a melting glacier. Additionally, glacier geometry is dynamically adapted by reducing the glacier area after the melt out of glacier levels.

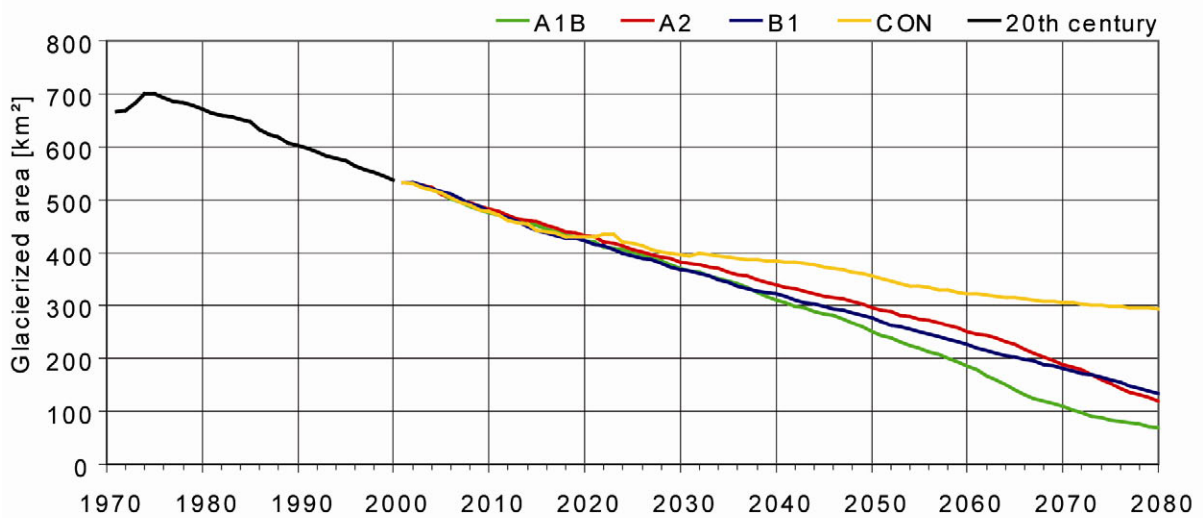


Figure 6.10: The development of the glacier area in the Lhasa River catchment from 1971 to 2080 according to the IPCC SRES scenarios.

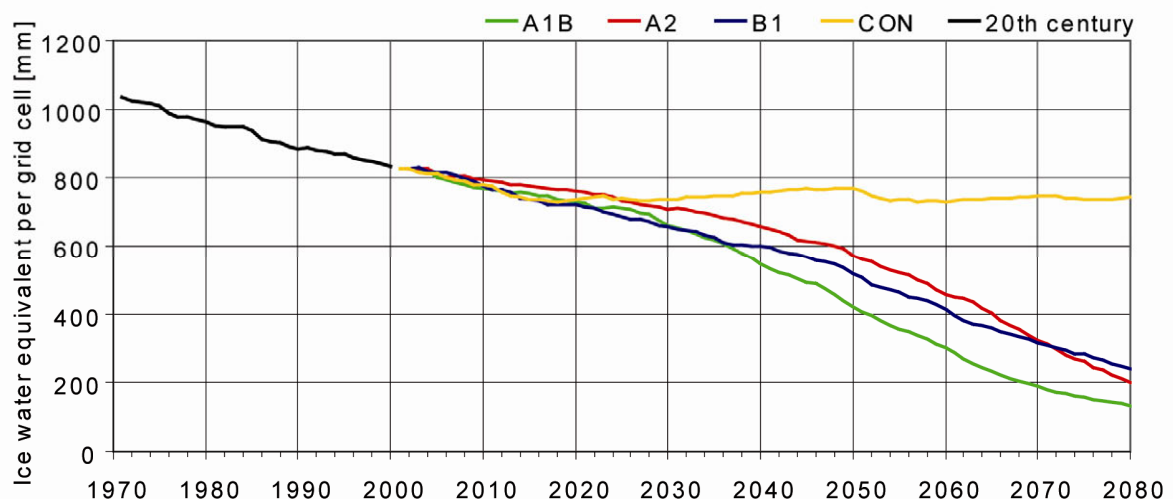


Figure 6.11: The development of the water stored as ice equally distributed over the Lhasa River catchment from 1971 to 2080 according to the IPCC SRES scenarios.

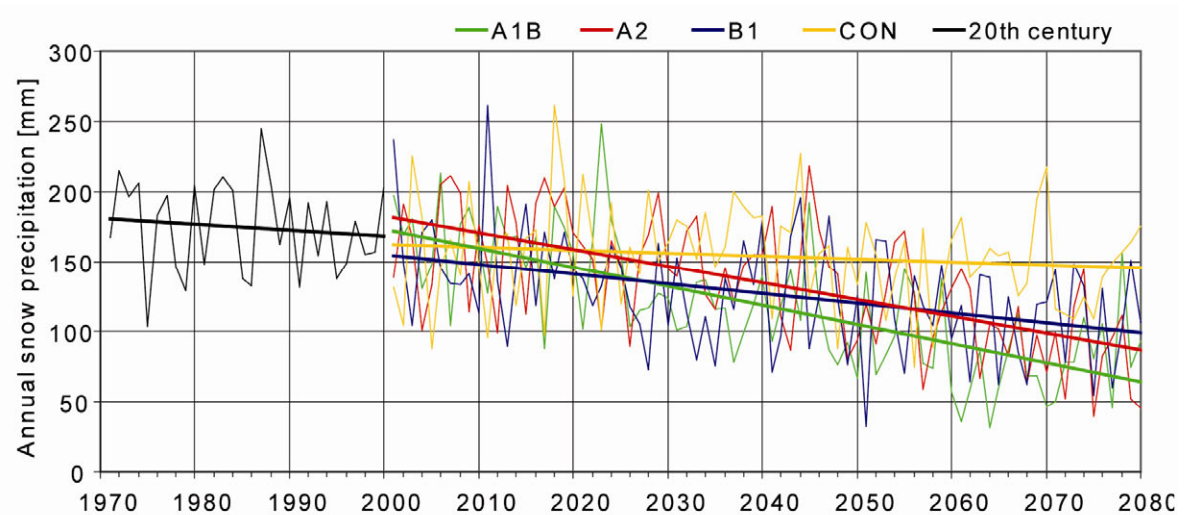


Figure 6.12: The development of annual snow precipitation in the Lhasa River catchment from 1971 to 2080 according to the IPCC SRES scenarios

Table 6.8: Changes in glacial coverage and stored ice water reservoir in the Lhasa River catchment for the four scenarios.

Glacier characteristics	1971 – 2000	Scenario	2011 – 2040		2051 – 2080	
				$\Delta$ [%]		$\Delta$ [%]
Glacier Area [km <sup>2</sup> ]	629	A1B	395	-37	147	-77
		A2	406	-35	215	-66
		B1	392	-38	202	-68
		CON	416	-34	316	-50
Ice water reservoir [mm/km <sup>2</sup> ]	928	A1B	686	-26	247	-73
		A2	731	-21	386	-58
		B1	682	-26	362	-61
		CON	743	-20	740	-20
Mean annual mass balance [m]	-0.33	A1B		-0.54		-1.23
		A2		-0.33		-1.39
		B1		-0.39		-1.09
		CON		-0.04		-0.05

Table 6.8 compares the changes in the glacial coverage and the ice water equivalent for the future periods of 2011 to 2040 and 2051 to 2080 to the period from 1971 to 2000. The mean mass balances are also tabulated for the three periods. In order to directly compare the size of the ice water reservoir to annual precipitation, the total amount is distributed across all grid cells of the catchment. In the past, about one and a half times annual precipitation were stored as ice. However, about 20 percent of ice water storage for each grid cell in the basin melted away from 1971 to 2000. In the first future period, 2011 to 2040, both the retreat of the ice water reservoir and the glacier area are quite similar for all scenarios, varying between 21 and 26 percent for the water reservoir. A retreat of 35 to 37 percent is simulated for the glacial coverage. In the second scenario period, the decrease fluctuates at around 65 percent for the A2 and B1 scenario. For the A1B



scenario, a maximum reduction of around 75 percent for both the ice water and the glacier area is simulated. The different mass balances confirm the results. While the retreat in the first future period is slightly larger than that of the past, at about 0.4 m per year, it increases to more than one meter in the second scenario phase, with a maximum of 1.4 m for the A2 simulation.

The development of the spatial distribution of the future ice water reservoir for all decades from 2000 to the end of the scenario period in 2080 is illustrated in Figure 6.13 (A1B) and Figure 6.14 (B1). The initializing status of 1970 is also mapped. All decade maps are shown separately in higher resolution in Appendix 19. The changes in the past period are small, but glaciers did melt, particularly at their edges. In the scenario simulations, the retreat until 2030 is small (see Figure 6.11), but some small glaciers in the northeastern parts disappear. Afterwards, an accelerating melt is simulated, and large storages with reservoirs over 75 m w.e. per km<sup>2</sup> decrease. More grid cells lose glacierization. In both scenario simulations, only around the Nyainqêntanglha Mountain peak is an amount larger than 75 m w.e. per km<sup>2</sup> stored as glacier ice in 2070, whereas a level of 25 m w.e. is rarely exceeded in all the other regions. The glaciers in the north-east melted completely. The retreat can also be seen in the higher mountain ranges. In the final decade, ending in 2080, the shrinkage continues, with clear differences between the two scenarios. The ice reservoir at the end of the future period is noticeably smaller in the A1B results than in the B1 model run. Along the south-western and the south-eastern catchment border, the glaciers overcome the impact of climate change because of increasing precipitation and the comparatively minor reduction in snowfall. Moreover, the temperature increase is not as large as that in the Nyainqêntanglha Mountain range, which is clearly affected by the changing climatic conditions.

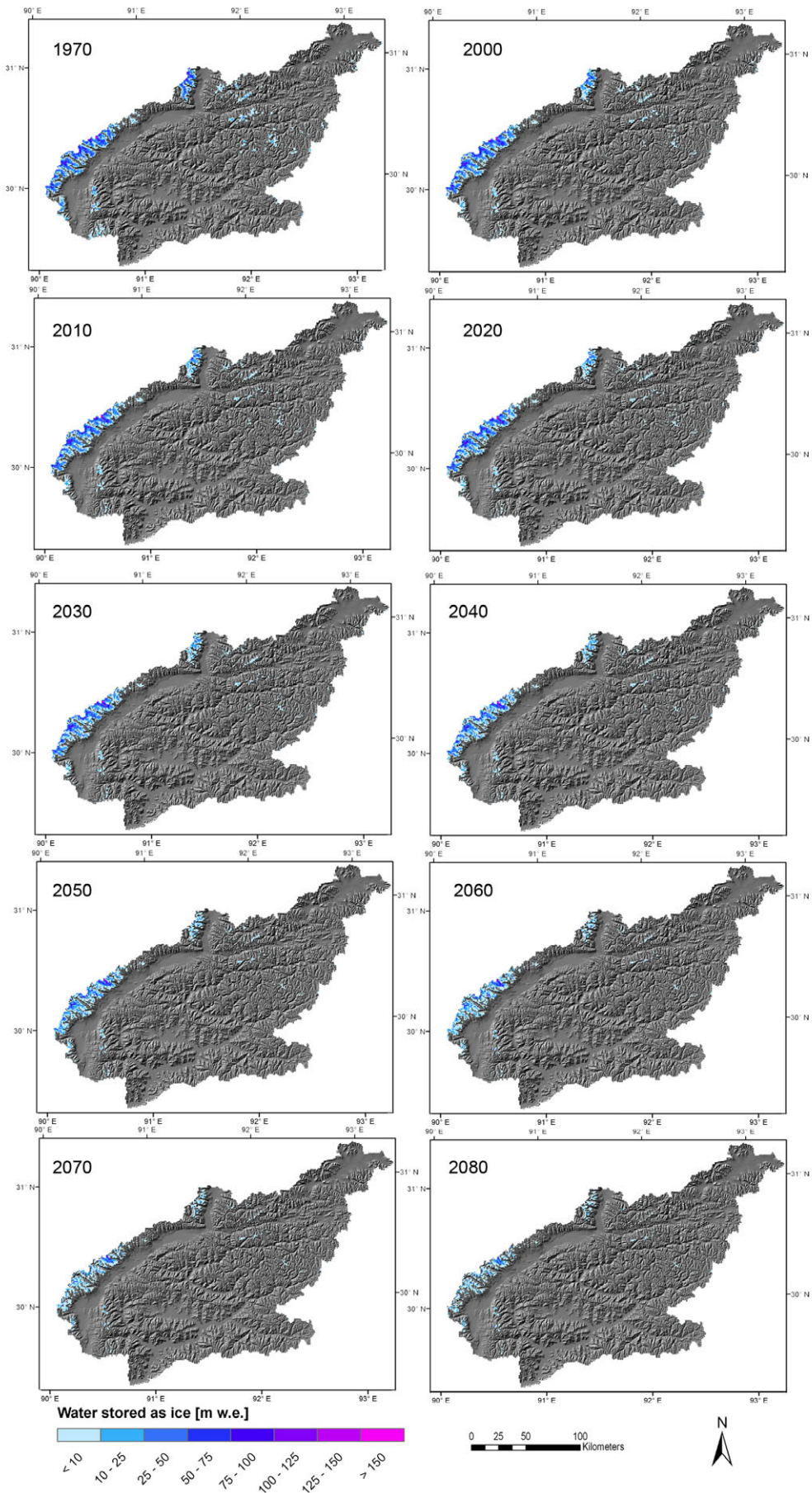


Figure 6.13: The development of the simulated ice water equivalent distribution from 1970 to 2080 over the decades according to the CLM ECHAM5 IPCC A1B scenario model run.

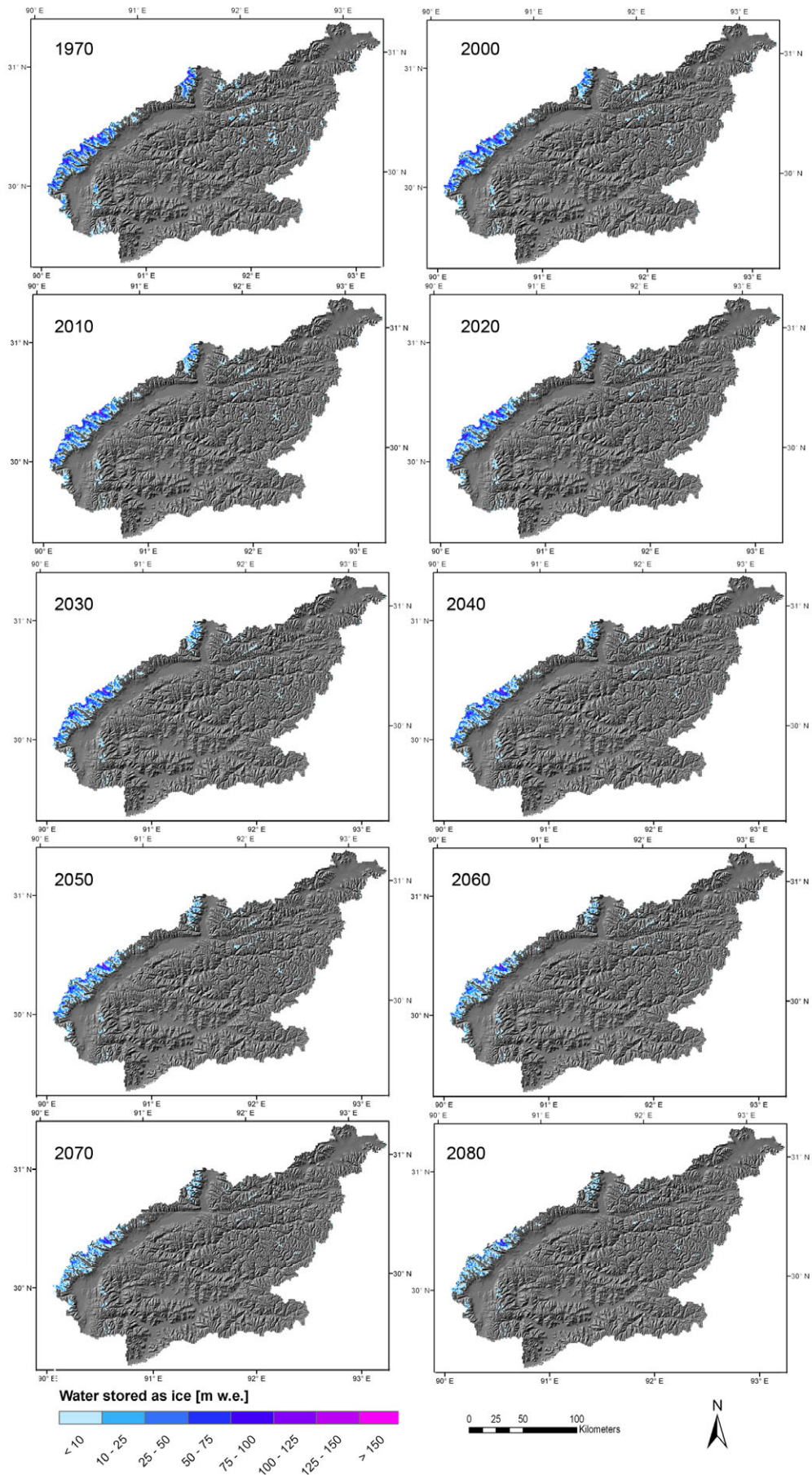


Figure 6.14: The development of the simulated ice water equivalent distribution from 1970 to 2080 over the decades according to the CLM ECHAM5 IPCC B1 scenario model run.



## 6.4 Future Development of Snow- and Ice-Melt

Future climatic conditions affect the amount of water stored as snow and ice in the Lhasa River basin, as presented in the previous chapters. The impact on the amount of snow- and ice-melt is presented below. The amount of snowmelt has (Figure 6.15), like snow precipitation (see Figure 6.12), been decreasing since 1970. This negative trend continues until the end of the simulation period in 2080. As a result, the 215 mm mean amount of the past is reduced by 118 percent in the A1B model run from 2051 to 2080, as a worst-case scenario. Even in the CON model run, a decrease of 40 percent is modelled, because of the slight temperature increase (Table 6.9). In contrast to the uniformly negative trend of the amount of snow-melt, the future development of ice-melt water release varies between the scenario results. In the B1 simulation, the amount varies around 10 mm with no significant trend. Under A1B climatic conditions, the development of the ice-melt shows an increase to approximately 15 mm by 2050, falling to 5 mm in the final decade. By contrast, the maximum ice-melt is reached in the A2 scenario, where it exceeds 15 mm after 2040. In the CON run, a decrease to 5 mm until 2020 is simulated, which only small changes until the end of the simulation period (Figure 6.16).

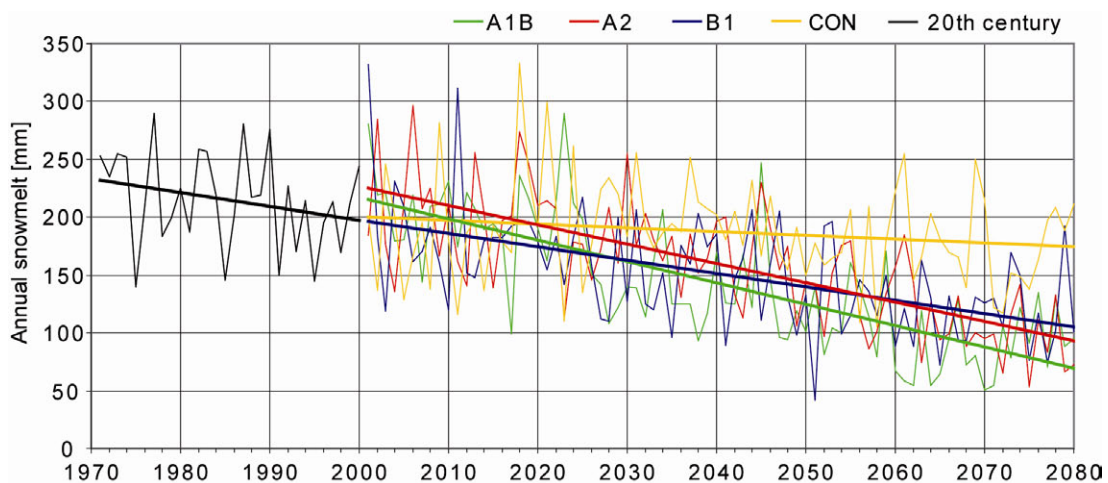


Figure 6.15: Development of annual snowmelt in the Lhasa River catchment from 1971 to 2080 according to the CLM ECHAM 5 IPCC SRES scenarios.

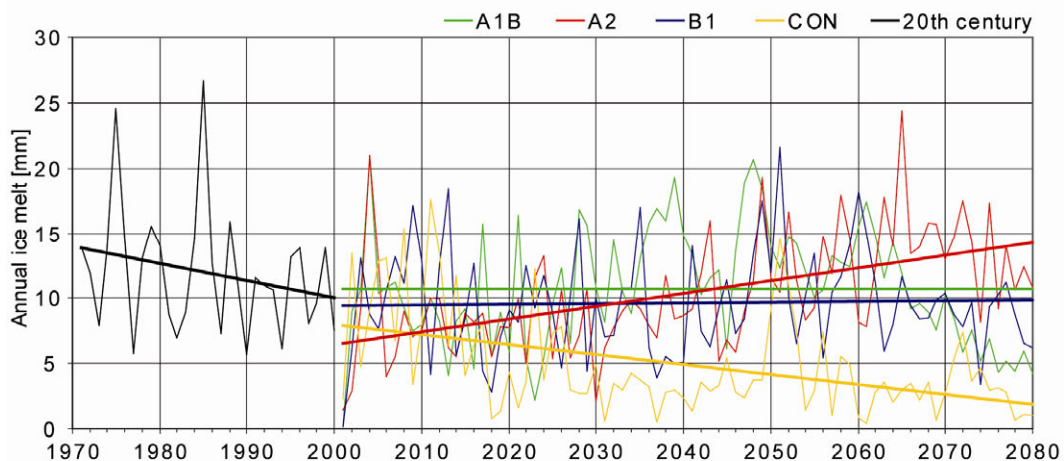


Figure 6.16: Development of annual ice-melt in the Lhasa River catchment from 1971 to 2080 according to the CLM ECHAM 5 IPCC SRES scenarios.

Additionally, the development of the ice-melt is characterised by large interannual variations. The annual amount fluctuates between almost zero and 25 mm. Comparing the ice-melt curves with the course of the number of days of complete snow cover (Figure 6.17) reveals that long snow cover periods are frequently correlated with low meltwater release and vice versa. Hence, variation of the ice-melt can be explained by the markedly varying number of snow-cover days. The total amount of ice-melt water is small, however, and accounts only for one fifth of the snowmelt. The clear decrease of glacial coverage and stored ice water equivalent is therefore not pronounced in the course of the ice-melt. Furthermore, shorter snow periods because of higher air temperatures enable the melting of ice at higher elevations. As a consequence, the reduction of the ice water reservoir is balanced by larger or longer snow-free glacier areas.

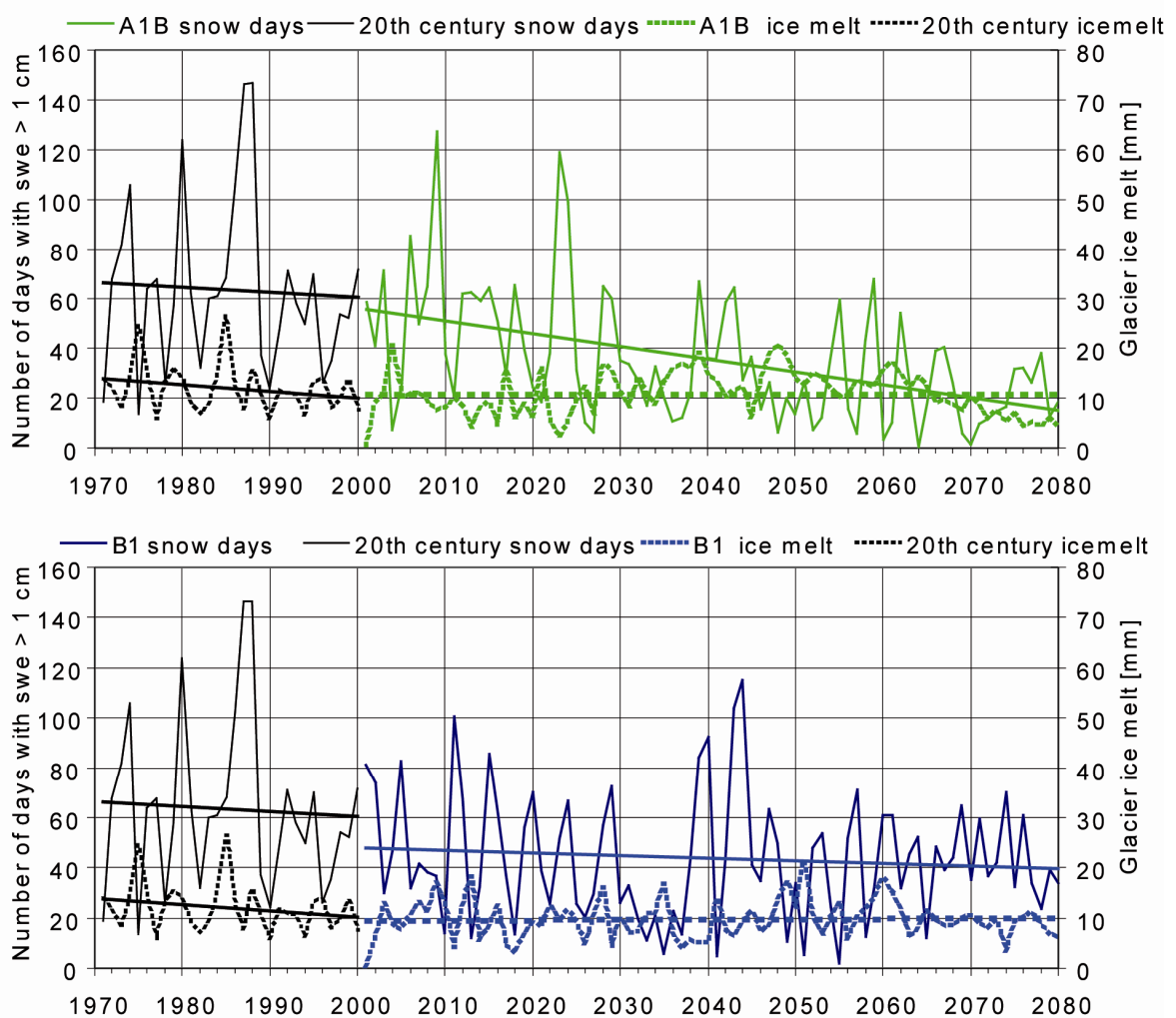


Figure 6.17: Development of annual ice-melt and the number of days with complete snowcover (s.w.e. > 10 mm) in the Lhasa River catchment from 1971 to 2080, according to the IPCC SRES A1B (green) and B1 (blue) scenario.

Table 6.9: Changes in annual snow- and ice-melt in the Lhasa River catchment for the four scenarios.

	1971 – 2000	Scenario	2011 – 2040		2051 – 2080	
				$\Delta$ [%]		$\Delta$ [%]
Snowmelt [mm]	215	A1B	168	-47	97	-118
		A2	186	-28	114	-101
		B1	170	-45	122	-93
		CON	202	-13	175	-40
Ice-melt [mm]	12	A1B	11	-1	10	-2
		A2	8	-4	13	1
		B1	9	-3	10	-2
		CON	5	-7	4	-8

### 6.5 The Future Water Balance

In assessing future water availability, important water balance values include not only the amount of precipitation, snow- and ice-melt, but also the development of evapotranspiration. In accordance with the rising air temperature, evapotranspiration increased slightly during the period of 1971 to 2000. This positive trend continues in the future simulations. The increase is strongest in the A1B scenario run, as is also the case for temperature development (see Figure 6.3), whereas the B1 scenario results in the smallest increase under conditions of increasing greenhouse gas emissions (Figure 6.18). By contrast, no significant trend is found in the CON run. Table 6.10 lists the average evapotranspiration sums of the past climate period and changes in the future periods according to the various scenario runs.

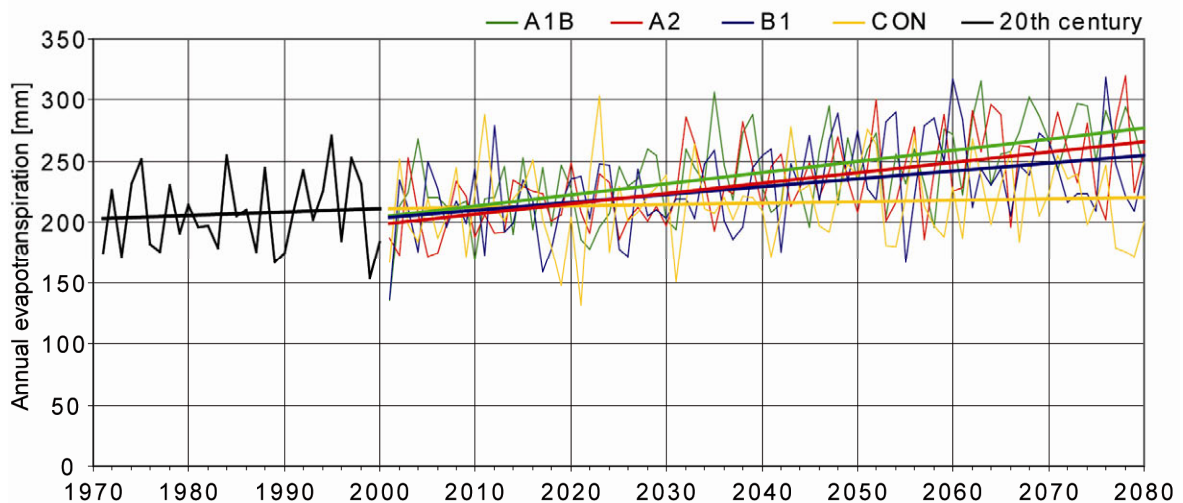


Figure 6.18: Development of annual evapotranspiration in the Lhasa River catchment from 1971 to 2080 according to the CLM ECHAM 5 IPCC SRES scenarios.

Table 6.10: Changes in annual evapotranspiration and water availability in the Lhasa River catchment for the four scenarios.

	1971 – 2000	Scenario	2011 – 2040		2051 – 2080	
				Δ [%]		Δ [%]
Evapotranspiration [mm]	207	A1B	231	+12	263	+27
		A2	221	+7	253	+22
		B1	216	+4	245	+18
		CON	215	+4	219	+6
Runoff [m <sup>3</sup> /s]	441	A1B	410	-7	349	-21
		A2	441	0	383	-13
		B1	430	-3	399	-10
		CON	409	-7	385	-13

The spatial distribution of the past average annual evapotranspiration (Figure 6.19, top) shows the correlation between the amount of evapotranspiration and air temperature. In the southern river valleys, maximum values of between 500 and 750 mm per year are simulated. In the high mountains, a 100 mm evapotranspiration level is not exceeded. The pattern of the various land cover classes is also reproduced. As a result, the large amount of evaporation in the north-eastern basin is attributed to a small lake. In contrast, less evapotranspiration is simulated for Lhasa due to the impervious areas of a town with little surface water and few plants. The changes in evapotranspiration in the future periods are illustrated for the scenarios A1B and B1 in Figure 6.19 (middle and top). From 2011 to 2040, a slight increase of up to 50 mm is modelled for both scenarios throughout the basin. The mountainous areas and the southern regions form an exception however, with almost no differences from the past. In the second future climate period, the amount of evapotranspiration increases further, particularly in the A1B scenario, which has the largest temperature increase. As the temperature rise is larger at higher elevations, the changes are also greater (except the Nyainqêntanglha Mountains). In addition, water availability resulting from a precipitation gain in the north-east leads to an increase in evapotranspiration of up to 150 mm per year.

All factors described above, together with soil water content and groundwater changes, determine the river runoff. Figure 6.20 shows the various courses of the mean annual discharge at the catchment outlet of the Lhasa River. All four scenario runs result in a decrease, which is only significant for the A1B and A2 scenarios. In considering the seasonal changes in the runoff, a larger decrease is assessed during summer (April - September) than during winter (October – March). In accordance with the annual trends, only for the A1B and the A2 (summer only) scenarios are the trends significant. All statistical values are given in Appendix 22. A comparison of the future climate periods with those of the past confirms the results, as listed in Table 6.10.



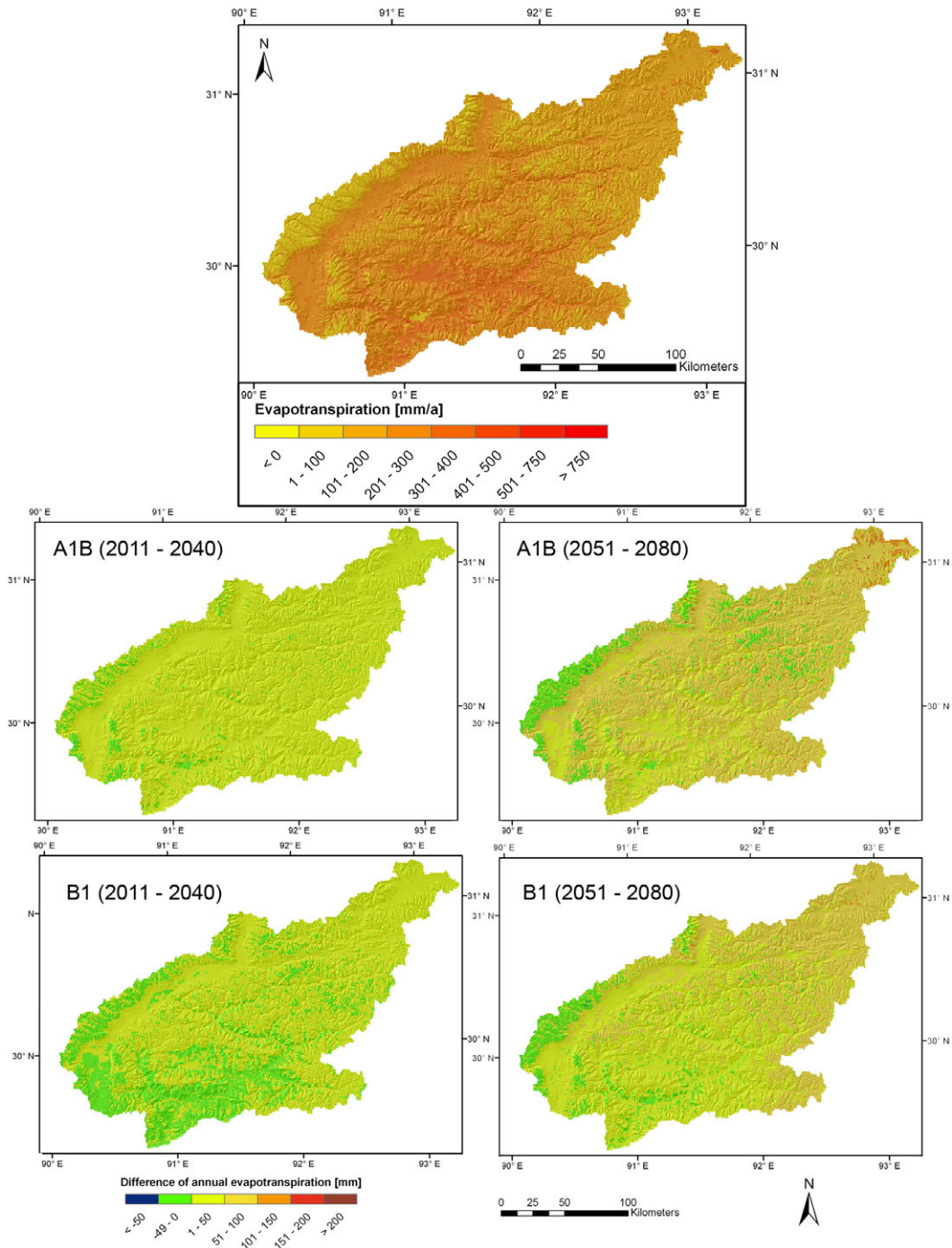


Figure 6.19: Mean annual evapotranspiration from 1971 to 2000 (top) and the changes in the periods of 2011 to 2040 (left) and 2051 to 2080 (right) according to the A1B scenario (middle) and B1 scenario (bottom).

The seasonal runoff pattern for the three climate periods after scenario A1B (top) and B1 (bottom) is shown in Figure 6.21. In the A1B simulation, the runoff decreases significantly (see statistical analysis in Appendix 24) during the summer months from May to August, which can clearly be seen in the final period of 2051 – 2080. By contrast, a significant decrease in the monthly runoff is only stated for June and July at a significant level (0.1) in the B1 scenario. A reduction is accordingly simulated for these two months, whereas the water availability in the other months stays constant. Peak discharge even increases in August. The monthly runoff at the catchment outlet by decade (Figure 6.21,

right) decreases continuously from May to July. In contrast, the past runoff peak is exceeded in August in the A1B scenario. The largest runoff is simulated from 2011 to 2020, whereas the smallest discharge is modelled from 2061 to 2070. The variations within decades are sizeable, fluctuating between 1,000 and 1,600 m<sup>3</sup>/s in August. The results under B1 climatic conditions are similar, although the decrease from May to July is not as continuous as that of the A1B run. The maximum runoff is also simulated in the last decade of the simulation period, whereas from 2041 to 2050 the minimum is modelled.

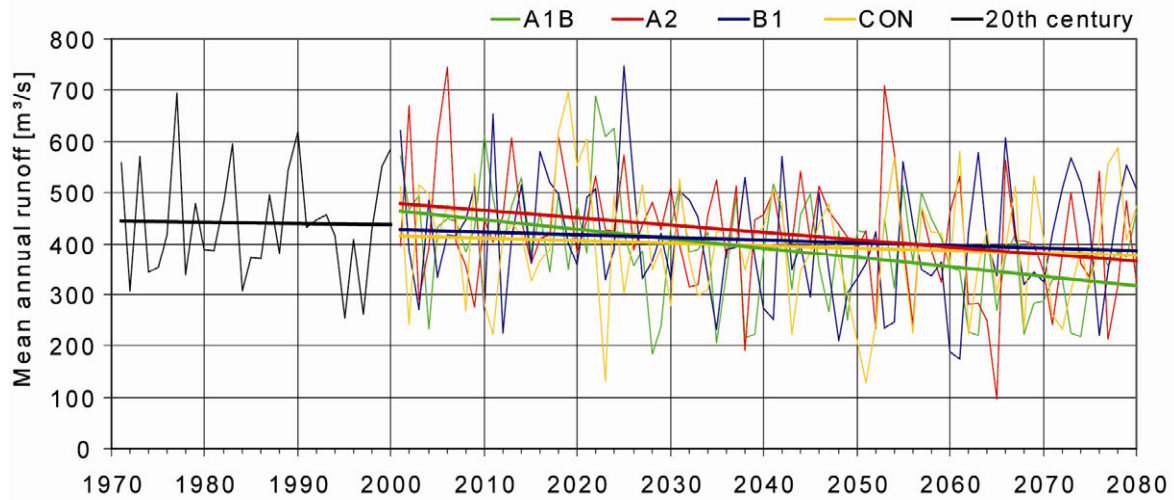


Figure 6.20: Development of the annual runoff in the Lhasa River catchment from 1971 to 2080 according to the CLM ECHAM 5 IPCC SRES scenarios.

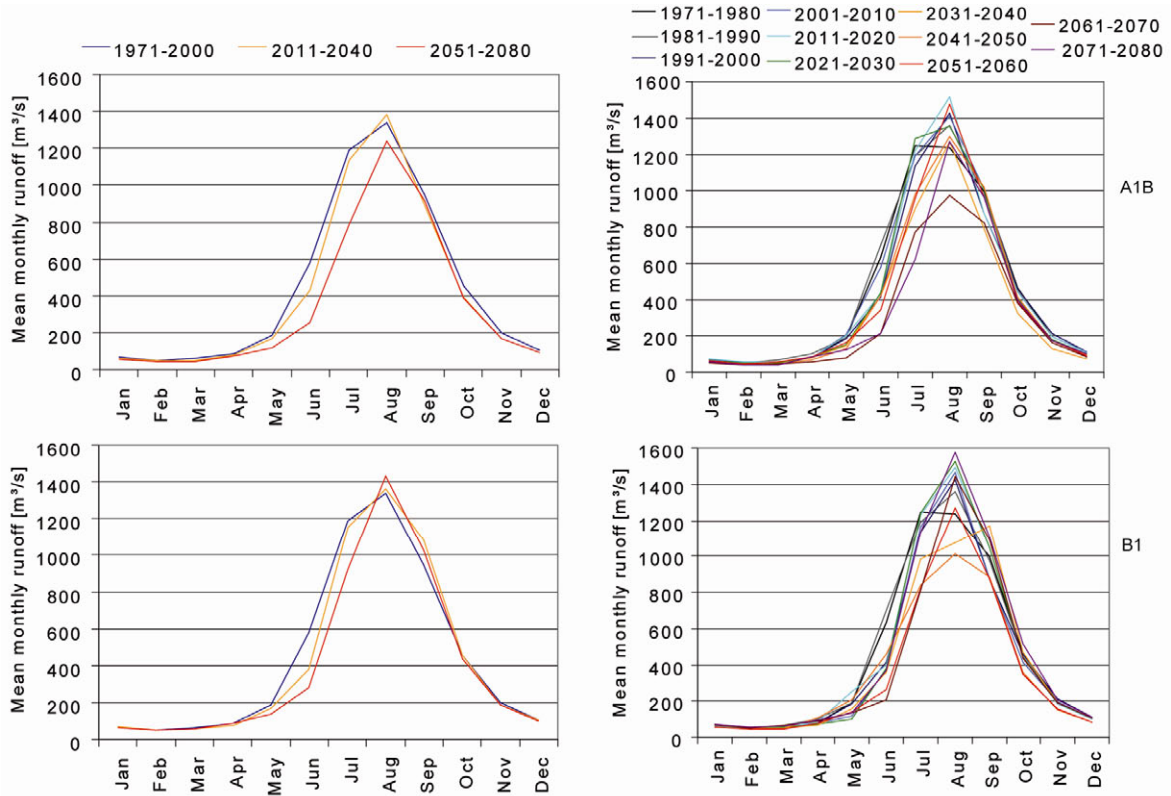


Figure 6.21 Comparison of mean monthly runoff at the basin outlet between climate periods (left) and decades (right), according to the A1B scenario (top) and the B1 scenario (bottom).

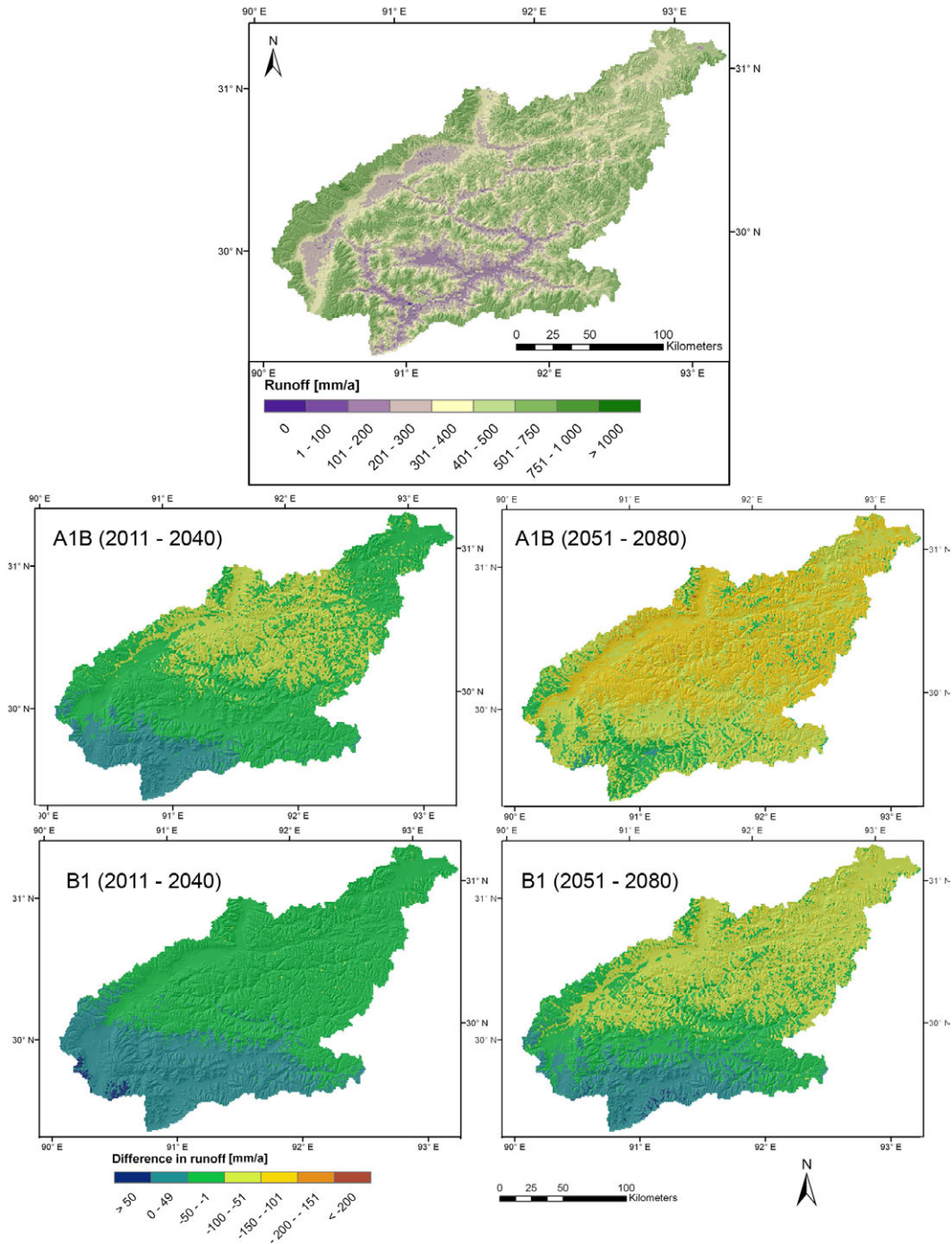


Figure 6.22: Mean annual runoff from 1971 to 2000 (top) and the changes in the periods of 2011 to 2040 (left) and 2051 to 2080 (right), according to the A1B scenario (middle) and B1 scenario (bottom).

In order to determine the spatial distribution of future water availability in the Lhasa River basin, the difference between precipitation and evapotranspiration was calculated under the assumption that storage is in a steady state throughout a 30-year period. Although this in reality is not the case, the influences of precipitation and evapotranspiration dominate, as analysed in section 6.6. This spatial pattern of changes provides, accordingly, reliable information (Figure 6.22). The spatial distribution of the water balance is relatively similar to the precipitation pattern (Figure 6.4): precipitation is thus a determinant of water

availability. Variations in the amount of evapotranspiration also can be recognized, and water availability is larger in the mountainous areas than in the valleys.

The distribution of the changes in runoff also follows that of the precipitation changes. In the southern parts of the basin, an increase of up to 50 mm is simulated, whereas a decrease is modelled in the central and the northern parts of the basin. This decrease varies between 1 mm and 100 mm during the period of 2011 to 2040, and in the period of 2051 to 2080 a reduction of up to 200 mm is simulated in the A1B scenario. In contrast, the decrease in the B1 simulation does not exceed 100 mm. Overall, the absolute changes in water availability are larger than the changes in precipitation, because of the rise in evapotranspiration.

## 6.6 Analysis of the Influence of Ice-Melt on Runoff

The simulation of snow and ice-melt and of the water balance enables to determine the influence of glacier ice-melt on runoff. In order to determine the amount of glacier ice-melt water, which contributes to the river runoff, the model is run under two different model settings. Whereas in the first setting, glacier ice melt is not injected in the river network and subsequently does not contribute melt water, in the second case the contribution from glaciers, which flows directly into the river channel, is fully considered. The difference between the runoffs of the two model settings corresponds to glacier ice-melt. This method allows determining the proportion of glacier ice-melt water to runoff in the river channel network throughout the catchment.

Figure 6.23 (separate maps in Appendix 25) shows the mean annual amount of glacier ice-melt water in the river channels of the Lhasa River basin for the past and the future periods. Most of the rivers contain meltwater from the glaciers. Only a few small valleys along the southern and the northeastern watershed and the south-central area do not contain melt water because of the absence of glacierization. About 1 m<sup>3</sup>/s is contributed by the glaciers in the mountain headwatersheds. After the confluence of river channels in the valleys, the amount increases, reaching 8 percent at the catchment outlet. In order to determine the percentage of ice-melt water, the difference in the simulated runoff of the two model settings is divided by total runoff including ice-melt water. The percentage of the melt water in the mean annual runoff is illustrated in Figures 6.24 and 6.25 (separate maps in Appendix 26). While ice-melt water amounts to between 50 and 100 percent in the glacier headwatersheds, it rapidly decreases as basin area increases. Only between 1 and 5 percent of the water in larger rivers can be attributed to glacier melt. As the glacial coverage of the south-eastern region is larger than that of the other regions, the Toelung River, the western river confluencing with the Lhasa River after the city of Lhasa (see Figure 2.1), contains between 5 and 10 percent ice-melt water. This figure consequently increases for the Lhasa River increases from 2 percent to 4 percent after its confluence with the Toelung River.



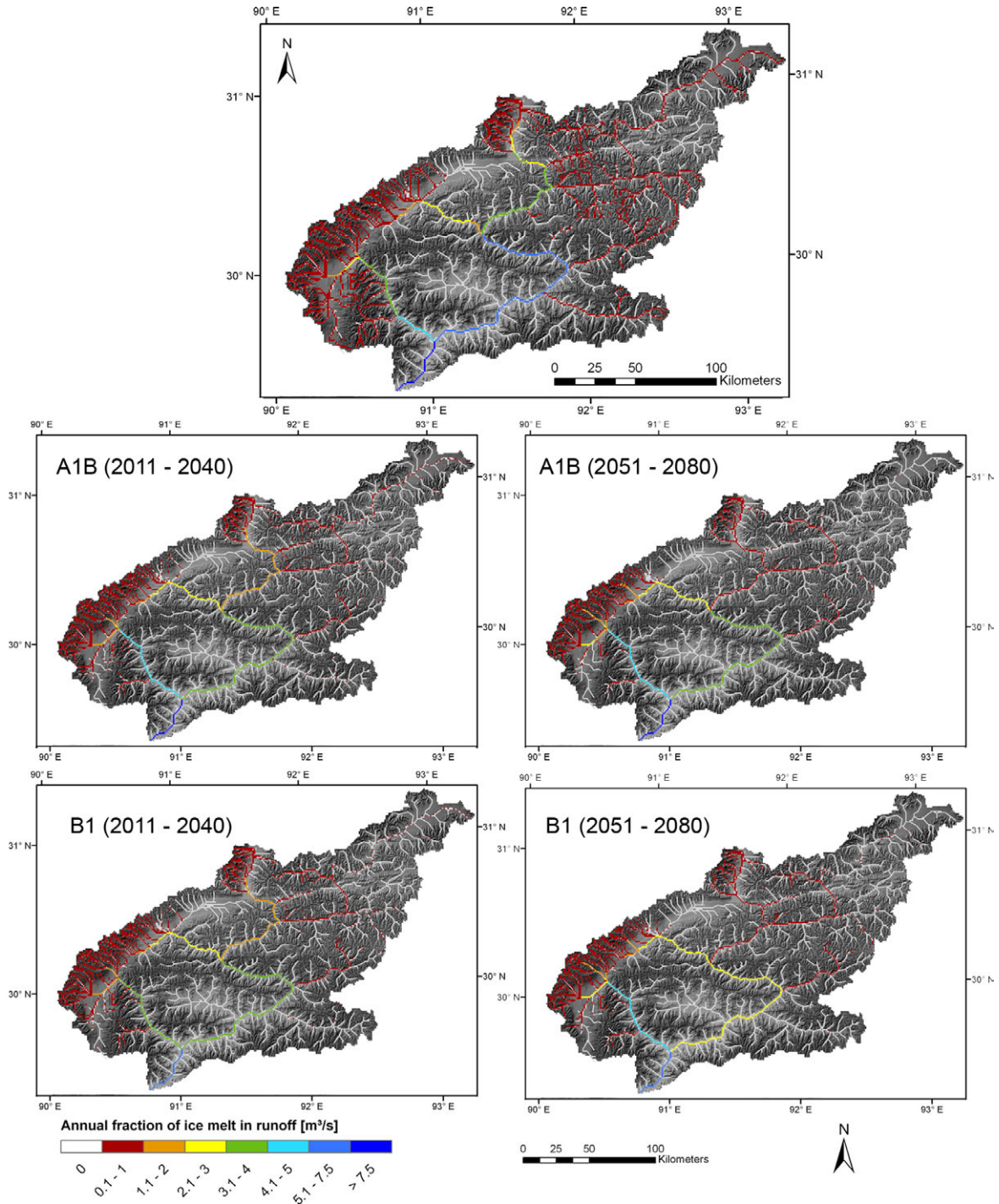


Figure 6.23: Mean annual ice-melt contribution to runoff from 1971 to 2000 (top), 2011 to 2040 (left) and 2051 to 2080 (right) according to the A1B scenario (middle) and B1 scenario (bottom).

Glacier melt water release decreases under future climatic conditions in some regions, corresponding with the retreat of the glaciers. In the first future period of 2011 to 2040, the small contribution in northeastern and the southern areas decreases further in both scenario runs. Ice-melt levels decrease in most rivers. Only in the A1B scenario a slight increase is simulated in the ice-melt contribution, for the Upper Toelung Chu. In the second future period, the glaciers in the north-east disappear. Consequently, no ice-melt water is contributed there. While the pattern under A1B conditions is similar to the first future period, a further decrease is modelled in the B1 simulation, except in the Toelung

Chu, where the amount of glacier meltwater increases. The annual percentage of ice-melt water in the scenario results (Figure 6.24 and Appendix 26) shows similar patterns for both the A1B and the B1 conditions. Except in the highly glaciated headwatersheds, the percentage of meltwater from the glacier ice clearly decreases.

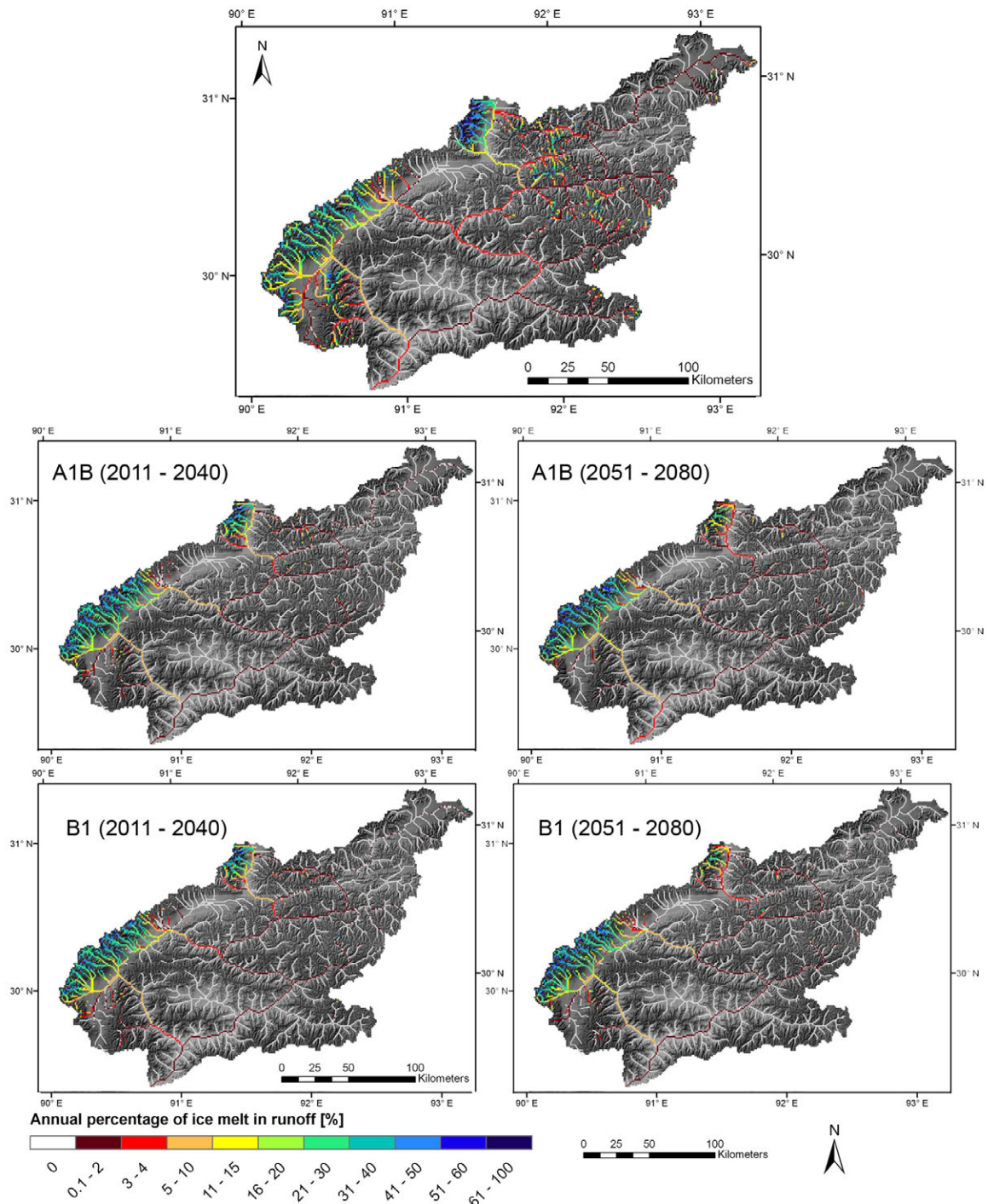


Figure 6.24: Mean annual percentage of ice-melt on runoff from 1971 to 2000 (top) and in the periods of 2011 to 2040 (left) and 2051 to 2080 (right) according to the A1B scenario (middle) and B1 scenario (bottom).

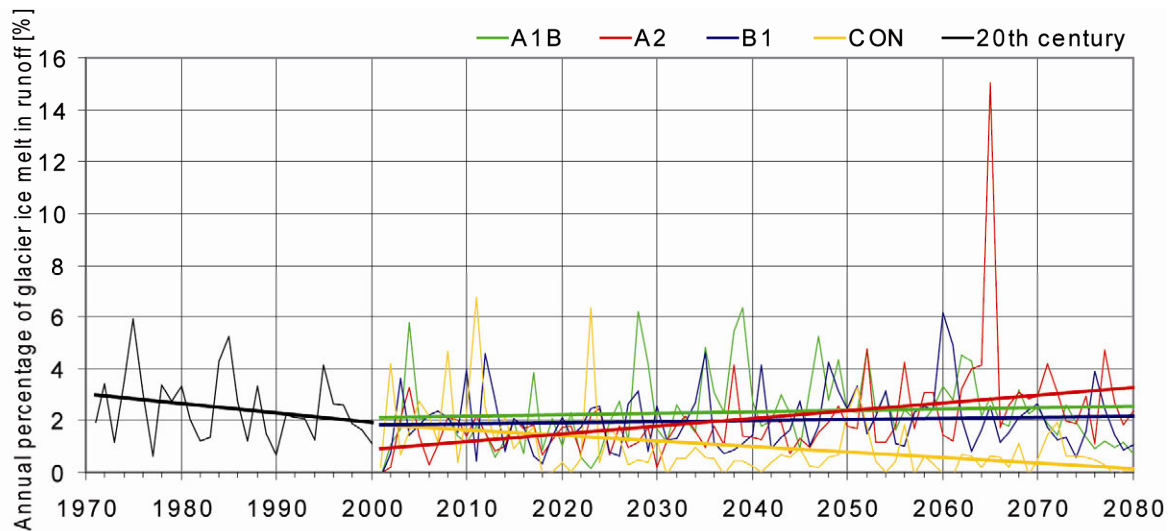


Figure 6.25: Development of the annual percentage of glacier ice-melt in runoff at the Lhasa River catchment from 1971 to 2080 according to the CLM ECHAM 5 IPCC SRES scenarios.

The development of the annual percentage of the glacier ice-melt for all four scenario runs under past and future climatic conditions is shown in Figure 6.25. A clear decrease is simulated for the past 30 years, whereas the percentage of ice-melt develops differently for the scenarios in the future. The changes in runoff are nevertheless considered: the trend follows the development of absolute ice-melt (see Figure 6.16). Thus almost no trend can be seen in the A1B and the B1 simulations, whereas an increase is modelled in the A2 scenario. However, differences occur between the course of the absolute amount of ice-melt and the percentage in some years. For example, in the model year 2023, the contribution by ice-melt is almost negligible, whereas in 2028 and 2038 the amount is above average in the A1B scenario. The peaks of 2060 in the B1, and especially of 2065 in the A2 scenario simulations are particularly remarkable. Their peaks correlate with peaks in the total amount of meltwater, but the magnitudes differ. Although the amount of meltwater is similar in the A1B and the B1 simulations, the percentage differs. The quantity of annual runoff is quite a determinant of magnitude, because the peaks correlate to the minimum runoff. In contrast, the minimal percentages of ice-melt are associated with relative runoff peaks. As the runoff minimum can predominantly be attributed to comparatively sparse precipitation, a balancing effect by increased glacier melt water release in those years is deduced.

However, not only is the annual amount of the melt water release decisive, but its seasonal distribution also proves the compensation effect of glaciers. Figure 6.26 shows the average monthly course of the glacier ice-melt contribution for the past and future 30-year periods of the A1B simulation at the catchment outlet and the Yangbajing gauge, considering two (sub-)basins with varying glacierization. In Figure 6.27 the results are illustrated parallel to the A1B scenario for the B1 scenario.



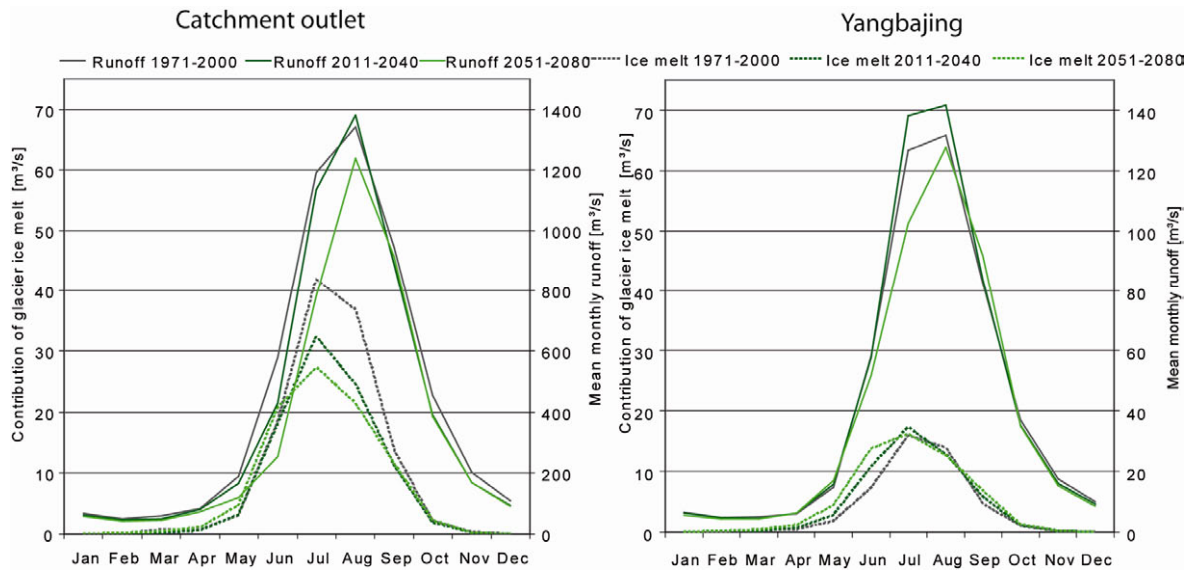


Figure 6.26: Seasonal distribution of glacier ice-melt contribution and runoff for the three climate periods of 1971 to 2000, 2011 to 2040 and 2051 to 2080 according to the A1B scenario at the catchment outlet and Yangbajing.

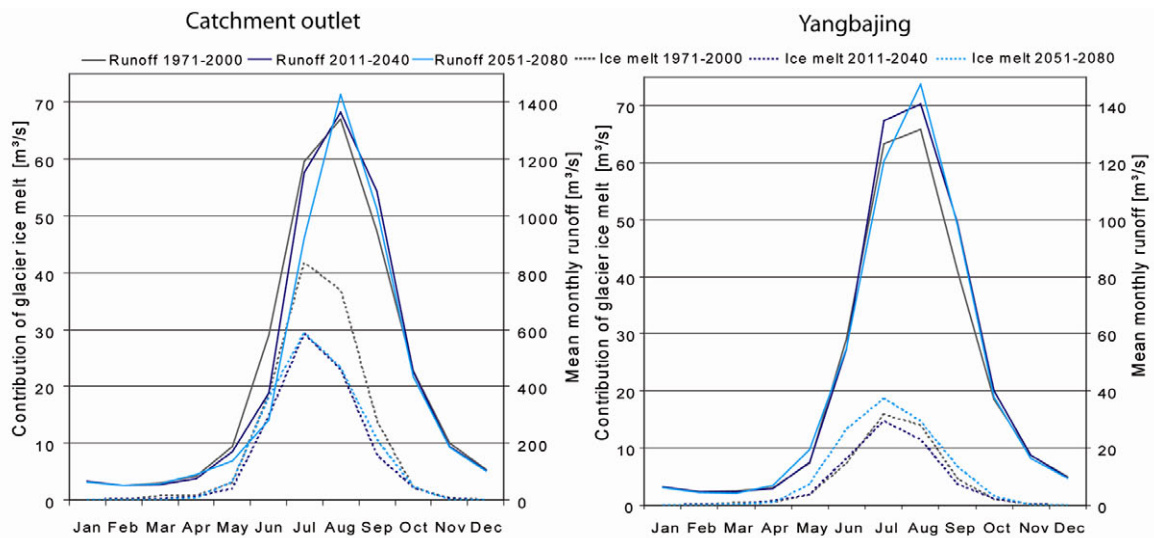


Figure 6.27: Seasonal distribution of glacier ice-melt contribution and runoff for the three climate periods of 1971 to 2000, 2011 to 2040 and 2051 to 2080 according to the B1 scenario at the catchment outlet and Yangbajing.

During winter, almost no ice-melt occurs, since the glaciers are snow-covered. Moreover, no melting conditions occur at the elevations of glaciers in general; rarely, little evaporation can occur because of the high solar radiation input. In accordance with increasing temperatures, the ice-melt begins before the monsoon precipitation starts. The maximum release is simulated for July, whereas the runoff peak is simulated for one month later. Afterwards, the ice-melt water decreases, and ends in October. In the seasonal course, both the peaks in runoff and ice-melt occur during summer, synchronous with the monsoon precipitation. Since precipitation falls as snow only in the highest areas, melting conditions dominate in the lower areas. Consequently, the glacier surface becomes snow-free. The seasonal course is similar under changing climatic conditions, whereas the melt water contribution clearly decreases during summer according to the

A1B and B1 scenario runs at the catchment outlet. In contrast, almost no changes are simulated at the catchment outlet under A1B climatic conditions. The contribution at Yangbajing does not increase during the final future period, according to the simulation.

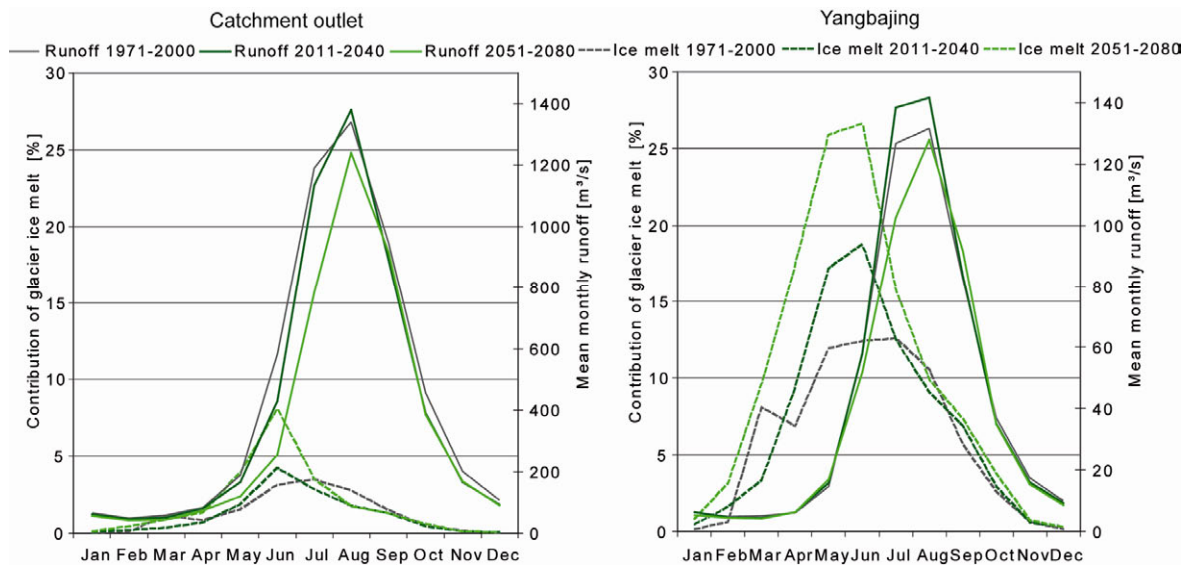


Figure 6.28: Seasonal distribution of the percentage of glacier ice-melt contribution and runoff for the three climate periods of 1971 to 2000, 2011 to 2040 and 2051 to 2080, according to the A1B scenario at the catchment outlet and Yangbajing.

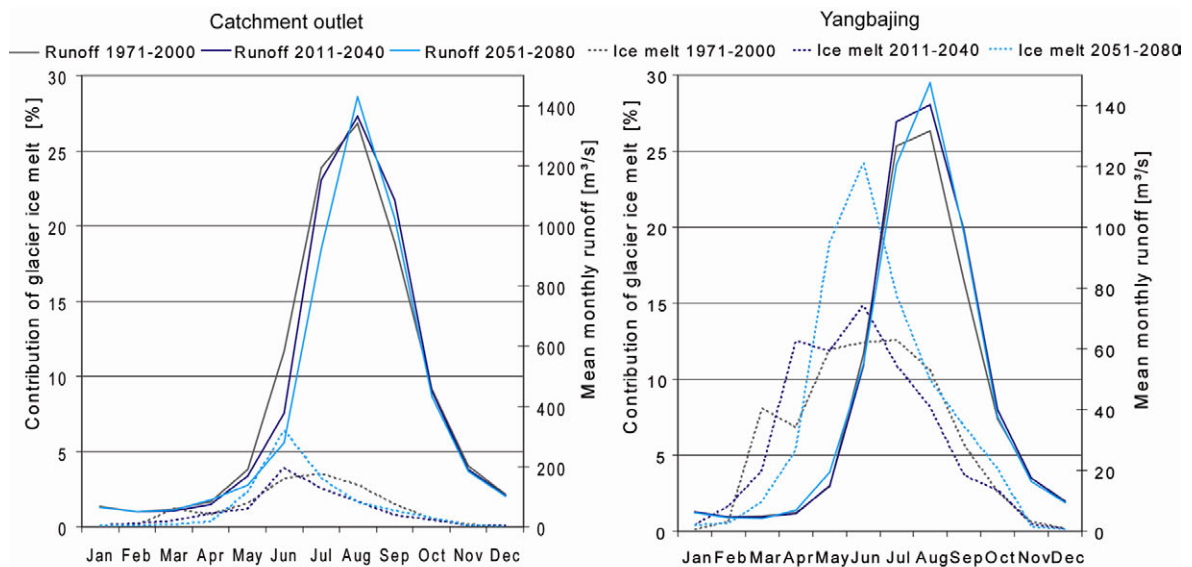


Figure 6.29: Seasonal distribution of the percentage of glacier ice-melt contribution and runoff for the three climate periods of 1971 to 2000, 2011 to 2040 and 2051 to 2080, according to the B1 scenario at the catchment outlet and Yangbajing.

The seasonal course of the percentage of ice-melt to monthly runoff (Figures 6.28 and 6.29) is similar to the total amount in the past, with its peak in July. However, the importance of the ice-melt is higher in spring, before the monsoon begins, than in the post-monsoon period when, for instance, the water storages of the soil are full. Rain and meltwater thus contribute to runoff. A maximum value of 4 percent at the catchment outlet was simulated for the past, whereas the Yangbajing percentage varies around 13 percent in July. Under future climatic conditions, the peak of the percentage shifts to June in both

scenarios and at both stations. In the early spring, the importance of the melt water release doubles at both stations while the runoff decreases, although the total amount of meltwater released is reduced. This effect can also be seen in the distribution of the annual values in Figures 6.23 and 6.24.

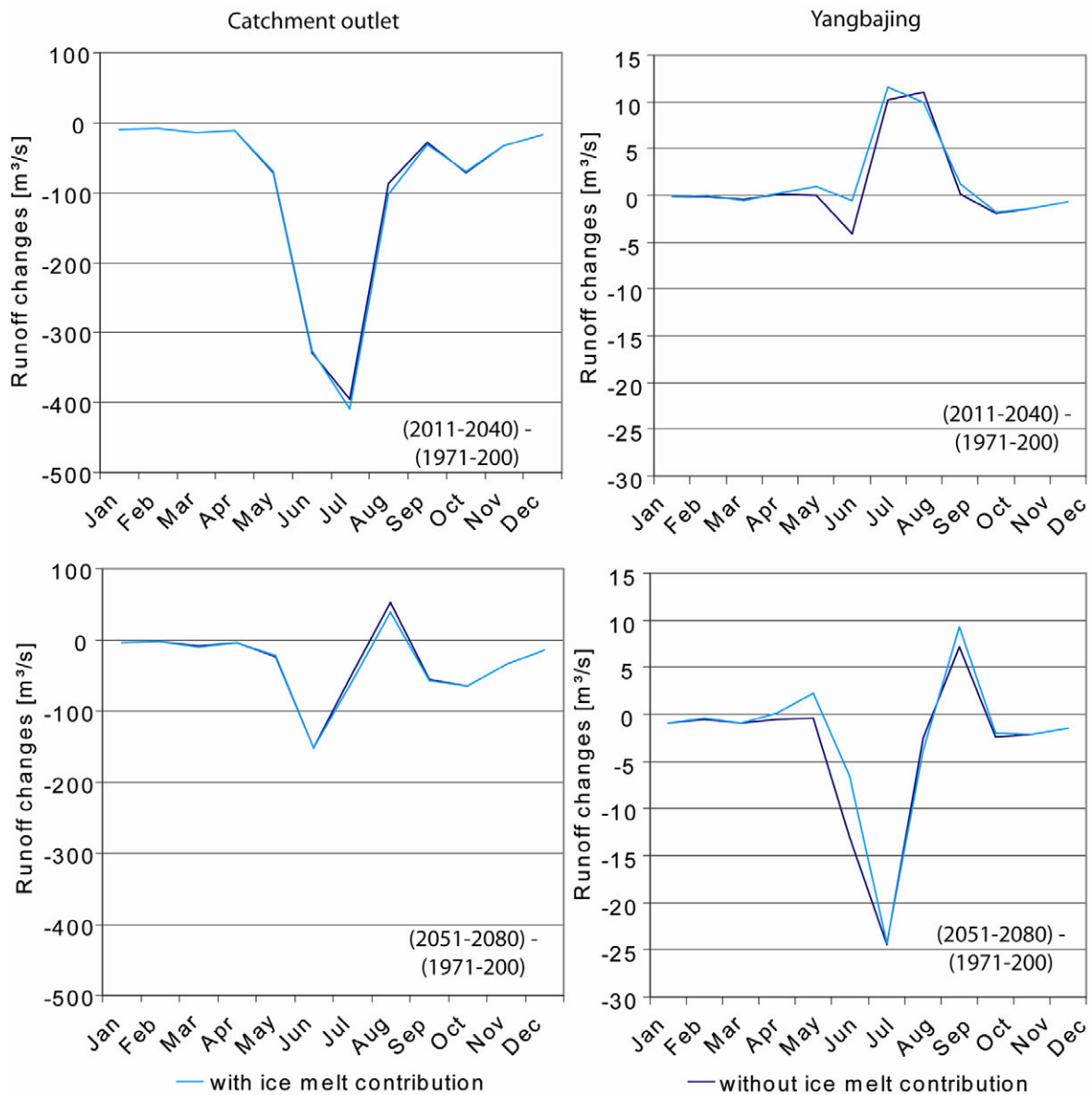


Figure 6.30: Comparison of future runoff changes with and without consideration of ice-melt contribution at catchment outlet (left) and at Yangbajing (right) and for 2011 to 2040 (top) and from 2051 to 2080 (bottom) in comparison to the period 1971-2000 for the A1B IPCC SRES scenario run.

In order to further analyse the contribution of the glacier melt water to runoff, the runoff changes of the two future periods relative to the past period are calculated with and without consideration of ice-melt (Figure 6.30). The changes are similar for both options at the catchment outlet. Consequently, glacier meltwater cannot compensate the decrease in runoff. In contrast, at Yangbajing there are differences between the results with and without consideration of ice-melt contribution. In May, June and July of the first future period, the increasing ice-melt compensates the small runoff reduction, and so a slight increase can be seen in the runoff. This compensation effect can also be seen in May and

June of the second future period, although the melt water only relaxes the situation somehow, but cannot fully compensate the runoff reduction.

The average contribution of the glacier ice-melt water to runoff in most parts of the Lhasa catchment is nevertheless very small. The comparison of the mean daily amount of precipitation, snow- and ice-melt to the daily runoff in Figure 6.31 shows the importance of the monsoon precipitation for runoff. The snowmelt's contribution to the runoff is the second most important factor, whereas the amount of ice-melt only varies about 0.1 mm per day. The decrease in runoff during spring under scenario conditions (Figure 6.31, A1B) can therefore be traced back to the changes in snowmelt. While the course of precipitation is almost stable throughout the year, the amount of snowmelt decreases, because of higher air temperatures and reduced snowfall (see section 6.2). This reduction is particularly significant in spring and early summer.

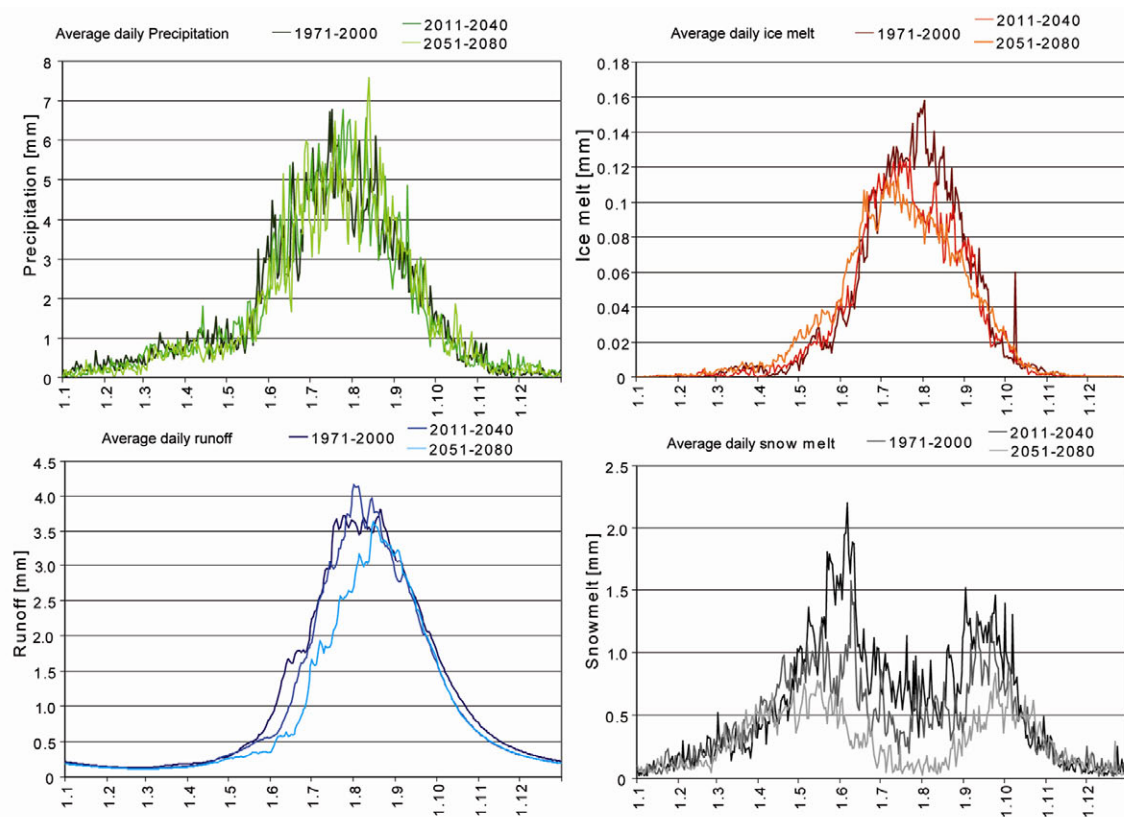


Figure 6.31: Comparison of changes in the mean daily courses of snow- and icemelt, precipitation and runoff for the three climate periods for the Lhasa River catchment under A1B IPCC SRES conditions.

The impact of the compensation effect of glacier ice-melt is analysed for years with lower than average monsoon precipitation. The model year 2039 of the A1B scenario is analysed in detail in Figure 6.32. In the simulation, little precipitation falls in June and July and almost no snow-melt is simulated for the same period. At the catchment outlet during this time, the percentage of glacier ice-melt to runoff increases to a maximum value of 35 percent at the outlet gauge (Figure 6.32, left), which is illustrated in light blue in the runoff line. Nevertheless, the runoff is reduced by about 75 percent compared to the average amount, which is then reached after considerable precipitation in August. The



ice-melt water contribution hence cannot compensate the missing rain- and snowmelt-fed discharge, which is then clearly reduced. The situation at the Yangbajing gauge is different: here, the glacier ice-melt water contributes up to 80 percent of the water in the river during the dry period. Although the rain is absent, the runoff decrease is not as pronounced as it is at the outlet gauge. The reduction only amounts to half of the average runoff. In this case, between 70 and 80 percent of the water comes from the melting of glacier ice. Thus, without the ice-melt contribution, illustrated in light blue in the runoff curve, almost no water would be available in Yangbajing (Figure 6.32, right).

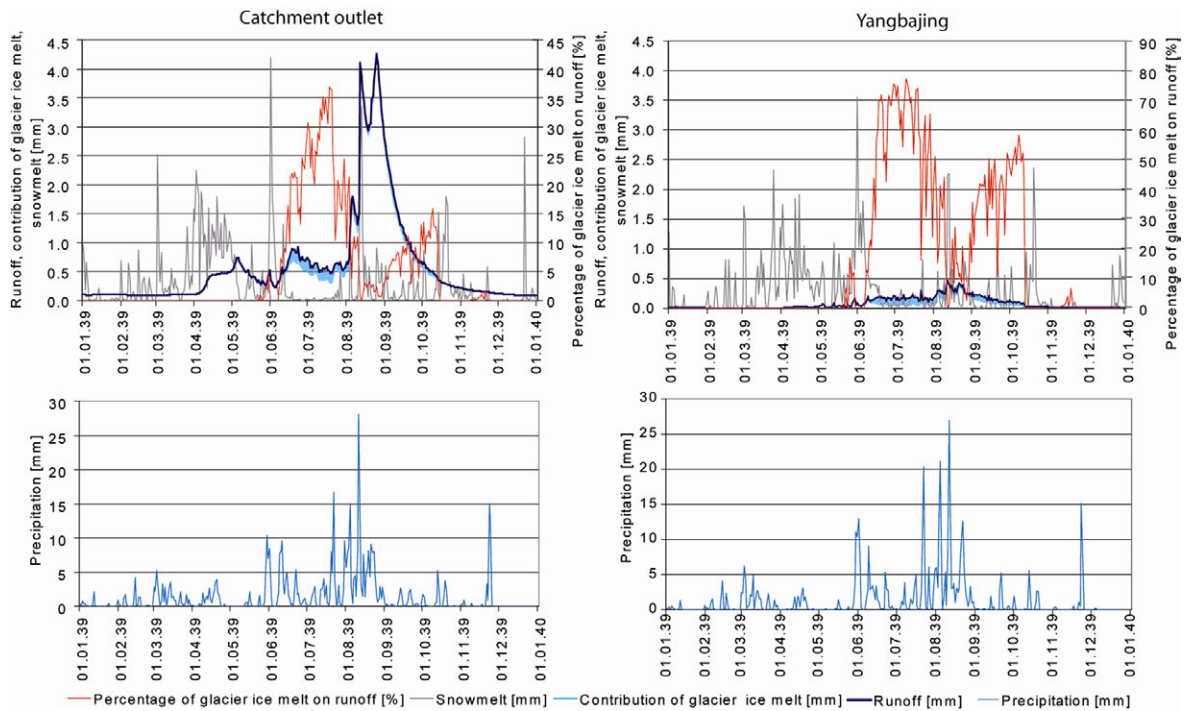


Figure 6.32: Influence of glacier ice-melt water in periods with little monsoon precipitation at the basin outlet (left) and at Yangbajing (right).

The previous analysis leads to the conclusion that changes in the monsoon pattern are not be fully compensated by glacier melt water. However, in regions with a glacial coverage above 10 percent, as it is the case in the sub-catchment of Yangbajing, glacier melt water contributes most of the discharge in this situation and balances the missing precipitation. Accordingly, only along the headwatersheds can a compensating effect be concluded for the Lhasa River basin. The spatial distribution of river channels, for which the effect can be assessed, is illustrated in yellow, green or blue in Figure 6.24, which also clarifies the changes under future climatic conditions. Although the ice water reservoir clearly decreases, the amount of melt water release decreases only slightly (see section 6.4) and the percentage even increases slightly due to changes in runoff.

In order to categorize glacier ice-melt among the various water balance factors, the input and output factors are separated, as illustrated, for all sub-catchments and the basin outlet in Figures 6.33 and 6.34 and in Appendices 27 and 28 for the period of 1971 to 2000 and the periods 2011 to 2040 and 2051 to 2080. Input factors comprise rainfall, snow- and icemelt and evapotranspiration and runoff are output factors of the water balance. Changes in soil water content and ground water are below 1 percent.

Consequently, they are stable in the Lhasa River basin in the simulations and so are not considered.

The minor importance of the ice-melt in comparison to such other factors as rainfall, snowmelt and evapotranspiration is clearly demonstrated. While a contribution of 8 percent was simulated at Yangbajing, at the other gauges it varies between 1 and 2 percent. Snowmelt amounts to around 30 to 40 percent, whereas rainfall is the most important factor throughout the Lhasa River basin. As the ice-melt and the monsoon rainfall occur simultaneously, the average importance is low. The output parameters of the water balance, such as runoff and evapotranspiration, are also illustrated. About 30 percent of the water evaporates, whereas 70 percent is released as runoff.

Under future climatic conditions, the annual percentage of ice-melt remains almost stable, although an increase to 10 percent is simulated in Yangbajing in both the A1B and the B1 scenario, whereas a decrease to 1 percent is modelled at the gauges of Pangdo and Tangga. The retreat is explained by the disappearance of glaciers in the north-eastern parts of the basin. In contrast to the annual changes in ice-melt during the climate periods presented, the decrease in snowmelt is significant. During the final future period, it varies between 13 percent in Yangbajing and 20 percent in Pangdo in the A1B. Since the changes of the meteorological parameters are smaller in the B1 scenario, snowmelt varies between 19 percent in Yangbajing and 24 percent in Pangdo in the B1 run. The importance of rainfall consequently increases at all gauges. Because evapotranspiration also rises noticeably (see also Figure 6.18), its influence on the water balance also increases. Due to an almost stable precipitation level, runoff decreases.

To sum up, the amount of precipitation and evapotranspiration determine water availability for the water balance in the Lhasa River basin. Significant changes in snowmelt and evapotranspiration cannot be compensated by ice-melt in most parts of the catchment. Thus, less runoff on average is simulated under changing climatic conditions. In areas with glacial coverage of above approximately 10 percent, the reduction is nonetheless lower, as a result of increasing proportions of ice-melt.

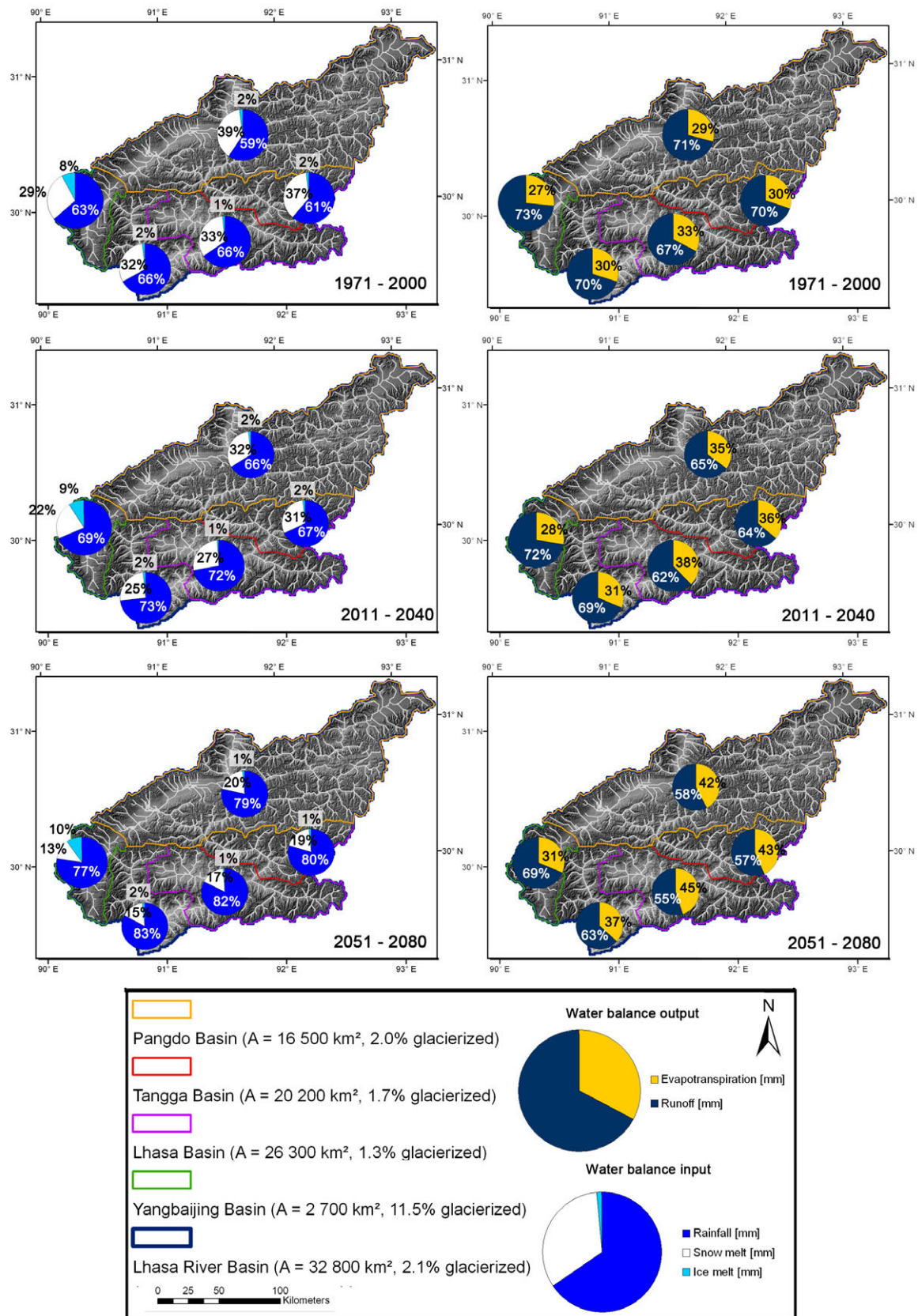


Figure 6.33: Mean annual percentage of inputs and outputs to the water balance in the sub-catchments from 1971 to 2000 (top), and in the periods of 2011 to 2040 (middle) and 2051 to 2080 (bottom) according to the A1B scenario.



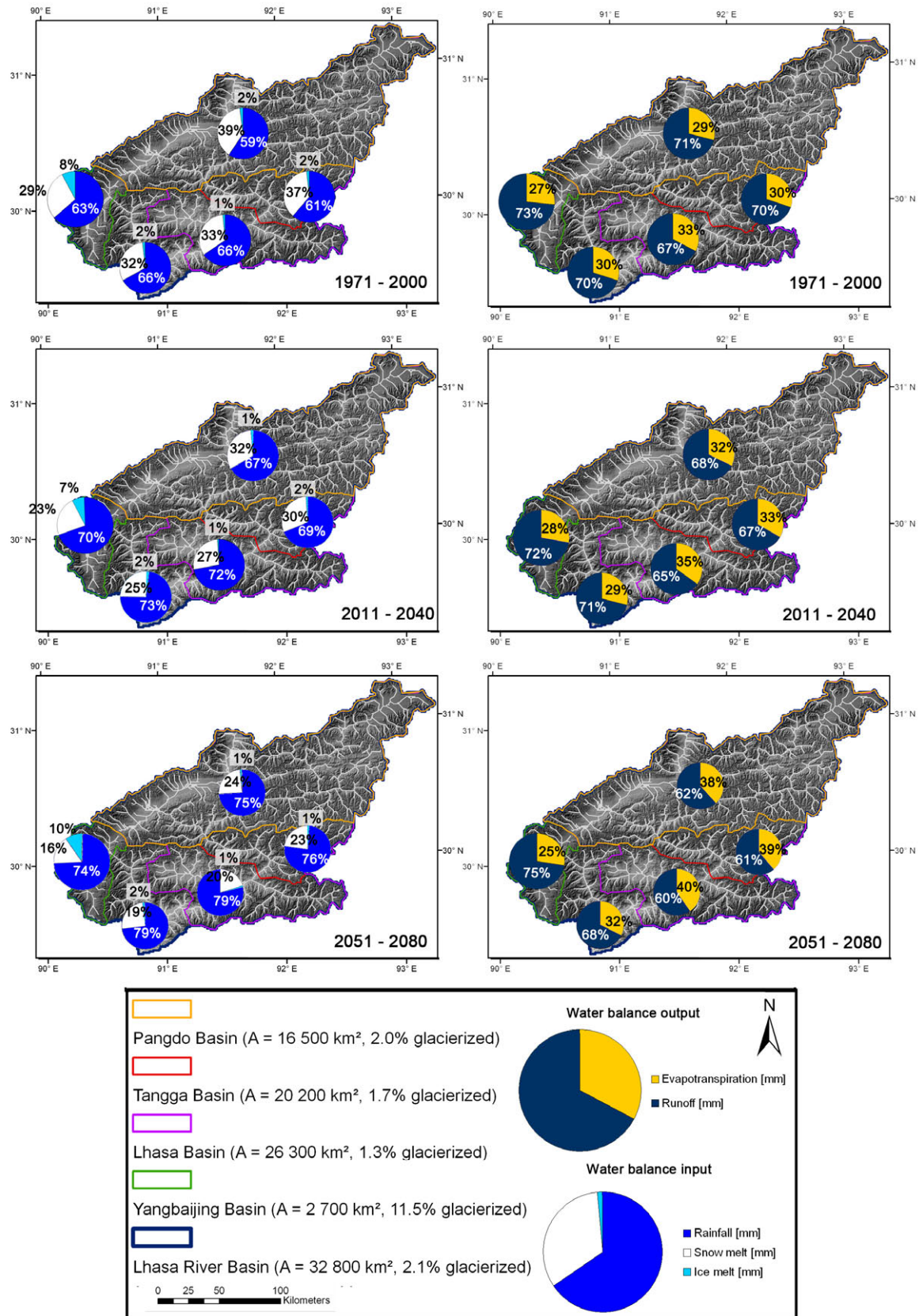


Figure 6.34: Mean annual percentage of inputs and outputs to the water balance in the sub-catchments from 1971 to 2000 (top), and in the periods of 2011 to 2040 (middle) and 2051 to 2080 (bottom) according to the B1 scenario.

## 7 Conclusion and Outlook

The modelling approach presented, of SURGES integrated in PROMET, enables spatially distributed simulation of the main processes of meltwater release acting on a glacier, together with detailed simulation of all relevant hydrological processes. The regional heterogeneities of a meso- or macroscale river basin are considered, with their physiogeographic characteristics, by using a fully spatially distributed raster model with a resolution of 1 x 1 km. Since the models are based on physical principles, use universal parameters, conserve mass- and energy balances and are not calibrated to measured runoff, they fulfil the requirements for application under future climatic conditions. The coupling tool SCALMET allows RCM outputs to be used as meteorological drivers.

Although the models require a broad range of input data due to the complexity of the subject to be modelled, this study demonstrates their applicability in remote regions by using publicly available data. The validation for the Lhasa River catchment presented proves the reliability of the model results for glaciers and for the hydrological water balance. This also includes the application of the downscaled CLM ERA 40 and ECHAM 5 meteorological drivers.

The analysis of the model results shows the dominant dependency of the Lhasa River runoff on precipitation and evapotranspiration. The amount of snowfall and the subsequent duration of snow cover are particularly important for discharge. As a consequence, the seasonal course is determined by snowmelt and rainfall. The runoff course follows the monsoon precipitation, peaking in summer. Under average climatic conditions, the amount of meltwater contribution from glacier ice, considered independently of snow-melt release, is only significant in headwatersheds with a glacial coverage of above approximately 10 percent. In the Lhasa River basin, this is the case for about 8 percent of all river channels, e.g. for those reaching from the sub-basin to the gauge in Yangbajing. Solely considering the channels that contain meltwater from glaciers, the contribution is significant for approximately 50 percent of them. In Figure 6.24, the spatial distribution of such river channels is illustrated in yellow, green or blue. Those rivers are mainly located along the northwestern watershed of the Nyainqêntanglha Mountains.

Even though the amount of water contributed to runoff by glaciers is small on average in most parts of the Lhasa River basin, the glacier ice reservoir serves as a reliable water source in certain cases. When the monsoon is delayed, or brings sparse precipitation, glacier meltwater is still released. In these cases, up to 40 percent of runoff originates from glaciers at the catchment outlet of the Lhasa River basin. However, the quantity of the water does not replace the missing precipitation, and so the runoff is clearly lower than average. At Yangbajing, the ice-melt contribution increases to 80 percent in such dry periods, but the runoff is still reduced to approximately half of the mean discharge. Nevertheless, the comparison of runoff with and without ice-melt contribution shows improved water availability in those regions compared to rivers without glacier headwatersheds. At this point, the direct release of the meltwater into the river channel, in

contrast to precipitation, which first fills soil water storage, should be mentioned. This enhances its impact in comparison to precipitation with delayed contribution.

Under future climatic conditions, the simulation results show a continuous decrease in the runoff for all CLM ECHAM 5 IPCC SRES scenario runs applied, with varying significance. In both the mid-term (2011-2040) and the long-term (2051-2080) future decades, the reduction in water availability compared to the past decades (1971-2000) is strongest in the Lhasa River basin in the A1B scenario. The reason for the decrease is the modelled temperature increase, whereas precipitation remains almost stable. The amount of evapotranspiration consequently increases, whereas snowfall is significantly reduced. Snow cover duration is shortened at all elevation levels. As a result, the glacier ice reservoir and the glacier area shrink throughout the Lhasa River basin. Since no longer periods with above-average snowfalls are simulated by the CLM runs, no recovery periods with mass gain by the glaciers occur. As a consequence, the additional melt due to increasing temperatures can not be compensated. However, changes in the amount of melt water release from glaciers are marginal. Less snowfall and shorter snow periods with a reduction of between two and three months because of higher air temperatures enable the melting of ice during longer periods. Additionally, a shift of the snow conditions of about 500 to 1000 m results in larger snow-free glacier areas where melt occurs. Accordingly, the continuous reduction of glacierized area and glacier ice reservoir is compensated by ongoing snow cover shifts with larger melting areas and longer melting periods. Furthermore, the large ice reservoirs at altitudes between 5600 and 6100 m a.s.l. (see Figures 4.3 and 4.7), particularly in the Nyainqêntanglha Mountains, resist increasing melting conditions for a long time, so that the total melt out of glaciers is not reached until 2080 according to the scenario simulations (see Figure 6.11). Since glaciers in the Lhasa River basin extend over altitudes up to 7000 m a.s.l., there are still glacierized areas left where melting conditions are similar to the present situation despite the impact of GCC. This is for example a major difference to the glacier retreat in the Eastern Alps with altitudes up to 4000 m a.s.l.

The contribution of ice melt water to runoff at the catchment outlet is slightly reduced in the future periods, whereas the quantity remains almost stable from the sub-basin to the Yangbajing gauge, as enough ice water reservoir remains despite the retreat. In contrast, a total retreat of glaciers is simulated for the northern regions of the Lhasa River basin. The contributed meltwater is thus reduced at the catchment outlet.

The analysis of the seasonal runoff course and ice-melt contribution shows a compensation effect at Yangbajing during spring, whereas no significant differences with or without ice-melt contribution to runoff can be seen at the catchment outlet. Hence, in basins with a glacial coverage of above approximately 10 percent, a compensational effect of the glacier ice-melt to runoff decrease is deduced. Significantly more water is therefore available altogether, although a runoff reduction is simulated in some months. After the total retreat of glaciers such as that of the northeastern parts of the Lhasa River catchment, substantially less water will be available in those sub-basins, especially during dry periods.

The results presented allow the conclusion that the reduced glacier reservoir has no significant impact on runoff under average conditions in the Lhasa River basin, contrary to IPCC statements (IPCC 2007A). The monsoon precipitation and subsequent snowfall are the key factors for water availability in the Lhasa River basin. Moreover, low flow situations usually occur during winter. As almost no glacial meltwater is released in the winter months, no balancing effect during low flow can be caused by glaciers. Shifts in the timing and intensification of the precipitation pattern and an earlier snowmelt will therefore significantly influence water availability. However, according to the simulations driven by CLM ECHAM 5 model outputs in this study, no significant changes during winter runoff are predicted. In accordance with the results found by THAYYEN AND GERGAN (2010) for a "Himalayan catchment", defined as dominated by monsoon precipitation and a runoff peak in summer, precipitation determines the amount of discharge in the simulation. Furthermore, below-average flows are related to low precipitation and cannot be compensated by increased meltwater. The future development of monsoon precipitation under global climate change conditions, which is most important for water availability in this region, still needs further investigation, because of, for example, the complicated relation between the El Niño Southern Oscillation phenomenon and Himalayan / Eurasian snow cover. Spatial distribution is still especially difficult to simulate (KRIPALANI ET AL. 2007, DOBLER AND AHRENS 2010). Hence, significantly increased monsoon precipitation would modify the simulation result for runoff and glacier changes. However, an extensive precipitation increase would be required to stop glacier retreat, since 10 percent increase in precipitation per degree of warming is not sufficient, according to OERLEMANS ET AL. (1998).

Since the impact of Global Climate Change differs regionally due to varying physiographic conditions, spatially distributed simulations are required to reliably assess the consequences and subsequently derive appropriate adaptation strategies. The impact on rivers originating in the Himalayas particularly requires distributed analysis, not only because the monsoon varies a lot, but also because the local climatic conditions themselves also vary distinctly. The basins in the Kashmir and Karakorum region are dominated by winter snowfall. In Ladakh, cold-arid climatic conditions occur, in contrast to the monsoon precipitation in summer in India and in parts of Tibet, as is the case in the Lhasa River basin. Accordingly, no general conclusions about the Himalayas can be drawn without distinguishing regional conditions (THAYYEN AND GERGAN 2010).

Finally, the ability of hydro-glaciological models to couple with climate models allows the simulation of a variety of predicted climatic conditions. This is important because the models differ, particularly when simulating the monsoon precipitation (KRIPALANI ET AL. 2007). As its amount is the key to water availability in the Lhasa River basin, the results are limited to the quality of input of the CLM ECHAM 5 outputs and the applied downscaling. However, the results reproduced past conditions in hourly and daily resolutions, as shown above. Further uncertainties of the results presented emerge from the derived initial conditions of the glacier inventory. Ice-thickness, which determines the durability of glacier ice at the chosen elevation levels, and the consequent meltwater release were derived with an approach using relations derived in the Alps. Although the

glaciers there are similar to those of the Lhasa River basin, the approach requires further validation in Asian regions with available ice thickness data. Mass balance data from glaciers in the basin would further improve the reliability of the results. Nevertheless, the simulations are in accordance with values stated for this region. Disregarding the effect of delivering ice from the accumulation to the ablation area by means of ice flow limits the simulated decrease in ice coverage. Although the glacier geometry is dynamically adapted in the reduction of area after the ice melt and the ice flow slows down in shrinking glaciers, it has to be adequately considered. The CON simulation provides an informative basis for that. Although the climatic conditions are almost constant and the ice reservoir stays almost constant throughout the basin, the glacier area clearly decreases after the equilibrium is reached, indicating the consequences of missing ice flows. The reverse conclusion can therefore be drawn, that the amount of glacier ice transported from the accumulation area to the ablation area can be estimated in determining the required ice mass. The glacier area thus would almost stay constant. Accordingly, a redistribution factor to describe the amount of transported ice could be deduced. Further enhancements of the glacier model include the consideration of more subscale processes on a physical basis. This includes the shading of the mountains, which is important in mountainous regions, especially on the Tibetan Plateau with the high solar radiation input. Wind-induced snow transport, together with the shading, enables the formation of a glacier in some cases, and so its inclusion in model could improve the simulation. Taking into account lateral heat flows from surrounding snow-free rocks to the neighbouring glaciers would also enhance the modelling approach. Finally, coupling with climate models should be bidirectional at a high spatial resolution, to consider, for instance, changes in snow and ice. The feedback of the disappearance of snow and glaciers significantly modifies the albedo, altering the radiation balance. The energy consumed for melting snow and ice reduces warming: as a result, the temperature increase is above-average after the melt, especially in mountainous regions, an effect which can also be found for the Tibetan Plateau (LIU AND CHEN 2000). Changes in permafrost result in an increase in debris cover on the glacier surface resulting in decreased albedo. Considering the feedbacks to both absorbing radiation and protecting the glacier surface of the coverage could also enhance simulation of the melt water release. This also applies to rock glaciers.

To sum up, the approach presented in the thesis enables the distributed simulation of ice-melt water release from glaciers and the influence of this contribution on water balance in a remote largescale river basin with sparse data availability. The characteristics of the models enable application under past and future climatic conditions using RCMs as meteorological drivers. Although there are still uncertainties, the approach delivers reliable results in high spatial and temporal resolution forms the basis for developing IWRM strategies to adapt to GCC.

## 8 Summary

This thesis presents an approach to simulating the role of glacier meltwater in runoff, in comparison to such other water balance variables as snow-melt, evapotranspiration and precipitation, under past and future climatic conditions in the Himalayan catchment of the Lhasa River with its scarce data availability. Mountain regions are of global importance in providing fresh water downstream. The function of temporal storage of precipitation and its delayed release during melting is one of the key characteristics of glaciers. Simulating the impact of global climate change on glaciers and on melt water release therefore provides information for the assessment of adaptation strategies in order to support future water availability.

The Lhasa River catchment provides an appropriate largescale test site, with the Nyainqêntanglha Mountains that form the northern watershed, as part of one of the largely glacierized regions of Central Asia. Because sparse data are available, the transferability of the modelling approach to remote regions is also evaluated. The natural characteristics of the catchment are determined by the high elevation of the Tibetan Plateau and its mountainous relief. The monsoon precipitation during summer and the dry season in winter are relevant for water availability, causing a clear seasonal runoff course which peaks in August.

The glaciers in the catchment amount to 670 km<sup>2</sup>. They are classified as mountain and valley glaciers, and small glacierets can also be found. Their properties resemble those of the glaciers of the Eastern Alps (Chapter 2).

In order to model the contribution of glacier meltwater under changing climatic conditions, several requirements should be fulfilled by the modelling approach as presented in the introduction (Chapter 3). This includes the use of universal parameters, conservation of mass and energy, the use of physical principles as model basis and the abandonment of calibration to measured runoff. As the meltwater release from glaciers is dependent on the snow-free area, glacier geometry and mass and energy balances on the glacier need to be considered in the model. However, the hydrological model should also reproduce the regional heterogeneities of a meso- or largescale river basin in simulating processes for the runoff formation. As the requirements are fulfilled, the following models are applied in the study. The SURGES subscale glacier simulator was implemented within the PROMET hydrological model, to simulate the main glaciers and the detailed hydrological processes. PROMET is a fully spatially distributed raster model with a resolution of 1 x 1 km, and runs on an hourly time step. For simulation of hydrological processes under changing climatic conditions, it uses distinct components for meteorology, land surface energy and mass balances, vegetation, snow and ice, soil hydraulics and soil temperature. Groundwater and channel-flow components with hydraulic structures are also included. In order to capture the small-scale processes for melt water release acting on the heterogenic glacier surfaces, SURGES uses a subscale approach. The area elevation of the glacier is approximated in subscale units with similar surface elevations. The simulation of the processes includes meteorological data extrapolation to all elevation levels, calculation of



the mass and energy balances on the glacier surfaces, snow metamorphism and glacier geometry changes. The SCALMET coupling tool enables the application of RCM outputs as meteorological drivers in downscaling the coarse resolution of the climate model outputs to the PROMET resolution of 1 x 1 km (Chapter 3).

Since sparse data are available for running the model framework in the Lhasa River basin, a method of deriving the required input data by using publicly available data is introduced. As well as the application of the RCM outputs of the CLM ERA 40 and ECHAM 5 model runs and land surface data parameterization, the glacier input data derivation is also presented in detail. The Chinese Glacier Inventory provides the glacier area. By intersecting it with a digital elevation model, elevation levels for all glaciers in the Lhasa River basin are deduced. Finally, the ice thickness for every elevation level is deduced by considering the slope of the elevation levels and their position on the glacier (bottom, top or middle). Relationships from the Alps are transferred to the Lhasa River basin (Chapter 4).

In Chapter 5, the approach presented is validated in detail, in comparing the model results to observations, whereby the following validation steps are carried out. First, the processes on the glacier such as accumulation and ablation of snow and ice are checked. Next, the reproduction of glacier geometry changes over a long time period is evaluated. Since the study focuses on meltwater release from glaciers, the simulated runoff of a highly glacierized basin is compared to measurements, and the necessity of the subscale approach is also tested. In the next validation step, the accuracy of the derivation of the glacier input data is checked. Finally, the performance of the modelling framework in the Lhasa River basin is evaluated. This includes the accuracy of the downscaled CLM meteorological data, the glacier changes and the water balance during the period of 1971 to 2000 (Chapter 5).

Because the model framework captures the processes relevant to simulating the influence of glacier meltwater release on runoff for past and present climatic conditions, and because the models fulfil the requirements for application under future climatic conditions, four IPCC SRES scenarios are chosen to simulate of the impact of climate change. While the level of precipitation remains almost constant in the scenario runs, the areal temperature increases significantly. As a result, the amount of snowfall and the subsequent duration of snow cover decreases, whereas evapotranspiration increases. Consequently less runoff is simulated. Thus, less water will be available in the future in the Lhasa River basin. Both the glacier ice reservoir and the glacier area continuously shrink, but do not disappear in the complete test site during the simulation period. Nevertheless, meltwater release stays almost constant under future scenario conditions, because the continuous reduction of glacierized area and glacier ice reservoir is compensated by ongoing snow cover shifts with larger melting areas and longer melting periods. Additionally, the large ice reservoirs at altitudes between 5600 and 6100 m a.s.l. (see Figures 4.3 and 4.7), particularly in the Nyainqêntanglha Mountains, resist increasing melting conditions for a long time.

The overall percentage of ice-melt contribution to runoff is small in the Lhasa River basin, although spatial differences and seasonal changes are distinguished. For sub-basins with a glacierization of above approximately 10 percent, a compensation effect by glacier meltwater is deduced, as shown for the gauge in Yangbajing. The reduction in runoff in spring because of the absence of snowmelt is attenuated by the contribution of glacier meltwater. In special cases when the monsoon is delayed or delivers only a small amount of precipitation, significantly more water is available in basins with a glacierization of above 10 percent. The contribution by the ice-melt water does not, at the catchment outlet, suffice to balance the lack of precipitation.

Consequently, the conclusion is drawn that the reduced glacier reservoir has no significant impact on runoff under average conditions in the Lhasa River basin. In fact, the monsoon precipitation and subsequent snowfall are key factors in water availability. Additionally, low flow situations occur during winter, when neither precipitation nor glacier ice-melt contribute water. Shifts in the timing and intensity of the precipitation pattern and an earlier snowmelt will therefore influence water availability most significantly. Increasing evapotranspiration also reduces future water availability.

To sum up, the approach presented in the thesis enables the distributed simulation of ice-melt water release from glaciers and of the influence of this contribution on the water balance in a remote, largescale river basin with sparse data availability. The characteristics of the models enable application under both past and future climatic conditions, using RCMs as meteorological drivers. Although uncertainties remain, the approach delivers reliable results at high spatial and temporal resolution and forms the basis for developing IWRM strategies to adapt to GCC.

## 9 References

- ALFORD, D. AND ARMSTRONG, R. (2010): The role of glaciers in stream flow from the Nepal Himalaya. *The Cryosphere Discussions*, Vol. 4, pp. 469-494.
- BACH, H., APPEL, F. AND MAUSER, W. (2008): Provision of snow information from satellite data within Polar View and application example for a mesoscale Alpine catchment using PROMET. In: STRASSER, U. AND VOGEL, M. (EDS.): Proceedings Alpine\*Snow\*Workshop, Munich, October 5-6, 2006, Germany. *Berchtesgaden National Park research report, Nr. 53.*, Berchtesgaden, pp. 18-23.
- BAHR, D. H., MEIER, M. AND PECKHAM, S. (1997): The physical basis of glacier volume-area scaling. *Journal of Geophysical Research*, Vol. 102, N. B9, pp. 20355 - 20362.
- BALDOCCHI, D.D., HICKS, B.B. AND CAMARA, P. (1987): A canopy stomatal resistance model for gaseous depositions to vegetated surfaces. *Atmospheric Environment*, Vol. 21, pp. 91-101.
- BARNES, H.H., (1967): Roughness Characteristics of Natural Channels. *US Geological Survey Water Supply Papers*, No. 1849. United States Government Printing Office, Washington, DC.
- BARNETT, T.P., ADAM, J.C. AND LETTENMAIER, D.P. (2005): Potential impacts of a warming climate on water availability in snow-dominated regions. *Nature*, Vol. 438, pp. 303 – 309.
- BAUMGARTNER, A. AND LIEBSCHER, H.-J. (1996): Allgemeine Hydrologie. Quantitative Hydrologie, Gebrüder Bornträger, Berlin, Stuttgart, 694 p.
- BAYERISCHE GLETSCHER (2009): Bayerische Gletscher. <http://www.bayerische-gletscher.de>
- BENISTON, M. (2003): Climatic Change in Mountain Regions: A Review of Possible Impacts. *Climatic Change*, Vol. 59, pp. 5-31.
- BOSTON UNIVERSITY (2004): NASA TERRA/MODIS HDF-EOS MOD12Q1 V004 Land Cover Product Binary Data, Eurasia subset, IGBP Class Scheme. Available from <http://duckwater.bu.edu/lc/mod12q1.html> (26.04.2007).
- BRAHMATWINN (2006 – 2009): Twinning European and South Asian River Basins to enhance capacity and implement adaptive management approaches. Project funded within the European Commission Sixth Framework Program. <http://www.brahmatwinn.uni-jena.de>

- BRAITHWAITE, R.J. AND ZHANG, Y. (1999): Modelling changes in glacier mass balance that may occur as a result of climate changes. *Geografisker Annaler*, Vol. 81A, No. 4, pp. 489-496.
- BRAUN, L.N., ESCHER-VETTER, H., HEUCKE, E., SIEBERS, M. AND WEBER, M. (2004): Experiences with the new "Vernagtbach" hydro-meteorological station. In: Extended abstracts of the presentation at the workshop "Automatic Weather Stations on Glaciers". Pontresina, 28-31 March 2004. IMAU. Utrecht-University, pp. 38-44.
- BRAUN, L.N., WEBER, M. AND SCHULZ, M. (2000): Consequences of climate change for runoff form Alpine regions. *Annals of Glaciology*, Vol. 31, pp. 19-25.
- BURRIDGE, D. M. AND GADD, A. J. (1974): The Meteorological Office operational 10 level numerical weather prediction model. U.K. Meteorological Office Technical Notes, 12 and 48.
- CAMPBELL, G.S. AND NORMAN, J.M. (1998): An Introduction to Environmental Biophysics, second ed. Springer, New York, 286 p.
- CASASSA, G., LÓPEZ, P., POUYAUD, B. AND ESCOBAR, F. (2009): Detection of changes in glacial run-off in alpine basins: examples form North America, the Alps, central Asia and the Andes. *Hydrological Processes*, Vol. 23, pp. 31-41.
- CHEN, J. AND OHMURA, A. (1990): Estimation of Alpine glacier water resources and their change since 1870s. Hydrology in Mountain Regions. I – Hydrological Measurements; the Water Cycle (Proceedings of two Lausanne Symposia, August 1990). *IAHS Publications*, No. 193, pp. 127–135.
- CHEN, J. AND OHMURA, A. (1990): On the influence of Alpine glaciers on runoff. In: Hydrology in Mountainous areas. I. Hydrological Measurements, The Water Cycle. Proceedings of the two Lausanne Symposia, August 1990. *IAHS Publications*, No. 193, pp. 117–125.
- CHEN, Y. (ED.) (1990): Geological Map of China. Peoples Republic of China, Ministry of Geology and Mineralogy, Beijing, China. Available from <http://library.wur.nl/isric/index2.html?url=http://library.wur.nl/WebQuery/isric/17859>
- CHINESE ACADEMY OF SCIENCES (1984): Scientific Working Group on the Qinghai-Tibet Plateau: The Climate of Xizang. The Series of the Scientific Expedition to the Qinghai-Xizang Plateau, Beijing, 304 p.
- CHRISTENSEN, J.H., HEWITSON, B., BUSUIOC, A., CHEN, A., GAO, X., HELD, I., JONES, R., KOLLI, R.K., KWON, W.-T., LAPRISE, R., MAGAÑA RUEDA, V., MEARN, L., MENÉNDEZ, C.G., RÄISÄNEN, J., RINKE, A., SARR, A. AND WHETTON, P. (2007): Regional Climate Projections. In: SOLOMON, S., QIN, D., MANNING, M., CHEN, Z., MARQUIS, M., AVERYT, K.B., TIGNOR, M. AND MILLER, H.L. (EDS.): *Climate Change 2007: The Physical Science*

- Basis. Contribution of Working Group I to the Fourth Assessment Report of the Intergovernmental Panel on Climate Change. Cambridge University Press, Cambridge, United Kingdom and New York, NY, USA.
- CHU, D., LU, L. AND ZHANG, T. (2007): Sensitivity of Normalized Difference Vegetation Index (NDVI) to Seasonal and Interannual Climate Conditions in the Lhasa Area, Tibetan Plateau, China. *Arctic, Antarctic, and Alpine Research*, Vol. 39, No. 4, pp. 635-641.
- CLM (2010): Climate Limited-area Modelling Community. [www.clm-community.eu](http://www.clm-community.eu)
- CRAWLEY, D., HAND, J. AND LAWRIE, L. (1999): Improving the Weather Information Available to Simulation Programs. Proceedings of the Conference "Building Simulation '99".
- CUNGE, J.A. (1969): On the subject of a flood propagation computation method (Muskingum method). *Journal of Hydraulic Research*, Vol.7, No. 2, pp. 205–230.
- DAJUN, S. (1995): Research on the rational use of water resources on the Lhasa River, Tibet. Modelling and Management of Sustainable Basin-scale Water Resource Systems (Proceedings of a Boulder Symposium, July 1995), *IAHS Publications*, No. 231, pp. 151-156.
- DAVIS, A. M., AITCHISON, J.C., BADENGZHU, LUO, H. AND ZYABREV, S. (2002): Paleogene island arc collision-related conglomerates, Yarlung-Tsangpo suture zone, Tibet. *Sedimentary Geology*, Vol. 150, pp. 247-273.
- DENOTH, A. (2003): Structural phase changes of the liquid water component in Alpine snow. *Cold Regions Sciences and Technology*, Vol. 37. pp. 227-233.
- DEPARTMENT OF POPULATION, SOCIAL, SCIENCE AND TECHNOLOGY STATISTICS OF THE NATIONAL BUREAU OF STATISTICS OF CHINA AND DEPARTMENT OF ECONOMIC DEVELOPMENT OF THE STATE ETHNIC AFFAIRS COMMISSION OF CHINA (EDS.) (2003): Tabulation on Nationalities of 2000 Population Census of China. 2 Vols., Nationalities Publishing House, Beijing.
- DOBLER, A. AND AHRENS, B. (2008): Precipitation by a regional climate model and bias correction in Europe and South Asia. *Meteorologische Zeitschrift*, Vol. 17, No. 4, pp. 499-509.
- DOBLER, A. AND AHRENS, B. (2010): Analysis of the Indian summer monsoon system in the regional climate model COSMO-CLM. *Journal of Geophysical Research*, doi:10.1029/2009JD013497, in press.
- DOMRÖS, M. AND GONGBING, P. (1988): The Climate of China. Springer Verlag GmbH, 361 p.

- DREYER, J.T. (2003): Economic Development in Tibet under the People's Republic of China. *Journal of Contemporary China*, Vol. 12, Iss. 36, pp. 411-430.
- EAGLESON, P.S. (1978): Climate, soil and vegetation. 3. A simplified model of soil movement in the liquid phase. *Water Resources Research*, Vol. 14, pp. 722–730.
- ERSDAC (EARTH REMOTE SENSING DATA ANALYSIS CENTER) (2009): The Ministry of Economy, Trade, and Industry (METI) of Japan and the United States National Aeronautics and Space Administration (NASA): Aster Global Digital Elevation Model (GDEM), available from <http://www.ersdac.or.jp/GDEM/E/2.html> (7.7.2009).
- ESRI (1999 – 2008): ArcGIS Desktop 9.3 Service Pack 1.
- FAO, IIASA, ISRIC, ISSCAS, JRC (2009): Harmonized World Soil Database (version 1.1). FAO, Rome, Italy and IIASA, Laxenburg, Austria.
- FARINOTTI, D., HUSS, M., BAUDER, A., FUNK, M. AND TRUFFER, M. (2009): A method to estimate the ice volume and ice-thickness distribution of alpine glaciers. *Journal of Glaciology*, Vol. 55, No. 191, pp. 422–430.
- FARQUHAR, G.D., VON CAEMMERER, S. AND BERRY, J.A. (1980): A biochemical model of photosynthetic CO<sub>2</sub> assimilation in leaves of C<sub>3</sub> species. *Planta*, Vol. 149, pp. 78–90.
- FERNANDEZ, A. (1998): An energy balance model of seasonal snow evolution. *Physics and Chemistry of the Earth*, Vol. 23(5-6), pp. 661-666.
- FISCHER, A. (2009): Calculation of glacier volume from sparse ice-thickness data, applied to Schaufelferner, Austria. *Journal of Glaciology*, Vol. 55, No. 191, pp. 453–460.
- FISCHER, A., SPAN, N., KUHN, M., MASSIMO, M. AND BUTSCHEK, M. (2007): Radarmessungen der Eisdicke Österreichischer Gletscher. Band II: Messungen 1999 bis 2006. *Österreichische Beiträge zur Meteorologie und Geophysik*, Heft 39.
- FP6 (2002-2006): European Commission Sixth Framework Programme. [http://ec.europa.eu/research/fp6/index\\_en.cfm](http://ec.europa.eu/research/fp6/index_en.cfm)
- FRAUENFELDER R. AND KÄÄB A. (2009): Glacier mapping from multi-temporal optical remote sensing data within the Brahmaputra river basin. Proceedings of the 33rd International Symposium on Remote Sensing of Environment, 4-8 May, 2009, Stresa, Italy.
- GARBRECHT, J. AND MARTZ, L.W. (1999): TOPAZ Version 3.1. USDA, Agricultural Research Service Grazinglands Research Laboratory, Oklahoma, USA.
- GEIGER, R. (1961): Überarbeitete Neuausgabe von Geiger, R.: Köppen-Geiger / Klima der Erde. Wandkarte 1:16 000 000. Klett-Perthes, Gotha.



- GLOWA-DANUBE (2001 – 2010): Globaler Wandel des Wasserkreislaufs an der Oberen Donau. Research project within GLOWA, [www.glowa-danube.de](http://www.glowa-danube.de).
- GOOGLE EARTH (2010): Google Earth 5.0.1.
- GREUELL, J.W. (1992): The Hintereisferner: mass-balance reconstruction and numerical modelling of the historical length variations. *Journal of Glaciology*, Vol. 38, No. 129, pp. 233-244.
- GUDMUNDSSON, G. H. (1999): A three-dimensional numerical model of the confluence area of Unteraargletscher, Bernese Alps, Switzerland. *Journal of Glaciology*, Vol. 45, pp. 219-230.
- HAEBERLI, W. AND M. HOELZLE (1995): Application of inventory data for estimating characteristics of and regional climate-change effects on mountain glaciers: a pilot study with the European Alps. *Annals of Glaciology*, Vol. 21, pp. 206–212.
- HAEBERLI, W. AND ZEMP, M. (2009): Mountain Glaciers: On Thin Ice. Mountain glaciers as key indicators of climate change. In: Kohler, Th. and Maselli, D. (Eds.): Mountains and Climate Change - From Understanding to Action, Published by Geographica Bernensia with the support of the Swiss Agency for Development and Cooperation (SDC), and an international team of contributors. Bern, Switzerland, pp. 21 – 29.
- HAGG W., BRAUN L.N., KUHN M. AND NESGAARD T. I. (2007): Modelling of hydrological response to climate change in glacierized Central Asian catchments. *Journal of Hydrology*, Vol. 332, pp. 40–53.
- HANK, T. (2008): A Biophysically Based Coupled Model Approach for the Assessment of Canopy Processes Under Climate Change Conditions. Dissertation der Fakultät für Geowissenschaften, *Digitale Hochschulschriften der LMU München*, München, 307 pp., available from <http://edoc.ub.uni-muenchen.de/8725/>.
- HASNAIN, S.I. (2002): Himalayan glaciers meltdown: impacts on south Asian rivers. H.A.J. In: van Lanen, H.A.J. and Demuth, S. (Eds.): FRIEND 2002 - Regional Hydrology: Bridging the Gap between Research and Practice, *IAHS Publications*, No. 274, pp. 417-423.
- HE, S., KAPP, P, DECELLES, P.G., GEHRELS, G.E. AND HEIZLER, M. (2007): Cretaceous-Tertiary geology of the Gangdese Arc in the Linzhou area, southern Tibet. *Tectonophysics*, Vol. 433, pp. 15-37.
- HEWITT, K. (2005): The Karakoram Anomaly? Glacier Expansion and the 'Elevation Effect', Karakoram Himalaya. *Mountain Research and Development*, Vol. 25, No. 4, pp. 332-340.

- HOCK, R. (2003): Temperature index melt modelling in mountain areas. *Journal of Hydrology*, Vol. 282, pp. 104-115.
- HOFER, M., MÖLG, TH., MARZEION, B. AND KASER, G. (2010): Empirical-statistical downscaling of reanalysis data to high-resolution air temperature and specific humidity above a glacier surface (Cordillera Blanca, Peru). *Journal of Geophysical Research*, doi:10.1029/2009JD012800, in press.
- HORTON P., SCHAEFLI B., MEZGHANI A., HINGRAY B. AND MUSY A. (2006): Assessment of climate-change impacts on alpine discharge regimes with climate model uncertainty. *Hydrological Processes*, Vol. 20, pp. 2091–2109.
- HOTTEL, H. C. (1976): A simple method for estimating the transmittance of direct solar radiation through clear atmospheres. *Solar Energy*, Vol. 18, pp. 129-134.
- HÖVERMANN, J. AND LEHMKUHL, F. (1994): Die vorzeitlichen Vergletscherungen in Ost- und Zentraltibet. In: PÖRTGE, K.-H. AND JIAN, L. (1994): Beiträge zur Tibetforschung, *Göttinger Geographische Abhandlungen*, H. 95, pp. 71-114.
- HUSS, M., FARINOTTI, D., BAUDER, A. AND FUNK, M. (2008): Modelling runoff from highly glacierized alpine drainage basins in a changing climate. *Hydrological Processes*, Vol. 22, pp. 3888-3902.
- HUSS, M., JOUVET, G., FARINOTT, D. AND BAUER, A. (2010): Future high-mountain hydrology: a new parameterization of glacier retreat. *Hydrology and Earth System Sciences Discussions*, Vol. 7, pp. 345-387.
- HUTTER, K. (1982): A mathematical model of polythermal glaciers and ice sheets. *Geophysical and Astrophysical Fluid Dynamics*, Vol. 21, pp. 201-224.
- ICIMOD (2009): Meteorological station recordings, provided within BRAHMATWINN (2006-2009).
- IPCC (2007A): Climate Change 2007: Synthesis Report. Contribution of Working Groups I, II and III to the Fourth Assessment Report of the Intergovernmental Panel on Climate Change [Core Writing Team, Pachauri, R.K and Reisinger, A. (eds.)]. IPCC, Geneva, Switzerland, 104 p.
- IPCC (2007B): Summary for Policymakers. In: SOLOMON, S., QIN, D., MANNING, M., CHEN, Z., MARQUIS, M., AVERYT, K.B., TIGNOR, M. AND MILLER, H.L. (EDS.): Climate Change 2007: The Physical Science Basis. Contribution of Working Group I to the Fourth Assessment Report of the Intergovernmental Panel on Climate Change. Cambridge University Press, Cambridge, United Kingdom and New York, NY, USA, 996 p.
- IPCC (2007C): Asia. In: PARRY, M.L., CANZIANI, O.F. PALUTIKOF, J.P. VAN DER LINDEN, P.J. AND HANSON, C.E. (EDS.): Climate Change 2007: Impacts, Adaptation and

- Vulnerability. Contribution of Working Group II to the Fourth Assessment Report of the Intergovernmental Panel on Climate Change, Cambridge University Press, Cambridge, UK, 976pp.
- IPCC (2010): IPCC statement on the melting of Himalayan glaciers. Geneva, 20 January 2010, Switzerland. Available from: <http://ipcc-wg2.gov/publications/AR4/himalaya-statement-20january2010.pdf>
- ITP (2008): Runoff and climate observation data, provided by the Institute of Tibetan Plateau Research within the BRAHMATWINN project.
- IZIOMON, M. G., MAYER, H. AND MATZARAKIS, A. (2003): Downward atmospheric longwave irradiance under clear and cloudy skies: Measurement and parameterization. *Journal of Atmospheric and Solar-Terrestrial Physics*, Vol. 65, pp. 1107-1116.
- JANSSON, P., HOCK, R. AND SCHNEIDER, TH. (2003): The concept of glacier storage: a review. *Journal of Hydrology*, Vol. 282, pp. 116-129.
- JARVIS A., H.I. REUTER, A. NELSON AND E. GUEVARA (2006): Hole-filled seamless SRTM data V3, International Centre for Tropical Agriculture (CIAT), available from <http://srtm.csi.cgiar.org>.
- JARVIS, P.G. AND MORISON, J.I.L. (1981): The control of transpiration and photosynthesis by stomata. In: Jarvis, P.G. and Mansfield, T.A. (Eds.): *Stomatal Physiology*, pp. 248-279.
- JOUVET, G., HUSS, M., BLATTER, H., PICASSO, M. AND RAPPAZ, J. (2009): Numerical simulation of Rhonegletscher from 1874 to 2100. *Journal of Computational Physics*, Vol. 228, pp. 6426-6439.
- JOUVET, G., PICASSO, M., RAPPAZ, J. AND BLATT, H. (2008): A new algorithm to simulate the dynamics of a glacier: theory and applications. *Journal of Glaciology*, Vol. 54, No. 188, pp. 801-811.
- JUNGCLAUS, J.H., KEENLYSIDE, N., BOTZET, M., HAAK, H., LUO, J.-J., LATIF, M., MAROTZKE, J., MIKOLAJEWICZ, U. AND ROECKNER, E. (2006): Ocean circulation and tropical variability in the coupled model ECHAM5/MPI-OM, *Journal of Climate*, Vol. 19, pp. 3952-3972.
- KÄÄB, A., FRAUENFELDER, R. AND FRAUENFELDER KÄÄB, J. A. (2008): Glacier distribution and glacier area changes 1960s-2000 in the Brahmaputra river basin. *Geophysical Research Abstracts*, Vol. 10, EGU 2008 – A – 05334.
- KAISER, K., MIEHE, G., SCHOCH, W.H., ZANDER, A. AND SCHLÜTZ, F. (2006): Relief, soil and lost forests: Late Holocene environmental changes in southern Tibet under human

- impact. In: EITEL, B. (ED.): Holocene Landscape Development and Geoarchaeological Research. *Zeitschrift für Geomorphologie*, No. 142, pp. 149-173.
- KANG, S., CHEN, F., YE, Q., JING, Z., QIN, D. AND REN, J. (2007A): Glacier retreating dramatically on Mt. Nyainqêntanglha during the last 40 Years. *Journal of Glaciology and Geocryology*, Vol. 26, No. 6, pp. 869-873 [in Chinese with English summary].
- KANG, S., QIN, D., REN, J., ZHANG, Y., KASPARI, S., MAYEWSKI, P.A. AND HOU, S. (2007B): Annual Accumulation in the Mt. Nyainqentanglha Ice core, Southern Tibetan Plateau, China: Relationships to Atmospheric Circulation over Asia. *Arctic, Antarctic, and Alpine Research*, Vol. 39, No. 4, pp. 63-670.
- KARGEL, J.S., ARMSTRONG, R., ARNAUD, Y., BERTHIER, E., BISHOP, M. P., BOLCH, T., BUSH, A., COGLEY, G., FUJITA, K., GILLESPIE, A., HARITASHYA, U., KASER, G., KHALSA, S.J.S., LEONARD, G., RACOVITEANU, A., RAUP, B. AND VAN DER VEEN, C. (2010): Satellite-era glacier changes in High Asia. Background support presentation for NASA "Black Carbon and Aerosols" press conference associated with Fall AGU, Dec. 14, 2009, available from [http://www1.nasa.gov/pdf/411466main\\_carbon-pole\\_Kargel.pdf](http://www1.nasa.gov/pdf/411466main_carbon-pole_Kargel.pdf) .
- KENDALL, M. G. (1970): Rank correlation methods. 4<sup>th</sup> edition, Griffin, London, UK.
- KLOK, E. J. AND OERLEMANS, J. (2002): Model study of the spatial distribution of the energy and mass balances of Morteratschgletscher, Switzerland. *Journal of Glaciology*, Vol. 48, pp. 505–518.
- KNIGHT, P.G. (2006): Glacier science and environmental change: Introduction. In: Knight, P.G. (Ed.): Glacier science and environmental change. Oxford, pp. 1-2.
- KOTLYAKOV, V.M. AND SEVERSKIY, I.V. (2009): Glaciers of Central Asia: current situation, changes and possible impact on water resources. In: Braun, L. N., Hagg, W., Severskiy, I.V. and Young, G. (2009): Assessment of Snow, Glacier and Water Resources in Asia. Selected papers from the Workshop in Almaty, Kazakhstan, 2006. *IHP/HWRP-Berichte*, Heft 8, Koblenz.
- KRIPALANI, R.H., OH, J.H., KULKARNI, A., SABADE, S.S. AND CHAUDHARI, H.S. (2007): South Asian summer monsoon precipitation variability: Coupled climate model simulations and projections under IPCC AR4. *Theoretical and Applied Climatology*, Vol. 90, pp. 133-159.
- KUHN, M., DREISEITL, E., HOFINGER, S., MARKL, G., SPAN, N. AND KASER, G. (1999): Measurements and models of the mass balance of Hintereisferner. *Geografiska Annaler, Series A, Physical Geography*, Vol. 81, No. 4, pp. 659-670.
- KUHN, M., MARKL, G., KASER, G., NICKUS, U. AND OBLEITNER, F. (1985): Fluctuations of climate and mass balance. Different responses of two adjacent glaciers. *Zeitschrift für Gletscherkunde und Glazialgeologie*, Vol. 2, pp. 409-416.

- LAMBRECHT, A. AND KUHN, M. (2007): Glacier changes in the Austrian Alps during the last three decades, derived from the new Austrian glacier inventory. *Annals of Glaciology*, Vol. 46, pp. 177-184.
- LAMBRECHT, A. AND MAYER, CH. (2009): Temporal variability of the non-steady contribution from glaciers to water discharge in western Austria. *Journal of Hydrology*, Vol. 376, pp. 353-361.
- LE MEUR, E., GERBAUX, M., SCHÄFER, M. AND VINCENT, C. (2007): Disappearance of an Alpine glacier over the 21st Century simulated from modeling its future surface mass balance. *Earth and Planetary Science Letters*, Vol. 261, pp. 367-374.
- LEBER, D., HOLAWE, F. AND HÄUSLER, H. (1995): Climatic Classification of the Tibet Autonomous Region Using Multivariate Statistical Methods. *GeoJournal* 37, Vol. 4, pp. 451-473.
- LEHMKUHL, F., KLINGE, M. AND LANG, A. (2002): Late Quarternary glacier advances, lake level fluctuations and aeolian sedimentation in Southern Tibet. *Zeitschrift für Geomorphologie*, Suppl.-Bd. 126, pp. 183-218.
- LI, X. (2003): GLIMS Glacier Database. Boulder, CO: National Snow and Ice Data Center/World Data Center for Glaciology. Digital Media.
- LI, X., CHENG, G., JIN, H., KANG, E., CHE, R., JIN, R. WU, L., NAN, Z., WANG, J. AND SHEN, Y. (2008): Cryospheric change in China. *Global and Planetary Change*, Vol. 62, pp. 210-218.
- LINIGER, H., WEINGARTNER, R. AND GROSJEAN, M. (1998): Mountains of the World: Water Towers for the 21<sup>st</sup> Century. Mountain Agenda for the Commission on Sustainable Development, Center for Development and Environment, Berne, Switzerland.
- LISTON, G. E. AND ELDER, K. (2006): A Meteorological Distribution System for High-Resolution Terrestrial Modeling (MicroMet). *Journal of Hydrometeorology*, Vol. 7, pp. 217-234.
- LIU, B. Y. H. AND JORDAN, R. C. (1960): The interrelationship and characteristic distribution of direct, diffuse and total solar radiation. *Solar Engineering*, Vol. 4, pp. 1-19.
- LIU, X. AND CHEN, B. (2000): Climatic warming in the Tibetan Plateau during recent decades. *International Journal of Climatology*, Vol. 20, pp. 1729-1742.
- LUDWIG, R. AND MAUSER, W. (2000): Modelling catchment hydrology within a GIS based SVAT-model framework. *Hydrology and Earth System Science HESS*, Vol. 4, No. 2, pp. 239-249.

- LUDWIG, R. MAUSER, W., NIEMEYER, S., COLGAN, A., STOLZ, R., ESCHER-VETTER, H., KUHN, M., REICHSTEIN, M., TENHUNEN, J., KRAUS, A., LUDWIG, M., BARTH, M. AND HENNICKER, R. (2003): Web-based modelling of energy, water and matter fluxes to support decision making in mesoscale catchments – the integrative perspective of GLOWA-Danube. *Physics and Chemistry of the Earth*, Vol. 28, pp. 621-634.
- MANN, H. B. (1945): Nonparametric test against trends. *Econometrica*, No. 13, pp. 245 – 259.
- MARKE, T. (2008): Development and Application of a Model Interface to couple Regional Climate Models with Land Surface Models for Climate Change Risk Assessment in the Upper Danube Watershed, Dissertation der Fakultät für Geowissenschaften, *Digitale Hochschulschriften der LMU München*, München, 188 p., available from <http://edoc.ub.uni-muenchen.de/9162/>.
- MARKE, T. AND MAUSER, W. (2008): SCALMET – a tool for bidirectional coupling of climate models with physically-based simulations of land surface processes. In: BORSDORF, A., STÖTTER, J., VEULLIET, E. (EDS.): *Managing Alpine Future – IGF Forschungsberichte*, Vol. 2. Verlag der Österreichischen Akademie der Wissenschaften, Innsbruck, Austria, pp. 216–225.
- MAROWSKY, K. (2010): Die Validierung des Gletschermodells SURGES am Beispiel von Vernagtfenern sowie Nördlichem und Südlichem Schneefenern. Diplomarbeit am der Kommission für Glaziologie der Bayerischen Akademie der Wissenschaften München und der Katholischen Universität Eichstätt-Ingolstadt, 147 p.
- MAUSER, W. AND BACH, H. (2009): PROMET – Large scale distributed hydrological modelling to study the impact of climate change on the water flows of mountain watersheds. *Journal of Hydrology*, Vol. 376, pp. 362-377.
- MAUSER, W. AND LUDWIG, R. (2002): GLOWA-DANUBE – A research concept to develop integrative global changes of the water cycle. In: BENISTON, M. (ED.): *Climatic Change: Implications for the Hydrological Cycle and for Water Management. Advances in Global Change Research*, Vol. 10, Kluwer Academic Publishers, Dordrecht and Boston, pp. 171-188.
- MAUSER, W. AND SCHÄDLICH, S. (1998): Modelling the spatial distribution of evapotranspiration on different scales using remote sensing data. *Journal of Hydrology*, Vol. 212-213, pp. 250-267.
- MAUSER, W., PRASCH, M. AND STRASSER, U. (2007): Physically based Modelling of Climate Change Impact on Snow Cover Dynamics in Alpine Regions using a Stochastic Weather Generator. In: OXLEY, L. AND KULASIRI, D. (EDS): *MODSIM 2007 International Congress on Modelling and Simulation. Modelling and Simulation Society of Australia and New Zealand*, December 2007, pp. 2138-2145.



- MI, D., XIE, Z., LUO, S., FENG, Q., MA, M. AND JIN, D. (EDS). (2002). Glacier inventory of China XI. The Ganga drainage basin. XII. The Indus drainage basin. Xi'an, Xi'an Cartographic Publishing House. Academia Sinica, Lanzhou Institute of Glaciology and Geocryology. [In Chinese.]
- MIEHE, S., MIEHE, G., JIAN, H., TSEWANG, O., TSEREN, T. AND YANLI, T. (2000): Sacred Forests of Sout-Dentras Xizang and their Importance for the Restauration of Forest Resources. In: MIEHE, G. AND YILI, Z. (EDS.) (2000): Environmental Changes in High Asia. Proceedings of an International Symposium at the University of Marburg, Faculty of Geography, 29<sup>th</sup> of May to 1<sup>st</sup> of June 1997, *Marburger Geographische Schriften*, No. 135, pp. 228-249.
- MONTEITH, J.L. (1965): Evaporation and the environment. *Symposia of the Society for Experimental Biology*, Vol. 19, pp. 205-234.
- MONTEITH, J.L. (1973): Principles of Environmental Physics. Elsevier, New York, 241 p.
- MOORE, R.D., FLEMING, S.W., MENOUNOS, B., WHEATE, R., FOUNTAIN, A, STAHL, K., HOLM, K. AND JAKOB, M. (2009): Glacier change in western North America: Influences on hydrology, geomorphic hazards and water quality. *Hydrological Processes*, Vol. 23, pp. 42-61.
- MUERTH, M. (2008): A soil temperature and energy balance model for integrated assessment of Global Change impacts at the regional scale. Dissertation der Fakultät für Geowissenschaften, *Digitale Hochschulschriften der LMU München*, München, 147 pp., available from <http://edoc.ub.uni-muenchen.de/8810/>.
- NAKIĆENOVIĆ, N. AND SWART, R. (EDS.) (2000): IPCC Special Report on Emissions Scenarios. Cambridge University Press, Cambridge, 570 p.
- NASH, J. E. AND SUTCLIFFE, J. V. (1970): [River flow forecasting through conceptual models part I — A discussion of principles](#). *Journal of Hydrology*, Vol. 10, No. 3, pp. 282–290.
- NATIONAL SNOW AND ICE DATA CENTER (2009): World glacier inventory. World Glacier Monitoring Service and National Snow and Ice Data Center/World Data Center for Glaciology. Boulder, CO. Digital media 1999, updated 2009.
- NING, A., LIU, T., YIN, G. AND LIU, F. (2001): Study on the water environment and composition of Lhasa River. *Science in China (Series E)*, Vol. 44 Supp., pp. 96 – 100.
- OERLEMANS, J. (1997): A flow-line model for Nigardsbreen: projection of future glacier length based on dynamic calibration with the historic record. *Annals of Glaciology*, Vol. 24, pp. 382-389.
- OERLEMANS, J. (2001): Glaciers and climate change. Swets & Zeitlinger BV, Lisse, 148 p.

- OERLEMANS, J. (2010): The Microclimate of Valley Glaciers. Igitur, Utrecht Publishing & Archiving Services, Universiteitsbibliotheek Utrecht, 138 p.
- OERLEMANS, J. AND GRISOGONO, B. (2002): Glacier winds and parameterisation of the related surface heat fluxes. *Tellus*, Vol. 54 A, pp. 440-452.
- OERLEMANS, J., ANDERSON, B., HUBBARD, A., HUYBRECHTS, P., JOHANNESSEN, T., KNAP, W.H., SCHMEITS, M., STROEVEN, A.P., VAN DE WAL, R.S.W., WALLINGA, J. AND ZUO, Z. (1998): Modelling the response of glaciers to climate warming. *Climate Dynamics*, Vol. 14, No. 4, pp. 267-274.
- PAN, Y., COPELAND, P., RODEN, M. K., KIDD, W. S. F. AND HARRISON, T. M. (1993): Thermal and unroofing history of the Lhasa area, southern Tibet – evidence from apatite fission track thermochronology. *Nuclear Tracks and Radiation Measurements*, Vol. 21, No. 4, pp. 543-554.
- PATERSON, W.S. B. (1994): The Physics of Glaciers. Third Edition. Butterworth-Heinemann, Oxford, 481 p.
- PAUL, F. AND KOTLARSKI, S. (2010): Forcing a Distributed Glacier Mass Balance Model with the Regional Climate Model REMO. Part II: Downscaling Strategy and Results for Two Swiss Glaciers. *Journal of Climate*, Vol. 23, Iss. 6, pp. 1607-1620.
- PELLICCIOTTI, F., BROCK, B., STRASSER, U., BURLANDO, P., FUNK, M. AND CORRIPIO, J.G. (2005): An enhanced temperature-index Glacier melt model including shortwave radiation balance: development and testing for Haut Glacier d’Arolla, Switzerland. *Journal of Glaciology*, Vol. 51, No. 175, pp. 573-587.
- PRASCH, M., BERNHARDT, M., WEBER, M., STRASSER, U. AND MAUSER, W. (2008A): Physically based modelling of snow cover dynamics in Alpine regions, In: BORSDORF, A., STÖTTER, J., VEULLIET, E. (EDS.): Managing Alpine Future – *IGF Forschungsberichte*, Vol. 2. Verlag der Österreichischen Akademie der Wissenschaften, Innsbruck, Austria, pp. 322–330.
- PRASCH, M., STRASSER, U. AND MAUSER, W. (2008B): Validation of a physically based snow model for the simulation of the accumulation and ablation of snow (ESCIMO). In: STRASSER, U. AND VOGEL, M. (EDS.): Proceedings Alpine\*Snow\*Workshop, Munich, October 5-6, 2006, Germany. *Berchtesgaden National Park research report*, Nr. 53., Berchtesgaden, pp. 78-91.
- PRASCH, M., WEBER, M., STRASSER, U. AND MAUSER, W. (2009): Application of the physically based glacier model SURGES in the Lhasa River Catchment in Tibet. *Geophysical Research Abstracts*, Vol. 11, EGU2009-0, 2009, Vienna, Austria.
- PRESS, F. AND SIEVER, R. (1994): Understanding Earth. Freeman, New York, 593 p.

- PUTKONEN, J. K. (2004): Continuous Snow and Rain Data at 500 to 4400 m Altitude near Annapurna, Nepal, 1999-2001. *Arctic, Antarctic, and Alpine Research*, Vol. 36, No.2, pp. 244-248.
- RADIC, V. AND HOCK, R. (2006): Modeling future glacier mass balance and volume changes using ERA-40 reanalysis and climate models: A sensitivity study at Storglaciären, Sweden. *Journal of Geophysical Research*, Vol. 111, 12 p.
- RAPP, J. AND SCHÖNWIESE, CH.-D. (1995): Atlas der Niederschlags- und Temperaturrenns in Deutschland 1891-1990. *Frankfurter Geowissenschaftliche Arbeiten*, Serie B, Meteorologie und Geophysik, Band 5, 255 p.
- RAU, F., MAUZ, F., VOGT, ST., KHALSA, S.J.S. AND RAUP, B. (2005): Illustrated GLIMS Glacier Classification Manual. Glacier Classification Guidance for the GLIMS Glacier Inventory. Version 1.0, 36 p.
- RAUP, B.H., RACOVITEANU, A., KHALSA, S.J.S., HELM, C., ARMSTRONG, R. AND ARNAUD, Y. (2007): "The GLIMS Geospatial Glacier Database: a New Tool for Studying Glacier Change". *Global and Planetary Change*, Vol. 56, pp. 101-110.
- REES, H.G. AND COLLINS, D. N. (2006): Regional differences in response of flow in glacier Himalayan rivers to climatic warming. *Hydrological Processes*, Vol. 20, pp. 2154-2169.
- REES, W. G. (2006): Remote Sensing of snow and ice. Taylor and Francis Group, Boca Raton, Fl., 285 p.
- REISE-KNOW-HOW VERLAG (ED.) (2005): Tibet 1: 1 500 000. Bielefeld.
- ROECKNER, E., BÄUML, G., BONAVENTURA, L., BROKOPF, R., ESCH, M., GIORGETTA, M., HAGEMANN, S., KRICHNER, I., KORNBLUEH, L., MANZINI, E., RHODIN, A., SCHLESE, U. SCHULZWEIDEA, U. AND TOMPKINS, A. (2003): The atmospheric general circulation model ECHAM 5. Part I: Model description, *Max Planck Institute for Meteorology Rep.*, Vol. 349, 127 p.
- ROHRER, M. B. (1992): Die Schneedecke im Schweizer Alpenraum und ihre Modellierung. *Zürcher Geographische Schriften*, Vol. 49, 178 p.
- RÖTHLISBERGER, H. AND LANG, H. (1987): Glacial hydrology. In: Gumell, A. M. and Clar, M. J. (Eds.): *Glacio-Fluvial Sediment Transport: an Alpine Perspective*, John Wiley, Chichester, UK, pp. 207-284.
- SALERNO, F., BURASCHI, E., BRUCCOLERI, G., TARTARI, G. AND SMIRAGLIA, C. (2008): Glacier surface-area changes in Sagarmatha national park, Nepal, in the second half of the 20th century, by comparison of historical maps. *Journal of Glaciology*, Vol. 54, No. 187, pp. 738-752.

- SALMI, T., MÄÄTTÄ, A., ANITILA, P., TUIJA, R.-A., AND AMNELL, T. (2002): Detecting trends of annual values of atmospheric pollutants by the Mann-Kendall test and Sen's slope estimates – the excel template application MAKESENS. *Publications on Air Quality*, No. 31, Finnish Meteorological Institute, 35 p.
- SCHULTZ, J. (2005): *The Ecozones of the World. The Ecological Divisions of the Geosphere*. 2<sup>nd</sup> edition, Springer Verlag, Berlin, 252 p.
- SEVERSKIY, I. (2009): Current and projected changes of glaciation in Central Asia and their probable impact on water resources. In: Braun, L. N., Hagg, W., Severskiy, I.V. and Young, G. (2009): *Assessment of Snow, Glacier and Water Resources in Asia. Selected papers from the Workshop in Almaty, Kazakhstan, 2006. IHP/HWRP-Berichte*, Heft 8, Koblenz.
- SHI, X. Z., YU, D. S., WARNER, E. D., PAN, X. Z., PETERSEN, G. W., GONG, Z.G. AND WEINDORF, D.C. (2004): Soil Database of 1:1,000,000 Digital Soil Survey and Reference System of the Chinese Genetic Soil Classification System. *Soil Survey Horizons*, Vol. 45, No. 4, pp. 129-136.
- SINGH P. AND KUMAR N. (1997): Impact assessment of climate change on the hydrological response of a snow and glacier melt runoff dominated Himalayan river. *Journal of Hydrology*, Vol. 193, pp. 316–350.
- SINGH, P. AND BENGTSSON, L. (2004): Hydrological sensitivity of a large Himalayan basin to climate change. *Hydrological Processes*, Vol. 18, pp. 2363-2385.
- SMITH, C.A.S., CLARK, M., BROLL, G., PING, C.L., KIMBLE, J.M. AND LUO, G. (1999): Characterization of Selected Soils from the Lhasa Region of Qinghai-Xizang Plateau, SW China. *Permafrost and Periglacial Processes*, Vol. 10, pp. 211-222.
- SPAN, N., FISCHER, A., KUHN, M., MASSIMO, M. AND BUTSCHEK, M. (2005): Radarmessungen der Eisdicke Österreichischer Gletscher. Band 1: Messungen 1995 bis 1998. *Österreichische Beiträge zur Meteorologie und Geophysik*, Heft 33.
- STAHL, K., MOORE, R. D., SHEA, J. M., HUTCHINSON, D., AND CANNON, A. J. (2008): Coupled modelling of glacier and streamflow response to future climate scenarios. *Water Resources Research*, Vol. 44, 13 p.
- STRASSER, U. (2008): Modelling of the mountain snow cover in the Berchtesgaden National Park. *Berchtesgaden National Park research report*, Nr. 55, Berchtesgaden, 104 p.
- STRASSER, U. AND MAUSER, W. (2001): Modelling the spatial and temporal variations of the water balance for the Weser catchment 1965-1994. *Journal of Hydrology*, Vol. 254 (1-4), pp. 199-214.

- TASHI, N. (2005): Food Preparation from Hull-less Barley in Tibet. In: Grando, S. and Macperhson, H.G.: Food Barley: Importance, Uses and Local Knowledge. Proceeding of the International Workshop on Food Barley Improvement, 14-17 January 2002, Hammamet, Tunisia. ICARDA, Aleppo, Syria, 156 p.
- THAYYEN, R.J. AND GERGAN, J. T. (2010): Role of glaciers in watershed hydrology: a preliminary study of "Himalayan catchment". *The Cryosphere*, Vol. 4, pp.115-128.
- THORSTEINSSON, TH., RAYMOND, C.F., GUÐMUNDSSON, G.H., BINDSCHADLER, R.A., VORNBERGER, P. AND JOUGHIN, I. (2003): Bed topography and lubrication inferred from surface measurements on fast-flowing ice streams. *Journal of Glaciology*, Vol. 49, No. 167, pp. 481–490.
- TODINI, E. (2007): A mass conservative and water storage consistent variable parameter Muskingum–Cunge approach. *Hydrology and Earth System Sciences Discussions*, Vol. 4, pp. 1549-1592.
- U.S. DEPARTMENT OF ENERGY (2010): EnergyPlus Energy Simulation Software. Weather data. available from [http://apps1.eere.energy.gov/buildings/energyplus/cfm/weatherdata/weather\\_request.cfm](http://apps1.eere.energy.gov/buildings/energyplus/cfm/weatherdata/weather_request.cfm) (25.01.2010)
- UNEP AND WGMS (2008): Global Glacier Changes: facts and figures. 88 p.
- UNESCO (2006): Water – a shared responsibility. The United Nations World Water Development Report 2, Paris, France, 584 p.
- UPPALA, S.M., KALLBERG, P. W., SIMMONS, A. J., ANDRAE, U., BECHTOLD, V. D., FIORINO, M., GIBSON, J. K., HASELER, J., HERNANDEZ, A., KELLY, G. A., LI, X., ONOGI, K., SAARINEN, S., SOKKA, N., ALLAN, R. P., ANDERSSON, E., ARPE, K., BALMASEDA, M. A., BELJAARS, A. C. M., VAN DE BERG, L., BIDLOT, J., BORMANN, N., CAIRES, S., CHEVALLIER, F., DETHOF, A., DRAGOSAVAC, M., FISHER, M., FUENTES, M., HAGEMANN, S., HOLM, E., HOSKINS, B. J., ISAKSEN, L., JANSSEN, P. A. E. M., JENNE, R., MCNALLY, A. P., MAHFOUF, J. F., MORCRETTE, J. J., RAYNER, N. A., SAUNDERS, R. W., SIMON, P., STERL, A., TRENBERTH, K. E., UNTCH, A., VASILJEVIC, D., VITERBO, P. AND WOOLLEN, J. (2005): The ERA-40 re-analysis, *Quarterly Journal of the Royal Meteorological Society*, Vol. 131 (612, Part B), pp. 2961–3012.
- USGS (2009): Earth Resources Observation and Science Center: Landsat ETM+ Level-1 Products (GeoTIFF). Available from <http://edcsns17.cr.usgs.gov/EarthExplorer/> (21.8.2009).
- USGS (2010): MODFLOW and Related Programs. <http://water.usgs.gov/nrp/gwsoftware/modflow.html>, 25.01.2010.

- VIVIROLI, D. AND WEINGARTNER, R. (2004): The hydrological significance of mountains: from regional to global scale. *Hydrological and Earth System Sciences*, Vol. 8 (6), pp. 1016 – 1029.
- WANG, Y., HOU, SH. AND LIU, Y. (2009): Glacier changes in the Karlik Shan, eastern Tien Shan, during 1971/72 – 2001/02. *Annals of Glaciology*, Vol. 50, No.53, pp. 39-45.
- WDC (2009): Chinese Glacier Inventory of the World. Data Center For Glaciology and Geocryology, Lanzhou, China. Available from [http://wdcdgg.westgis.ac.cn/DATABASE/Glacier/glacier\\_inventory.asp](http://wdcdgg.westgis.ac.cn/DATABASE/Glacier/glacier_inventory.asp) (17.8.2009).
- WEBER, M. (2008): Mikrometeorologische Prozesse bei der Ablation eines Alpengletschers. *Abhandlungen – Bayerische Akademie der Wissenschaften, Mathematisch –Naturwissenschaftliche Klasse*, Neue Folge, H. 177, 258 p.
- WEBER, M., BRAUN, L., MAUSER, W. AND PRASCH, M. (2009): Die Bedeutung der Gletscherschmelze für den Abfluss der Donau gegenwärtig und in der Zukunft. The relevance of glacier melt for the Upper Danube River discharge today and in the future. *Mitteilungsblatt des hydrographischen Dienstes in Österreich*, No. 86, pp. 1-29.
- WEBER, M., PRASCH, M., KUHN, M., LAMBRECHT, A. AND HAGG, W. (2008A): Eisreserve – Teilprojekt Glaziologie, Kapitel 1.8. In: GLOWA-Danube-Projekt, LMU München (Ed.): Global Change Atlas. Einzugsgebiet Obere *Donau*, München.
- WEBER, M., PRASCH, M., STRASSER, U. UND MAUSER, W. (2008B): Embedded grid-modelling of 506 glaciers in the upper Danube basin. *Geophysical Research Abstracts*, Vol. 10, EGU 2008-A-00000, Vienna, Austria.
- WEHREN, B., WEINGARTNER, R., SCHÄDLER, B. AND VIVIROLI, D. (2010): General Characteristics of Alpine Waters. In: Bundi, U. (Ed.): Alpine Waters. Springer Verlag, Berlin, Heidelberg, pp. 17-58.
- WEINGARTNER, R., VIVIROLI, D. AND SCHÄDLER, B. (2007): Water resources in mountain regions: a methodological approach to assess the water balance in a highland-lowland-system. *Hydrological Processes*, Vol. 21, pp. 578-585.
- WGMS (2009): World Glacier Monitoring Service. <http://www.geo.unizh.ch/wgms/index.html>
- WINKLER, S. (2009): Gletscher und ihre Landschaften. eine illustrierte Einführung. Primus Verlag, Darmstadt, 183 p.
- YAO T., PU, J. AND LIU, S. (2006): Changing glaciers in High Asia. In: KNIGHT, P.G. (Ed.) (2006): Glacier science and environmental change. Oxford, pp. 275-282.

- YAO, T., PU, J., LU, A., WANG, Y. AND YU, W. (2007): Recent Glacial Retreat and Its Impact on Hydrological Processes on the Tibetan Plateau, China, and Surrounding Regions. *Arctic, Antarctic, and Alpine Research*, Vol. 39, No. 4, pp. 642-650.
- YAO, T., WANG, Y., LIU, S. PU, J., SHEN, Y. AND LU, A. (2004): Recent glacial retreat in High Asia in China and its impact on water resource in Northwest China. *Science in China Ser. D Earth Sciences*, Vol. 47, No. 12, pp. 1065-1075.
- YI, F. AND XIURONG, D. (EDS.) (1999): The National Physical Atlas of China. The Institute of Geography, Chinese Academy of Sciences, China Cartographic Publishing House, Beijing, 230p.
- YOU, Q., KANG, S., WU, Y. AND YAN, Y. (2007): Climate change over the Yarlung Zangbo River Basin during 1961-2005. *Journal of Geographical Sciences*, pp. 409-420.
- YOUNG, G. (2009): The elements of high mountain hydrology with special emphasis on Central Asia. In: Braun, L. N., Hagg, W., Severskiy, I.V. and Young, G. (2009): Assessment of Snow, Glacier and Water Resources in Asia. Selected papers from the Workshop in Almaty, Kazakhstan, 2006. *IHP/HWRP-Berichte*, Heft 8, Koblenz.
- YOUNG, K.C. (1994): A multivariate chain model for simulating climatic parameters from daily data. *Journal of Applied Meteorology*, Vol. 33, pp. 661-671.
- ZAPPA, M., POS, F., STRASSER, U., WAMERDAM, P. AND GURTZ, J. (2003): Seasonal water balance of an Alpine catchment as evaluated by different methods for spatially distributed snowmelt modelling. *Nordic Hydrology*, Vol. 34, pp. 179-202.
- ZHU, W., CHEN, L. AND ZHOU, Z. (2001): Several characteristics of contemporary climate change in the Tibetan Plateau. *Science in China (Series D)*, Vol. 44, Supp., pp. 410-420.
- ZOU, Z. AND OERLEMANS, J. (1997): Numerical modeling of the historic front variation and the future behaviour of the Pasterze glacier. *Annals of Glaciology*, Vol. 24, pp.235 – 241.



## 10 Appendix

### Appendix 1

Summary of model parameters (see Chapter 3).

Parameter	Symbol	Value	Unit
Albedo of freshly fallen snow	$\alpha$	0.90	-
Albedo of ice in regions with high amount of solar radiation	$\alpha$	0.50	-
Albedo recession factor at air temperature < 273.15 K	$k$	0.05	1/day
Albedo recession factor at air temperature $\geq$ 273.15 K	$k$	0.12	1/day
Condensation/sublimation heat of snow/Ice	$H_{is}$	2835500.	J/kg
Dry adiabatic lapse rate	$\Gamma$	0.00981	K/m
Emissivity of glacier ice	$\varepsilon$	0.98	-
Emissivity of snow	$\varepsilon$	1.	-
Freezing fraction of liquid water storage	$fr$	25	%
Gas constant of dry air	$R_d$	287	J kg <sup>-1</sup> K <sup>-1</sup>
Glacier ice density	$\rho_{ice}$	910.	kg/m <sup>3</sup>
Gravitational acceleration on earth	$g_o$	9.81	m/s <sup>2</sup>
Maximum albedo of snow	$\alpha_{max}$	0.9	-
Maximum liquid water storage capacity	$s_l$	7	%
Minimum albedo of snow	$\alpha_{min}$	0.55	-
Moist adiabatic lapse rate	$\Gamma$	0.0065	K/m
Molar mass of air	$M$	0.028964	Kg/mol
Snow density (settled snow)	$\rho_{snow}$	290.	kg/m <sup>2</sup>
Soil heat flux	$G$	2.	W/m <sup>2</sup>
Specific heat capacity of ice	$c_i$	2100.	J/(kgK)
Specific heat capacity of water	$c_w$	4180.	J/(kgK)
Specific melting heat of ice	$H_i$	337500.	J/kg
Stefan-Boltzmann-constant	$\sigma$	$5.67 \cdot 10^{-8}$	W/(m <sup>2</sup> K <sup>4</sup> )
Threshold wet bulb temperature	$T_w$	2.	°C
Time step	$\Delta t$	3600.	s
Universal gas constant	$R$	8.31432	Nm/(mol K)

## Appendix 2

Pictures of the investigation area, taken during the Brahmawinn field trip to Tibet in September 2006.

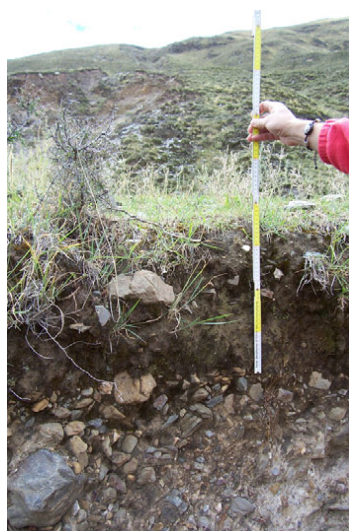


*Large barley fields near Linzhou (18.09.2006).*

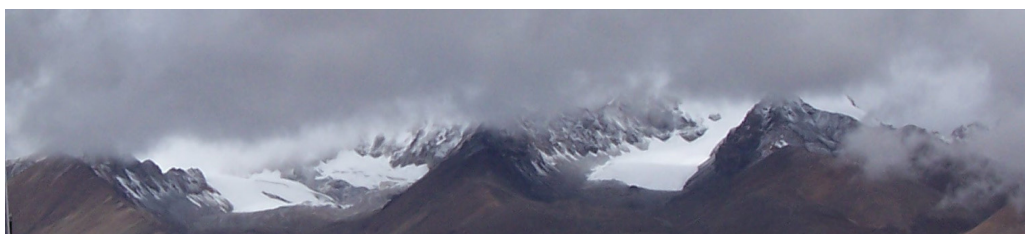


*Mixture of grassland and shrubland (14.09.2006).*





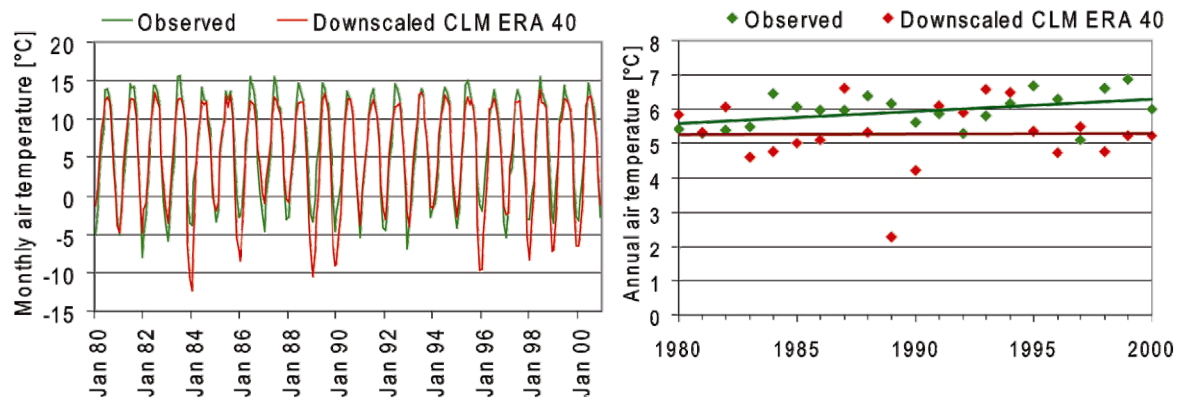
*Soil profiles of the Lhasa River basin (18.9.2006 und 14.9.2006)*



*Glaciers of the Nyaingêntanglha Mountains (24.09.2006).*

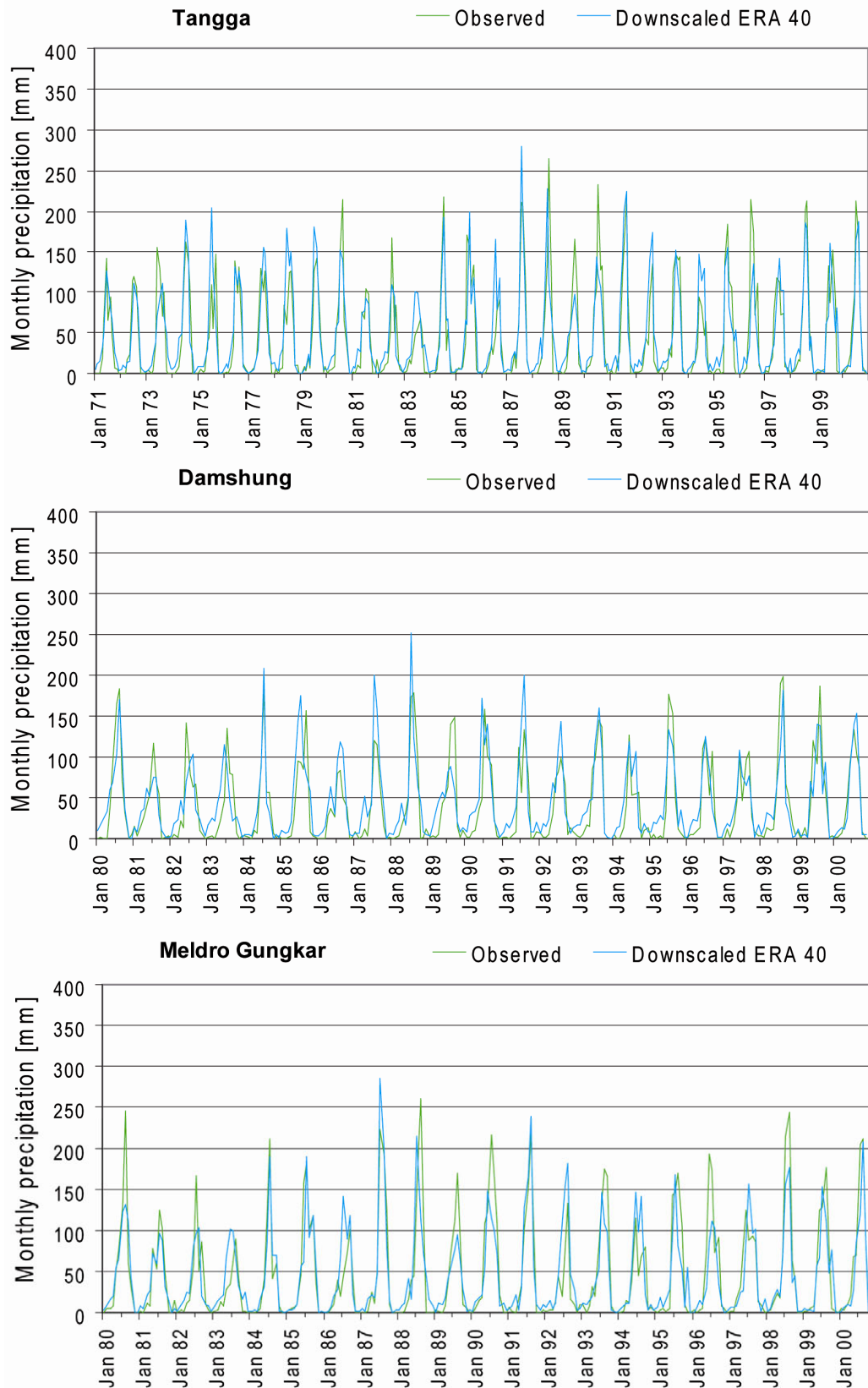
### Appendix 3

Observed and modelled (CLM ERA 40) trend of the monthly and annual air temperature at the Meldro Gungkar station for 1980-2000 (for other stations see Figure 5.16 and Figure 5.17).



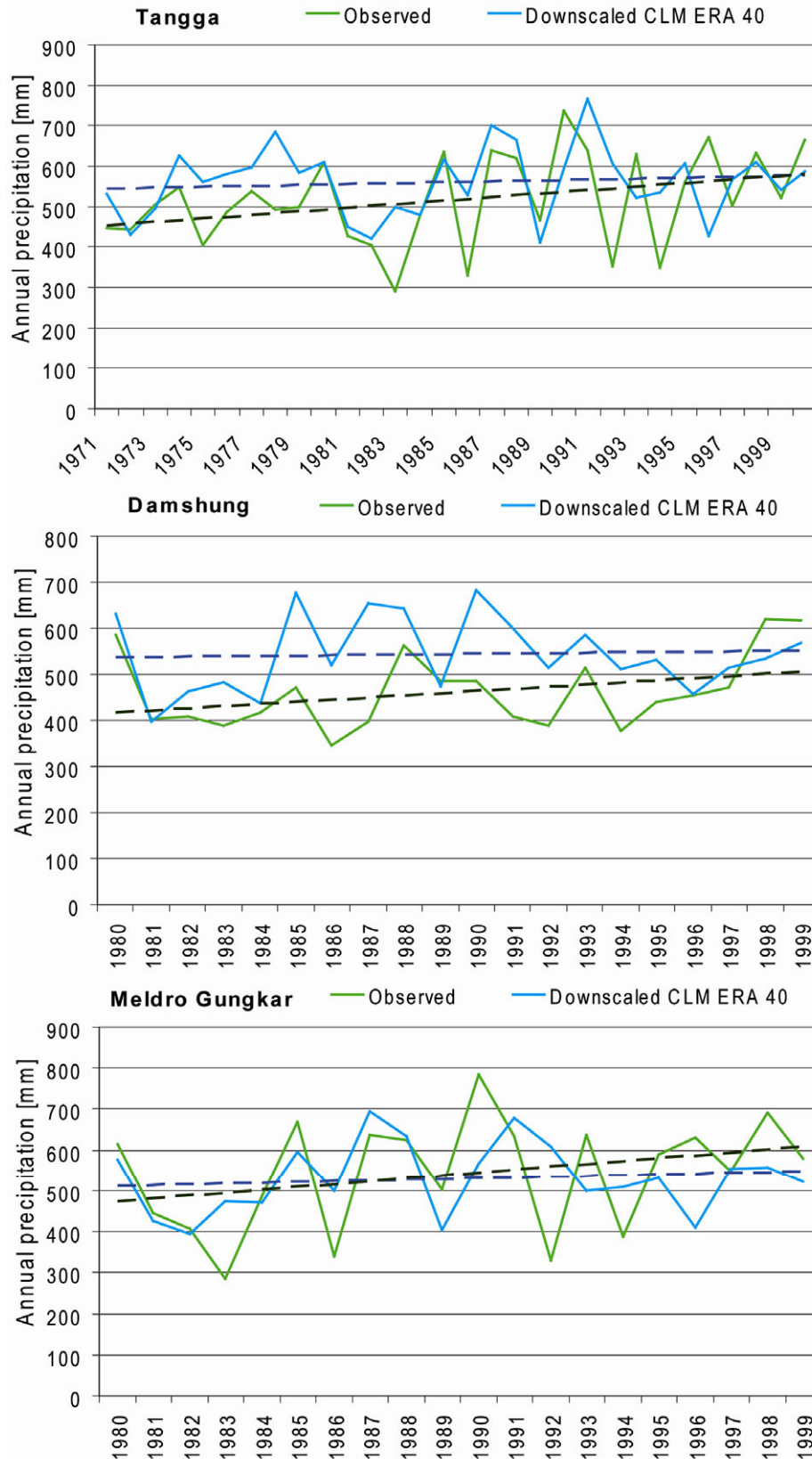
## Appendix 4

Development of modelled (CLM ERA 40) and observed monthly precipitation for the Tangga (1971-2000), Damshung (1980-2000) and Meldro Gungkar (1980-2000) stations.



## Appendix 5

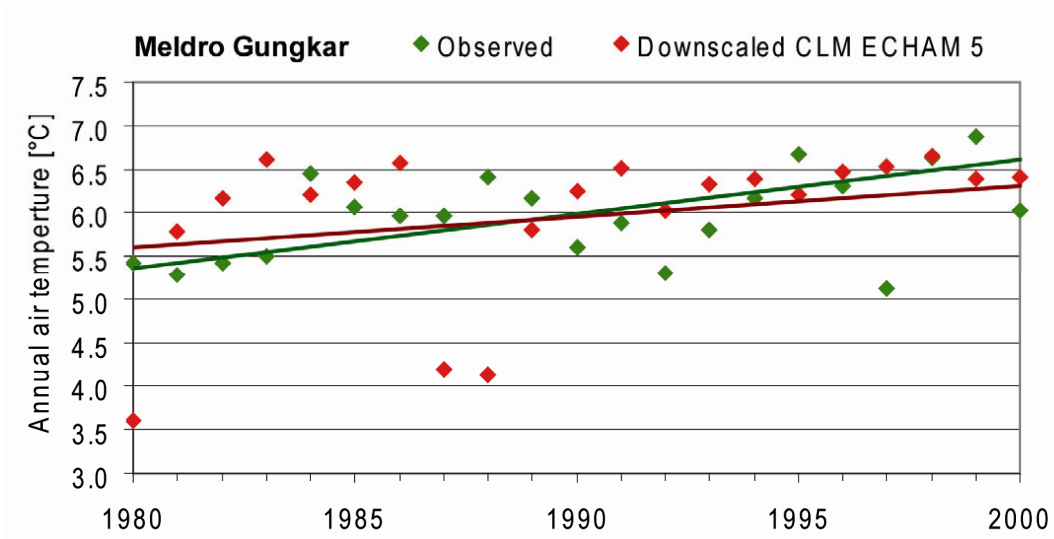
Observed and modelled (CLM ERA 40) trend of the annual precipitation sum at the Tangga (1971-2000), Damshung (1980-2000) and Meldro Gungkar stations.





## Appendix 6

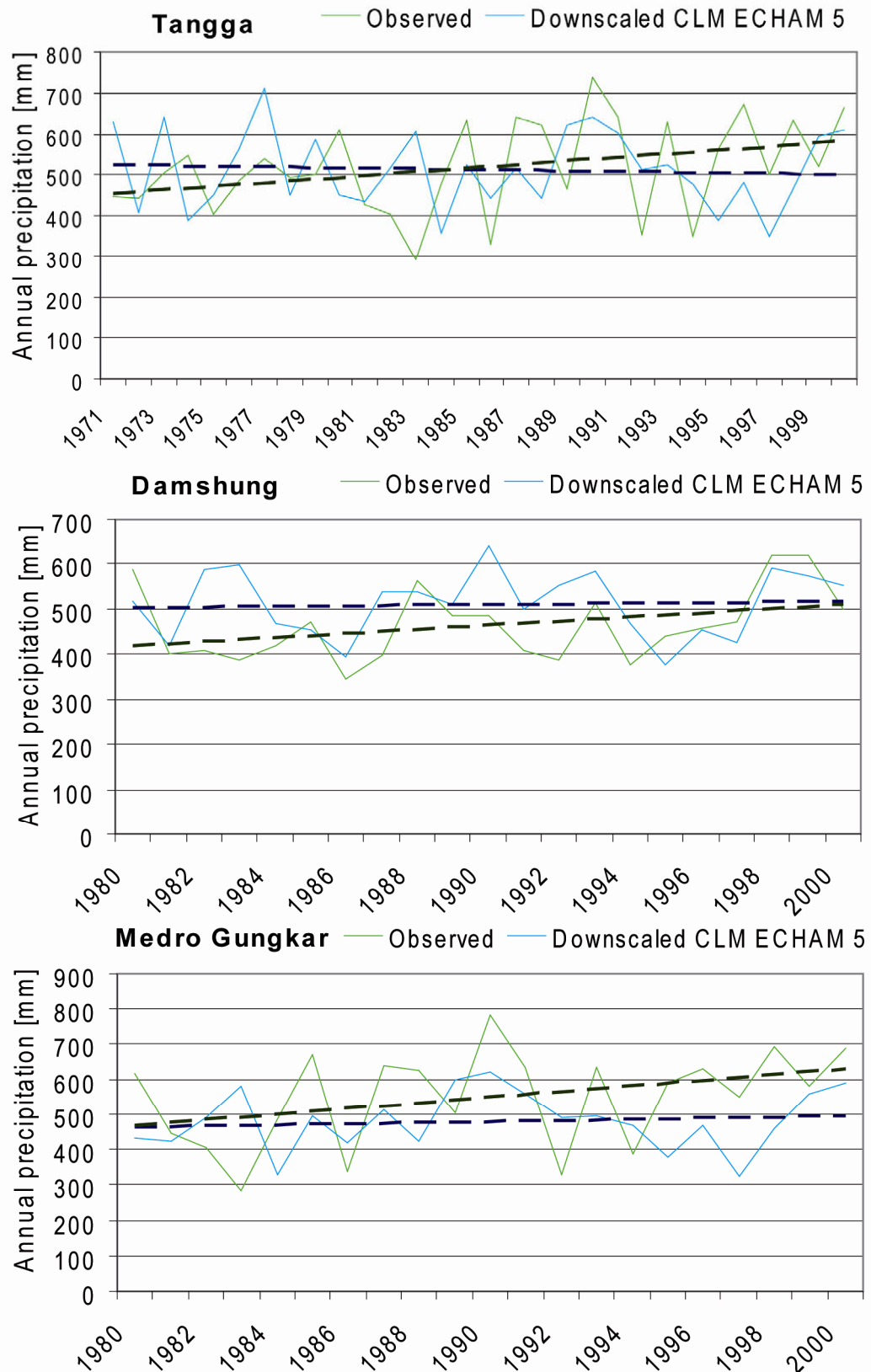
Observed and modelled CLM ECHAM 5 trend of the annual air temperature at the Meldro Gungkar station for 1980-2000.





## Appendix 7

Observed and modelled CLM ECHAM 5 trend of the annual precipitation sum at the Tangga, Damshung und Meldro Gungkar stations for 1970 / 1976-2000.



## Appendix 8

Extract of statistics of the WMO station in Lhasa (U.S. DEPARTMENT OF ENERGY 2010, CRAWLEY ET AL. 1999).

Statistics for CHN\_Lhasa.555910\_CTYW

Location -- Lhasa Tibet CHN {N 29° 40'} {E 91° 7'} {GMT +8.0 Hours}

Elevation -- 3650m above sea level

Standard Pressure at Elevation -- 64504Pa

WMO Station 555910

### Monthly Statistics for Relative Humidity %

	Jan	Feb	Mar	Apr	May	Jun	Jul	Aug	Sep	Oct	Nov	Dec
Max.	93	72	99	95	91	97	99	97	99	99	90	72
Day:H	23:03	23:09	31:06	19:06	11:04	19:10	30:07	28:06	27:07	4:01	4:07	5:09
Min.	3	3	3	1	5	14	22	22	17	5	5	4
Day:H	9:02	7:17	7:21	3:14	17:18	9:18	10:21	31:16	13:16	26:15	6:17	10:18

### Average Hourly Relative Humidity %

	Jan	Feb	Mar	Apr	May	Jun	Jul	Aug	Sep	Oct	Nov	Dec
0:01- 1:00	31	25	27	43	49	54	67	72	73	49	40	36
1:01- 2:00	34	27	30	46	51	58	70	74	75	52	42	38
2:01- 3:00	36	29	33	48	52	61	73	75	76	56	44	40
3:01- 4:00	38	30	36	51	54	63	74	75	76	60	46	42
4:01- 5:00	40	33	39	54	57	66	76	77	78	65	50	43
5:01- 6:00	42	35	43	56	61	69	78	79	82	70	54	45
6:01- 7:00	44	38	46	57	63	70	80	81	85	73	56	45
7:01- 8:00	45	38	46	55	62	68	78	81	83	68	55	45
8:01- 9:00	43	36	41	50	55	63	74	76	76	58	50	42
9:01-10:00	39	32	35	44	47	56	67	70	67	47	43	39
10:01-11:00	33	28	28	37	40	50	61	63	59	38	36	35
11:01-12:00	26	23	22	30	34	45	57	57	53	33	29	32
12:01-13:00	20	20	19	26	31	41	53	52	49	29	24	28
13:01-14:00	16	17	16	23	28	37	49	48	45	25	19	24
14:01-15:00	14	15	14	21	26	34	46	44	42	22	15	20
15:01-16:00	12	13	13	20	24	32	43	42	39	20	14	18
16:01-17:00	13	13	13	21	23	31	42	41	39	20	14	17
17:01-18:00	14	12	13	21	22	31	43	42	41	23	16	17
18:01-19:00	16	13	15	22	23	32	45	46	45	28	19	20
19:01-20:00	19	15	17	24	25	35	48	50	50	35	23	23
20:01-21:00	22	17	19	27	29	38	52	55	56	40	28	27
21:01-22:00	25	19	20	32	34	42	55	60	61	43	32	30
22:01-23:00	27	21	22	36	40	46	59	65	66	45	36	32
23:01-24:00	29	23	24	41	45	50	63	69	70	46	38	33
Max Hour	8	8	7	7	7	7	7	7	7	7	7	7
Min Hour	16	18	17	16	18	17	17	17	17	16	16	17

Monthly Statistics for Solar Radiation (Direct Normal, Diffuse, Global Horizontal) Wh/m<sup>2</sup>

	Jan	Feb	Mar	Apr	May	Jun	Jul	Aug	Sep	Oct	Nov	Dec
Direct Avg	6213	6632	5264	6283	7023	7802	6816	6763	7138	8131	7341	7246
Direct Max	8911	9837	9247	9842	10462	12143	10919	11210	10720	10301	9553	8903
Day	23	27	20	15	20	25	10	31	14	8	10	9
Diffuse Av	928	1186	2031	2178	2404	2238	2474	2217	1686	1085	869	665
Global Av	3804	4746	5117	6396	7139	7868	7497	7032	6420	5588	4369	3931

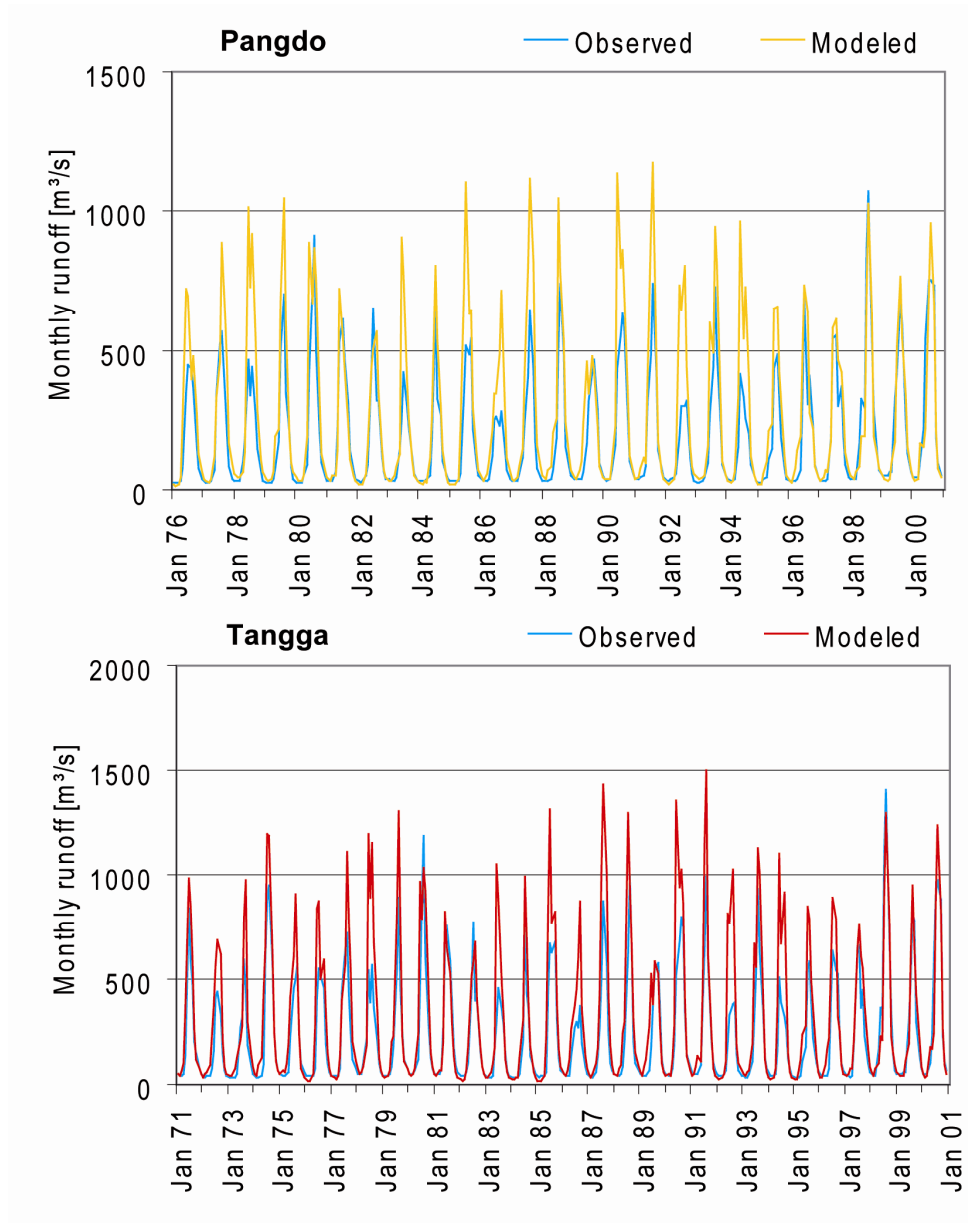
Maximum Direct Normal Solar of 12143 Wh/m<sup>2</sup> on Jun 25

Average Hourly Statistics for Direct Normal Solar Radiation Wh/m<sup>2</sup>

	Jan	Feb	Mar	Apr	May	Jun	Jul	Aug	Sep	Oct	Nov	Dec
0:01- 1:00	0	0	0	0	0	0	0	0	0	0	0	0
1:01- 2:00	0	0	0	0	0	0	0	0	0	0	0	0
2:01- 3:00	0	0	0	0	0	0	0	0	0	0	0	0
3:01- 4:00	0	0	0	0	0	0	0	0	0	0	0	0
4:01- 5:00	0	0	0	0	0	0	0	0	0	0	0	0
5:01- 6:00	0	0	0	0	0	0	0	0	0	0	0	0
6:01- 7:00	0	0	0	0	0	0	0	0	0	0	0	0
7:01- 8:00	0	0	0	144	425	395	227	120	3	0	0	0
8:01- 9:00	0	77	444	613	731	607	470	489	518	724	410	10
9:01-10:00	716	748	730	733	840	680	538	597	709	914	940	769
10:01-11:00	895	879	800	814	905	777	612	716	814	943	1008	930
11:01-12:00	910	881	786	818	901	780	646	720	828	929	986	950
12:01-13:00	869	849	684	771	779	781	682	715	808	883	919	941
13:01-14:00	808	796	536	689	562	809	748	742	798	841	800	930
14:01-15:00	725	724	429	563	454	724	708	685	732	798	745	893
15:01-16:00	597	633	331	414	379	641	627	598	635	769	654	822
16:01-17:00	433	521	245	307	368	573	597	551	561	732	573	663
17:01-18:00	257	390	190	255	328	480	485	460	467	558	307	339
18:01-19:00	2	135	89	161	270	367	346	319	265	40	0	0
19:01-20:00	0	0	0	2	81	189	130	51	0	0	0	0
20:01-21:00	0	0	0	0	0	0	0	0	0	0	0	0
21:01-22:00	0	0	0	0	0	0	0	0	0	0	0	0
22:01-23:00	0	0	0	0	0	0	0	0	0	0	0	0
23:01-24:00	0	0	0	0	0	0	0	0	0	0	0	0
Max Hour*	12	12	11*	12	11*	14	14	14	12	11*	11*	12
Min Hour	1	1	1	1	1	1	1	1	1	1	1	1

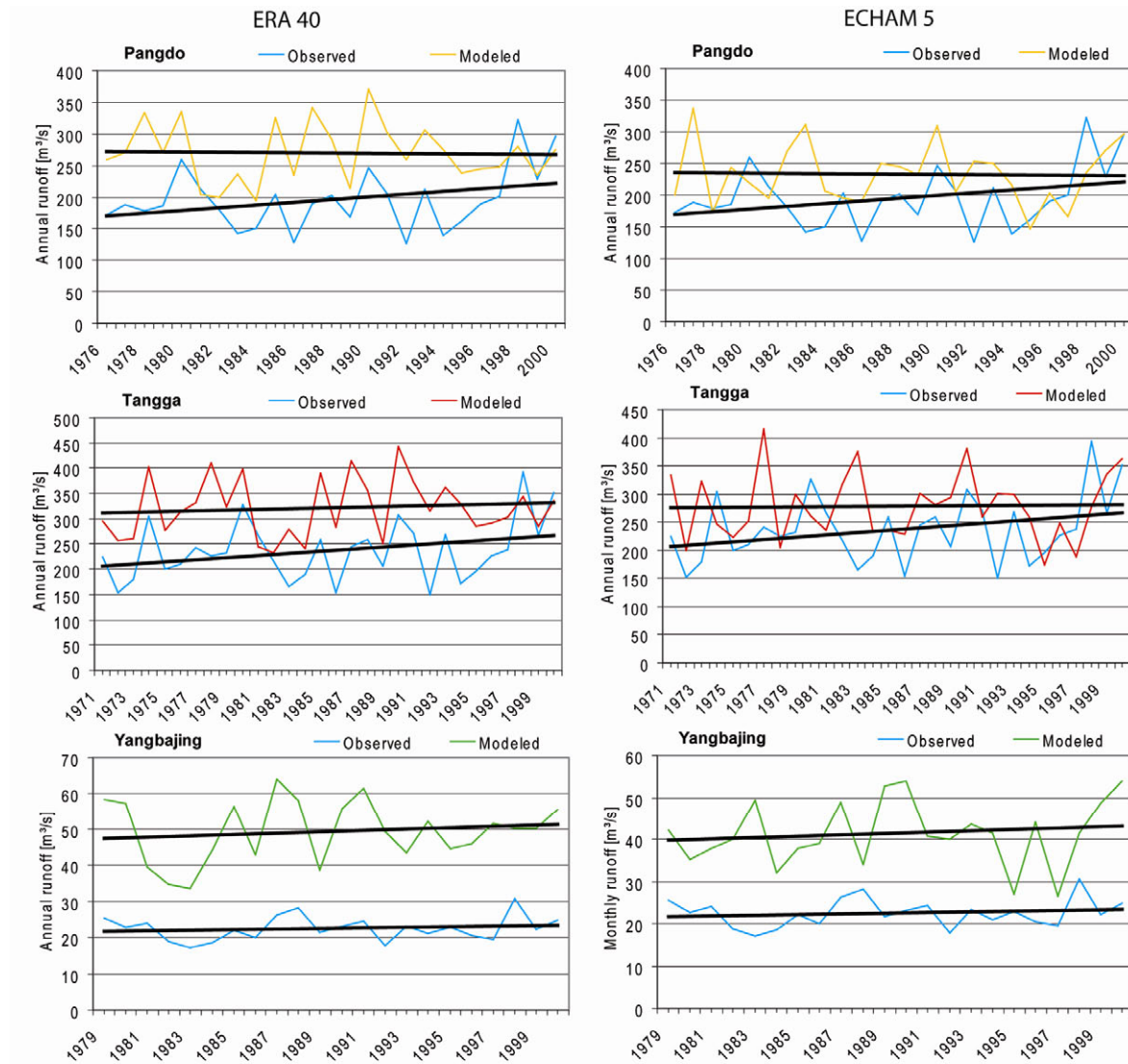
**Appendix 9**

Monthly modelled and observed runoff at the Pangdo and Tangga gauges from 1971-2000 (ERA 40).



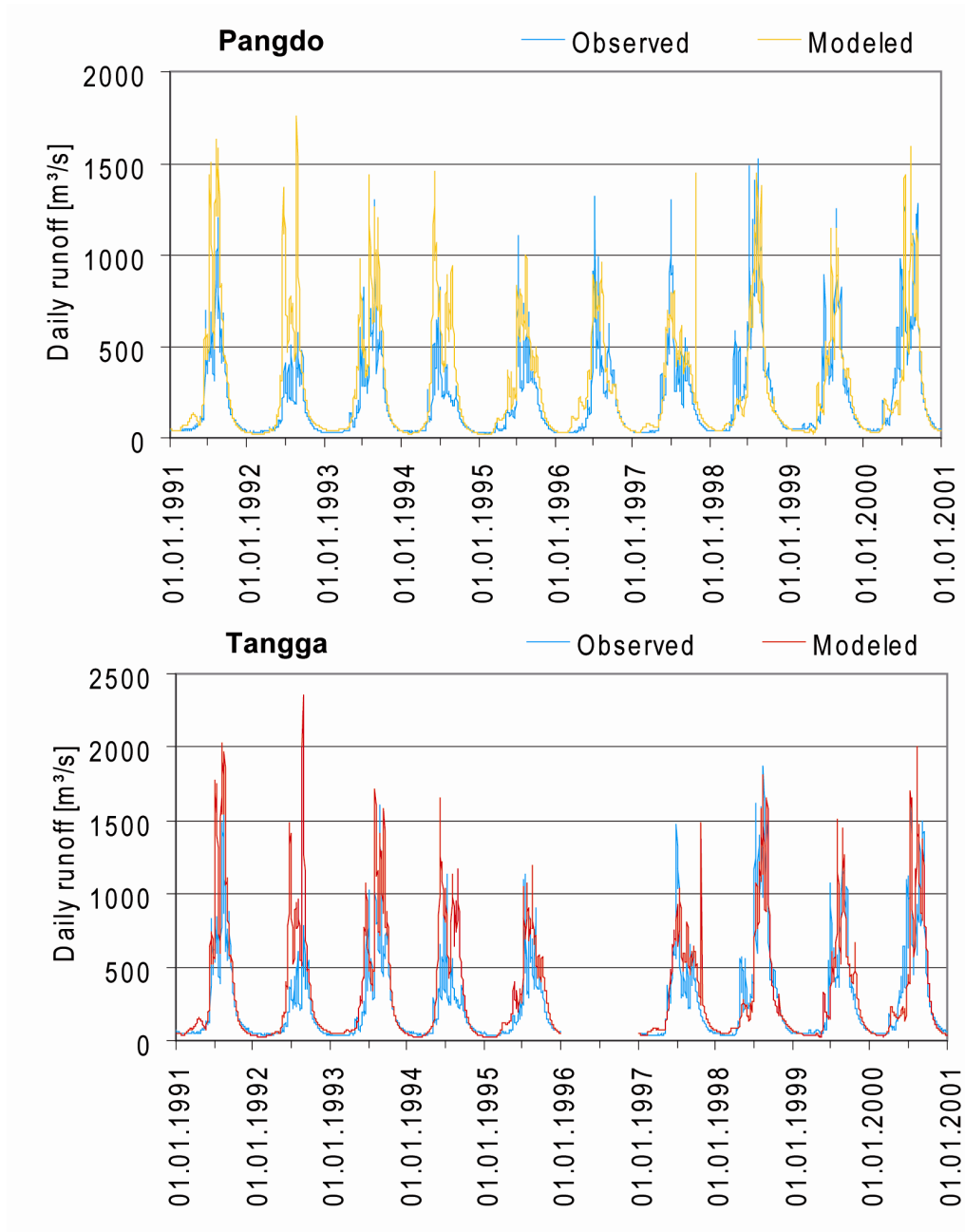
## Appendix 10

Annual modelled and observed runoff at the Pangdo, Tangga and Yangbajing gauges from 1971-2000 for ERA 40 (left) and ECHAM 5 (right) meteorological data.



**Appendix 11**

Development of daily observed and modelled runoff at the gauge in Pangdo and Tangga from 1991 to 2000 (CLM ERA 40).





**Appendix 12**

Quality criteria for modelled daily runoff, driven by CLM ERA 40 meteorological data.

Period	Criterion	Lhasa	Pangdo	Tangga
1996 – 2000	R <sup>2</sup>	0.73	0.72	0.75
	NSC	0.67	0.70	0.73
1991 – 2000	R <sup>2</sup>	0.67	0.65	0.67
	NSC	0.34	0.41	0.44
1991	R <sup>2</sup>	0.87	0.87	0.88
	NSC	0.25	0.22	0.43
1992	R <sup>2</sup>	0.73	0.71	0.72
	NSC	-6.23	-3.75	-3.81
1993	R <sup>2</sup>	0.76	0.77	0.76
	NSC	0.45	0.39	0.49
1994	R <sup>2</sup>	0.75	0.73	0.72
	NSC	-3.05	-2.29	-1.82
1995	R <sup>2</sup>	0.78	0.78	0.75
	NSC	0.37	0.42	0.38
1996	R <sup>2</sup>	0.65	0.67	no observations
	NSC	0.61	0.55	no observations
1997	R <sup>2</sup>	0.69	0.69	0.71
	NSC	0.31	0.50	0.60
1998	R <sup>2</sup>	0.88	0.82	0.86
	NSC	0.86	0.81	0.85
1999	R <sup>2</sup>	0.65	0.69	0.67
	NSC	0.53	0.67	0.64
2000	R <sup>2</sup>	0.75	0.70	0.72
	NSC	0.68	0.66	0.67

### Appendix 13

Statistical values for the analysis of annual air temperature, precipitation sum and global radiation sum. The time period for the past is 1971 to 2000, whereas the scenario period is set from 2001 to 2080.

Meteoro-logical variable	Scenario	Average	Abso-lute trend	Standard deviation $\sigma$	Trend-to-noise ratio T/N	Mann-Kendall value Q	Signifi-cance level $\alpha$
Air temperature [°C]	Past	-0.1	0.7	0.8	0.9	2.46	0.05
	A1B		4.6	1.5	3.1	9.77	0.001
	A2		4.3	1.5	2.8	8.40	0.001
	B1		2.4	1.0	2.4	6.64	0.001
	CON		0.4	0.9	0.5	1.57	-
Precipitation [mm]	Past	630	4	87	0.0	0.36	-
	A1B		-73	86	0.8	-2.16	0.05
	A2		-57	99	0.6	-1.15	-
	B1		3	100	0.0	0.18	-
	CON		-26	92	0.3	-1.34	-
Global radiation [W/m <sup>2</sup> ]	Past	288515	-200	43388	0.0	-0.04	-
	A1B		93298	45812	2.0	5.50	0.001
	A2		68122	49497	1.4	3.83	0.001
	B1		66429	49575	1.3	3.60	0.001
	CON		35975	54532	0.7	0.30	-

## Appendix 14

Statistical values for the analysis of summer (April to September) and winter (October – March) air temperature and precipitation sum. The time period for the past is 1971 to 2000, whereas the scenario period is set to 2001 to 2080.

Meteoro-logical variable	Scenario	Average	Abso-lute trend	Standard deviation $\sigma$	Trend-to-noise ratio T/N	Mann-Kendall value Q	Signifi-cance level $\alpha$
Summer air temperature [°C]	Past	5.9	0.3	0.7	0.4	0.71	-
	A1B		4.2	1.4	3.1	9.39	0.001
	A2		3.8	1.3	2.9	8.92	0.001
	B1		2.9	1.1	2.7	7.60	0.001
	CON		0.4	0.8	0.5	1.23	-
Winter air temperature [°C]	Past	-6.1	1.1	1.3	0.9	1.28	-
	A1B		5.0	1.8	2.8	8.53	0.001
	A2		4.9	2.0	2.5	6.83	0.001
	B1		1.9	1.3	1.5	3.97	0.001
	CON		0.5	1.5	0.3	0.88	-
Summer precipitation [mm]	Past	551	-3	92	0.0	0.29	-
	A1B		-58	82	0.7	-1.77	0.1
	A2		-51	96	0.5	-0.98	-
	B1		-3	97	0.0	0.03	-
	CON		-24	94	0.3	-1.03	-
Winter precipitation [mm]	Past	78	6.2	21	0.3	0.54	-
	A1B		-15	21	0.7	-1.71	0.1
	A2		-7	29	0.2	-0.46	-
	B1		6	23	0.3	0.79	-
	CON		-2	26	0.1	-0.42	-

## Appendix 15

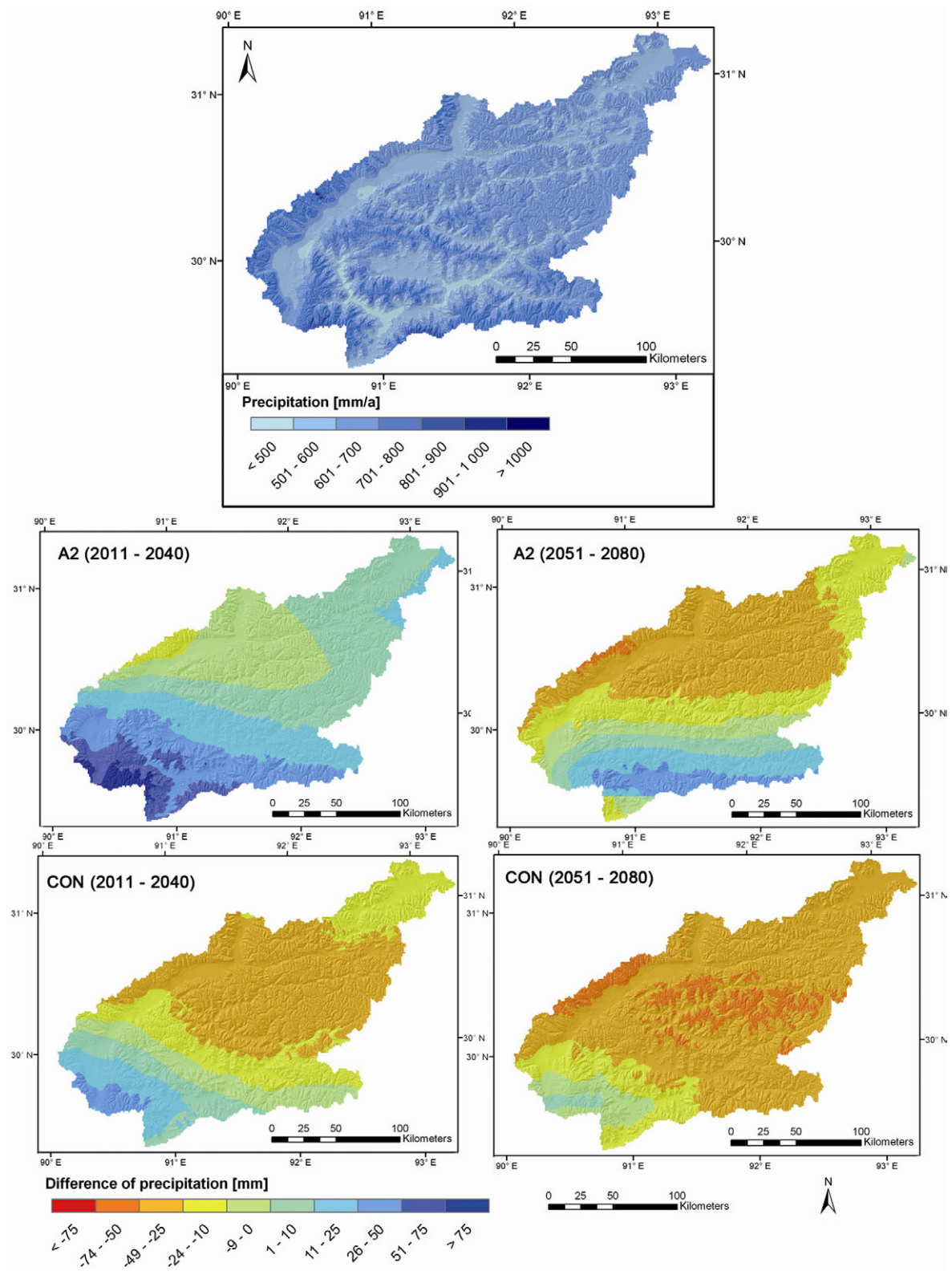
Statistical values for the analysis of monthly air temperature and precipitation sum according to the four different IPCC SRES scenarios. The time period for the past is 1971 to 2000, whereas the scenario period is set to 2001 to 2080.

Meteorological variable	Scenario	Mann-Kendall value Q	Significance level $\alpha$	Mann-Kendall value Q	Significance level $\alpha$
		Air temperature [°C]		Precipitation [mm]	
January	Past	1.18		0.21	
	A1B	5.84	0.001	-2.08	0.05
	A2	5.31	0.001	-3.02	0.01
	B1	2.47	0.05	-1.92	0.1
	CON	-0.95		-0.26	
February	Past	0.00		-0.54	
	A1B	6.66	0.001	-2.70	0.01
	A2	5.11	0.001	-0.91	
	B1	3.09	0.01	2.36	0.05
	CON	0.44		-0.59	
March	Past	-0.07		0.68	
	A1B	5.76	0.001	-0.64	
	A2	5.04	0.001	0.13	
	B1	2.72	0.001	-0.22	
	CON	0.74		0.41	
April	Past	-0.54		0.18	
	A1B	6.30	0.001	-2.40	0.05
	A2	4.67	0.001	-1.92	0.1
	B1	3.44	0.001	-0.49	
	CON	1.02		0.22	
May	Past	0.75		-1.07	0.05
	A1B	7.49	0.001	-2.04	
	A2	5.76	0.001	-1.92	0.1
	B1	5.80	0.001	-1.52	
	CON	0.86		-1.33	
June	Past	1.25		0.00	
	A1B	6.39	0.001	-0.44	
	A2	6.93	0.001	-1.72	0.1
	B1	5.41	0.001	0.10	
	CON	0.41		-0.52	

Meteorological variable	Scenario	Mann-Kendall	Significance	Mann-Kendall	Significance
		value Q	level $\alpha$	value Q	level $\alpha$
		Air temperature [°C]		Precipitation [mm]	
July	Past	1.28		0.79	
	A1B	7.26	0.001	-2.75	0.01
	A2	7.41	0.001	-1.03	
	B1	5.60	0.001	-0.84	
	CON	1.31		0.14	
August	Past	0.29		0.54	
	A1B	8.60	0.001	1.53	0.1
	A2	7.73	0.001	1.74	
	B1	7.47	0.001	1.33	
	CON	1.30		-0.39	
September	Past	0.11		-1.75	0.1
	A1B	7.83	0.001	0.57	
	A2	7.04	0.001	0.12	
	B1	5.70	0.001	0.23	
	CON	0.88		-0.10	
October	Past	0.57		1.00	
	A1B	7.11	0.001	0.12	
	A2	5.52	0.001	0.74	
	B1	4.73	0.001	0.55	
	CON	0.59		0.24	
November	Past	1.82	0.1	-1.11	
	A1B	4.75	0.001	-2.46	0.05
	A2	5.60	0.001	-1.12	
	B1	3.07	0.01	0.39	
	CON	-0.24		0.69	
December	Past	1.57		0.61	
	A1B	6.06	0.001	-1-13	
	A2	5.72	0.001	-1.31	
	B1	1.72	0.1	-1.33	
	CON	0.98		-0.80	

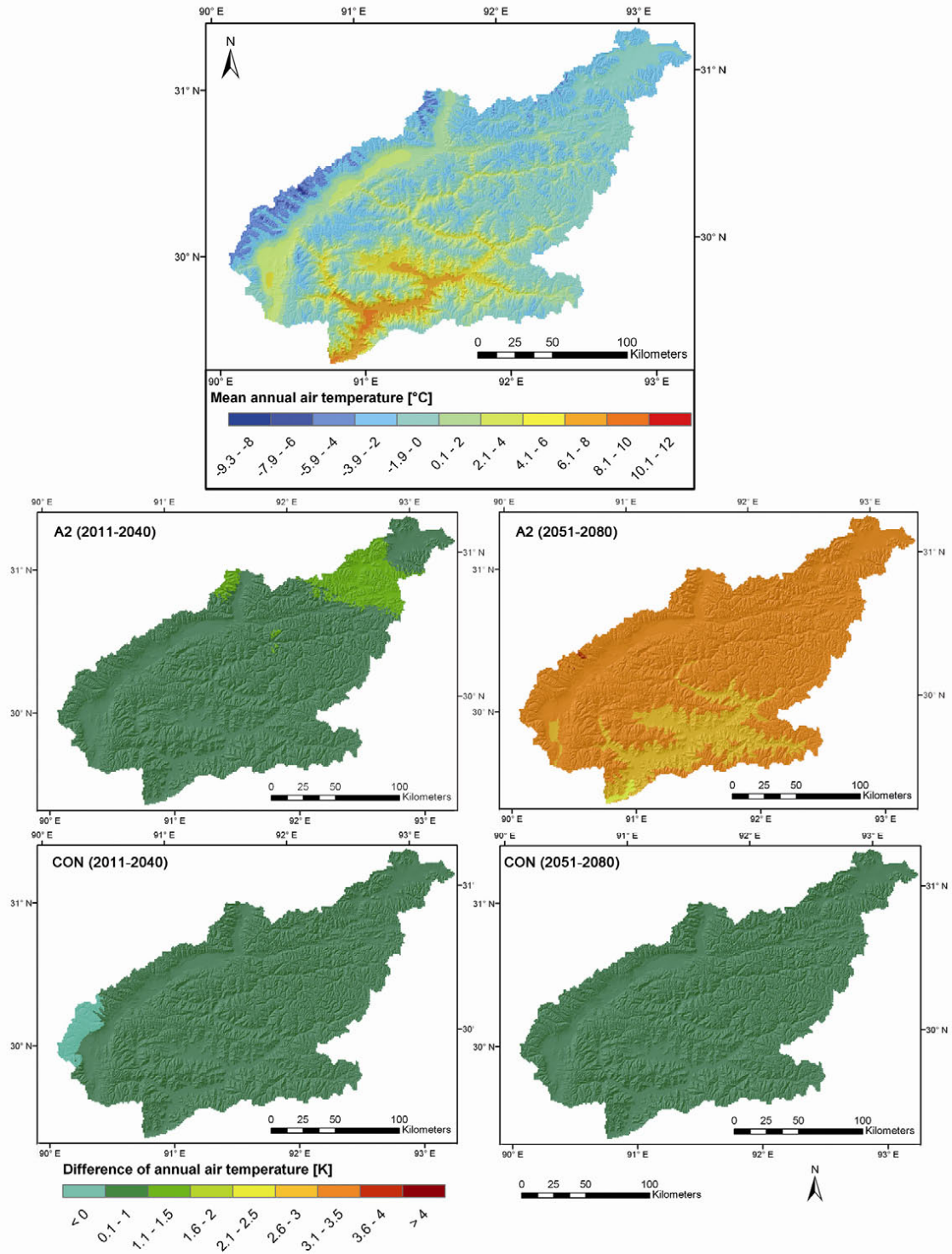
### Appendix 17

Mean annual precipitation from 1971 to 2000 (top) and the changes in the periods 2011 to 2040 (left) and 2051 to 2080 (right) according to the A2 scenario (middle) and CON scenario (bottom).



## Appendix 16

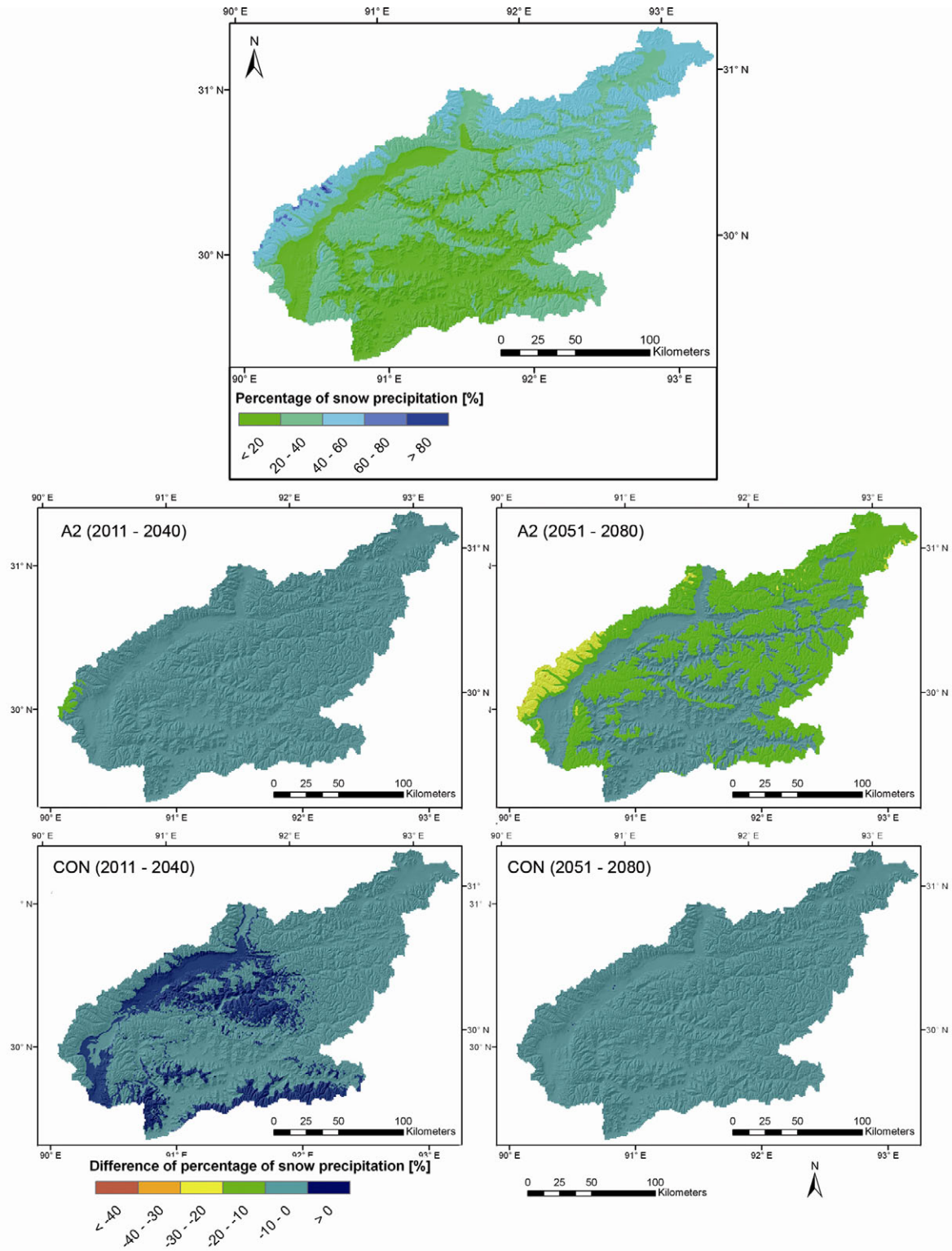
Mean annual air temperature from 1971 to 2000 (top) and the changes in the periods 2011 to 2040 (left) and 2051 to 2080 (right) according to the A2 scenario (middle) and CON scenario (bottom).





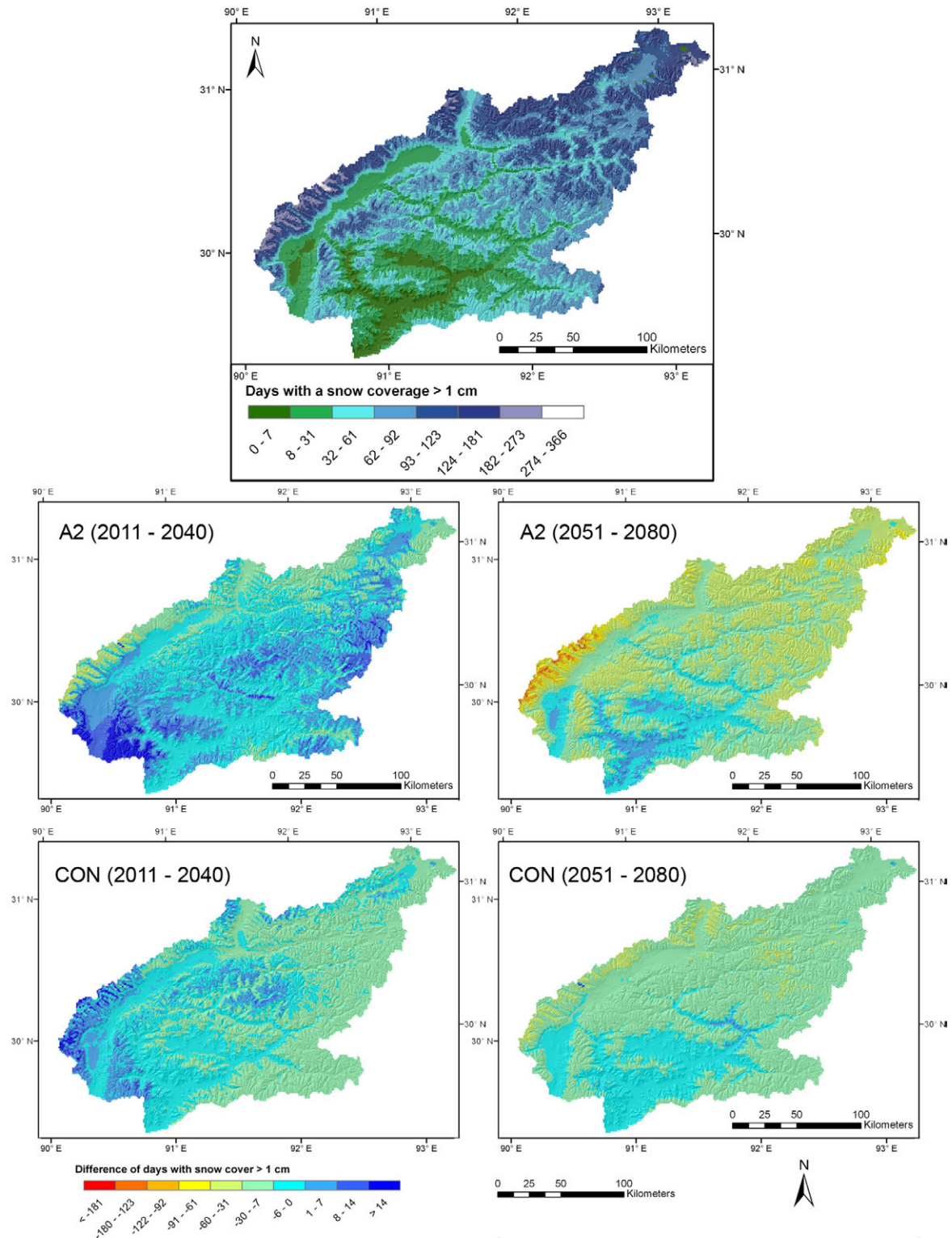
## Appendix 18

Mean annual percentage of snow precipitation from 1971 to 2000 (top) and the changes in the periods 2011 to 2040 (left) and 2051 to 2080 (right) according to the A2 scenario (middle) and CON scenario (bottom).



## Appendix 19

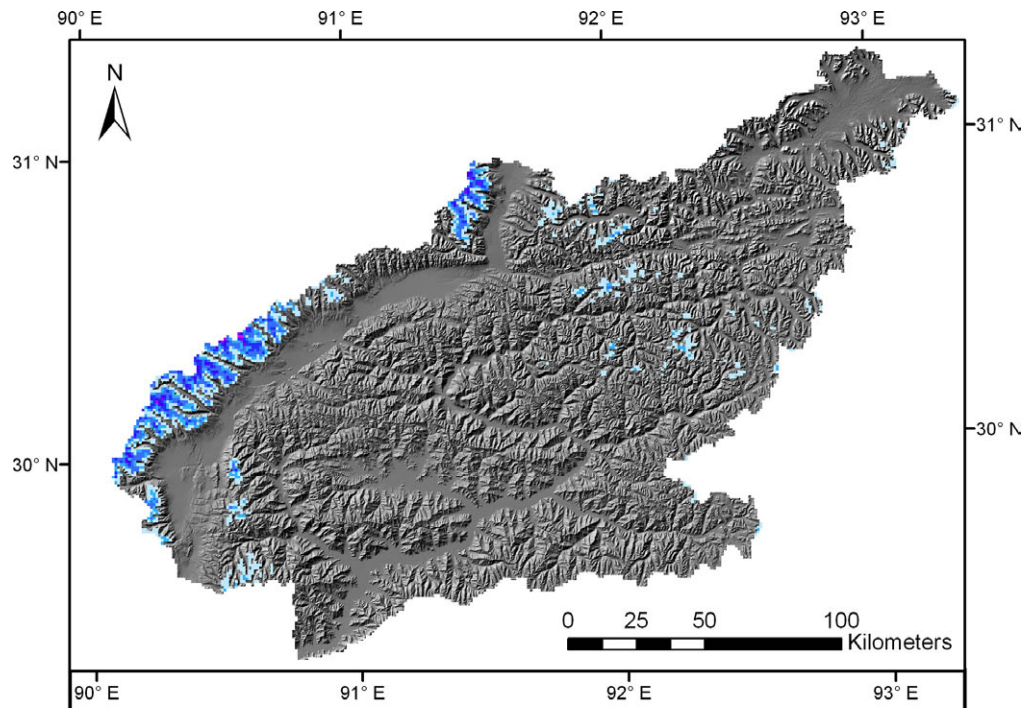
Mean annual days with snow cover (swe > 10 mm) from 1971 to 2000 (top) and the changes in the periods 2011 to 2040 (left) and 2051 to 2080 (right) according to the A2 scenario (middle) and CON scenario (bottom).



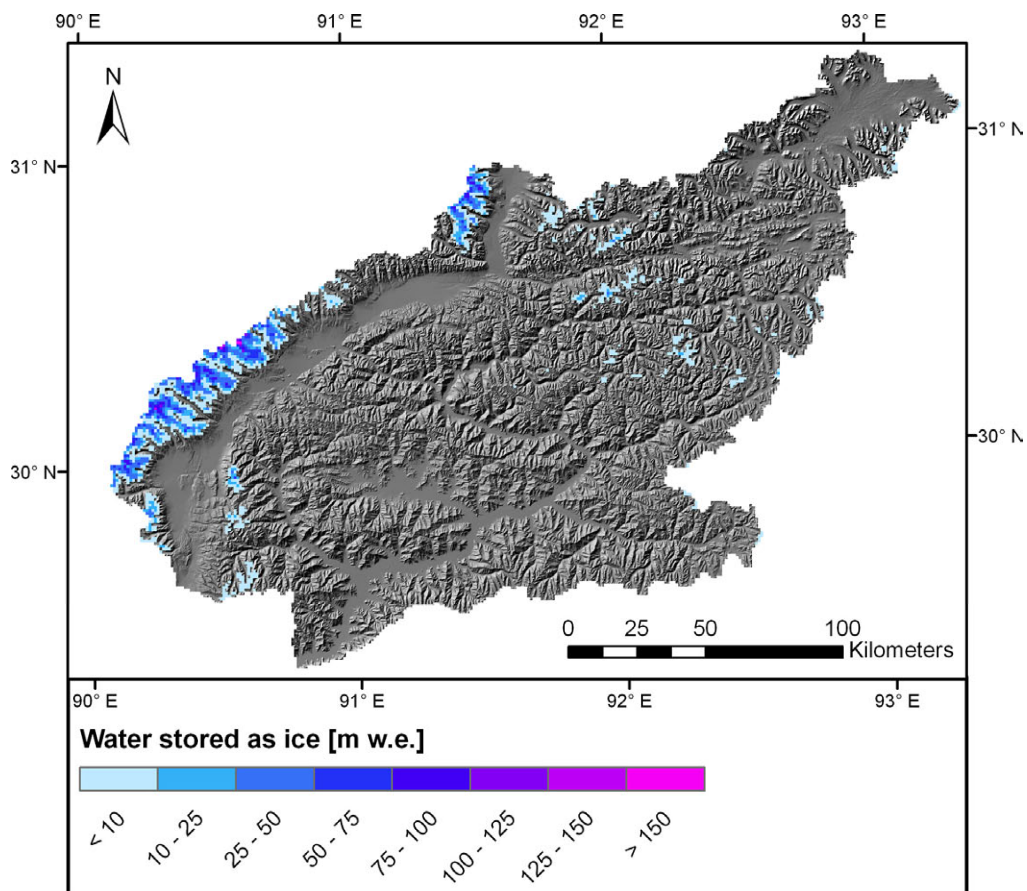
## Appendix 20

The development of the simulated ice water equivalent distribution from 1970 to 2080 over the decades according to the CLM ECHAM5 IPCC Past, A1B and B1, A2 and CON scenario model runs.

1970

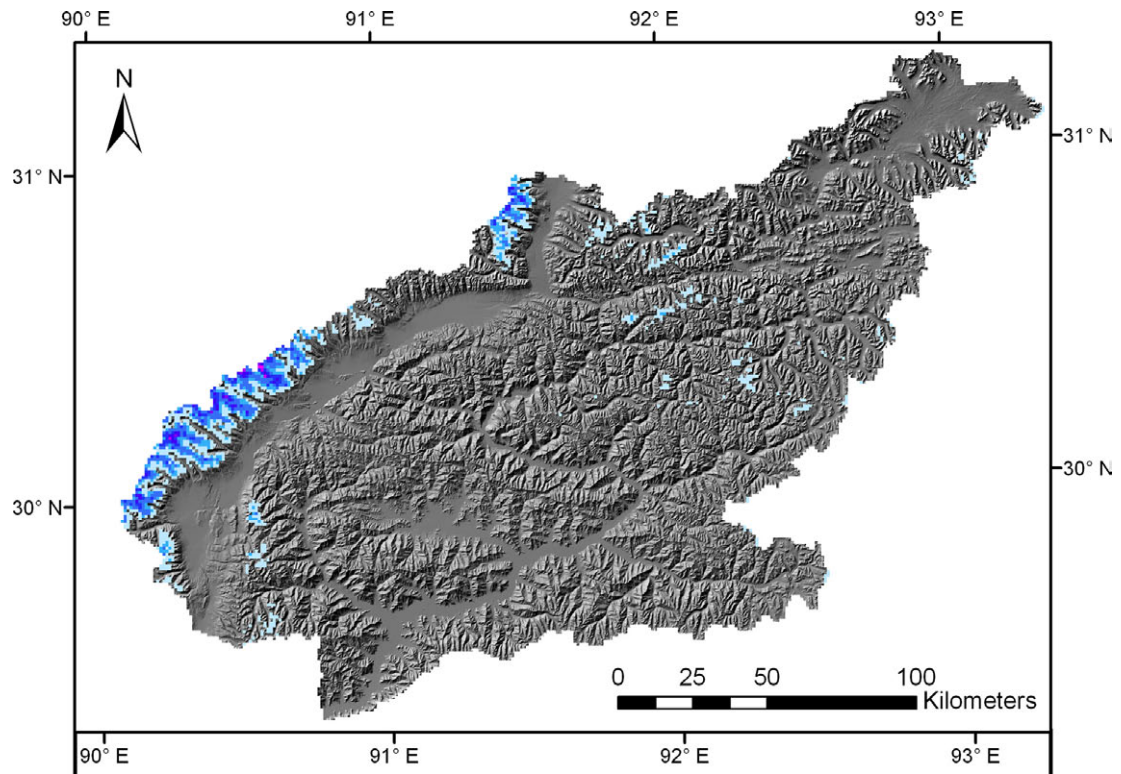


1980

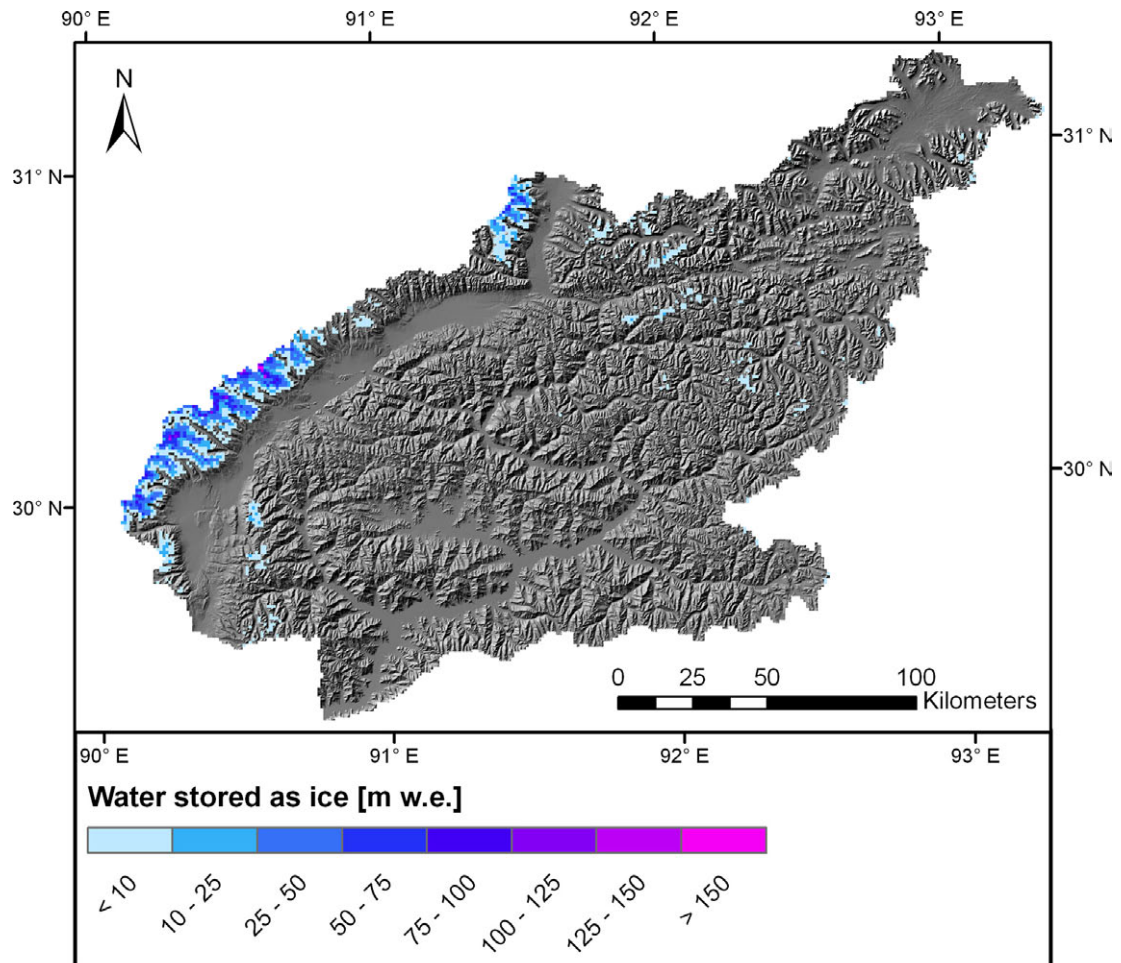




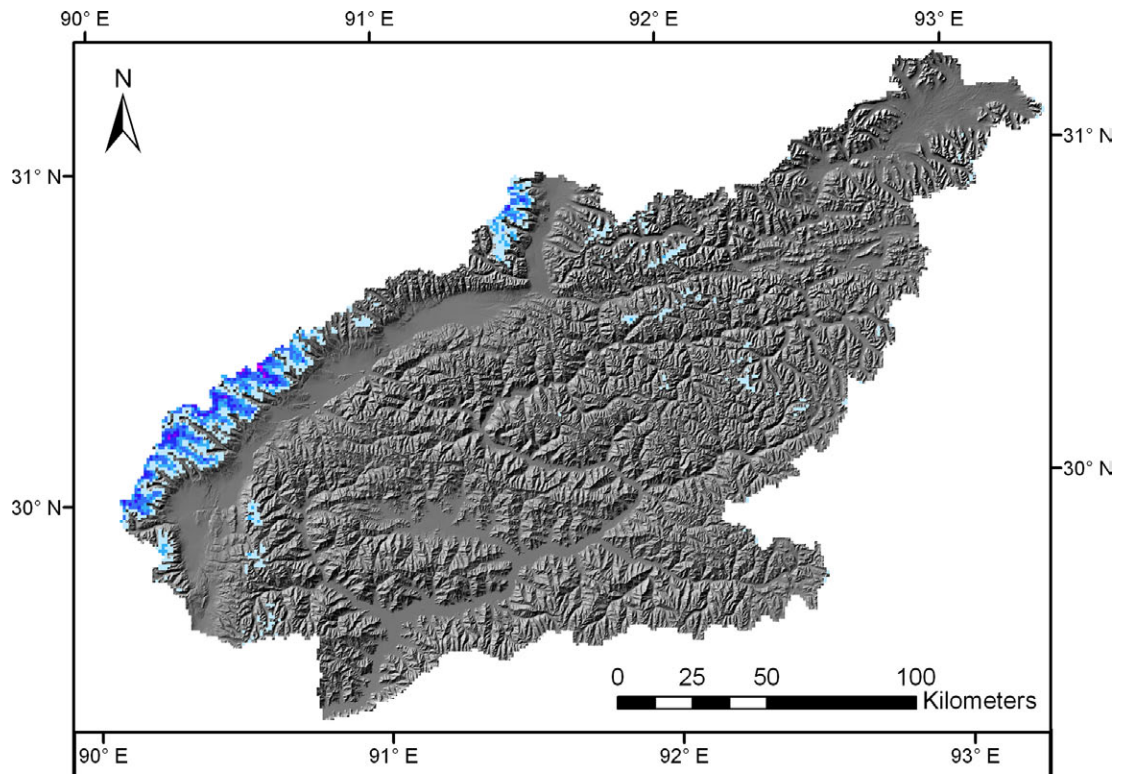
1990



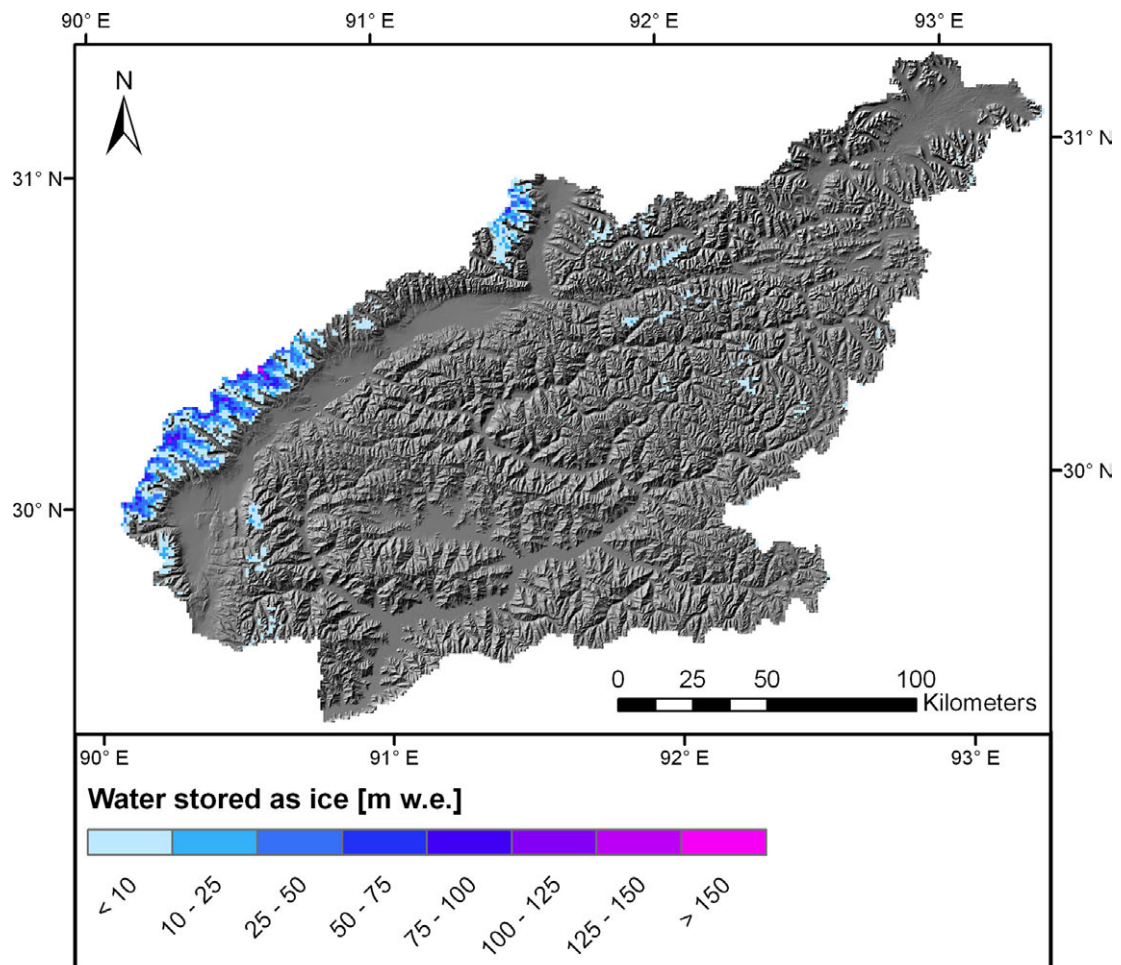
2000



2010 A1B

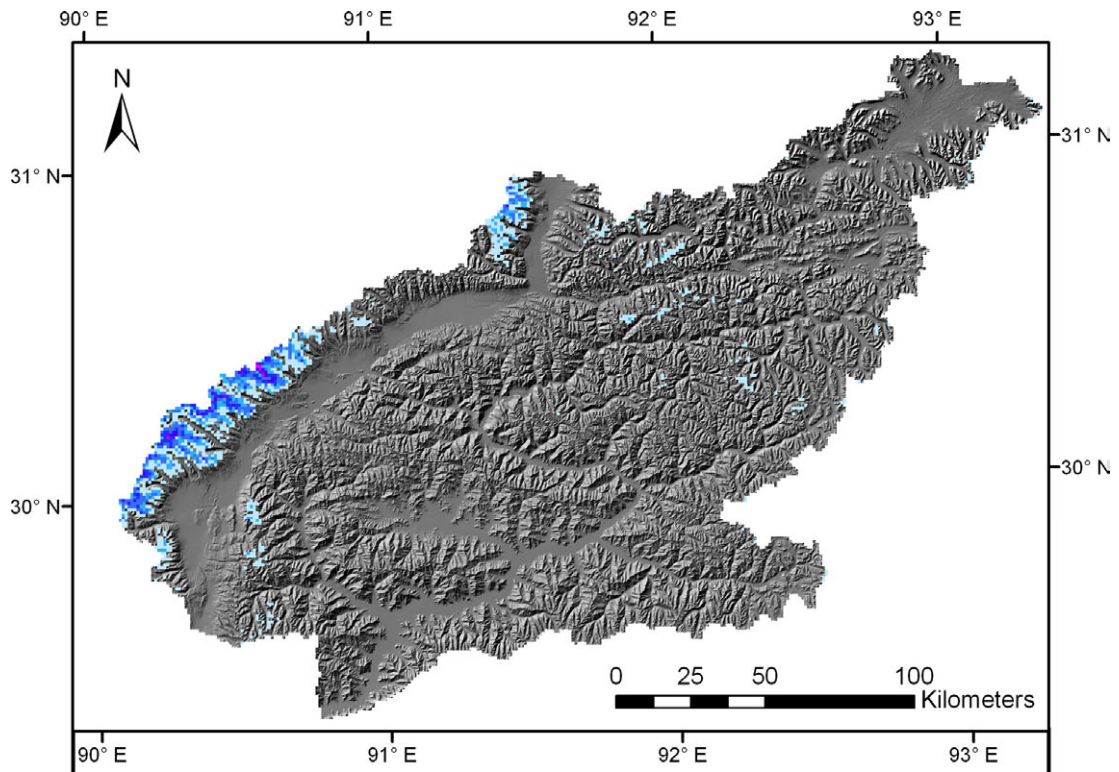


2010 B1

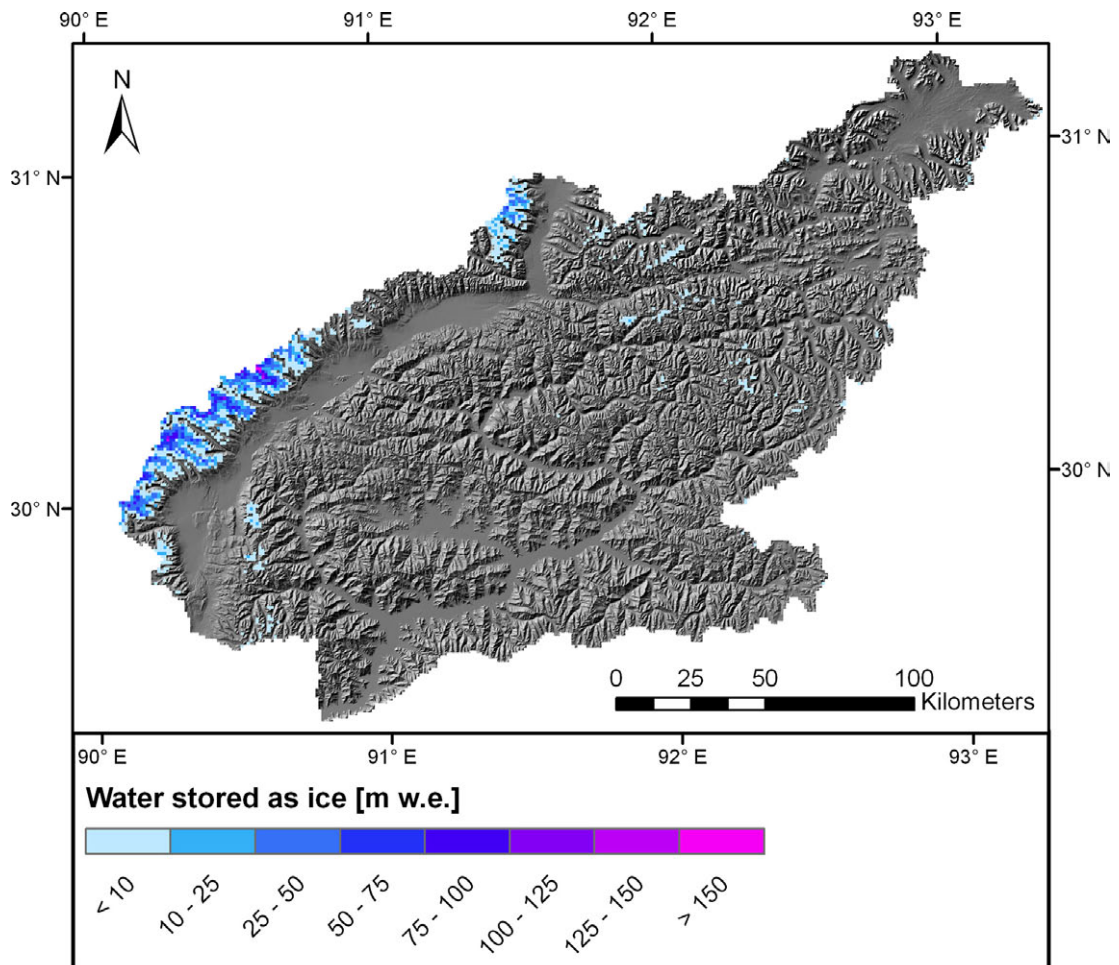




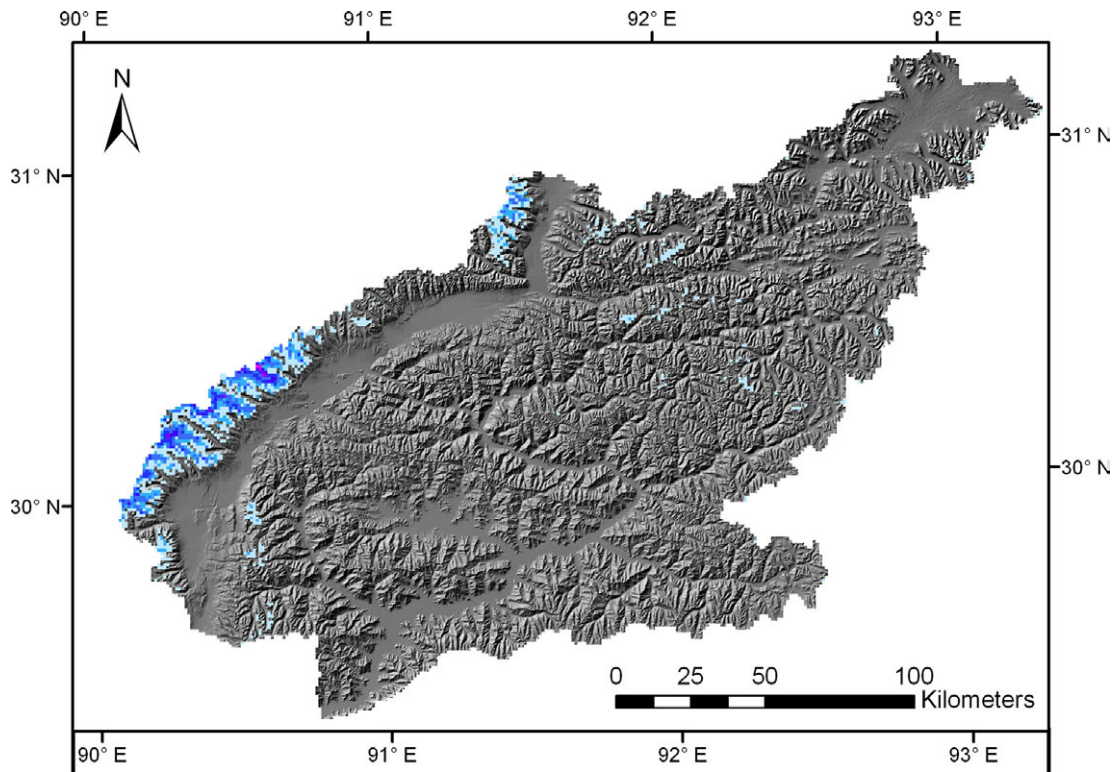
2020 A1B



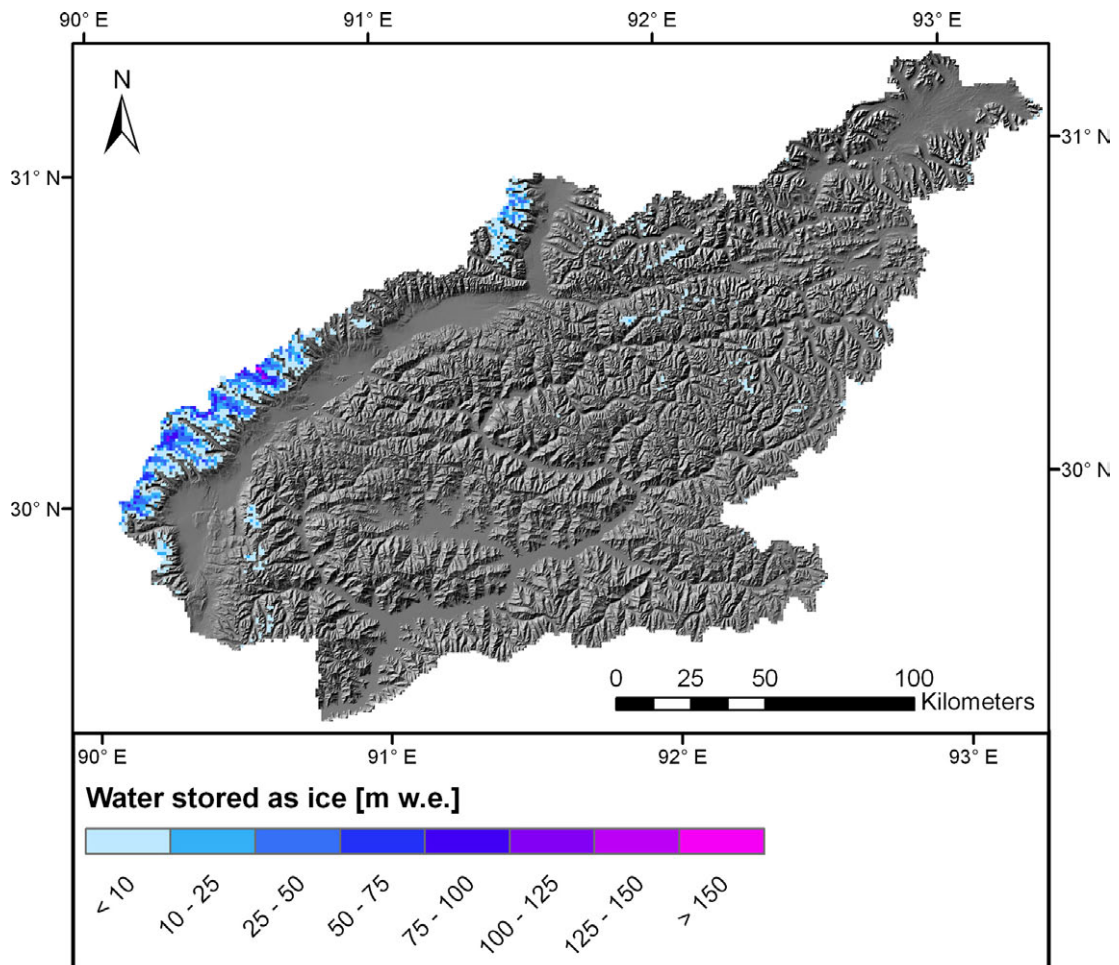
2020 B1



2030 A1B

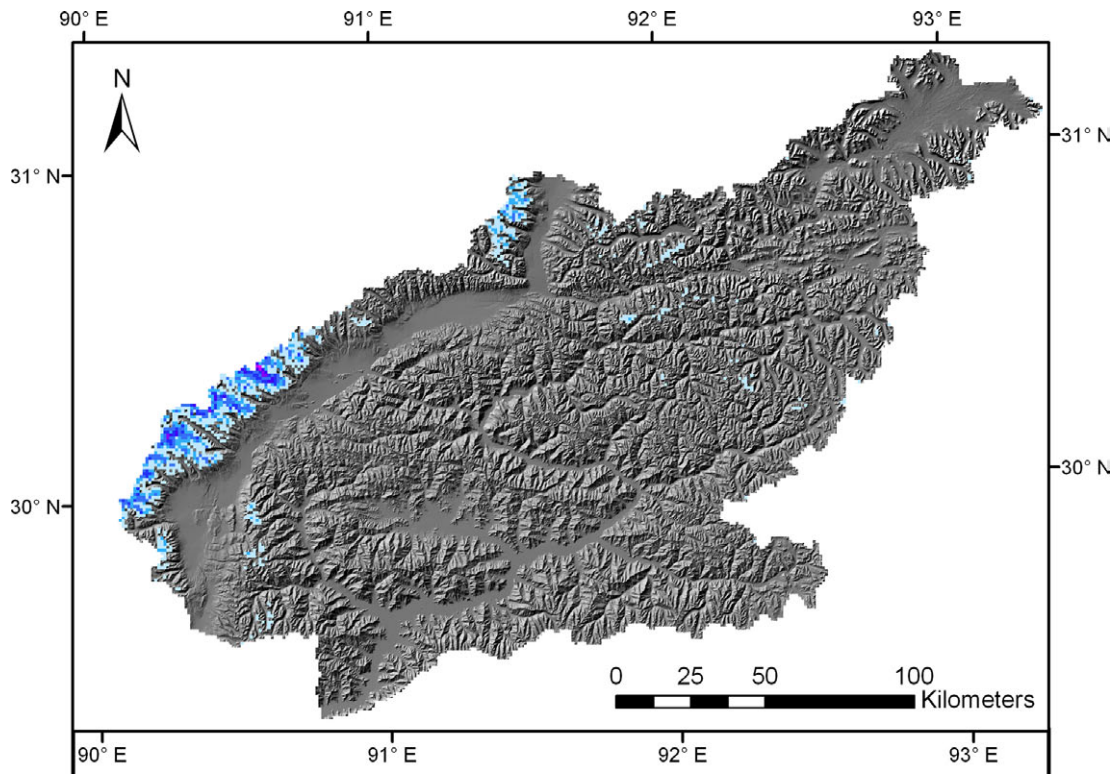


2030 B1

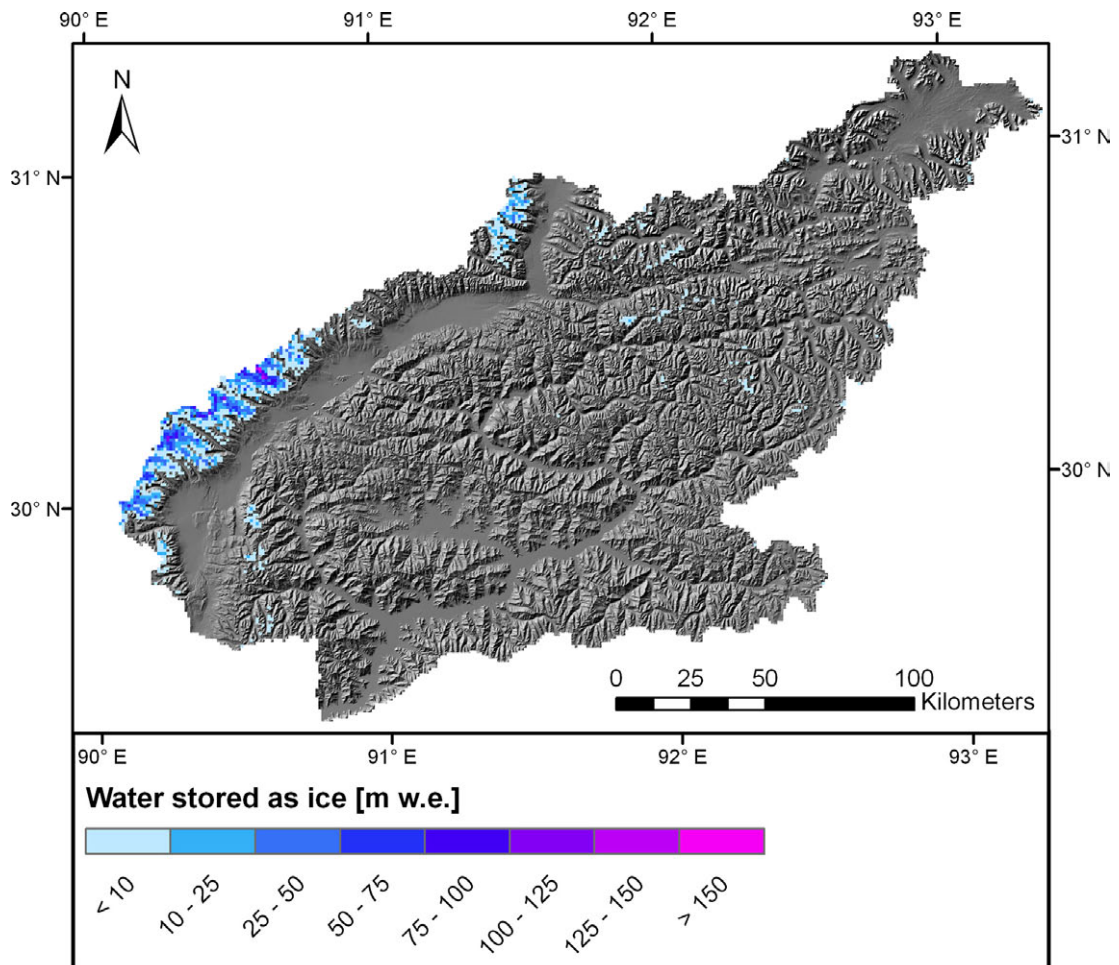




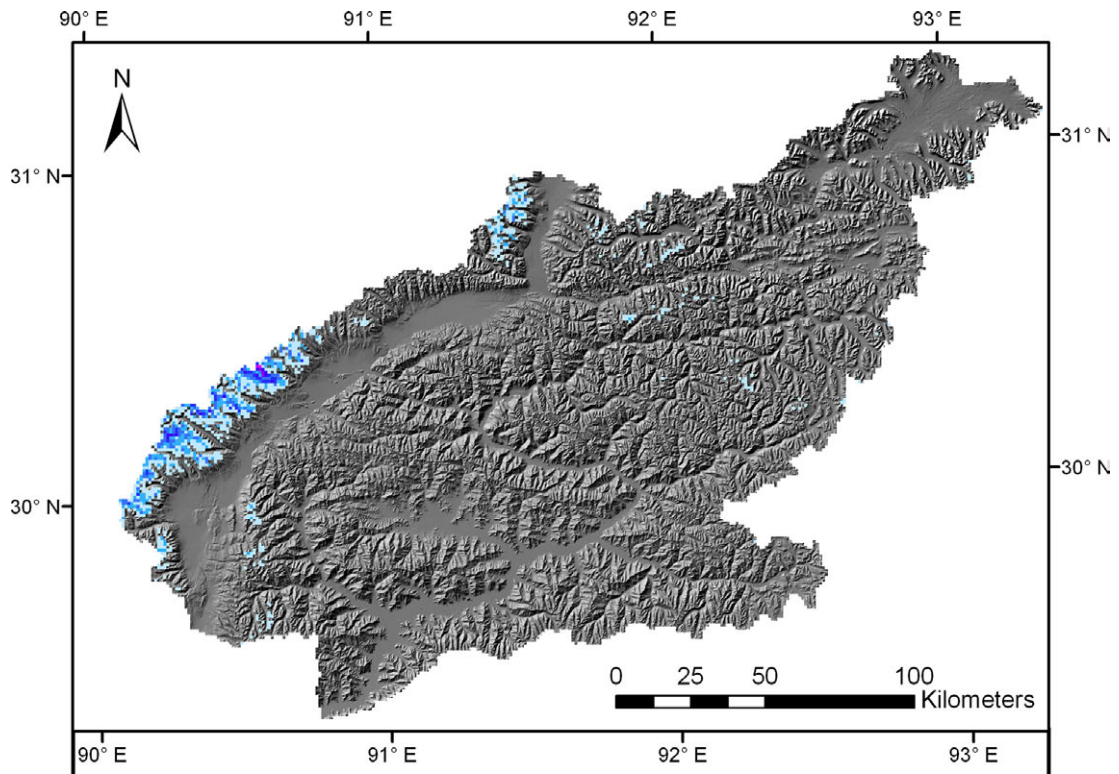
2040 A1B



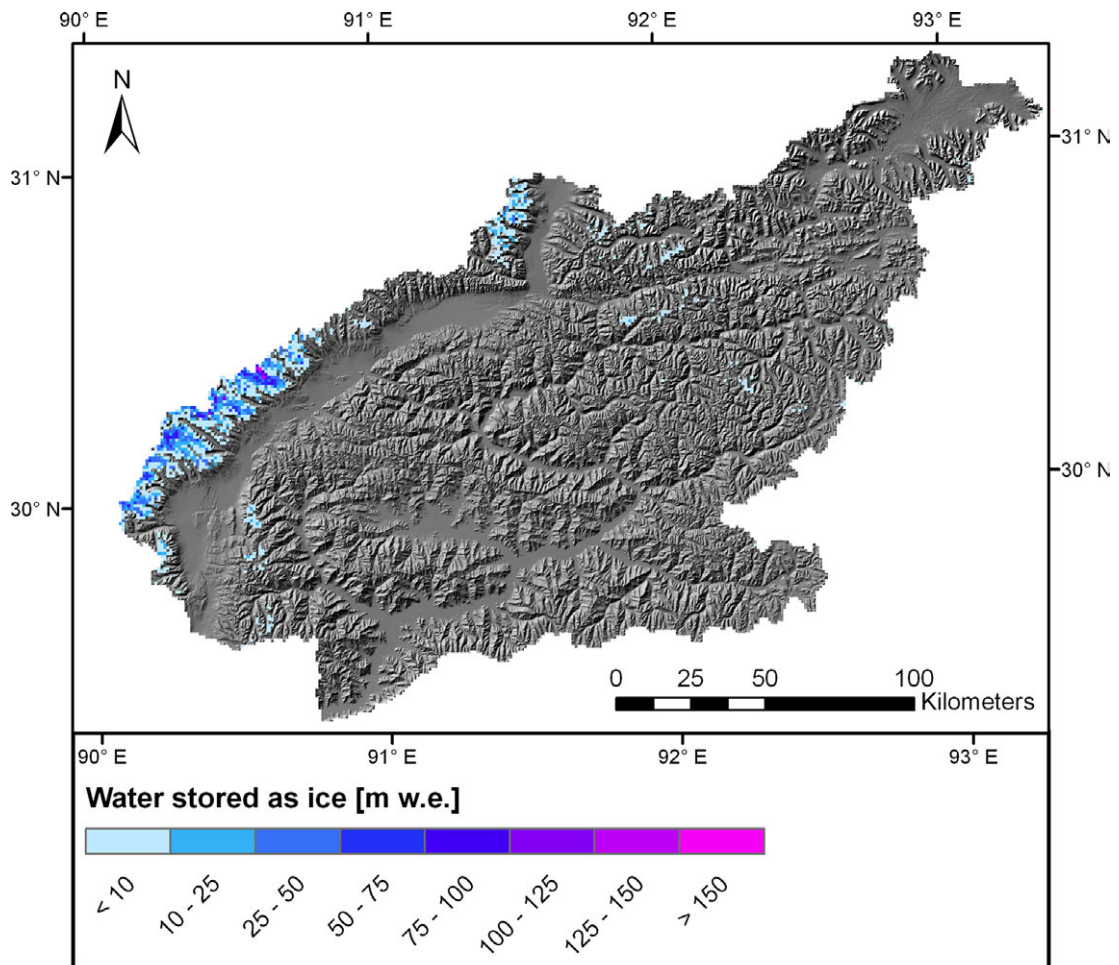
2040 B1



2050 A1B

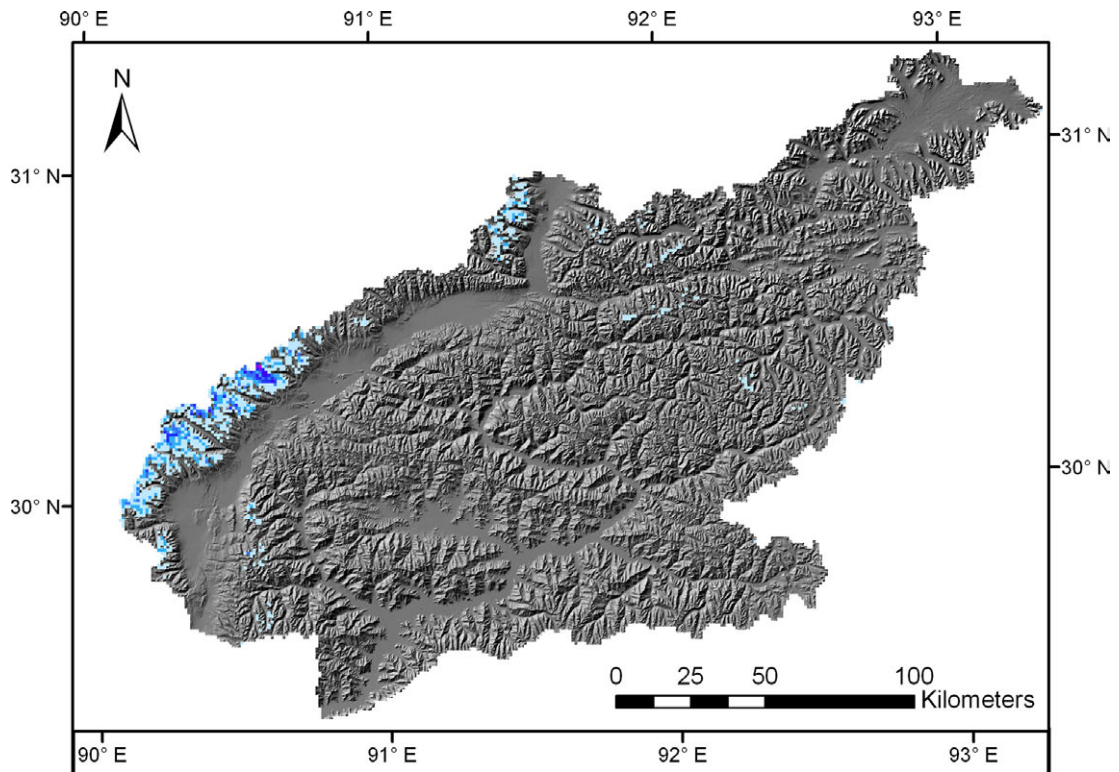


2050 B1

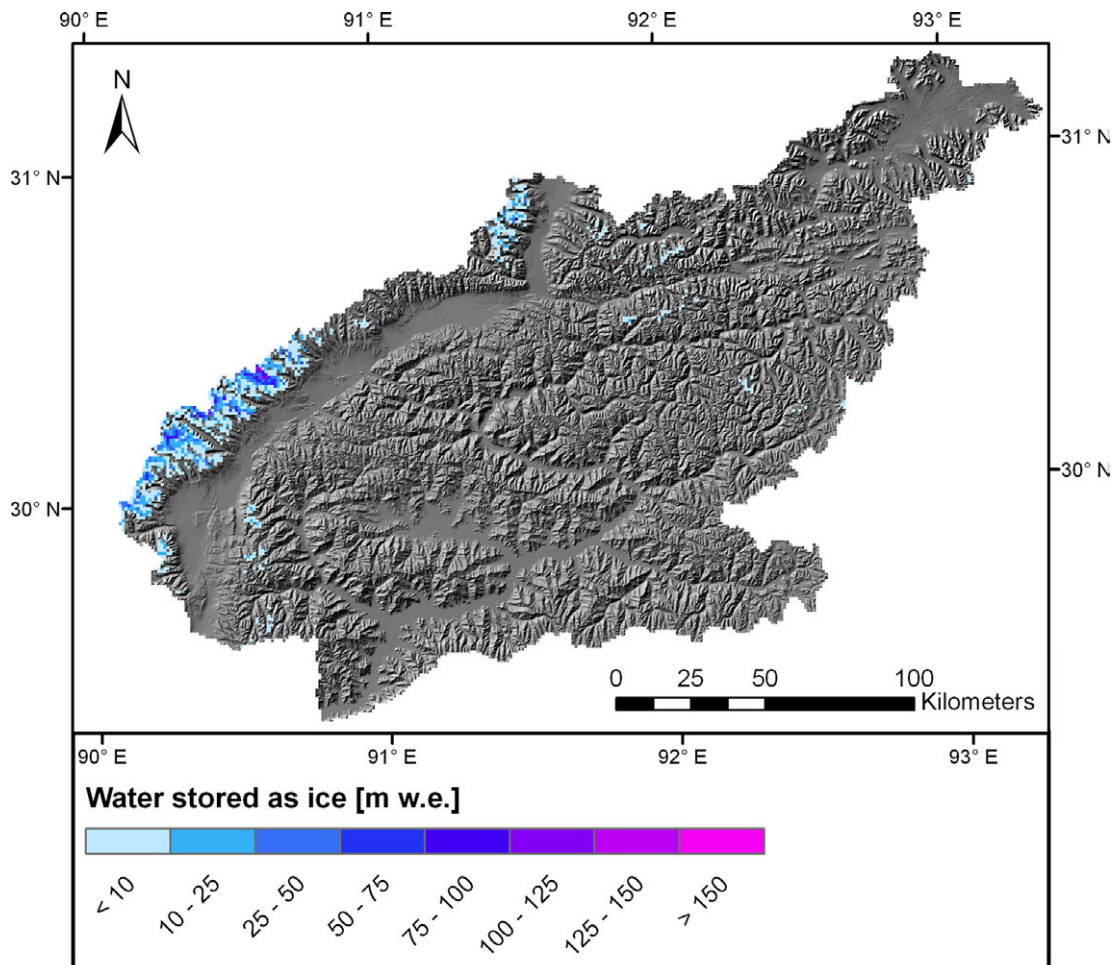




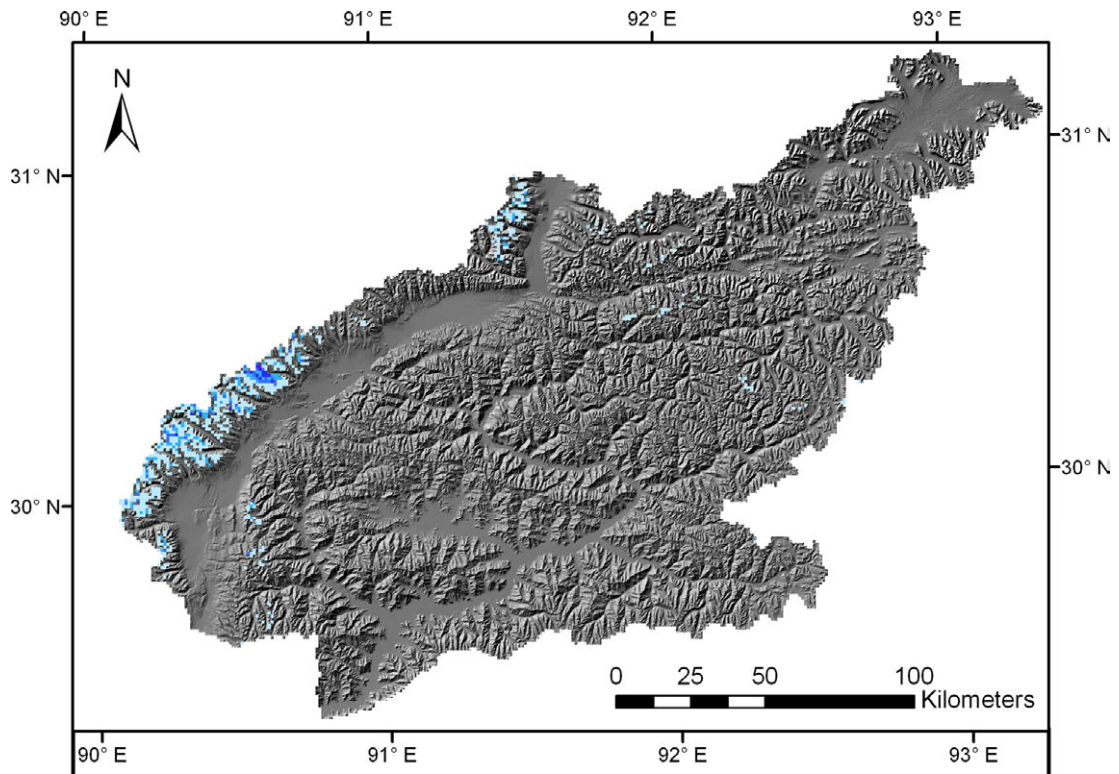
2060 A1B



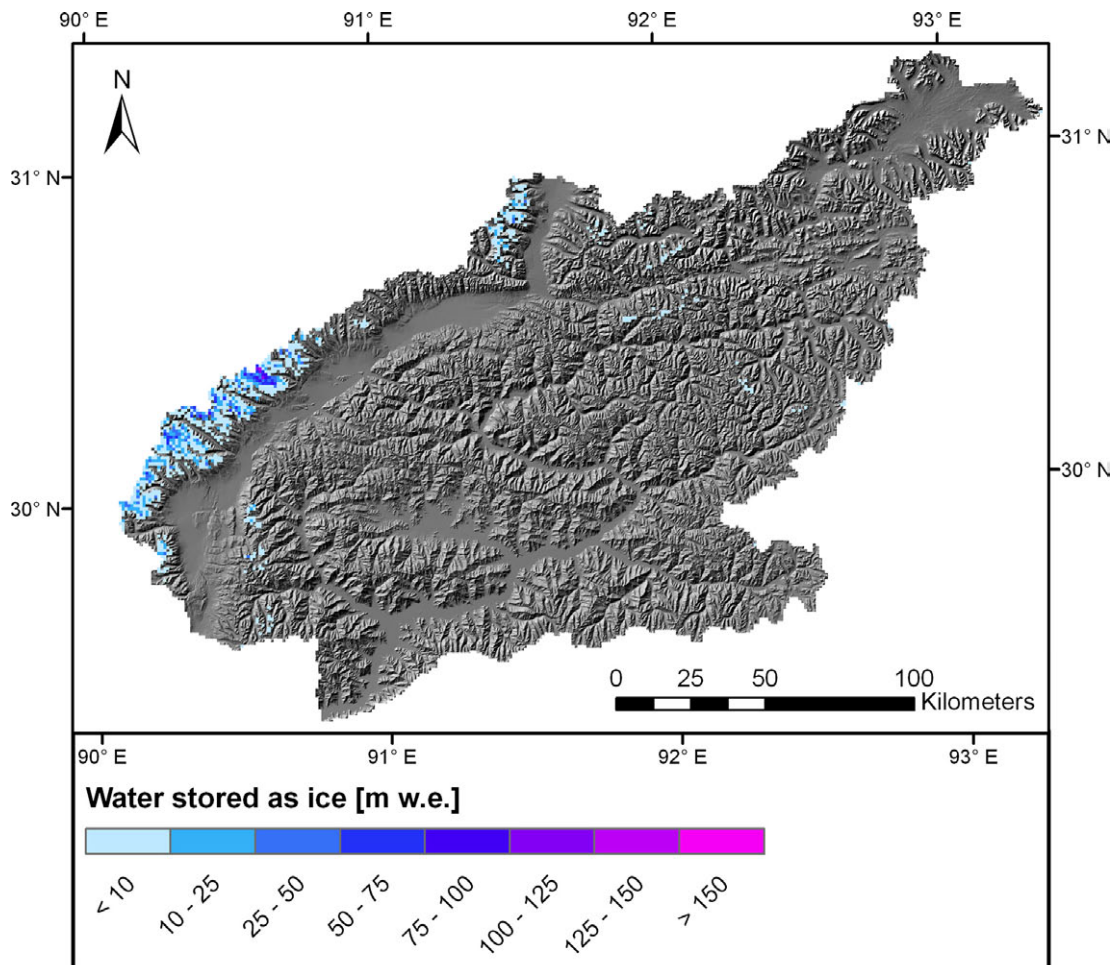
2060 B1



2070 A1B

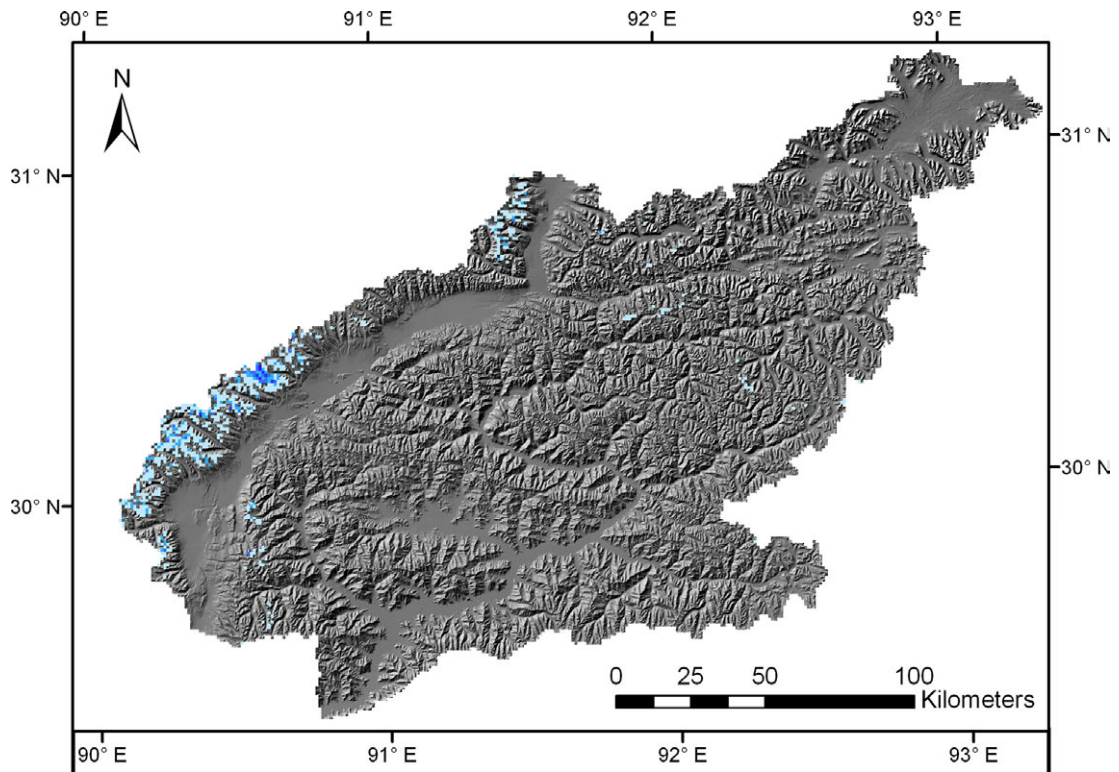


2070 B1

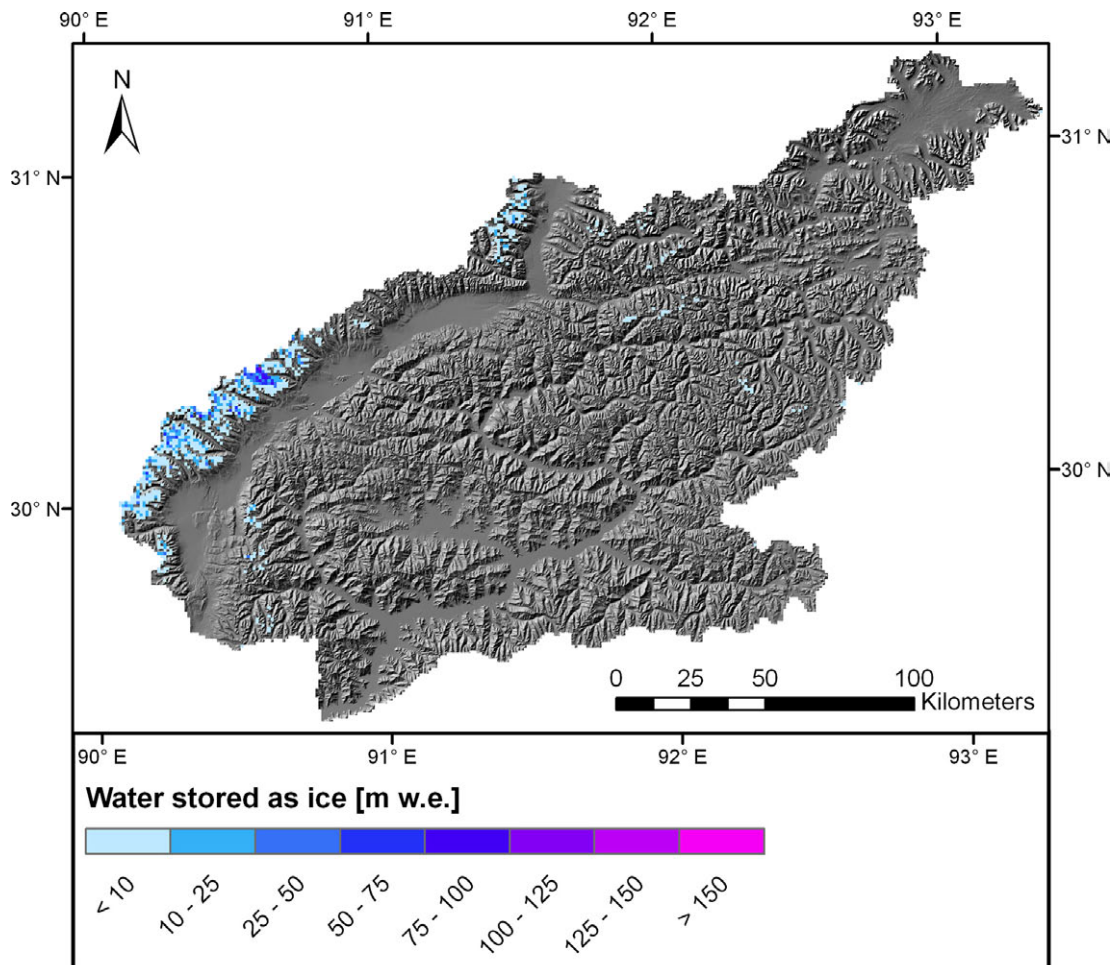




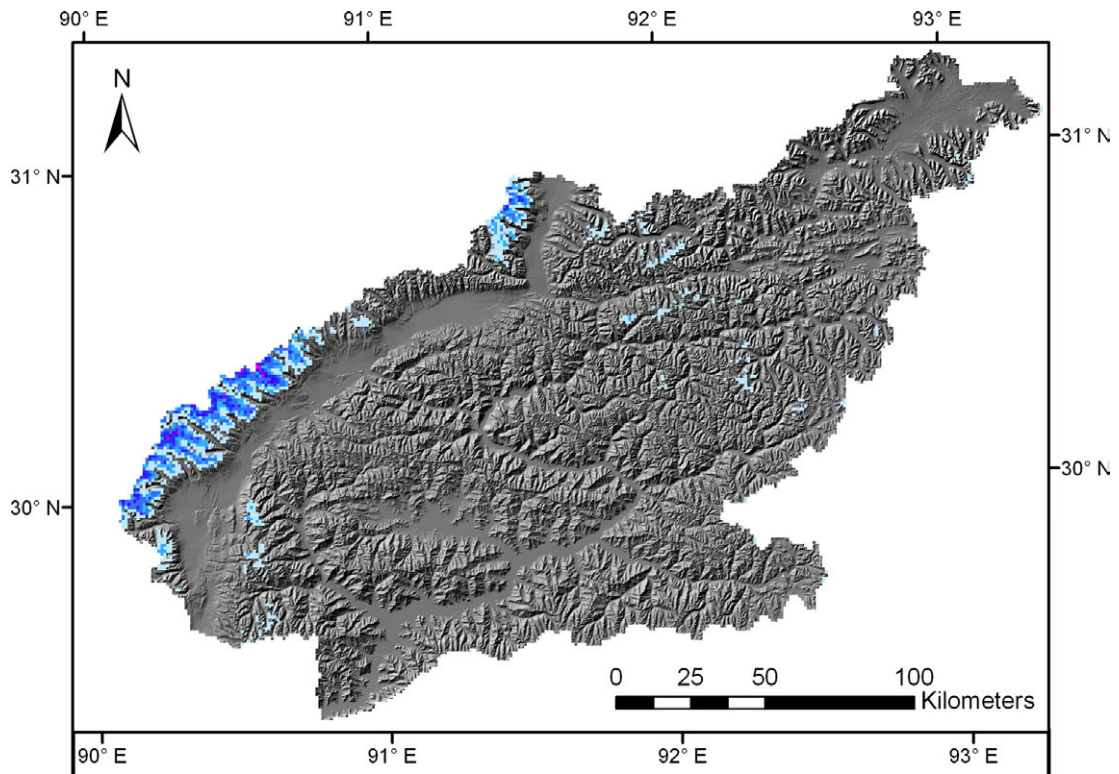
2080 A1B



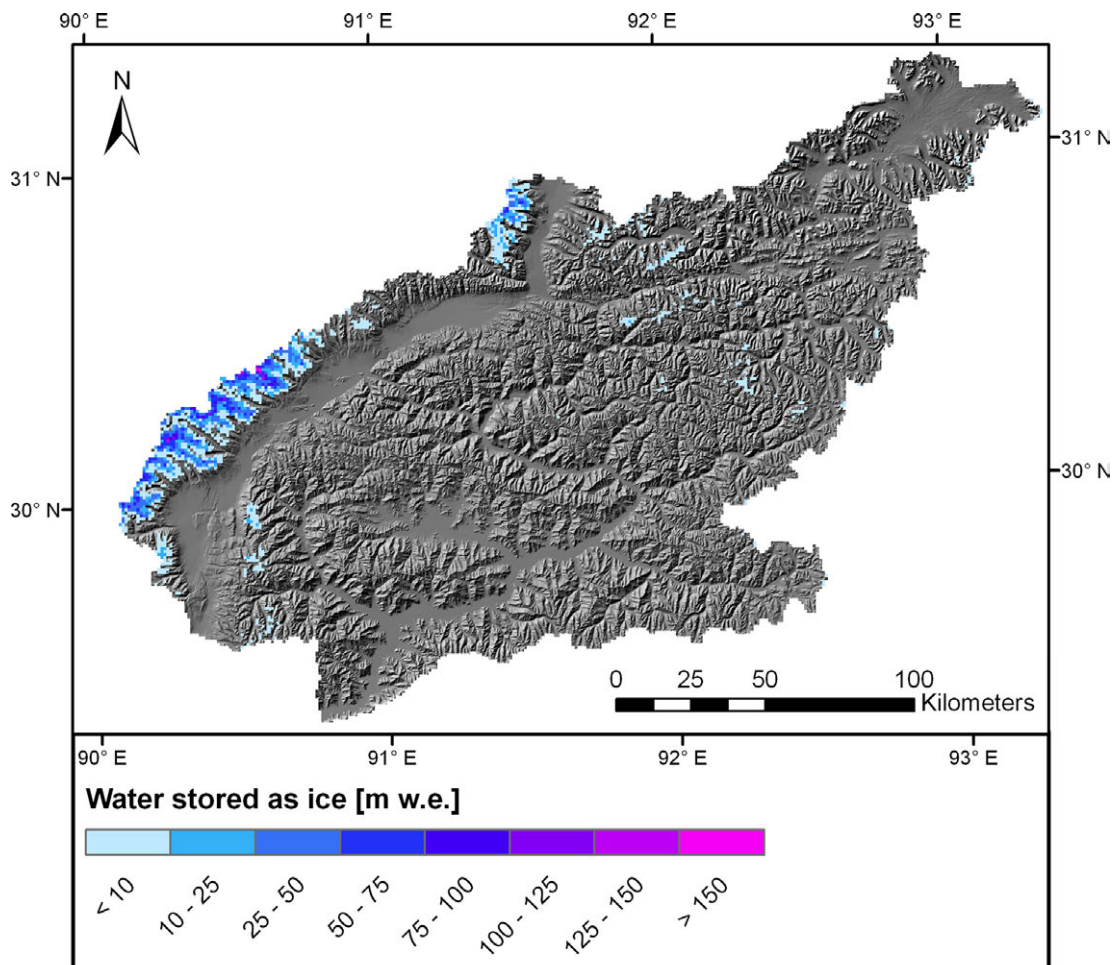
2080 B1



2010 A2

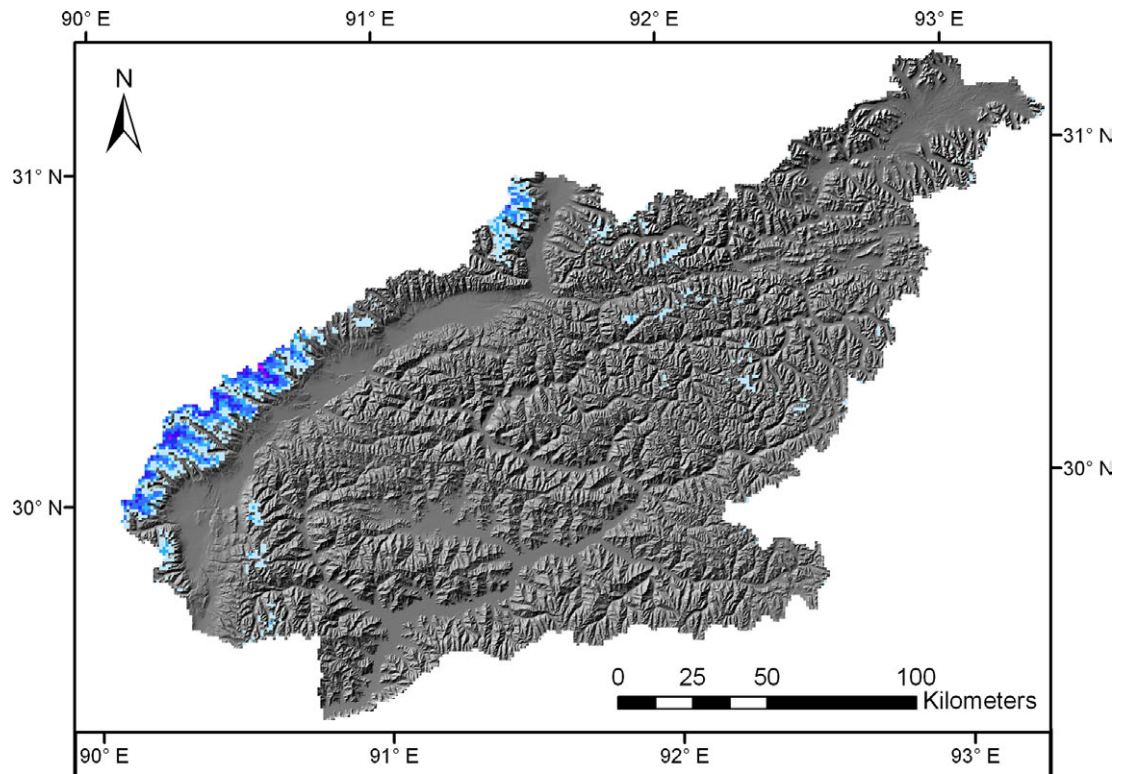


2010 CON

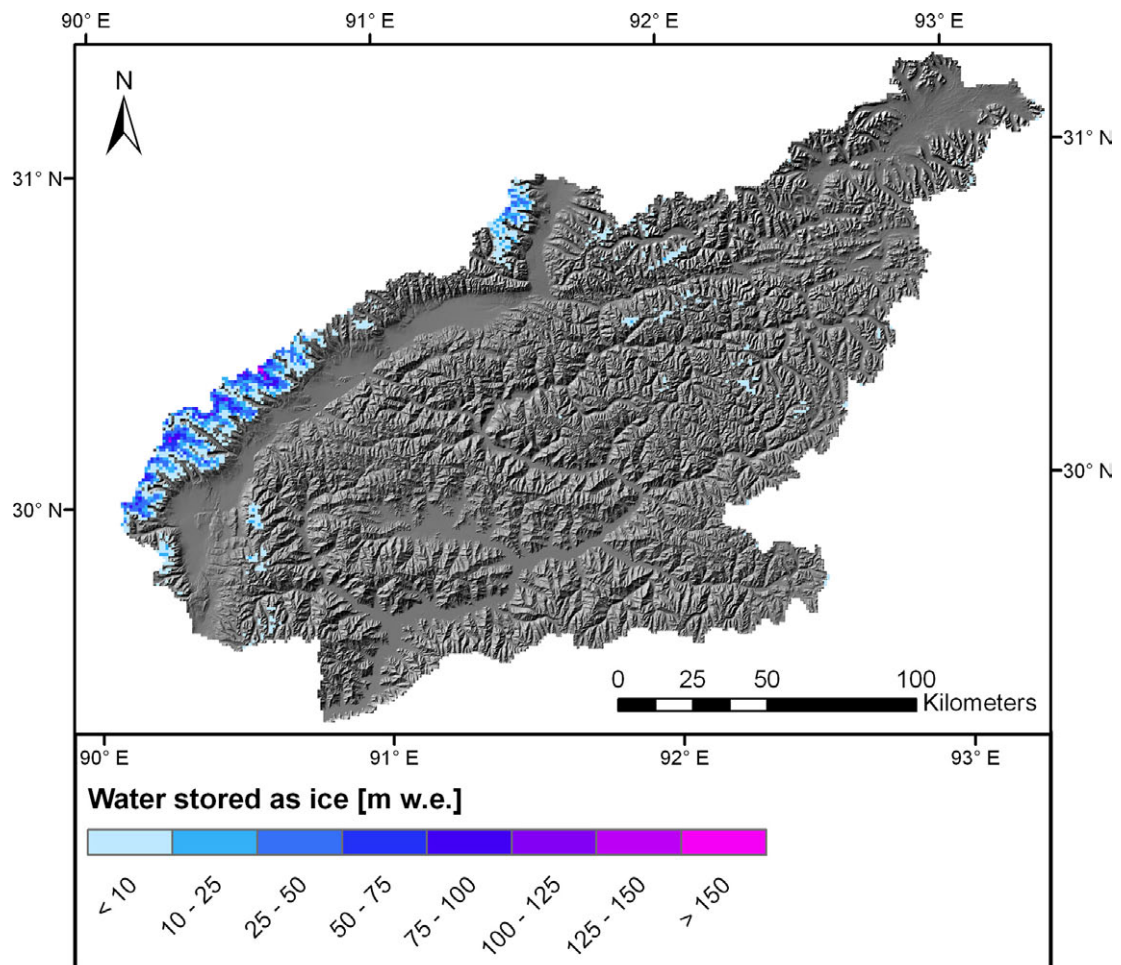




2020 A2

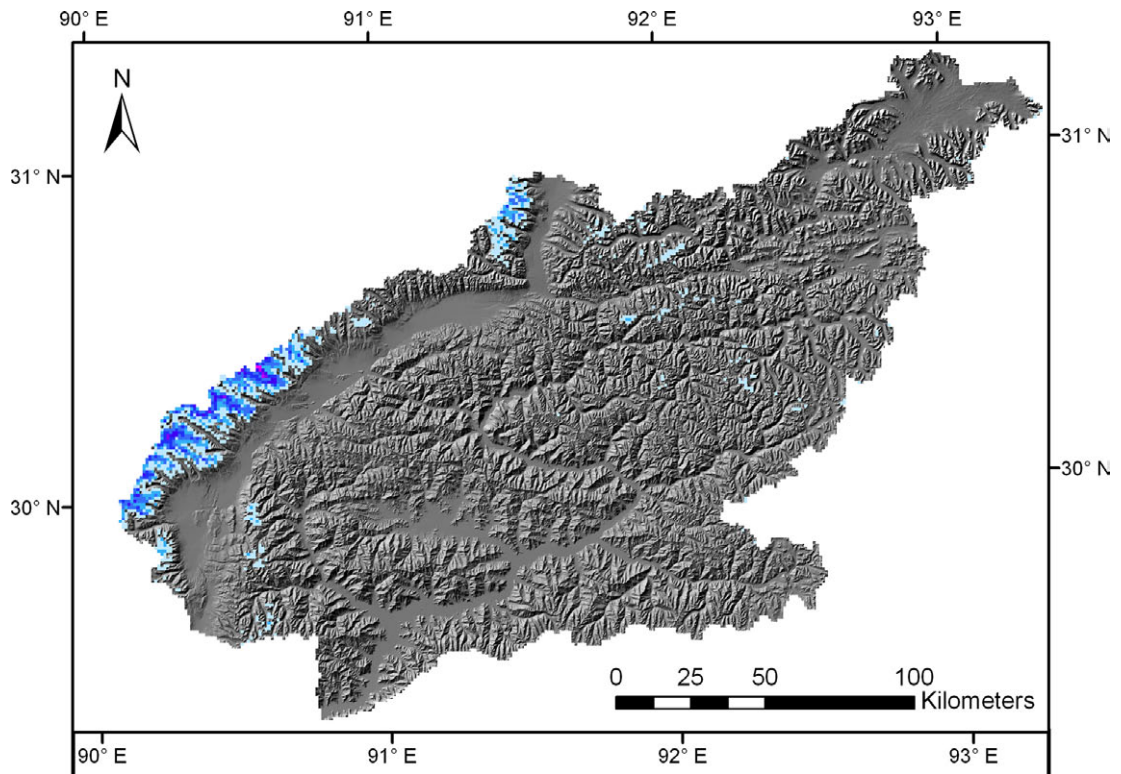


2020 CON

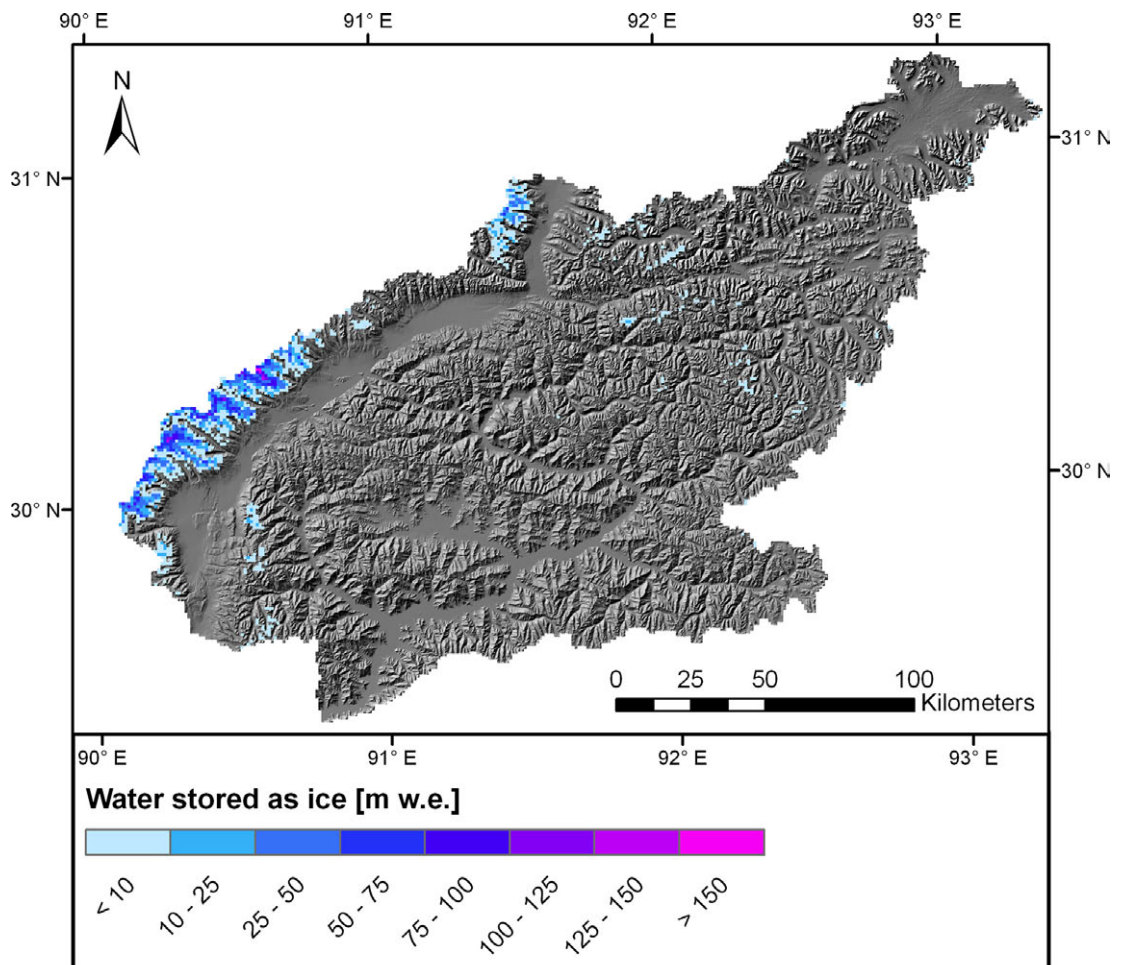




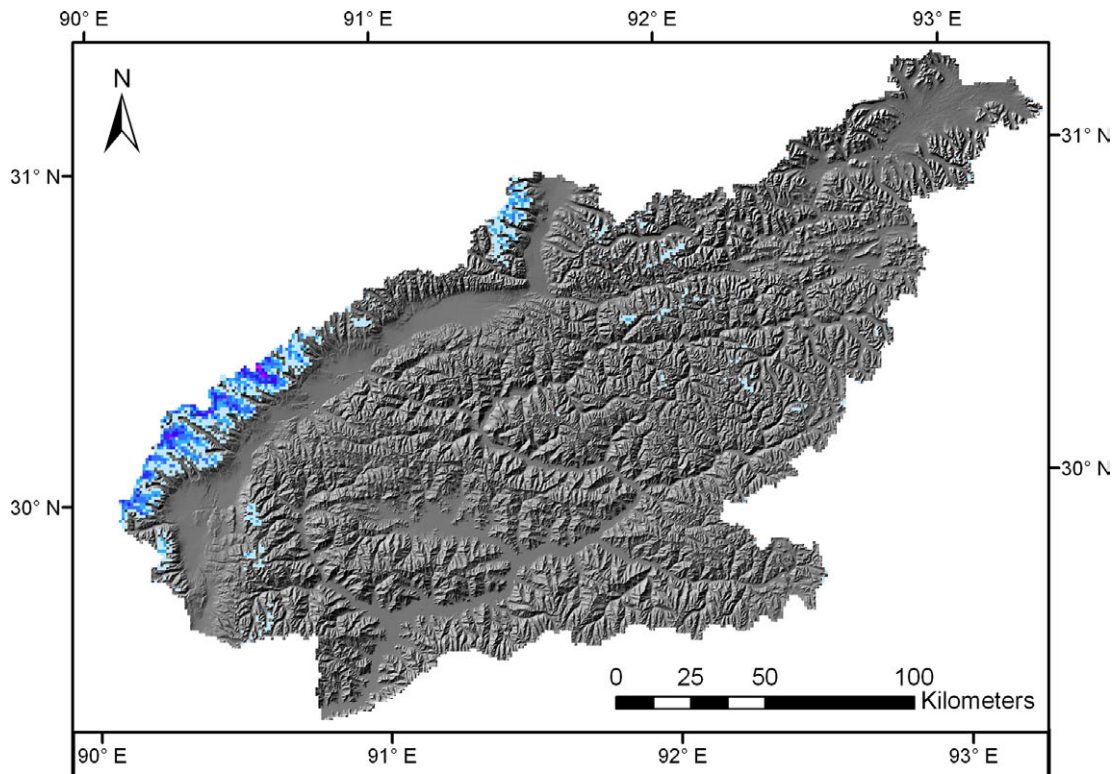
2030 A2



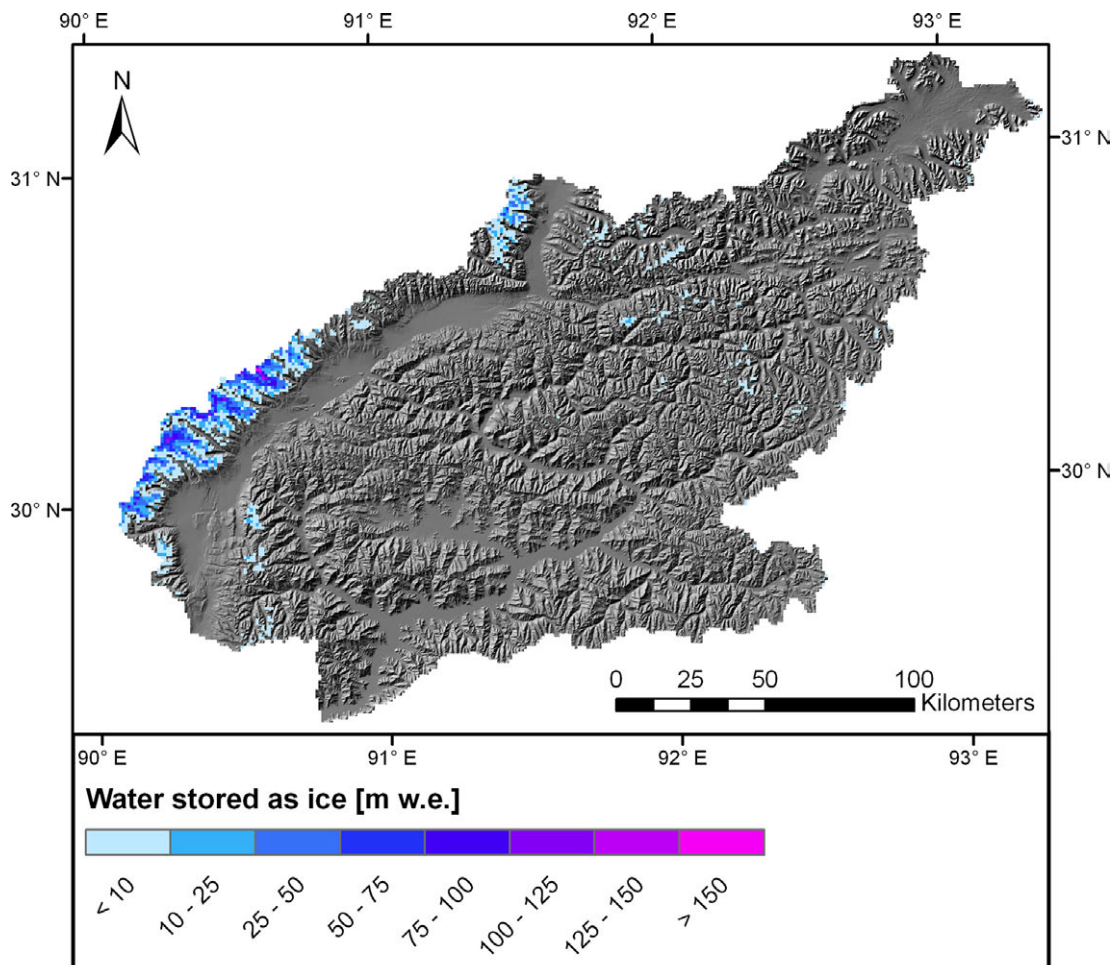
2030 CON



2040 A2

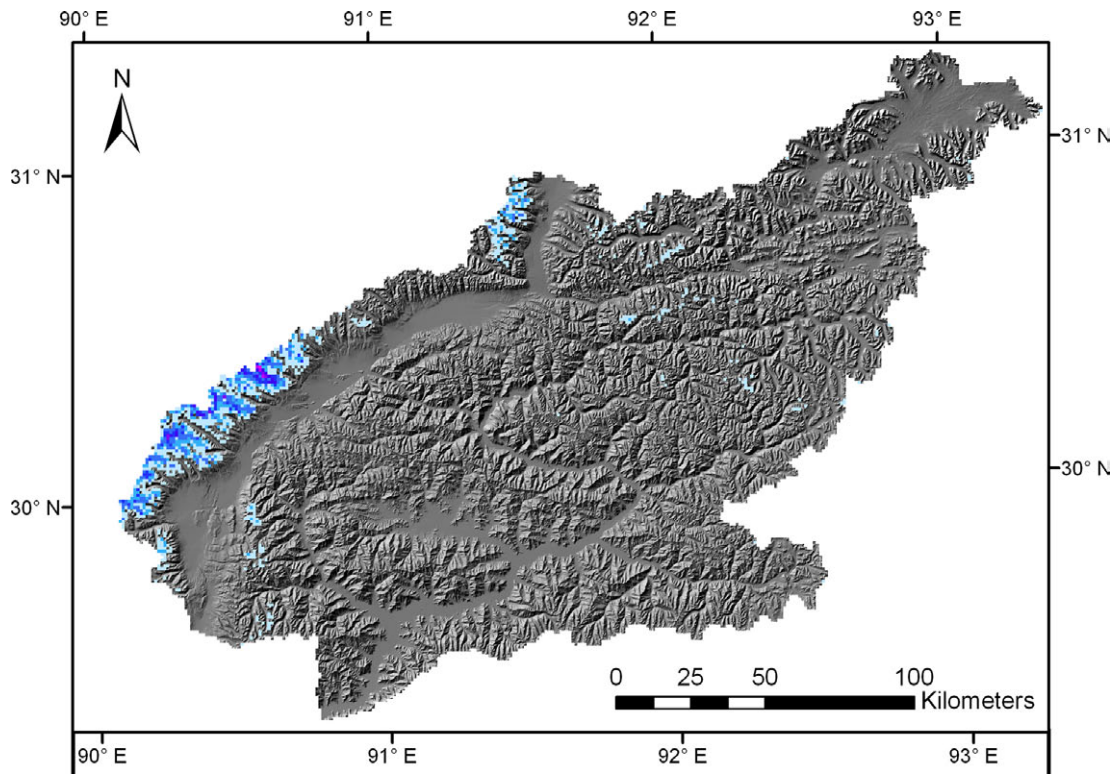


2040 CON

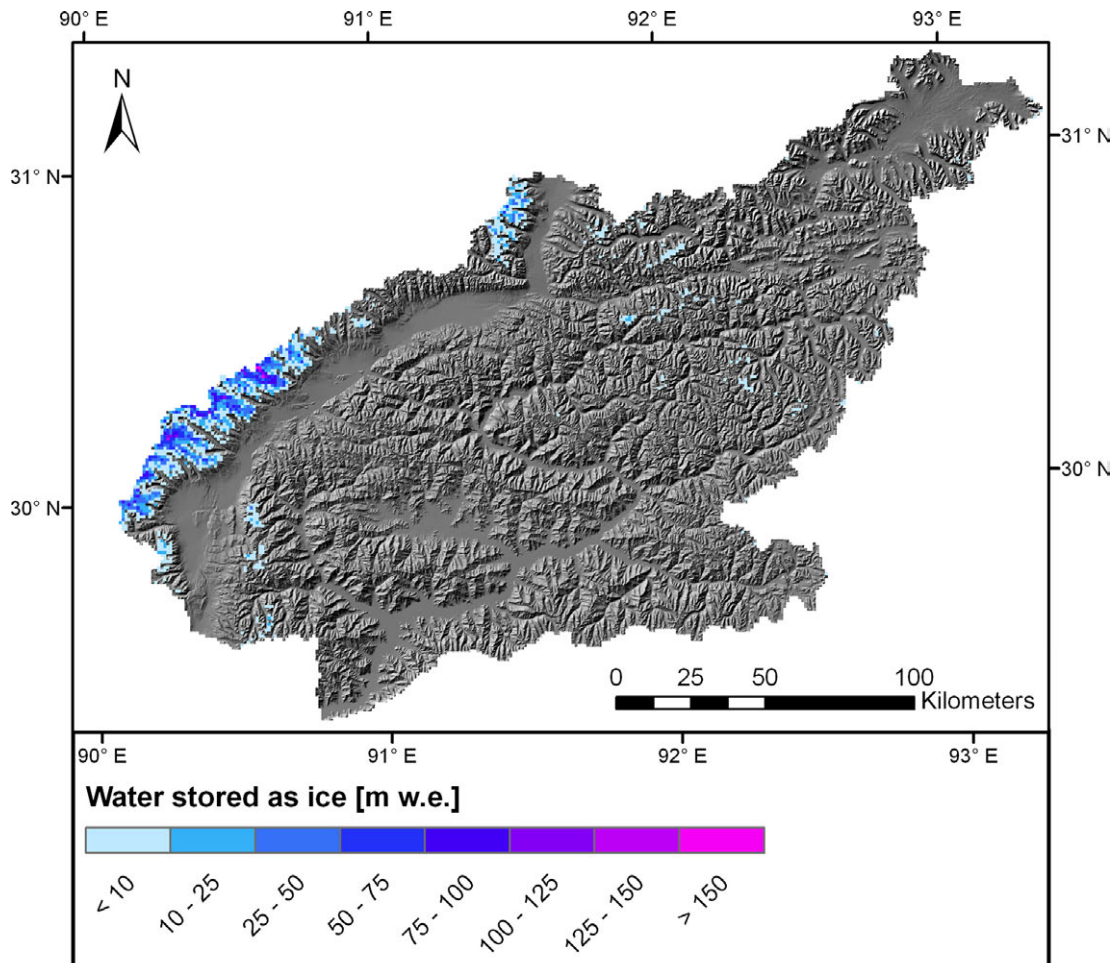




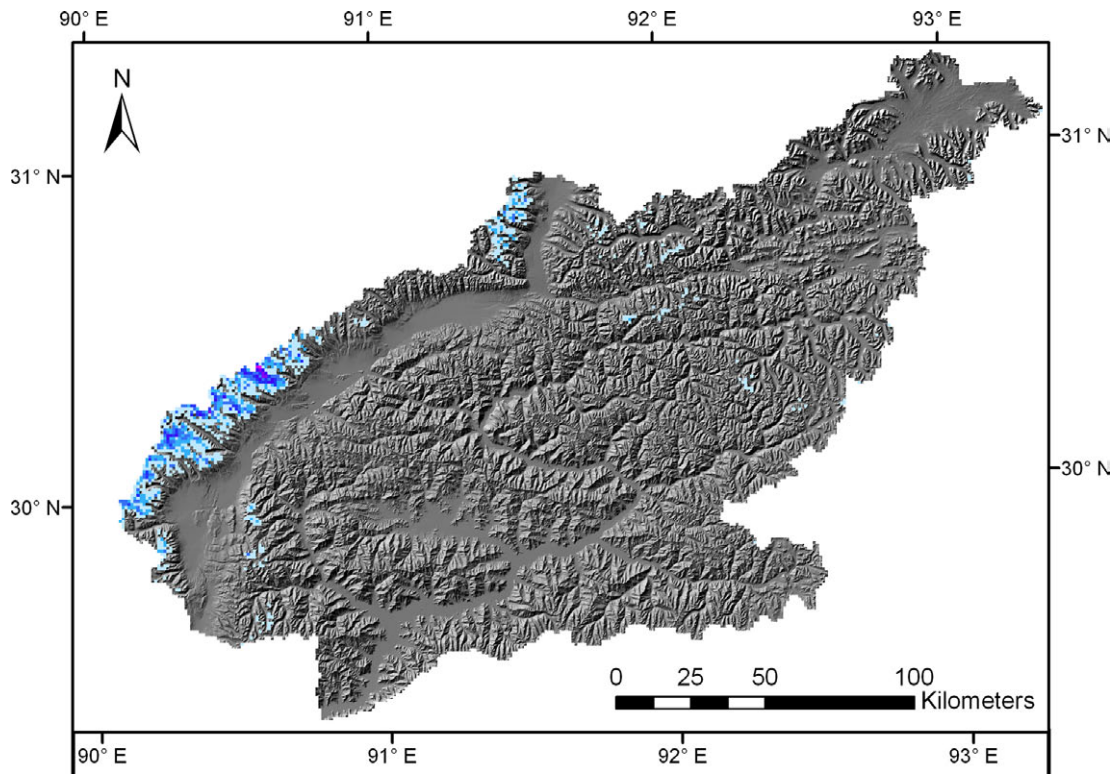
2050 A2



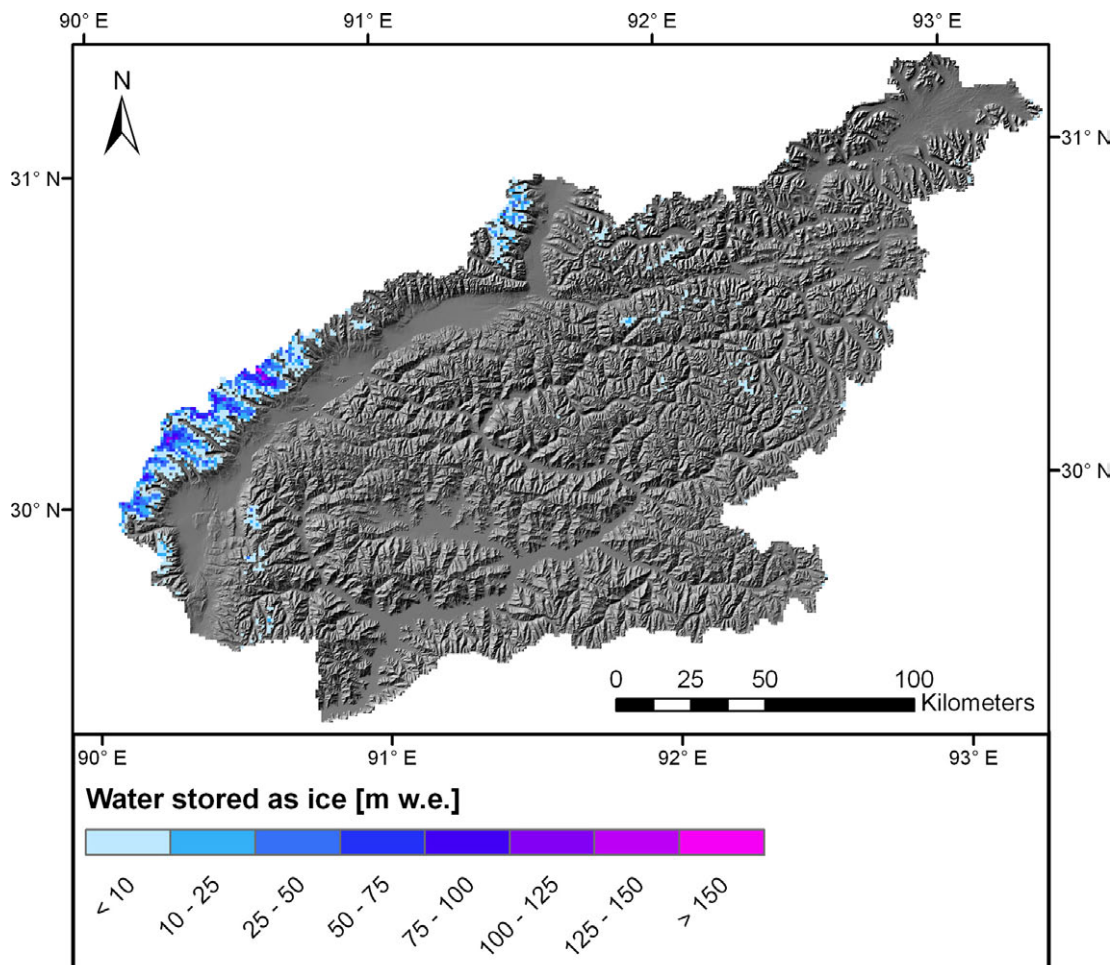
2050 CON



2060 A2

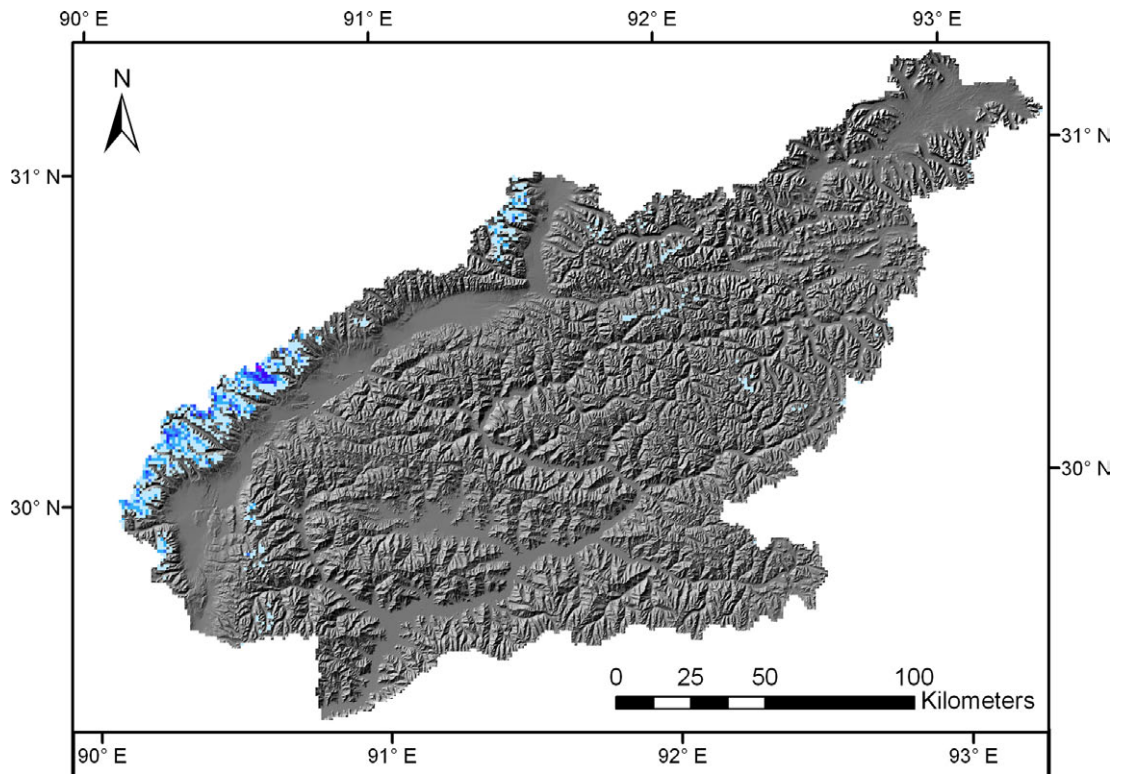


2060 CON

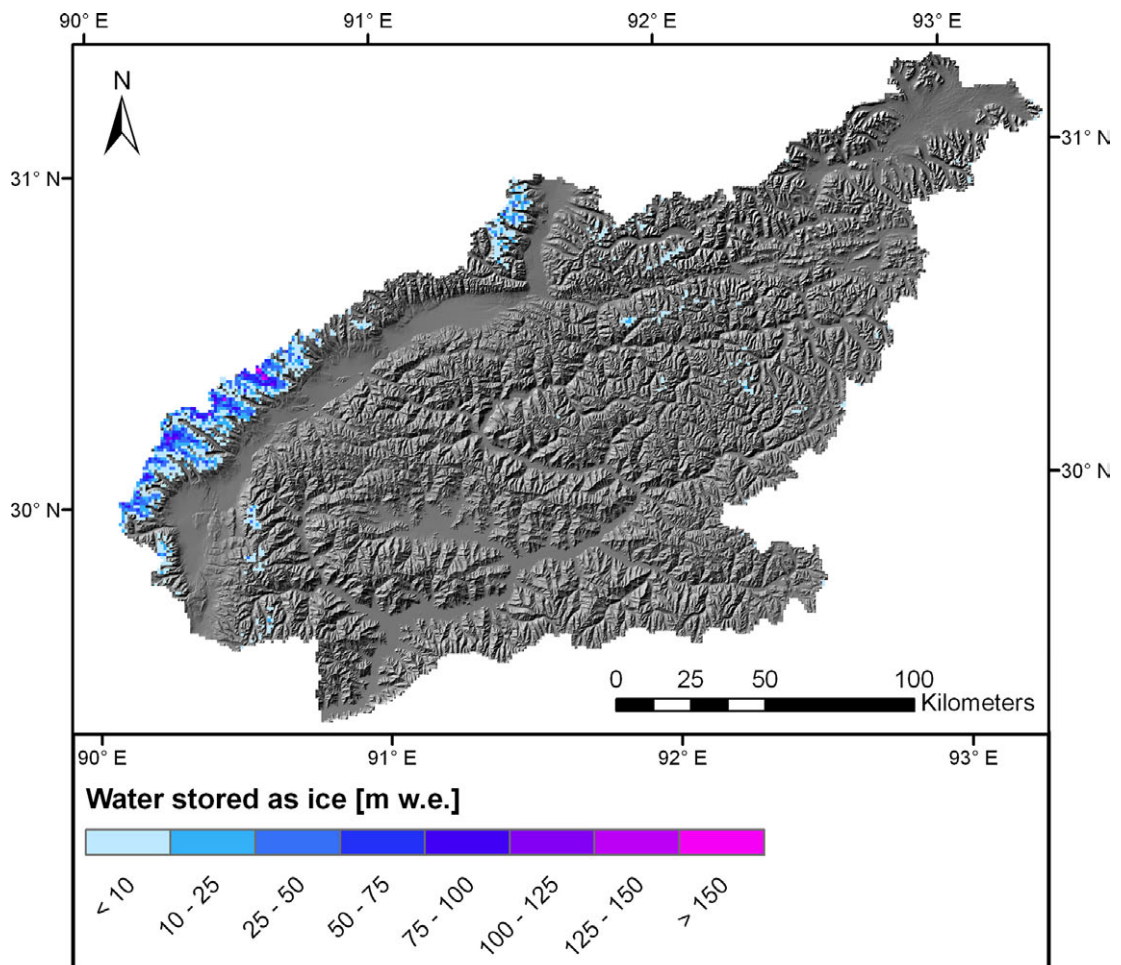




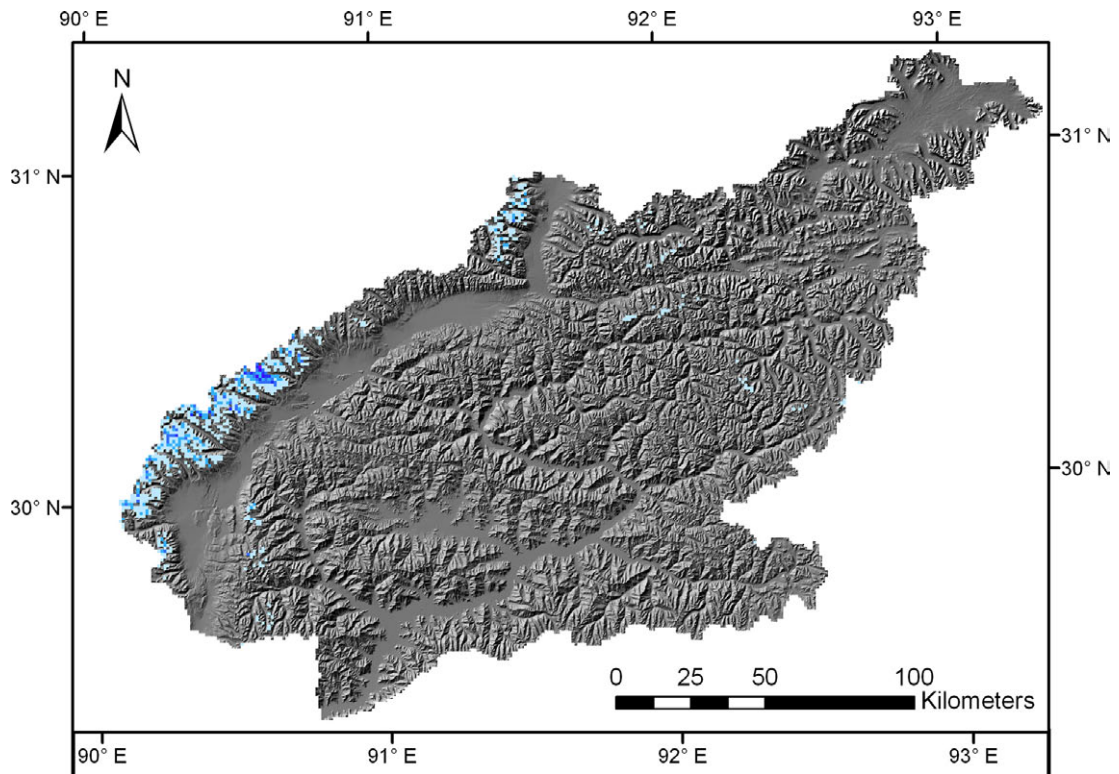
2070 A2



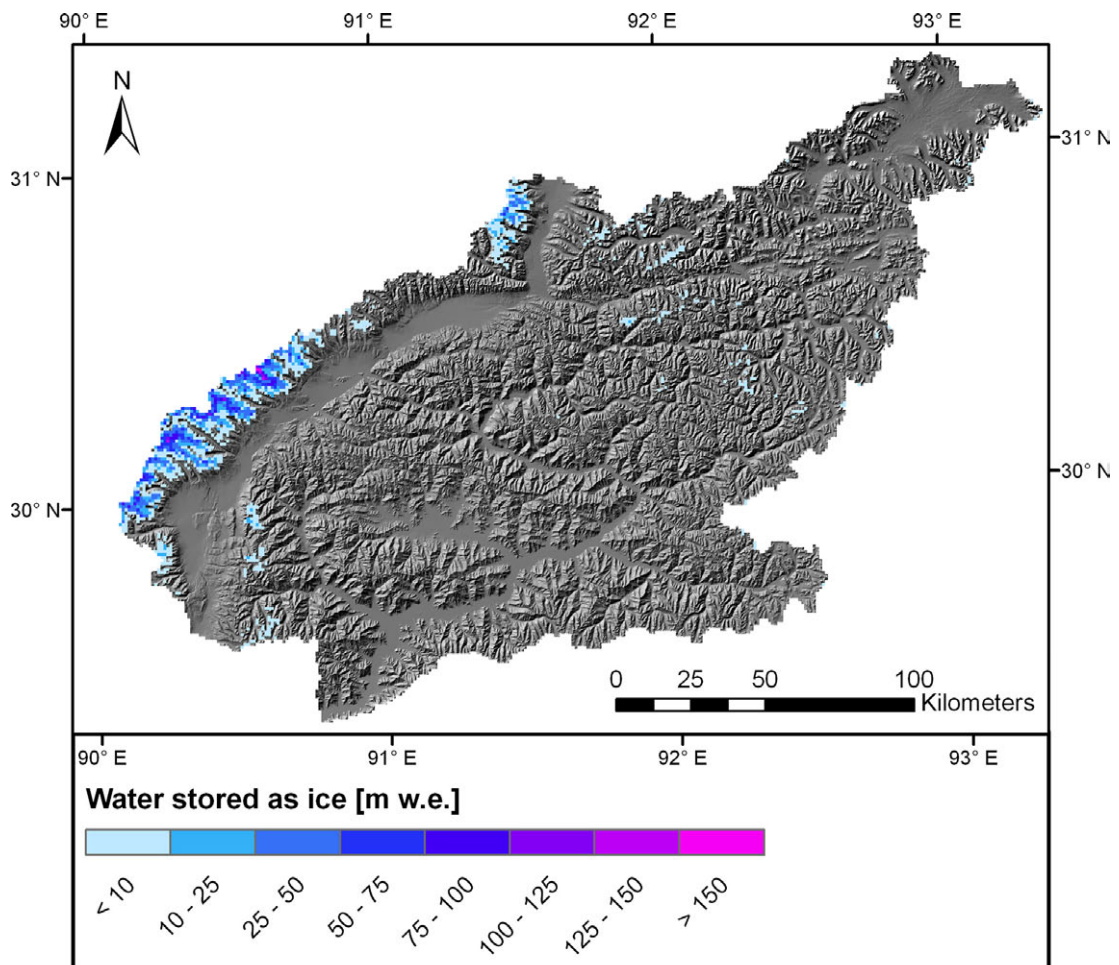
2070 CON



2080 A2



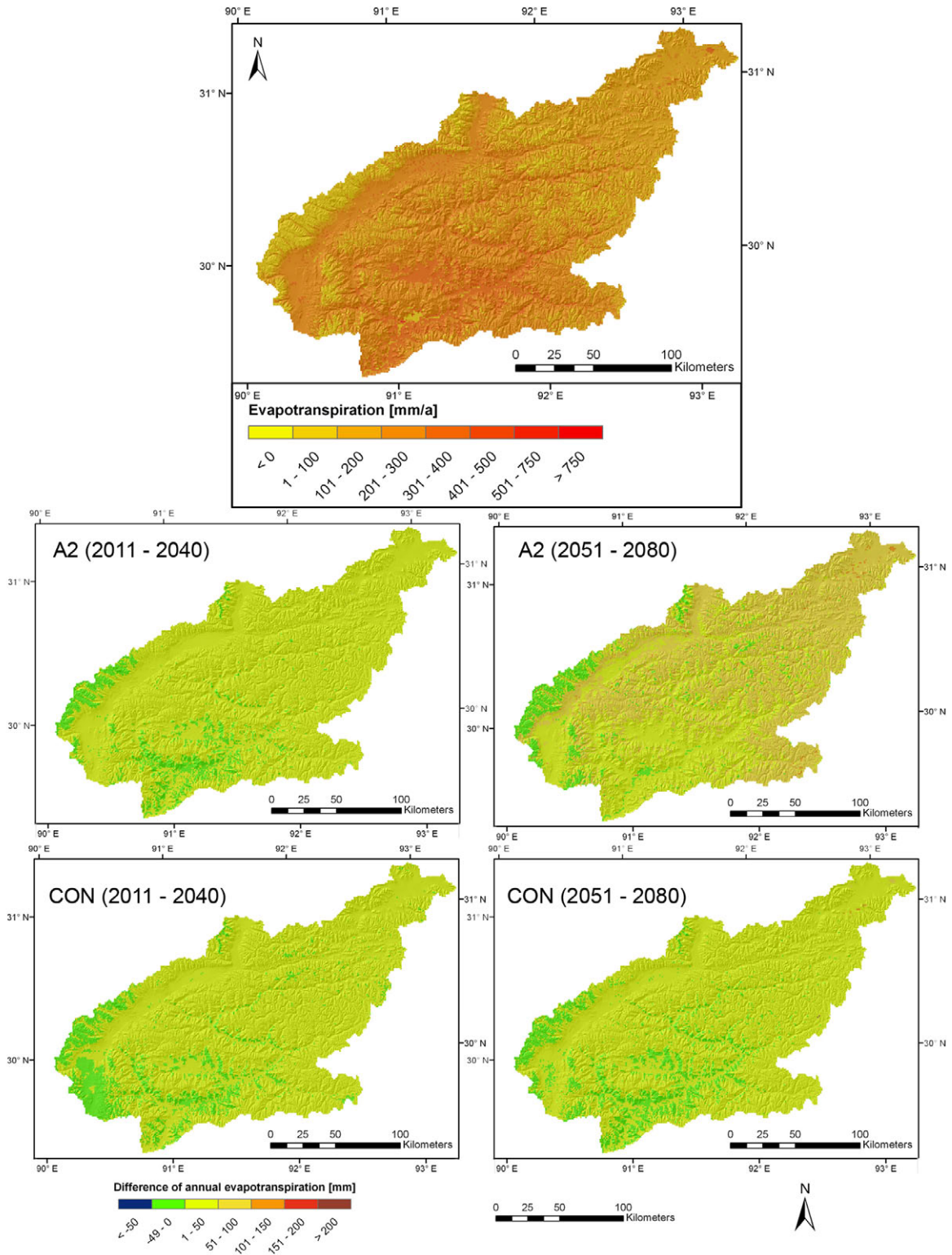
2080 CON





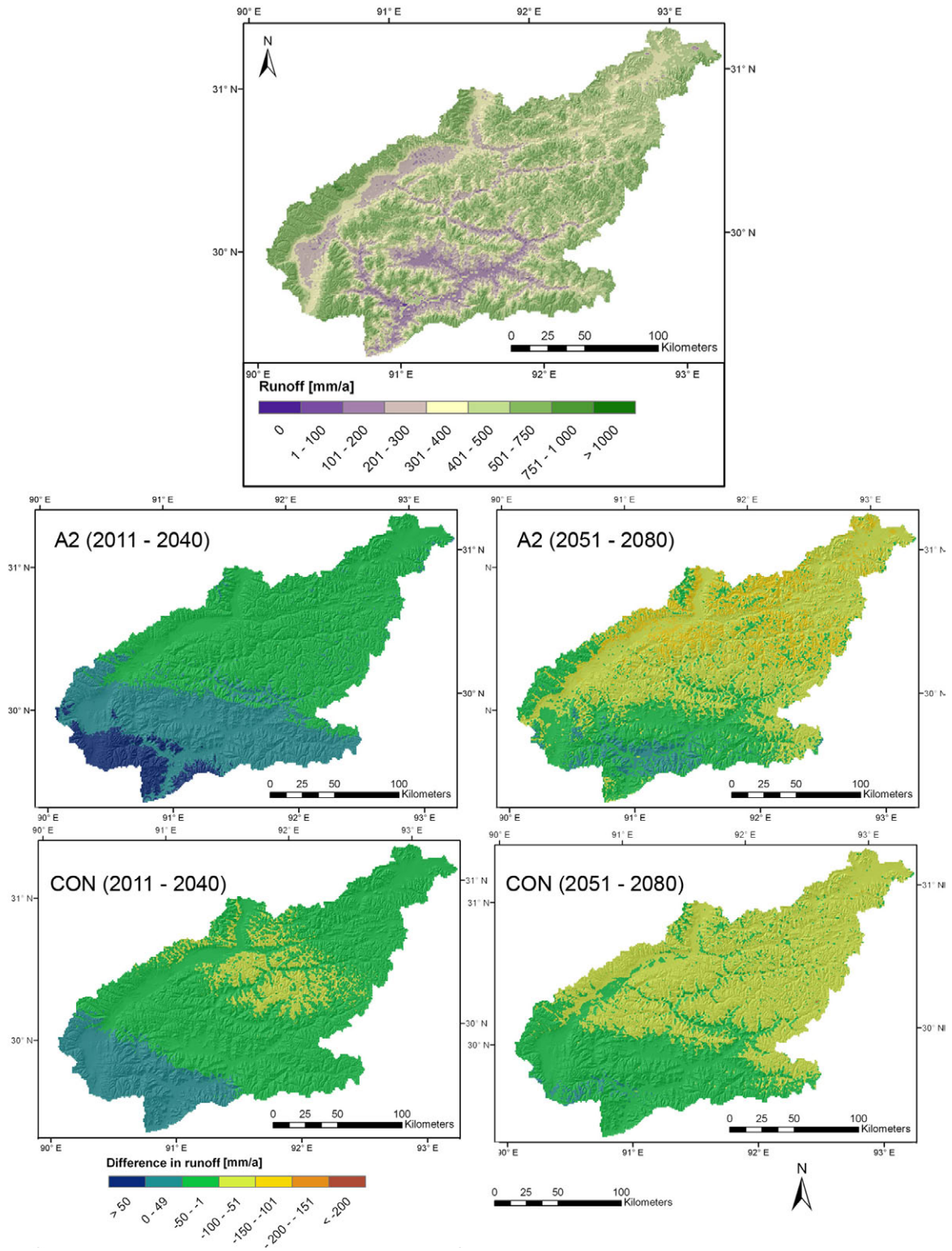
### Appendix 21

Mean annual evapotranspiration from 1971 to 2000 (top) and the changes in the periods of 2011 to 2040 (left) and 2051 to 2080 (right) according to the A2 scenario (middle) and CON scenario (bottom).



## Appendix 22

Mean annual runoff from 1971 to 2000 (top) and the changes in the periods of 2011 to 2040 (left) and of 2051 to 2080 (right) according to the A2 scenario (middle) and CON scenario (bottom).



### Appendix 23

Statistical values for the analysis of the mean annual summer (April to September) and winter (October – March) runoff. The time period for the past is 1971 to 2000, whereas the scenario period is set to 2001 to 2080.

	Scenario	Average	Abso- lute trend	Standard deviation $\sigma$	Trend- to-noise ratio T/N	Mann- Kendall value Q	Signifi- cance level $\alpha$
Mean annual runoff [m <sup>3</sup> /s]	Past	440	-7	109	0.06	0.43	-
	A1B	389	-145	108	1.34	-3.59	0.001
	A2	420	-114	114	1.00	-21.9	0.05
	B1	406	-40	115	0.35	-0.78	-
	CON	395	-39	115	0.34	-0.79	-
Mean summer runoff [m <sup>3</sup> /s]	Past	722	-16	199	0.08	0.61	-
	A1B	641	-265	195	1.36	-3.59	0.001
	A2	687	-212	200	1.06	-2.26	0.05
	B1	665	-80	199	0.40	-0.94	-
	CON	644	-72	210	0.34	-0.92	-
Mean winter runoff [m <sup>3</sup> /s]	Past	157	+3	32	0.09	0.39	-
	A1B	137	-25	43	0.58	-1.89	0.1
	A2	153	-16	45	0.35	-1.02	-
	B1	147	0	53	0.00	-0.25	-
	CON	147	-6	40	0.15	-0.42	-

## Appendix 24

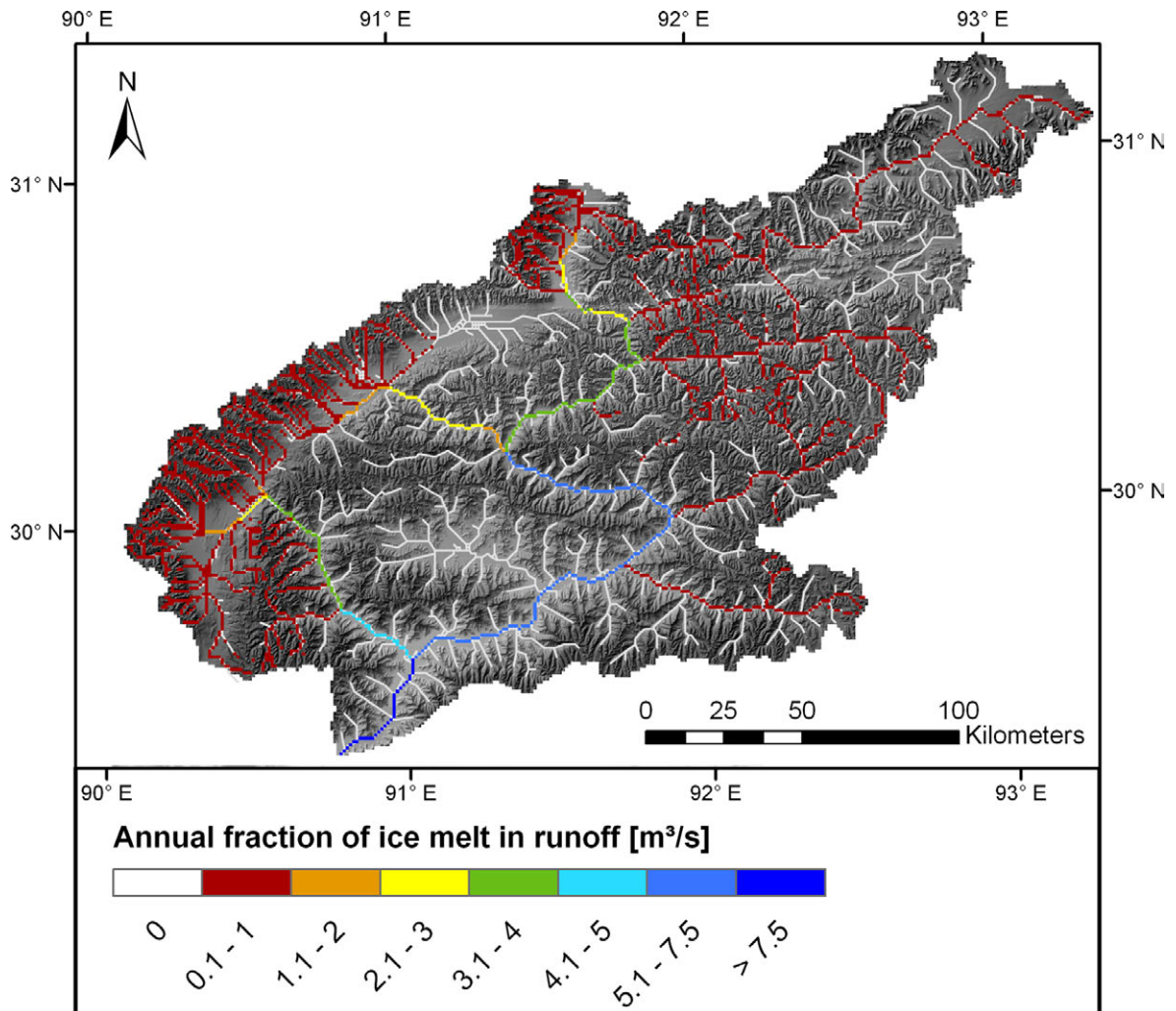
Statistical values for the analysis of the monthly runoff at the catchment outlet of the Lhasa River basin. The time period for the past is 1971 to 2000, whereas the scenario period is set to 2001 to 2080.

Scenario	Month	Mann-Kendall value Q	Significance level $\alpha$	Month	Mann-Kendall value Q	Significance level $\alpha$
Past		0.43			0.39	
A1B		-1.71	0.1		-3.29	0.001
A2	January	-0.76		July	-3.32	0.001
B1		0.36			-1.72	0.1
CON		-0.10			-0.40	
Past		0.57			0.82	
A1B		-1.82	0.1		-1.72	0.1
A2	February	-1.03		August	-1.32	
B1		0.25			-0.12	
CON		0.03			-0.75	
Past		-1.18			-1.32	
A1B		-2.50	0.05		0.01	
A2	March	-1.43		September	0.66	
B1		0.27			0.05	
CON		-0.45			-0.73	
Past		-0.11			-0.04	
A1B		-0.84			-1.26	
A2	April	-0.43		October	-0.68	
B1		1.23			-0.39	
CON		-0.96			-0.18	
Past		0.46			0.54	
A1B		-3.35	0.001		-1.65	0.1
A2	May	-2.09	0.05	November	-0.80	
B1		-0.05			-0.47	
CON		-0.67			-0.42	
Past		-1.00			0.68	
A1B		-3.19	0.01		-1.52	
A2	June	-3.61	0.001	December	-0.75	
B1		-1.76	0.1		-0.18	
CON		-0.94			-0.58	

**Appendix 25**

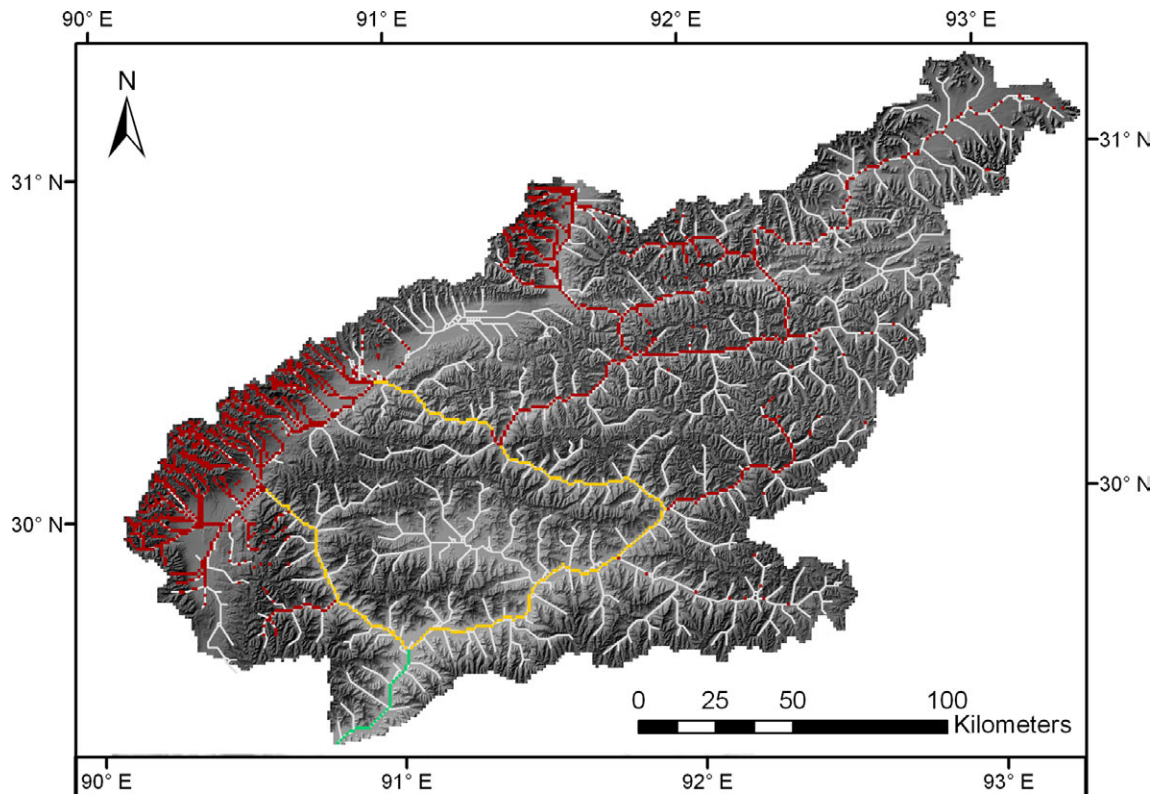
Mean annual ice-melt contribution to runoff from 1971 to 2000 and in the future periods of 2011 to 2040 and 2051 to 2080 according to the four IPCC SRES scenario runs.

1971 – 2000 (ECHAM 5)

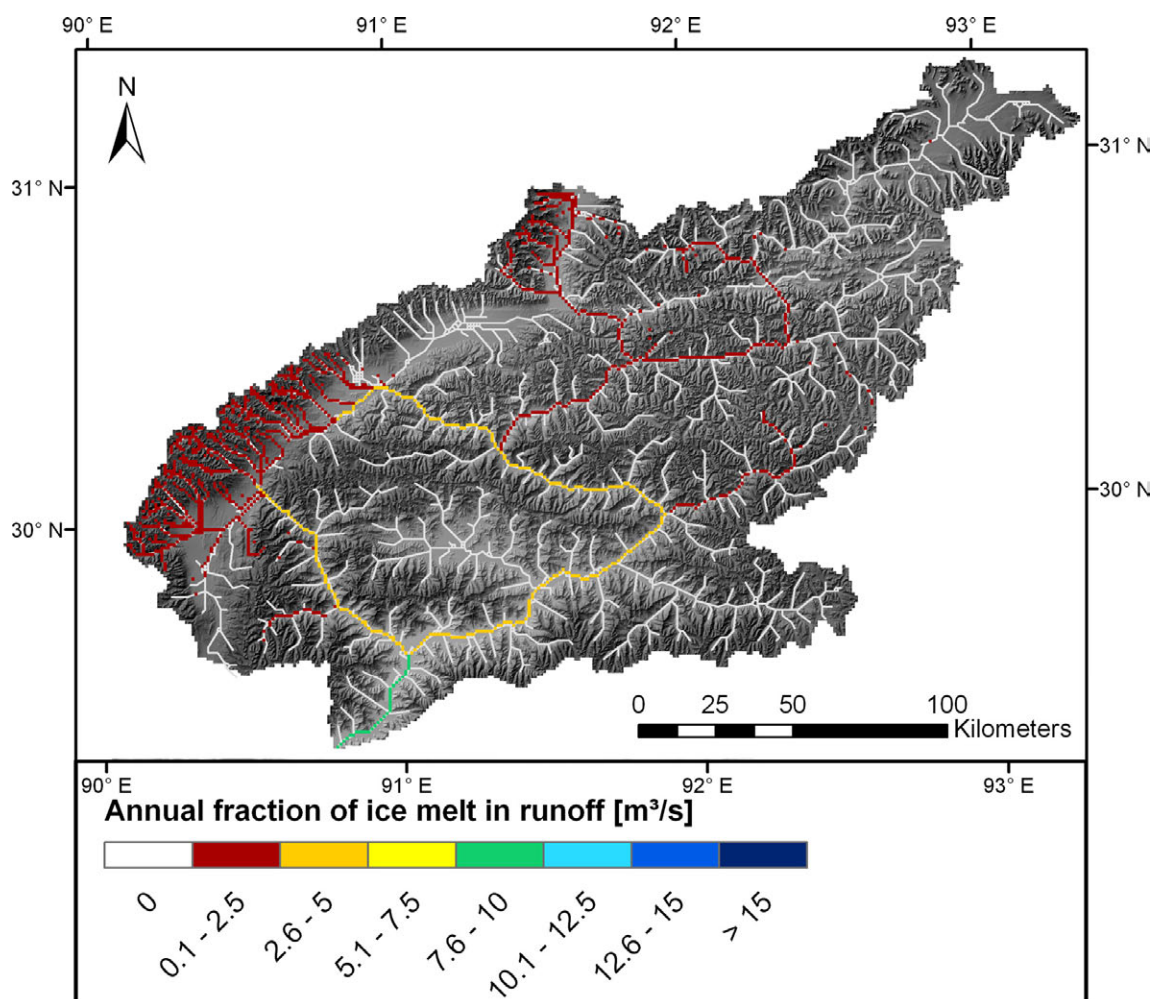




2011-2040 A1B

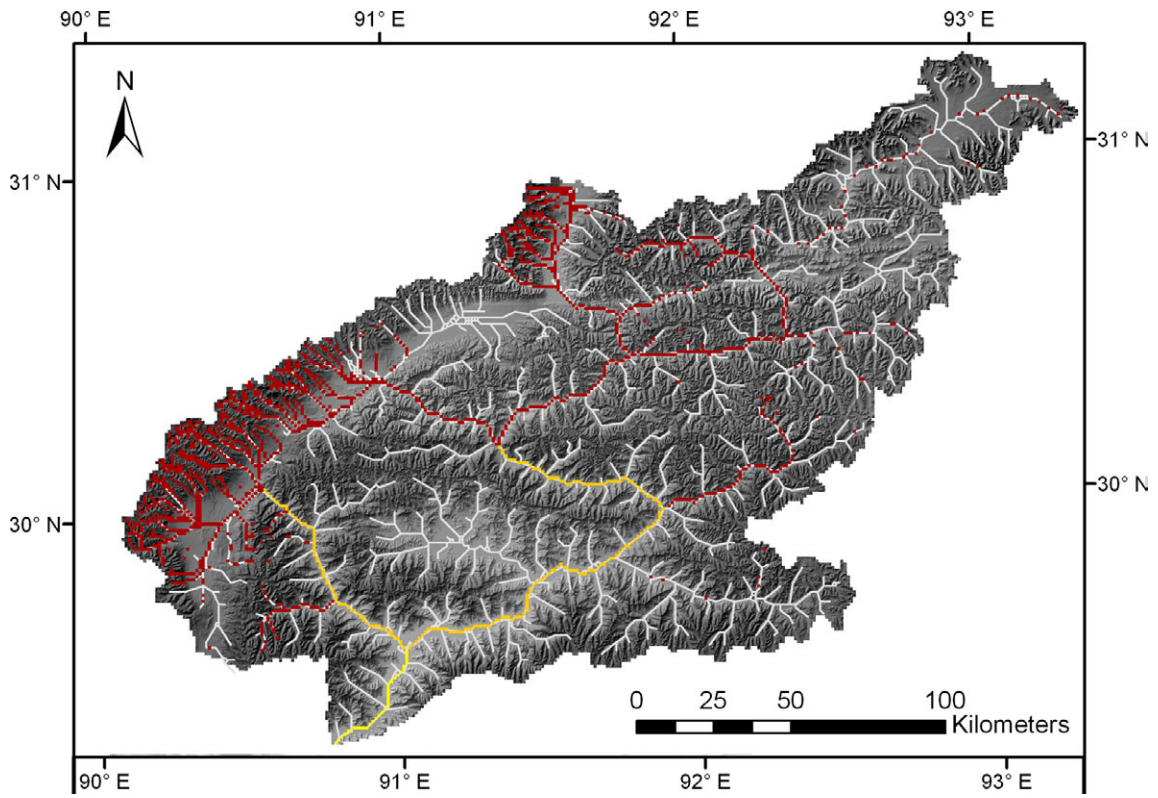


2051-2080 A1B

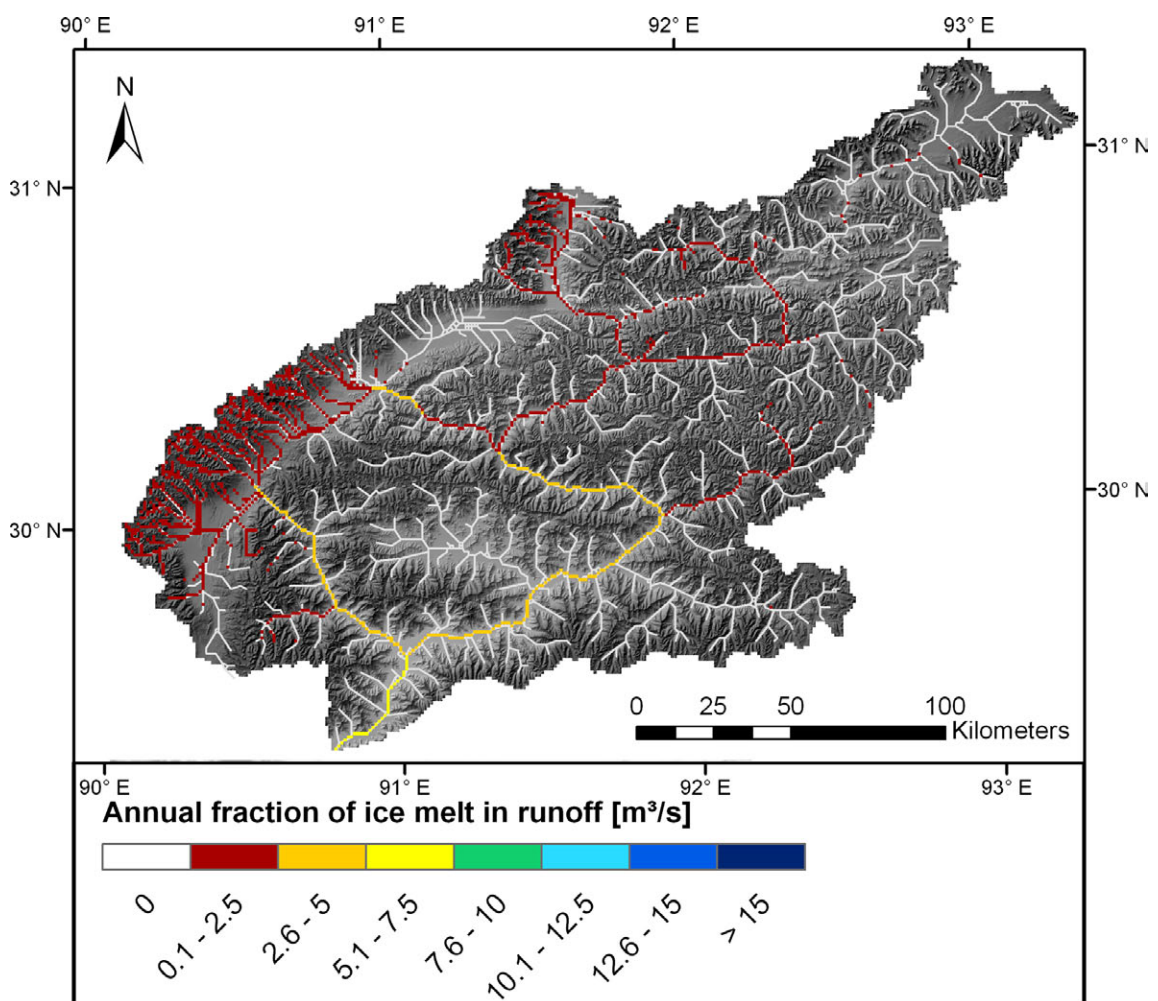




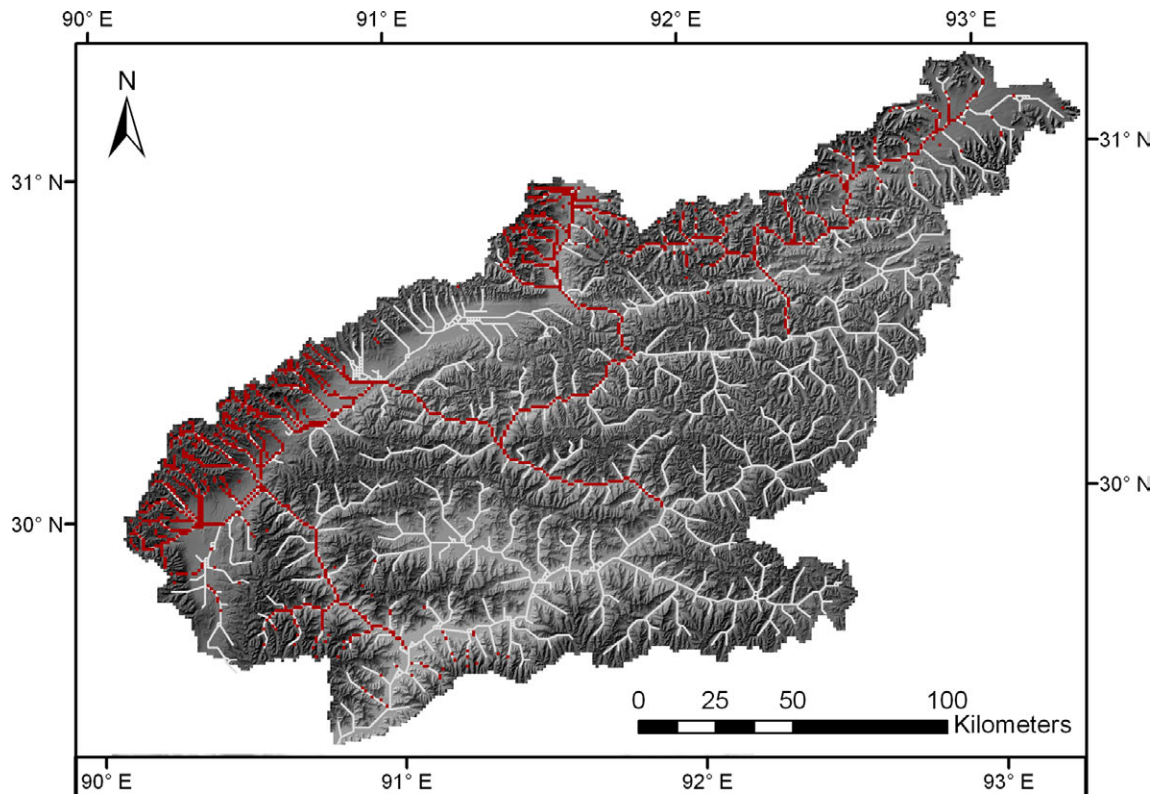
2011-2040 B1



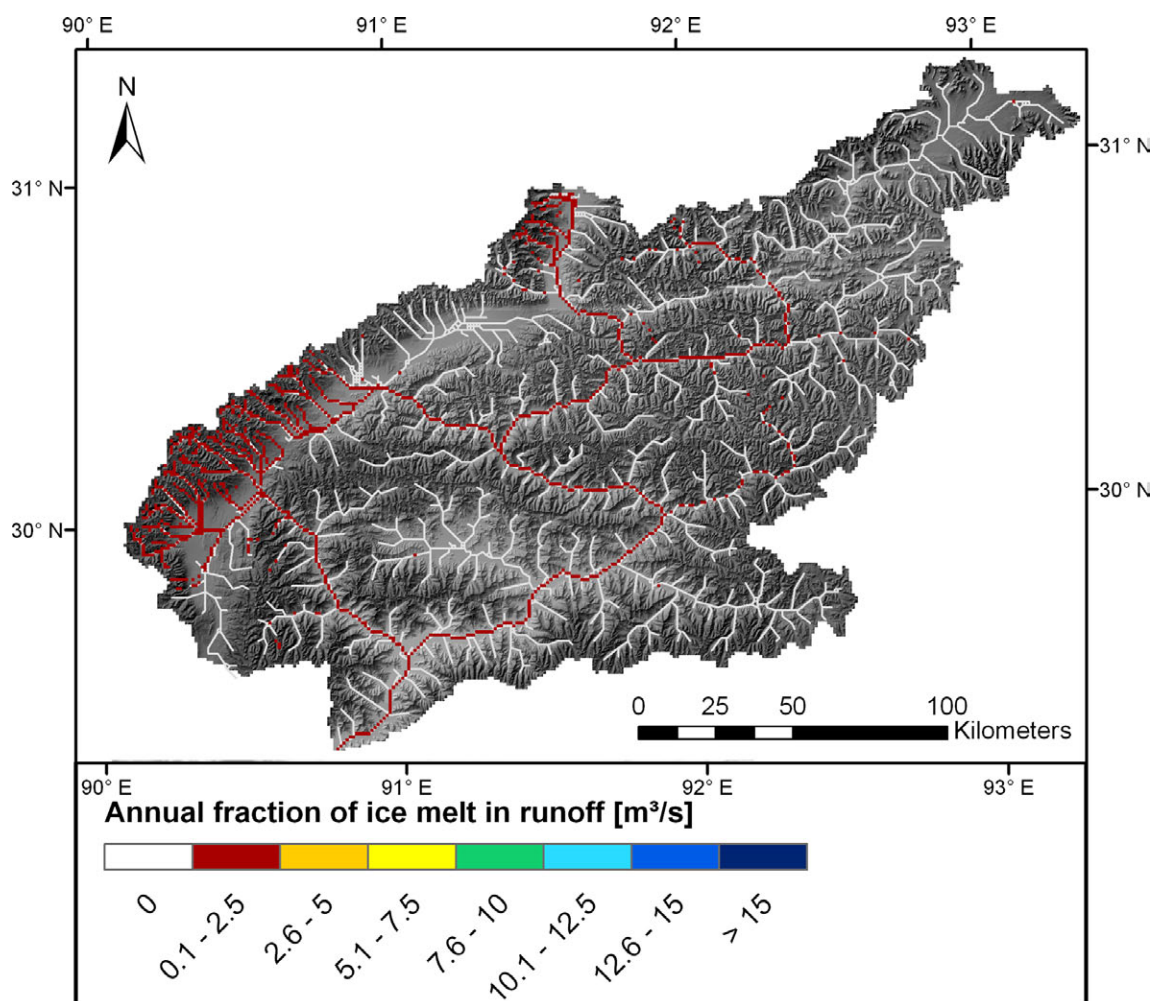
2051-2080 B1



2011-2040 CON

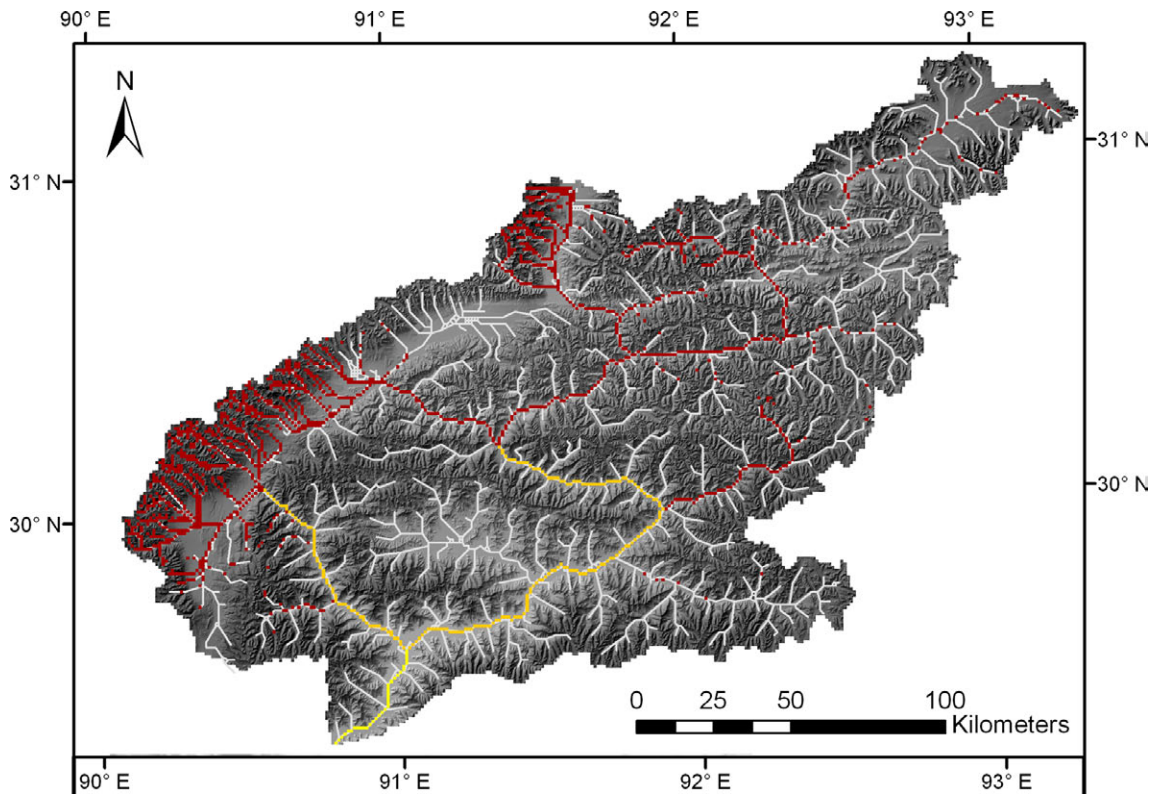


2051-2080 CON

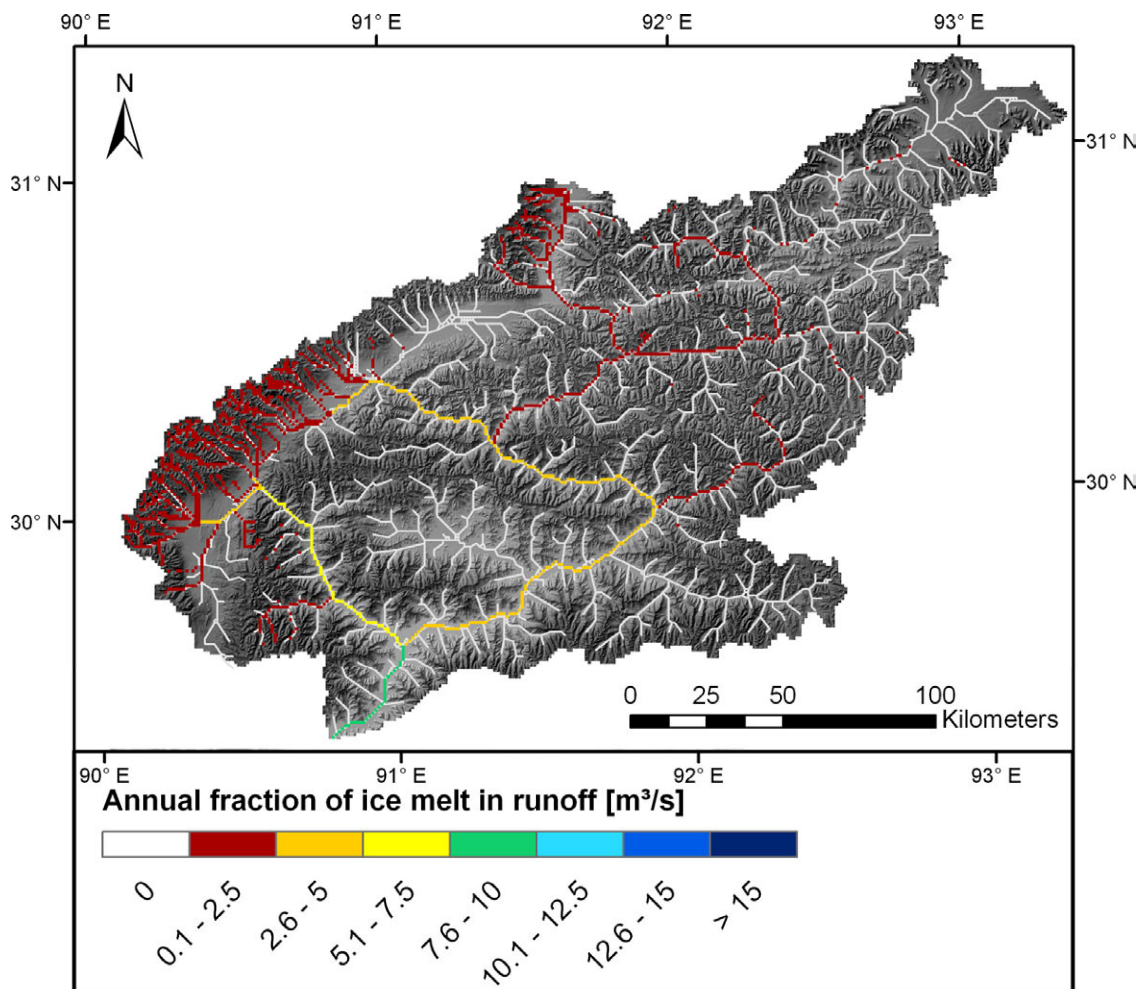




2011-2040 A2



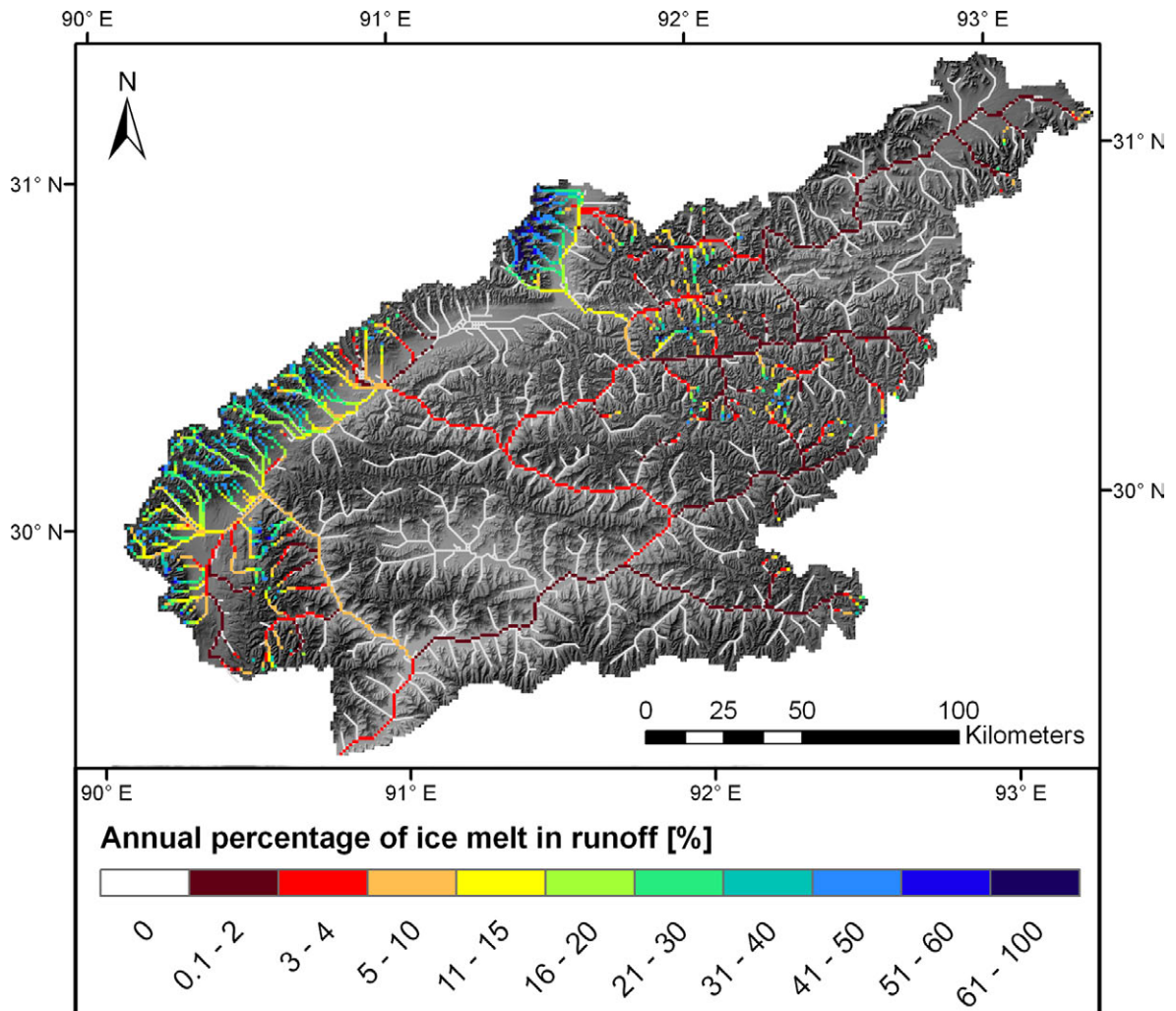
2051-2080 A2



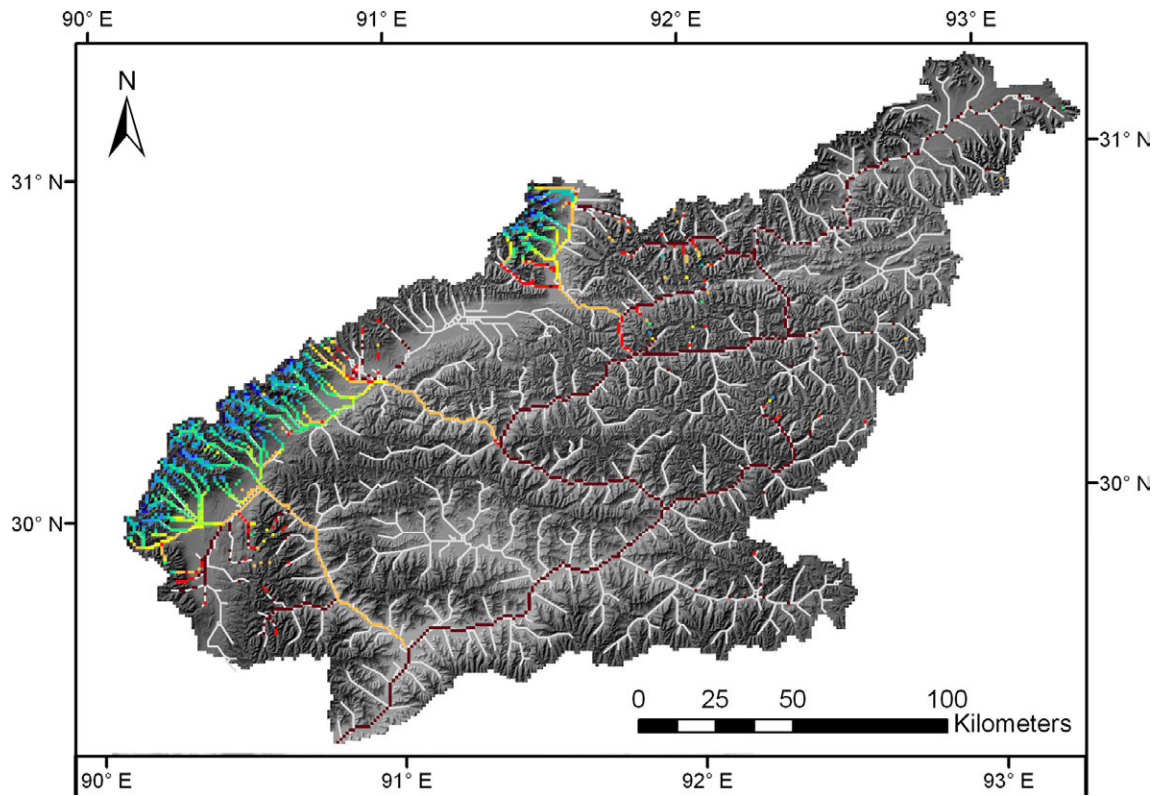
## Appendix 26

Mean annual percentage of ice-melt on runoff from 1971 to 2000 and in the future periods of 2011 to 2040 and 2051 to 2080 according to the four IPCC SRES scenario runs.

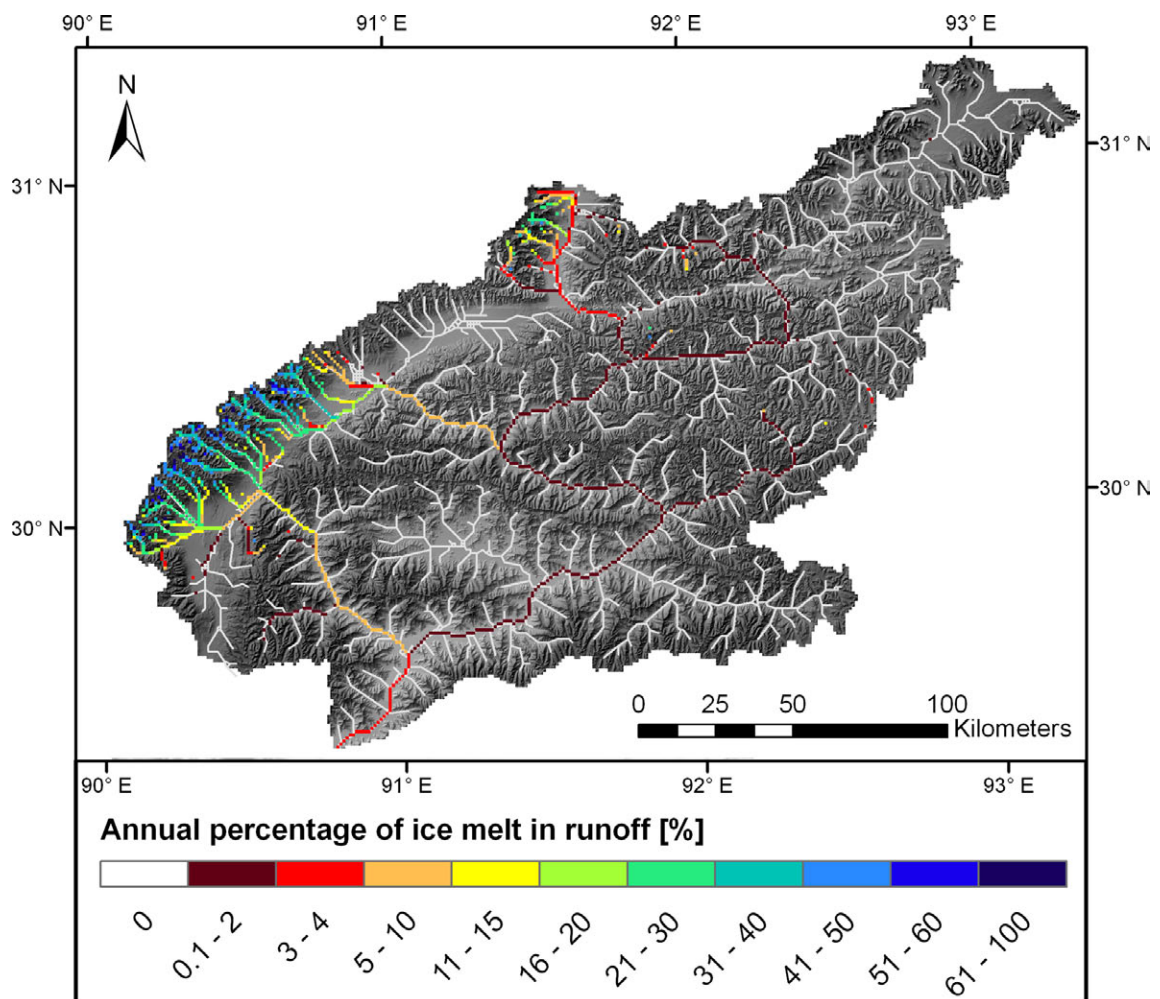
1971-2000 (ECHAM 5)



2011-2040 A1B

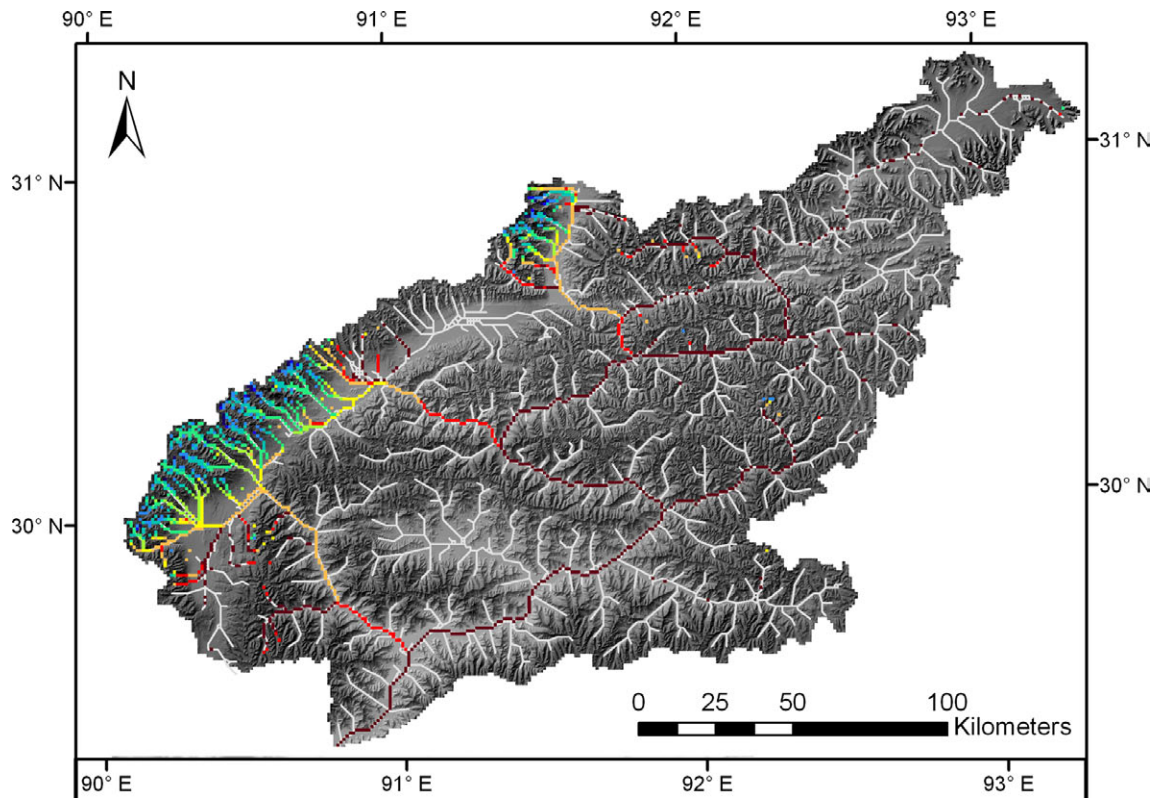


2051-2080 A1B

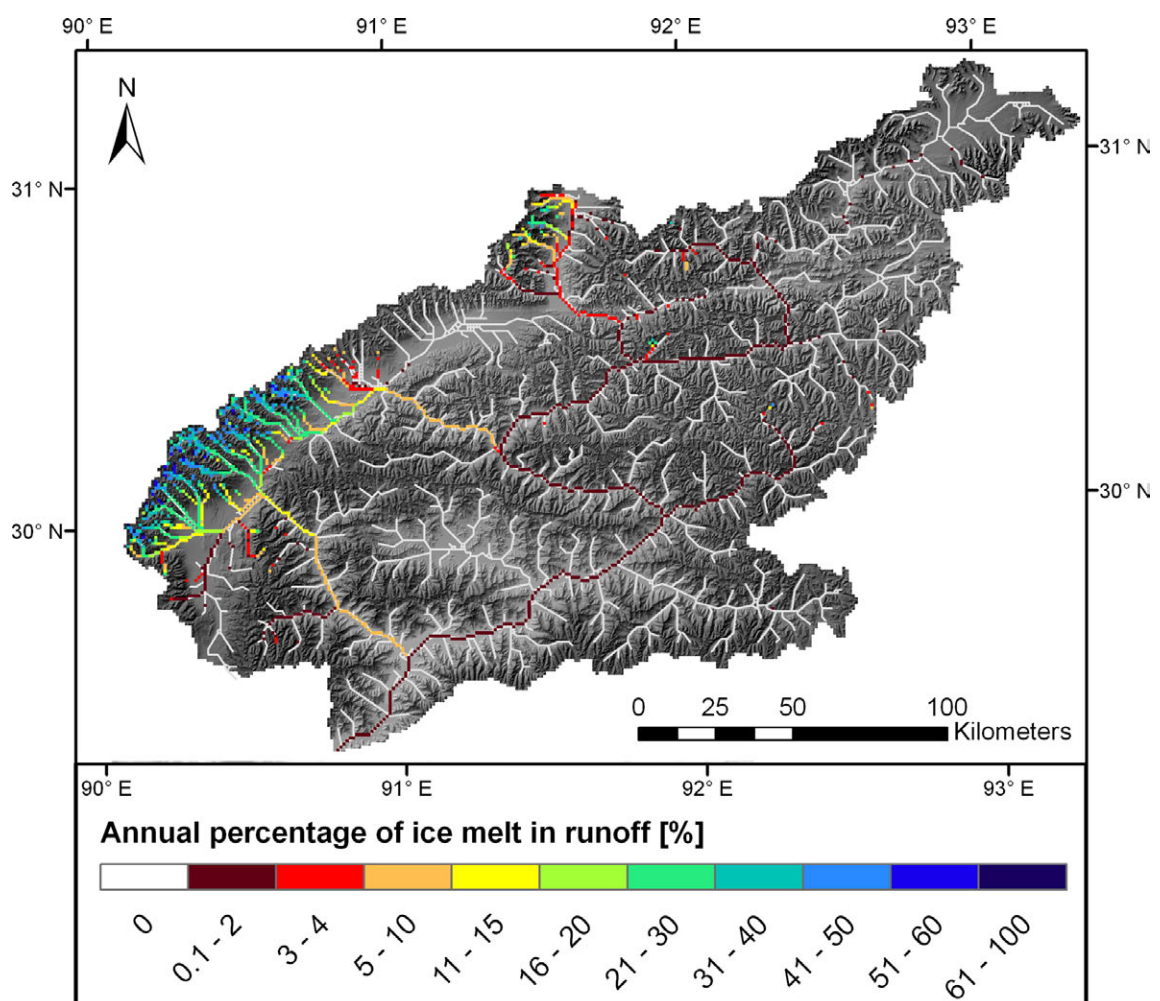




2011-2040 B1

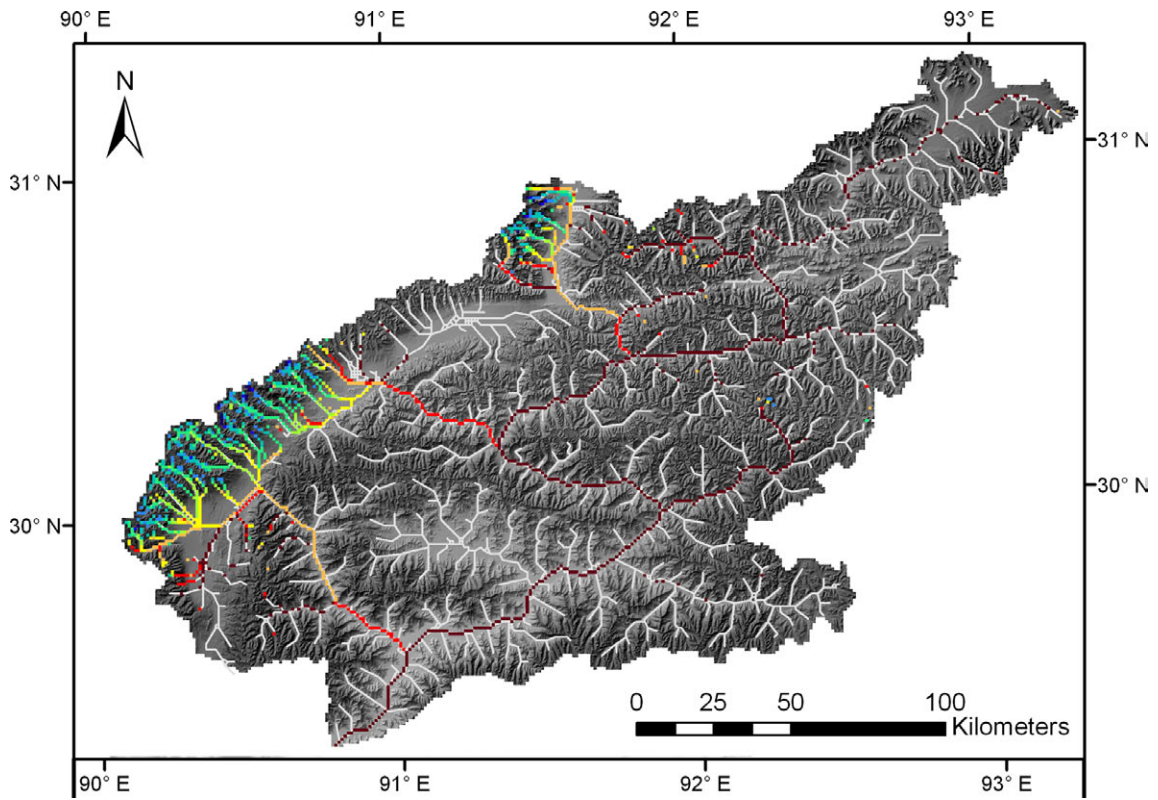


2051-2080 B1

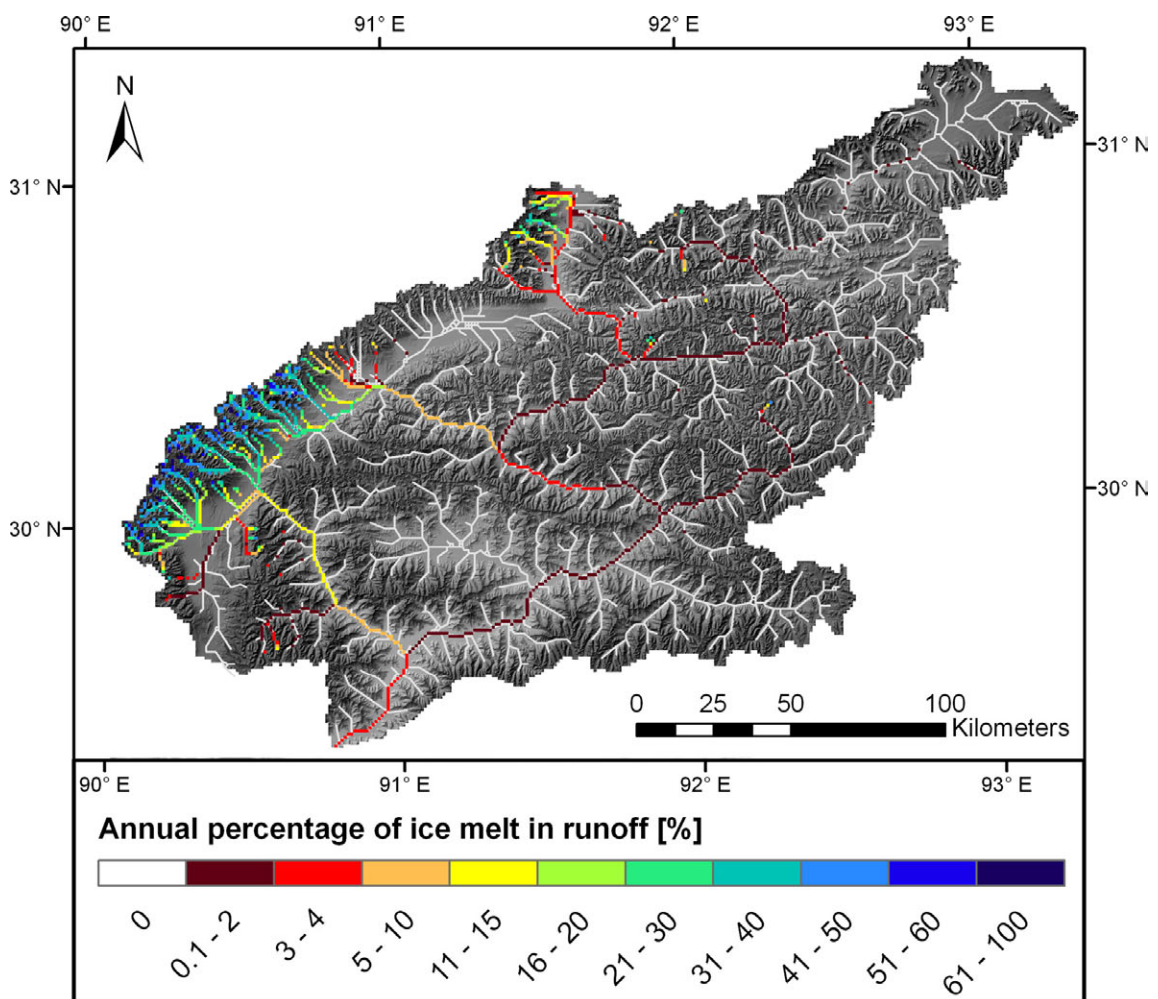




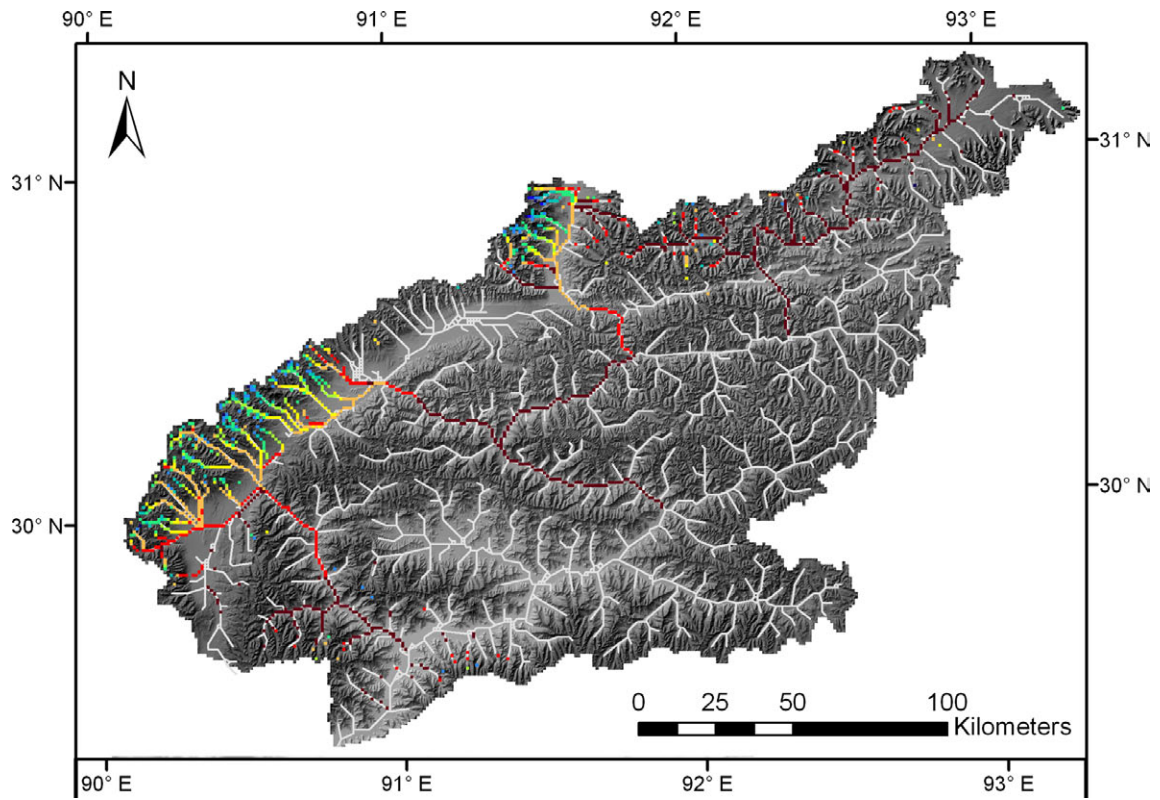
2011-2040 A2



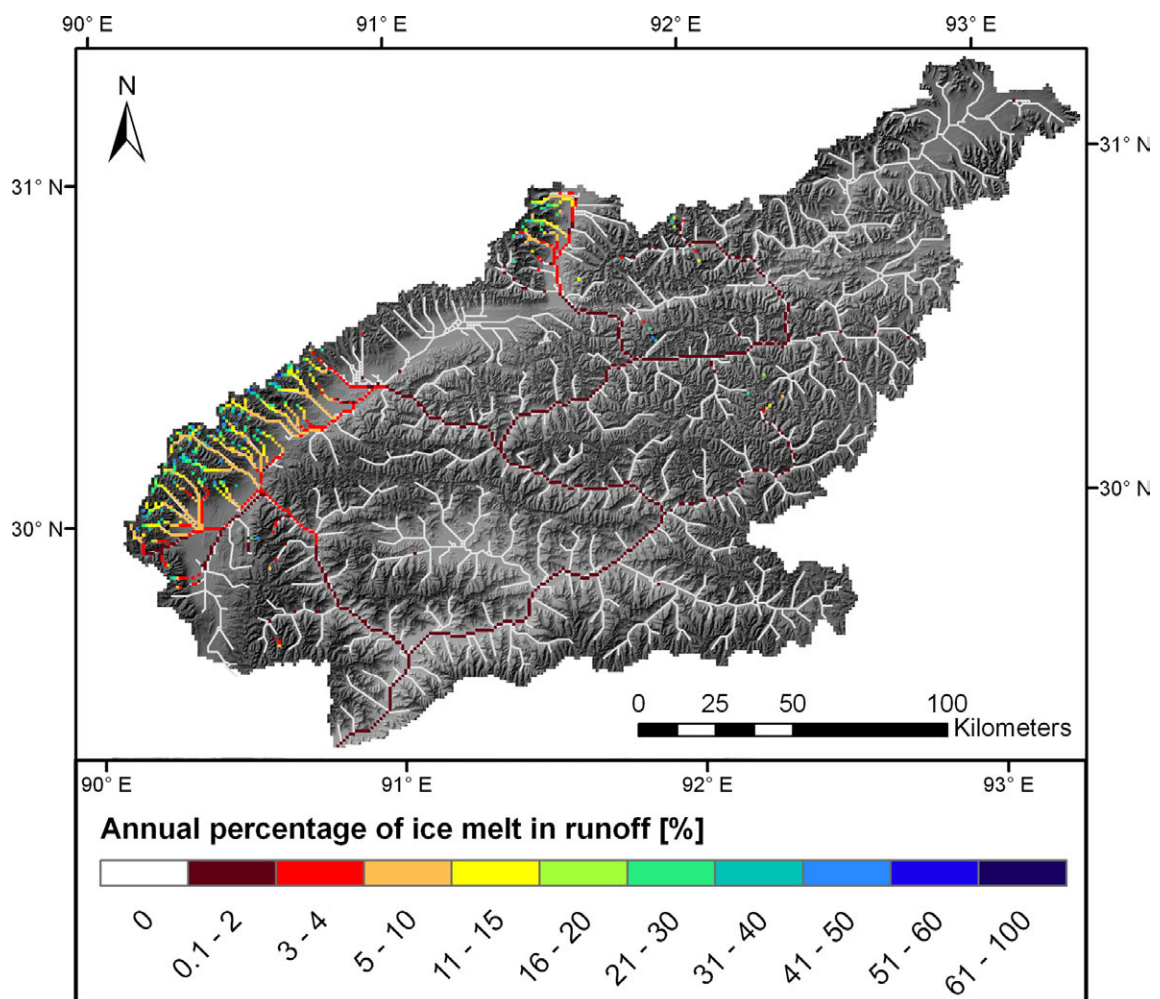
2051-2080 A2



2011-2040 CON



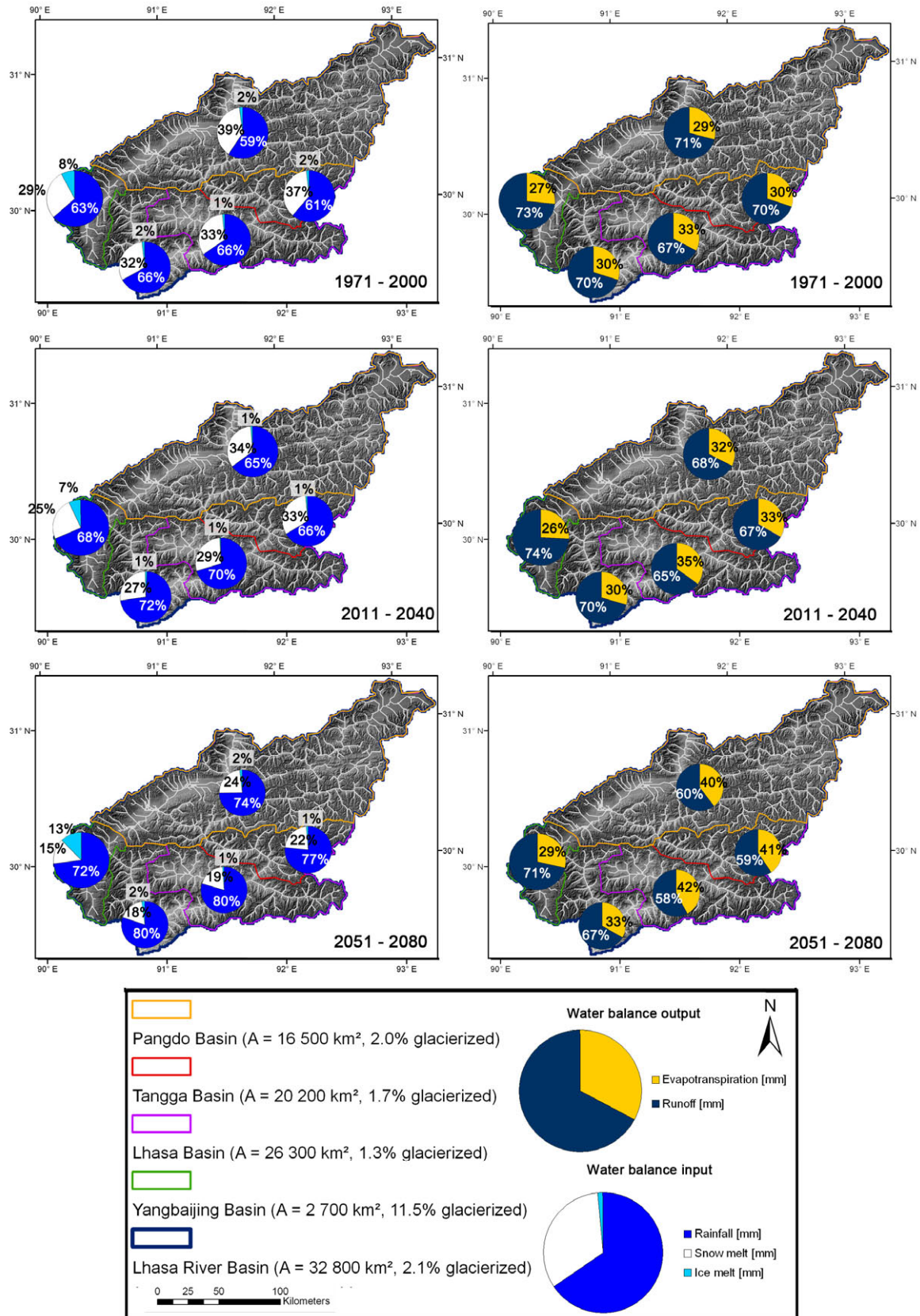
2051-2080 CON





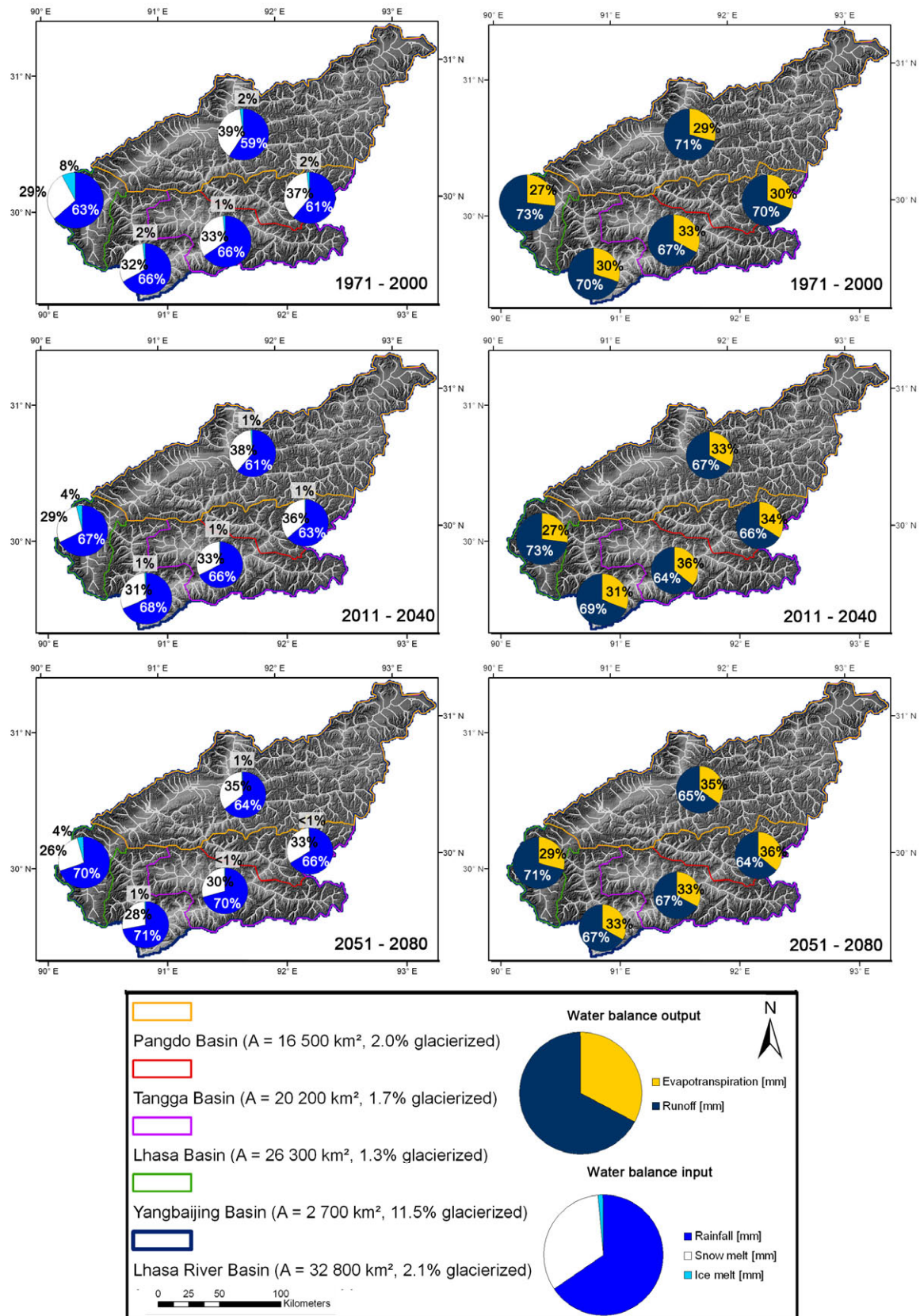
### Appendix 27

Mean annual percentage of inputs and outputs to the water balance in the sub-catchments from 1971 to 2000 (top), and in the periods of 2011 to 2040 (middle) and 2051 to 2080 (bottom) according to the A2 scenario.



### Appendix 28

Mean annual percentage of inputs and outputs to the water balance in the sub-catchments from 1971 to 2000 (top), and in the periods of 2011 to 2040 (middle) and 2051 to 2080 (bottom) according to the CON scenario.



# 11 Curriculum Vitae

## Personal Information

Name: Monika Luise Prasch, née Rothbart

Office address: Lehrstuhl für Geographie und geographische Fernerkundung  
Luisenstraße 37  
80333 Munich  
Germany

Telephone: 089 – 2180 6687

Email: [m.prasch@iggf.geo.uni-muenchen.de](mailto:m.prasch@iggf.geo.uni-muenchen.de)

## Education

2006 - 2010 PhD studies at the Ludwig-Maximilians-University of Munich, Germany

1998 – 2004 Studies of physical geography at the Ludwig-Maximilians-University of Munich, Germany, with the degree: Diplom-Geographin (Univ.), naturwissenschaftliche Richtung  
Minor subjects: physics, remote sensing  
Optional subject: meteorology  
Diploma thesis: „Die flächenverteilte Modellierung des Stickstoffhaushalts im Einzugsgebiet der Rott“ (Distributed modelling of the Nitrogen Balance in the Rott Catchment)

1997 – 1998 Undergraduate studies of meteorology at the Ludwig-Maximilians-University of Munich, Germany

1988 – 1997 Secondary School at the Gymnasium der Ursulinen in Straubing, Germany, with the Abitur (university-entrance diploma)

1984 – 1988 Elementary School in Rain, Germany



**Scientific career**

- Since 2007            Lecturer at the Chair of Geography and Geographical Remote Sensing, Department of Geography, Ludwig-Maximilians-University of Munich, Germany
- Since 2006            Collaboration in the EU (6<sup>th</sup> Framework Programme) founded project “Brahmatwinn” and the BMBF founded project “GLOWA-Danube”
- Since 2006            Scientific researcher at the Chair of Geography and Geographical Remote Sensing, Department of Geography, Ludwig-Maximilians-University of Munich, Germany
- 2004 – 2006           Scientific employee at Germany’s National Meteorological Service (Deutscher Wetterdienst), Business Area „Climate and Environment“, Department of Agrarmeteorology in Weihenstephan, Freising, Germany
- 2000 – 2002           Student researcher at the Chair of Geography and Geographical Remote Sensing, Department of Geography, Ludwig-Maximilians-University of Munich, Germany

**Internships**

- 08 – 09/2002           Agency of Natural Resources, Department of Environmental Conservation, Water Quality Division in Waterbury, Vermont, USA
- 08 – 09/2000           German Aerospace Center (Deutsches Zentrum für Luft- und Raumfahrt (DLR)), Remote Sensing Technology Institute in Oberpfaffenhofen-Wessling, Germany
- 03 – 06/1998           Authority for Rural Development (Direktion für Ländliche Entwicklung) in Landau an der Isar, Germany